A Radio Study of Gas Loss Processes in Nearby Galaxies

A Thesis

Submitted For the Degree of

DOCTOR OF PHILOSOPHY

in the Faculty of Science

by

Ananda Hota

DEPARTMENT OF PHYSICS

INDIAN INSTITUTE OF SCIENCE, BANGALORE

Bangalore – 560 012

JULY 2006

To my parents, Sykes and Aru

DECLARATION

I hereby declare that the matter embodied in the thesis entitled "**A Radio Study of Gas Loss Processes in Nearby Galaxies**" is the result of investigations carried out by me at the National Centre for Radio Astrophysics, Tata Institute of Fundamental Research, Pune, India under the supervision of Prof. D. J. Saikia and Prof. Chanda J. Jog and that it has not been submitted elsewhere for the award of any degree or diploma.

In keeping with the general practice in reporting scientific observations, due acknowledgement has been made whenever the work described is based on the findings of other investigators.

Ananda Hota

CERTIFICATE

We hereby certify that the matter embodied in this thesis entitled "**A Radio Study of Gas Loss Processes in Nearby Galaxies**" has been carried out by Mr. Ananda Hota at the National Centre for Radio Astrophysics, Tata Institute of Fundamental Research, Pune, India under our supervision and that it has not been submitted elsewhere for the award of any degree or diploma.

Prof. D. J. Saikia	Prof. Chanda J. Jog
(Research Supervisor	(Research Supervisor
NCRA-TIFR)	JAP-IISc)

I Thank ALL

Of course my parents would be the first I should thank for my existence. They have been a constant support for all my endeavours. Most of the credit for my personality development can be attributed to the environment of a small town in western part of Orissa called Sonepur. Till my B.Sc. I had all my education there in Sonepur. Although there are many people I feel grateful towards in the context of my research career it will become too long and let me just narrate a small event of my childhood and then start abruptly from my life as a JAP-IISc student.

There is an interesting event of my school days which is a surprising coincidence with me doing radio-astronomy research with the best telescopes of the world, the VLA and the GMRT. When I saw a chart of the electromagnetic spectrum (in an Oriya medium book) I suspected that the Sun, which is giving visible light and also heat (infrared light) may be radiating radio waves as well. To detect that, one day I got up early in the morning spread out a long iron wire over the staircase facing the east and connected it to the aerial of a small transistor (silently taken from my parents' bedroom). I was waiting for the sunrise so that when sunlight falls on the long wire radio waves will also come and the sound (noise) level of the radio will go up and I will detect radio waves from sky or Sun. In those days the only sources of radio waves were Sambalpur and Cuttack radio stations. Although I could not conclude anything from that radio astronomy experiment, my astronomy interest started with my optical telescope making, night sky watching and astrology arguments with my father.

IISc is fantastic. No comparison to any place in India. Arnab's

Introduction to Astronomy lecture course was just great for me as I was learning Astronomy for the first time from some professional astronomer. Lectures of Chanda were very interesting as I had never read about gas and dust in space. The classes of Shrini and Prajval I enjoyed the most. I miss Subhasis Sarangi my IISc friend. We used to logically argue, even whole night long on anything except political leaders and film actors. I thank all my friends Vikram, Poonam, Malaya da, Martha, Bijaya, Resmi, Pandey, Pushpa, Ravinder, Vivek, Shalima and Latha for a nice life in Bangalore. When I started worrying about a PhD guide, I have troubled my seniors a lot. I thank them all Chaitra, Ambika, Girish, Sanmuga and Niruj Mohan. As I was very keen to do well I focussed only on GMRT, the world's largest radio telescope at metre wavelengths. I was also clear to work on galaxies. During this time Prof. Govind Swarup visited Bangalore. I went to meet him and expressed my interest to work with the GMRT.

Interaction with Prof Gopal Krishna is always inspiring and I went to work with him in NCRA for my graduate school project. I worked on 'Cluster radio sources and the hot intra-cluster medium.' I thank Vasant for teaching me AIPS in those days. During this period company of Seema, Neeraj and Prabhu, Komal, Aparna, Arati, Sarad, Sidharth, Nissim, Poonam, Div and Jayashree was nice to remember for all time to come.

For my PhD I joined Prof. D.J. Saikia (Sykes) to work in the broad area of galaxies with outflows. He gave me lot many papers to read and two data tapes. Soon he left on his subbatical to Canada. During this period I worked with Prof Anantharamaiah, Dr Nimisha Kantharia and Dr Niruj Mohan on trying to detect radio recombination lines from the starburst galaxy M82 using the GMRT. After his return Sykes also joined. Shockingly before we could make any progress Prof. Anantharamaiah passed away. His death and the death of Prof. Bhaskar Dutta I sadly remember when I think of students and astrophysicists in India. Gradually we realized that getting good and quick results on RRLs with the GMRT at that stage was a very challenging

job. In those early days of AIPS data analysis the only senior in NCRA who could help me was Subhasish Roy, thanks a lot Subhasish! I left working on RRLs and got back to radio continuum observations and trying to detect outflows.

For my thesis work, I worked with a number of colleagues and collaborators whom I wish to thank. The pieces of work on NGC1482, NGC6764 and Abell 1367, were done in collaboration with Sykes, while the work on NGC4438 was done in collaboration with Sykes and Prof Judith Irwin. For the work on these objects, I have made all the radio images presented in this thesis and also done the interpretation. For the group of galaxies, Ho 124, I worked in collaboration with Dr Nimisha Kantharia, Prof. S. Ananthakrishnan and Prof. Rajaram Nityananda. For this piece of work, the images were made by Dr Nimisha Kantharia and I worked on the interpretation of the observations.

I also wish to thank Judith Irwin for giving me time at very short notices and especially when she was very busy. I thank her for the bicycle I am still enjoying. I thank Dr. Kohno Kotaro and Dr. Satoki Matsushita for collaboration on molecular line observations related to outflows, Dr. Dinh van Trung and Dr. Jeremy Lim for collaboration on interacting galaxies, Dr. Sylvan Veilleux and Dr. Dave Strickland for discussions on optical and X-ray outflows, Dr. Jonathan Braine for discussion on molecular line work and interacting galaxies. I thank him also for showing me the advanced form of VLA archival data down-loading. I thank Dr. Ashok Singal for discussions on synchrotron radiation. I thank Prof William Baan and his wife for great discussions on astrophysics and humanity respectively.

The training of accuracy in making a scientific statement from my guide Sykes is a lesson I have to practice throughout my life. He is a nice man and he is an inspiration to work; no matter whatever happens in my life, hope I will never forget him and be able to work hard. I am thankful (no word is appropriate) to him and beg apology for not being able change myself as he advised and being cause of (only a few!) his headaches.

NCRA where I have spent 6 years of my life has certainly given many happy (humanly) events apart from giving opportunity to do research in radio astronomy. It will be numerous to note and may become irrelevant. I thank Prasad and his mother for an Oriya environment for me when I was feeling really lonely in NCRA. I thank the Kalinga Cultural Society of Pune University for giving me a life outside astrophysics in Pune. How can one forget Dr. Rajiv K. Singh (RK jee), who is such a marvellous person with whom one can talk on anything with just logic and with the already available information. I thank the operators and the personnel who maintain and run the VLA, GMRT, NED, ADS, GoldMine, Sky view, astro-ph, Latex, GNU group, and also the Kanwal Rekhi fellowship for financial support. I thank Sunita, Suresh for the library facility, VVS for computer facility, and Sekhar, ABA, Lokhande, Rina, Annabhat, Shetty, Barve, Khatavkar, Solanki, Pawar, TVA. I thank the Canteen staffs, Security guards, cleaners. Most of my observations and the thesis went well with the numerous scientific, engineering and technical staff; they deserve due credit in this thesis. I would specially like to name all the GMRT operators Sanjay, Santaji, Sachin, Deepak, Manisha, Manish, Jayprakash, Jitendra and Mangesh. My office-mate Neeraj, what to say, we have discussed everything and I am sure we have tried to learn some good things from each other; he has been great during my NCRA stay. It has been a great time in Pune, Nirupam, Manojendu, Ekta, Ayesha, Viswesh, Kiran, Jayanta, Bhaswati, Chiranjib, Arpita, Mamta, Punya, Susmita, Soumya, Subharthi da, Sameer, Mayur, Prasad, his mother, Ganapati, Seeby, dhanya, Sushree, Kanan, Alok, Jyoti, all the lovely kids of NCRA and many more are thanked for that. Sanjay Bhatnagar, Sandip Sirothia, Nissim Kanekar, BC Joshi, R Srianand, Kandaswami Subramnian, Divya Oberoi, C.S. Stalin, Sambhunath Nayak, Subhendu Joardar, Raja jee, Jayaram Chengalur, Ranjeev Mishra, Niruj Mohan, Seema M, Rajvi Pandya, Late Srikumar jee, and few more are the people from whom, like Abadhuta

I have tried to learn something good. I thank Pramesh, Parvathi and Ananthakrishnan and Sudha for many other things and nice dinners. I thank Rajaram and Usha and Amma for nice singing sessions in their house, Dharam and Babita for many many treats in their flatlet-home. A nice/high Hello from NVN is unforgettable. I thank Bhalerao sir, my Yoga teacher. I thank Dipanjan da and Anindita di for making me feel their home as of my elder brothers. Another home for me was my sister Sandhya's home along with uncle and aunty.

When a sister has come let me thank all my dozens of sisters who have made my life really very beautiful. Sometime I feel sad about not being able to be at home when the family members need me. Bapa, Ma, Nani(Kalindi), Bhai(Gopal), DKA, DIKAN and my dearest Aru, thinking about them I feel guilty that I am not able to give as much as love and care I should give. I thank them all for still supporting me. I hope in future I will be able to take care of them better. There is no word to thank Aru who has shown unexpectedly high level of thinking and loved and supported me in all correct works.

Collaboration with Dr. Dinh van Trung and Dr. Jeremy Lim and meeting Dr Lim at GMRT was a pleasure. I consider my interaction with Dr. Jeremy Lim as one of the unforgettable event of my academic career. It was a happiest moment when I got a phone call from Prof. Paul T.P. Ho, Director, ASIAA, Taiwan and he offered me a post-doctorial position in ASIAA. I am grateful to everybody who supported me for this. After this happy inspiring event I am looking forward to finish my thesis well and start new works in ASIAA with Jeremy Lim and others on topics of my interest.

I thank IISc and TIFR directors for all the facilities I have got for completing this research. I thank NCRA director, IISc Dean, NCRA Dean, Chairman Department of physics for all the official supports. I thank my local guide Prof. Chanda J. Jog, Prof Arnab Raichoudhuri, Mrs Rakma and Mrs Meena . Again I thank all.

−Ananda Hota

Synopsis

Name of the student: Ananda Hota

Degree Registered: Ph.D.

Names of the supervisors: Prof. D. J. Saikia and Prof. Chanda J. Jog

Thesis Title: A Radio Study of Gas Loss Processes in Nearby Galaxies

---

The work in this thesis involves detailed multi-frequency radio continuum (from 325 MHz to 15 GHz) and HI spectroscopic studies of a few representative nearby galaxies which are experiencing gas-loss from their disks due to different physcial processes. These processes are starburst-driven superwind, active galactic nucleus (AGN)−driven nuclear outflow, ram pressure stripping and tidal interactions. Gas-loss could affect the evolution of individual galaxies with age as well as their evolution with cosmic epoch. We have made use of both the Giant Metrewave Radio Telescope (GMRT) and the Very Large Array (VLA) for our study.

Stars and gases are the two major constituents of a galaxy. The properties of the gaseous medium in them change with galaxy-types, such as the presence of large amount of gas in the late type disk galaxies and little interstellar medium (ISM) in the ellipticals or early−type galaxies. Galaxies in groups and clusters interact with each other and with the low density gaseous medium surrounding them, resulting in a possible evolution of their structures and physical properties. Basic differences in their observed properties depend on their history of interactions with the environment and also on the history of their central activities. Tidal interaction among galaxies may result in the flow of gas into the central region of the galaxy. This can trigger a central starburst and/or feed a central super-massive black hole to trigger

an AGN activity. These activities produce either starburst-driven superwind or AGN-driven nuclear outflows (accretion disk wind or bipolar radio jet/bubbles) and the galaxy may lose their metal-enriched central gas concentration to the intra-cluster (ICM) or intergalactic medium (IGM). There are suggestions that when large amount of gas is cleared out from the central region of an ultra-luminous infrared galaxy (ULIRG), the dust enshrouded hidden AGN may unveil itself as a bona fide quasi-stellar object (QSO). Galaxies also lose gas usually from the outer parts when they move through the intra-cluster medium (ICM) or intra-group medium (IGrM) due to ram pressure stripping. When the ram pressure is stronger than the pressure by which the gas is bound to the galaxy, most of the gas may be lost or displaced from the disk thus affecting the star formation and metal formation in the disk of the galaxy.

Starburst galaxies and superwinds: The starformation rate or the supernovae rate in some gas rich galaxies are 10−1000 times higher than that of the normal galaxies. This process can consume large amount (1−30$\times$ 10^9 $M_\odot$) of gas over a short time scale (10^{7-8} yr) in a small region (typically 1 kpc). During such bursts of starformation, the cumulative effect of many supernovae and stellar winds from the massive stars in the central region of a disk galaxy imparts huge amount of mechanical energy to the ISM of the galaxy which then creates a high pressure (4 orders of magnitude higher then the average ISM pressure in the Milky way), high temperature (10^{6-7} K) bubble of gas. This high pressure and high temperature bubble of gas expands and flows outwards in the direction of the steepest pressure gradient. This outflowing hot gas carries cooler gas and dust from the ISM along with it. It carries out heavy metals cooked in the central region of a galaxy to the external environment including the ICM or IGM. The typical outflow rate is 10−100$M_\odot$ yr^{-1} with typical outflow velocity of few 100−1500 km s^{-1} and it persists over few to 10 million yr. The observed sizes of such outflows are 1−20 kpc.

We have studied a remarkable starburst-superwind system, NGC1482. This early type galaxy has been discovered to have a bi-conical shaped soft X-ray outflow as well as Hα and [NII] outflow. The low-frequency radio-continuum flux density was used to estimate the supernova rate, which could be used to constrain the dynamics of the driving force. The high-frequency

high-resolution VLA observations revealed the central starforming region which is at the base of the bi-conical structure and presumably driving this outflow. The HI observations also have resulted in finding two blobs of HI on opposite sides of the galaxy defining an axis perpendicular to the outflow axis and rotating about it. We have also detected a multi-component broad ($\sim$ 250 km s^{-1}) HI-absorption spectrum against the central continuum source. The absorption spectrum is nearly 70 km s^{-1} asymmetric towards the blue side with a component blue-shifted by 120 km s^{-1}. The observed absorption could be due to the HI-clouds driven outward by the central superwind outflow.

Active galaxies and nuclear outflows: The inflow of gas to the central region of a galaxy triggers the starformation as well as the AGN activity. Co-existence of both these phenomena in some cases are well known. The accretion disk of the AGN can produce a hot wind emitting in X-rays in addition to the radio continuum jet perpendicular to the accretion disk. It is known that the AGN jets, in particular Seyfert jets have no correlation with the rotation axis of the host disk-galaxy. In such a scenario a very complex geometry can arise. Radio jets may interact with the starburst-driven winds or winds from the accretion disk or with the clouds of ISM of the galaxy accelerating and ionizing the gas. Sometimes the mass outflow rate may be ten times the mass accretion rate necessary to fuel the AGN, suggesting heavy mass loading of these AGN outflows. Depending on the energy of the outflow processes gas may be ejected out of the gravitational field of the galaxy.

We have studied a composite galaxy, NGC6764 with an AGN and a very young starburst with two episodes of starformation, one 3$-$5 and another 15$-$50 Myr ago. The high-resolution high-frequency radio-continuum observations reveal a radio core and roughly bi-conical radio emission oriented along the major axis of the galaxy with a feature which could be a jet. The lower-resolution images show bi-polar radio bubbles oriented along the minor-axis of the galaxy. These edge-brightened radio bubbles are asymmetric in size, extent (north-south) and luminosity. There is an east-west asymmetry in the spectral index of the bubbles. In a representative sample of dozen such radio bubbles in nearby galaxies we find that invariably all of these

have an AGN. Similar to few other galaxies in the sample we also found that the radio continuum bubbles in NGC6764 are well correlated with the Hα filaments extending along the minor-axis of the galaxy. The CO(J=2-1) and CO(J=1-0) flux density ratio is also higher at the tip of the bubbles. Molecular gas plumes are seen extending along minor axis and have components blue-shifted by 140 km s^{-1}. Our high-resolution HI observations also show an absorption component at the systemic velocity with a weak component blue shifted by 120 km s^{-1}. We have discussed the possibility of the radio plasma ejected from the AGN being carried outwards along the minor-axis by the superwind created by the young circumnuclear starburst. That bubble of hot gas from the superwind mixed with the relativistic plasma from the AGN is interacting with the cooler HI and molecular gas of the ISM and driving it outwards. This interaction which is possibly in an early phase of expansion is also giving rise to the outflowing Hα filaments in this interesting composite galaxy.

Cluster galaxies and stripping processes: When a galaxy moves through the hot and dense ICM with velocities $\sim$1000 km s^{-1}, the ram pressure exerted by the ICM can strip the loosely bound and more tenuous gas of the galaxy. As a result of this the dense molecular gas or the stars in the galaxy remain almost unaffected but the tenuous gas moving out of the galaxy's gravitational field could reach the ICM. The fate of such stripped gas is not well constrained. Recently very long tails with sizes of 50$-$125 kpc have been discovered. Some of these are magnetised, some ionised, some neutral and some are million degree hot. These tails may cool and eventually form galaxies or may evaporate and mix with the ICM. They enrich the ICM with metals and magnetic fields. In some cases galaxies are known to have become as high as 90 % deficient in HI in comparison to the corresponding field galaxy of same type, size and luminosity. In the cluster/group environment tidal interactions with other group/cluster members or the cluster potential well could also take place affecting the observed properties of the galaxy. In addition, tidal interactions could also facilitate the removal of gas by ram pressure due to the ICM or IGrM.

NGC4438 which we have studied in detail is an archetypal example of a galaxy which has been severely affected by the cluster environment. This

late-type galaxy in the central region of the Virgo cluster is known to have interacted with the northern companion NGC4435. We have unambiguously resolved the radio nucleus from the lobes of radio continuum emission, and have shown it to have an inverted spectrum confirming it to be the nucleus. The lobes are almost perpendicular to the central molecular or stellar disk which is seen nearly edge-on. Projected onto the plane of the sky the lobe-axis is roughly parallel to the direction of the ram pressure wind. The lobes are very asymmetric in its extent, size and luminosity. The lobes are shell-like in structure and are interacting strongly with the asymmetric ISM. In the region of interaction both Hα and soft X-ray emission shells are seen. We explore possible reasons for the asymmetry in the lobes which is unlikely to be only due to the asymmetry in the density of the ISM on opposite sides of the galaxy. On a larger scale we have imaged the diffuse lower-frequency radio-continuum emission 5 kpc away from the central region seen on the western side of the disk of the galaxy. This extended emission has flatter spectral index at higher frequencies which suggests it to be a mixture of thermal and non-thermal components. In this region Hα, soft X-ray, HI, molecular gas and relativistic plasma (i.e. all phases of the ISM) have been detected. We have found a linear structure on the western side near the same region with mass of nearly 200 million $M_\odot$. We have imaged the HI$-$emission from the stellar disk for the first time. The HI -velocity field shows that the extra-planar gas could be rotating slower then the disk as seen in cases of ram pressure stripping. At lower resolution we detect more HI from the halo of the galaxy. The iso-velocity contours appear to curve towards the axis of rotation or direction of the ram pressure wind, as you go away from the mid plane. We discuss whether this might be due due to the interaction of NGC4438 with NGC4435. We have discovered a 50 kpc long faint tail of HI having a mass of 140 million solar mass to the north-west of the NGC4438$-$NGC4435 system. This HI$-$tail partially coincides with an extremely faint ($\mu_v > 28$) stellar tail, which has been seen in the deep optical imaging of intra-cluster light. Such tails have not been predicted by the simulations of interaction between NGC4435 and NGC4438. Hence it seems to be a remnant of some past event in the evolution of this interesting system.

To further study the effects of ram pressure stripping and tidal interaction in galaxies in a group, we have studied the group Ho 124. We found that the

radio continuum bridge of tidal interaction between NGC2820 and NGC2814 has a very steep (α=−1.8) spectrum possibly due to the older relativistic plasma left in it. The HI of NGC2820 has sharp truncation on the south-eastern side parallel to the edge on disk, while it has a unipolar huge loop on the north-west. NGC2814 has both an HI and radio continuum tail different from the connecting bridge with sharp truncation again on the side opposite to the tail. Although there is reasonable radio continuum emission from the disk of NGC2820, there is no detectable emission corresponding to the huge one sided HI loop. The velocity field of the HI-loop trails that of the underlying stellar disk. Also in the galaxy NGC2805, a member of the same group, we find the HI to have accumulated on the northern side while there is a bow-shock shaped starformation arc on the southern side of the disk. All these features namely starformation arc, sharp cut off in the HI -disk, HI-loop and HI and radio continuum tails are signatures of ram pressure stripping. Ram pressure stripping in groups is relatively rare but this could get assistance from tidal interactions which help loosen the gravitational bound of the stellar disk on the tenuous ISM.

A more spectacular case of ram pressure stripping is seen in the cluster Abell 1367. We have studied a region of the cluster A1367 where three of its galaxies namely CGCG 09773, CGCG 09779 and CGCG 09787 exhibit amazingly long (50−75 kpc) tails of radio continuum and optical emission lines (Hα) pointing roughly away from the cluster centre. They also show arcs of starformation on the side facing the ram pressure of the cluster medium. In our HI study we found that all three of them have higher mass of HI on the down-stream side. Two of the galaxies (CGCG 09773 and CGCG 09779) exhibit sharper gradients in HI intensity on the side of the tail or on the down-stream side. However the HI emission in all the three galaxies extends to much smaller distances than the radio-continuum and Hα tails, and are possibly still bound to the gravitational pull of the respective galaxies. These results are in good agreement with the hydrodynamical simulations of ram pressure stripping in cluster medium.

In this study we have found a number of interesting results on a few nearby galaxies where different gas-loss processes have modified the morphology and kinematics of the ISM and/or the stellar distribution of the

respective parent galaxies. We have found evidence of blue-shifted HI absorption lines driven outwards by the starburst-driven superwinds and/or AGN-driven nuclear outflows. The synchrotron plasma outflowing from an AGN in a composite galaxy has been suggested to be interacting with the superwind which also drives other components of the ISM outwards. In groups or clusters of galaxies we have discovered an HI loop, HI tails, regions of compressed HI, trailing velocity fields, slow-rotating extra-planar gas, displaced ISM and asymmetries in various radio continuum or HI features as evidences of ram pressure stripping mechanism affecting the member galaxies. The results obtained from this study illustrates the manifestations of gas loss proceeses in galaxies existing in different environments, and should provide valuable insights for future investigations with larger statistical samples towards a more complete understanding of gas loss processes in galaxies and their implications on galaxy evolution.

0.1 Publications

In Refereed Journals

- A radio study of the superwind galaxy NGC 1482.
  Hota A. & Saikia D.J., 2005, MNRAS, 356, 998

- GMRT observations of the group Holmberg 124: Evolution by tidal forces and ram pressure?
  Kantharia N.G., Ananthakrishnan S., Nityananda R., Hota A., 2005, A&A, 435, 483

- Radio bubbles and superwind outflow in NGC6764.
  Hota A. & Saikia D.J., 2006, MNRAS, (in press)

- NGC 4438 and its environment at radio wavelengths.
  Hota A., Saikia D.J. & Irwin J.A., 2006 (to be submitted shortly)

- HI study of of three long-tailed irregular galaxies in A1367.
  Hota A. & Saikia D.J., 2006 (to be submitted shortly)

In Conference Proceerings

- Outflows from nearby active galaxies
  Hota A., Saikia D.J., Irwin J.A.
  XXVIIIth General assembly of URSI, New Delhi, October 2005

- GMRT Observations of the group Holmberg 124 + Priliminary results on Holm 377 and Holm 565
  Kantharia N.G., Ananthakrishnan S., Nityananda R., Hota A.
  XXVIIIth General assembly of URSI, New Delhi, October 2005

- Outflows from three active galaxies: NGC 1482, NGC 4438 and NGC 6764.
  Hota A., Saikia D.J., Irwin J.A.
  23rd Meeting of the Astronomical Society of India, ARIES, Nainital, India February 21-24, 2005
  2005, BASI, 33, 399

- Radio Study of a Superwind-galaxy: NGC1482
  Hota A., Saikia D.J.
  22nd Meeting of the Astronomical Society of India, Thiruvanthapuram, India, Feb 13-15, 2003
  2003, BASI, 31, 425

- Circumnuclear starbursts and nuclear activity: NGC6951
  Saikia D.J., Kantharia N.G., Hota A., Phookun B., Pedlar A., Kohno K.
  Active Galactic Nuclei: from Central Engine to Host Galaxy, Meudon, France, July 23-27, 2002
  Eds.: S. Collin, F. Combes and I. Shlosman. 2003, ASPC, 290, 543 (not included in the thesis)

List of Figures

List of Tables

Contents

CHAPTER 1

Introduction

The evolution and physical properties of individual galaxies as well as the evolution of their properties with cosmic epoch or redshift can be profoundly affected by the history of interactions with their environments and mass loss from their interstellar medium (ISM). We have studied a few galaxies using both the Giant Metrewave Radio Telescope (GMRT) and the Very Large Array (VLA) at a number of radio continuum wavelengths and have also made spectroscopic observations in the 21cm atomic hydrogen (HI) line towards understanding the different processes which affect their structures and mass loss from the disk of the galaxies in different situations. Observations at radio wavelengths are largely unaffected by absorption or extinction and enable us to probe deep into the nuclear regions of the galaxies. The galaxies chosen for this study exist in a range of environments and are either known or suspected to have signatures of the gaseous medium being affected by different processes such as a starburst-driven superwind, active galactic nuclei (AGN)-driven nuclear outflow, tidal interactions and ram pressure stripping.

1.1 Astrophysical relevance of the study

Stars and the different gaseous components are the major constituents of a galaxy. The properties of the stellar populations and the gaseous mediums

exhibit significant differences for different types of galaxies. For example, the presence of large amounts of gas and young stars are seen in the late-type disk galaxies as opposed to very little ISM and an older population of stars in the ellipticals or early-types galaxies. The galaxies interact with each other and with the gaseous medium surrounding them when they reside in groups or clusters, thus affecting their structures and physical properties. The higher redshift galaxies which formed early in the evolution of the Universe have noticeable differences with respect to the present day nearby galaxies (e.g. Butcher & Oemler 1984; Couch & Sharples 1987; Dressler et al. 1997). At the present epoch of observation the differences in their observed properties depend on their history of interactions with their environment and also on the history of their central energetic activities. The Butcher-Oemler effect demonstrates remarkably that clusters of galaxies at higher redshifts have bluer galaxies then their lower-redshift counterparts (Butcher & Oemler 1984), which is possibly due to higher rate of gas accretion and interaction among the gas rich galaxies in the earlier phases of the Universe. Tidal interactions among galaxies may result in gas inflow into the central region of the galaxy, and can trigger a central starburst and/or feed a central super-massive black hole to trigger AGN activity. These two activities can produce galactic-scale outflows which are termed either as starburst-driven superwinds or AGN-driven nuclear outflows. Both these forms of activity and their manifestations may be seen in the same galaxy. The starburst driven outflows are usually not well collimated with opening angles which could be $\geq 60^{\circ}$ and are oriented approximately along the minor axis of the parent galaxies. The AGN-driven outflows, often characterised by narrow jets, are better collimated and show no preferred orientation relative to the minor axis of the host galaxies (Ulvestad & Wilson 1984). There have been

suggestions that in the case of ULIRGs when large amount of gas is cleared off from the central region, the hidden, dust-enshrouded AGN may unveil itself as a bonafide quasi-stellar object or QSO (Sanders & Mirabel 1996). Galaxies also lose gas largely from the outer parts when they move through the intracluster medium (ICM) or intragroup medium (IGrM) due to ram pressure or viscous stripping (Gunn & Gott 1972). These processes affect the star-formation history of the galaxy. For example, while the galactic ISM may be largely stripped in a high ICM density region leading to a suppression of star formation, the star formation rate may be enhanced in a less dense ICM region where the ISM is only compressed rather than being completely stripped. Studies of such galaxies and the gas loss processes could provide useful insights towards understanding enrichment of the ISM and IGM, and the evolution of galaxies and the IGM.

1.2 Starburst galaxies and superwinds

At radio wavelengths the most well-known sources in the sky are the double-lobed radio galaxies and quasars with elliptical host galaxies. The spiral galaxies on the other hand have low radio luminosities and can exhibit both a starburst and AGN activity. When harbouring an AGN, as in the Seyfert galaxies, these often exhibit jets and double-lobed radio structures although usually of smaller size and lower luminosity than the classical double-lobed radio galaxies and quasars (Krolik 1998). While in AGNs such as radio galaxies, quasars and Seyfert galaxies the radio emission from the nucleus, jets and lobes are due to synchrotron emission, the radio emission from normal spiral galaxies consists of free-free thermal emission from the ionised gas in the starforming regions, in addition to synchrotron radiation from supernova

remnants and diffuse emission from cosmic rays in the galaxy (cf. Condon 1992).

Stars are usually formed in the giant molecular clouds of the galaxies. The massive O and B stars among them live for a relatively short time (typically few million years) and explode as supernovae and distribute the metals cooked in their interiors in the ISM. The supernova blast waves can trigger further collapse of gas clouds and a new generation of stars form. Thus a cycle of gas to stars and back continues in a galaxy. In this dynamic environment of a galaxy, X-ray emitting hot gas, optical line-emitting warm gas, molecular and atomic line-emitting cold/cool gas, relativistic plasma and magnetic field co-exist and remain largely bound to the galaxy (Ferriere 2001). In galaxies with AGNs or starbursts the kinematic and physical properties of the different components of the ISM can be significantly affected by these phenomena leading to outflows, non-circular motions and large velocity widths of the lines. The starformation rate or the supernovae rate in the central region of some gas-rich galaxies are $10-1000$ times higher than that of normal galaxies. This process can consume $1-30\times10^9$ $M_\odot$ of gas over a short time scale (10^{7-8} yr) in a small region, typically $\sim$1 kpc (Morwood 1996; Sanders & Mirabel 1996). The high starformation rate would be difficult to sustain over the life time of the galaxy suggesting that this must be a transient phase in its life.

As a galaxy moves in the gravitational potential of a cluster or group or another field galaxy they do interact tidally or collide with other galaxies. Such tidal processes take away some part of the angular momentum of the rotating gas in the disk and help gas to flow into the central region of the galaxy. Tidal processes also induce instabilities in the stellar disk leading to the formation of bars which can help gas to flow into the central regions

of galaxies (Norman & Silk 1983; Schwab 1984; Regan & Mulchaey 1999; Hernquist & Mihos 1995, Greene, Lim & Ho 2004). Such gas inflow can trigger a burst of starformation and/or fuel an AGN activity. During such bursts of starformation the cumulative effect of many supernovae and stellar winds from the massive stars in the central region of a disk galaxy imparts mechanical energy to the ISM. These supernovae and stellar winds in the central region of a galaxy can create a high pressure (4 orders of magnitude higher then the average ISM pressure in the Milky way), high temperature (10^{6-7} °K) bubble of gas. This high pressured and hot bubble expands and flows outwards along the minor axis, the direction of least resistance in the surrounding ISM. This fast flowing (few 100 to 2000 km s^{-1}) hot gas carries cold gas, dust and magnetic field lines from the ISM along with it up to distances of tens of kpc. These outflows are called 'galactic winds' or 'superwinds'. M82 and NGC253 are two of the well-known examples (Fig. 1.1; Heckman, Armus & Miley 1990; Veilleux, Cecil & Bland-Hawthorn 2005 for a review of the field and further references).

In these superwind galaxies the typical outflow rate is $10-100$ $M_{\odot}$ yr^{-1}, with typical outflow velocity of few $100-2000$ km s^{-1}, which persists over $0.1-10$ million yr. The observed sizes of such outflows are $1-20$kpc. A typical supernova imparts 10^{51} ergs of energy to the ISM. Stellar winds from young and massive OB stars also impart a similar amount of energy to the ISM. If such high inputs of energy persist for few to tens of million years and accounting for many supernovae and massive stellar winds simultaneously the total energy may reach 10^{60} ergs, which is comparable to the binding energy of a galaxy. Hence it is a dynamically important event in the life of a galaxy. Such 10^{60} ergs explosive events have been suggested to be dominant during the early phases of galaxy formation. These superwinds supply heat

Figure 1.1: Composite image of the superwind galaxy M82. Optical light from stars showing the disk of the galaxy (yellow-green), 10,000 K hydrogen gas emitting optical emission lines (orange), cool gas and dust emitting in infrared (red), and million degree K hot gas emitting in X-rays (blue) are seen outflowing perpendicular to the stellar disk. (Credit: X-ray: NASA/CXC/JHU/ D.Strickland; Optical: NASA/ESA/STScI/AURA/The Hubble Heritage Team; IR: NASA/JPL-Caltech/Univ. of AZ/C. Engelbracht)

and almost all heavy metals cooked in the central region of a galaxy to the ICM/IGM.

1.3 Active galaxies and nuclear outflows

As described earlier inflow of gas into the central region of the galaxy can trigger a starburst and/or an AGN activity. In the canonical model of an AGN, the source of energy is via accretion onto a supermassive black hole

whose mass ranges from$10^6 M_\odot$ in our Galaxy to $10^{9.5} M_\odot$for the most luminous sources (Kormendy & Richstone 1995). The accretion disk produces X-ray emission and could be emitting a hot-wind besides supplying energy for the jets of relativistic plasma traversing perpendicular to the accretion disk (Krolik 1998). These nuclear outflows could drive the ISM of the galaxy outwards. In nearby galaxies detailed interaction of the nuclear outflows with the ISM can be observed. The radio jets interact with the surrounding ISM of the host galaxy entraining material as they traverse outwards (Colbert et al. 1996; Baum 1993; Gallimore et al. 2006; Taylor et al. 1989, Capetti et al. 1996). The region of interaction not only are co-spatial with the region of optical line emission but also correlate with the emission line widths. There have also been suggestions of mass loading of these AGN-driven nuclear outflows (Bicknell et al. 1998). In these regions the synchrotron plasma has two orders of magnitude higher pressure then typical pressure of the ISM in Milky Way . These outflows created by radio jets can have energies similar to that of the superwind outflows. In many of the Seyferts the radio-jets transfer almost all of their energy content within the central few kpc of the ISM affecting the dynamics of the different gaseous components. Galactic-scale diffuse radio continuum emission due to these outflows are known to be common among nearby Seyfert galaxies (Gallimore et al. 2006; Baum et al. 1993; Colbert et al. 1996). Evidence of massive outflows have also been seen in gas-rich, luminous infrared galaxies via HI and optical emission or absorption lines (e.g. Mirabel & Sanders 1988; Rupke, Veilleux & Sanders 2005).

The galaxy NGC3079 which has a Seyfert nucleus and a far infrared luminosity similar to the starburst galaxies M82 and NGC253 is one of the

well-studied galaxies which exhibit multi-component high velocity galactic-scale outflows (Fig. 1.2, 1.3, Cecil et al. 2001, 2002; Irwin & Saikia 2003). The measured velocity field of the outflowing Hα filaments of NGC3079 (V_{sys} =1150 $\pm$ 25 km s^{-1}) has been modelled wherein filament space velocities accelerate to 3700 km s^{-1} at a distance of 1 kpc from the nuclear region (Cecil et al. 2001, 2002). Another well-studied galaxy with bi-polar radio continuum outflows is the Circinus galaxy in the southern hemisphere which has a ring of star formation and an AGN (Elmouttie et al. 1998).

The radio jets in an AGN may interact with the different components of the ISM including atomic and molecular gas and drive it outwards. For example in the galaxy IC 5063 broad (700 km s^{-1}) HI-absorption line blue-shifted by 600 km s^{-1} has been detected in the region of jet-ISM interaction (Morganti et al. 1998; Oosterloo et al. 2000). Although different components of the ISM can be entrained by the jets as they advance outwards these aspects need to be studied in greater detail both observationally and theoretically. In sources where AGN-driven nuclear outflows co-exist with the starburst-driven superwinds they provide us with an opportunity to understand the interplay between them.

1.4 Cluster galaxies and stripping processes

When a galaxy moves through the hot (million K) and dense (number density $\sim$ few 10^{-4} cm^{-3}) ICM with velocities near 1000$-$2000 km s^{-1} the ram pressure exerted by the ICM can strip the loosely bound and more tenuous gas of the galaxy. As a result of this the dense molecular gas or the stars in the galaxy remain almost unaffected but the tenuous gas moves out of the galaxy's gravitational field and can reach the ICM (Gunn & Gott 1972; Quilis

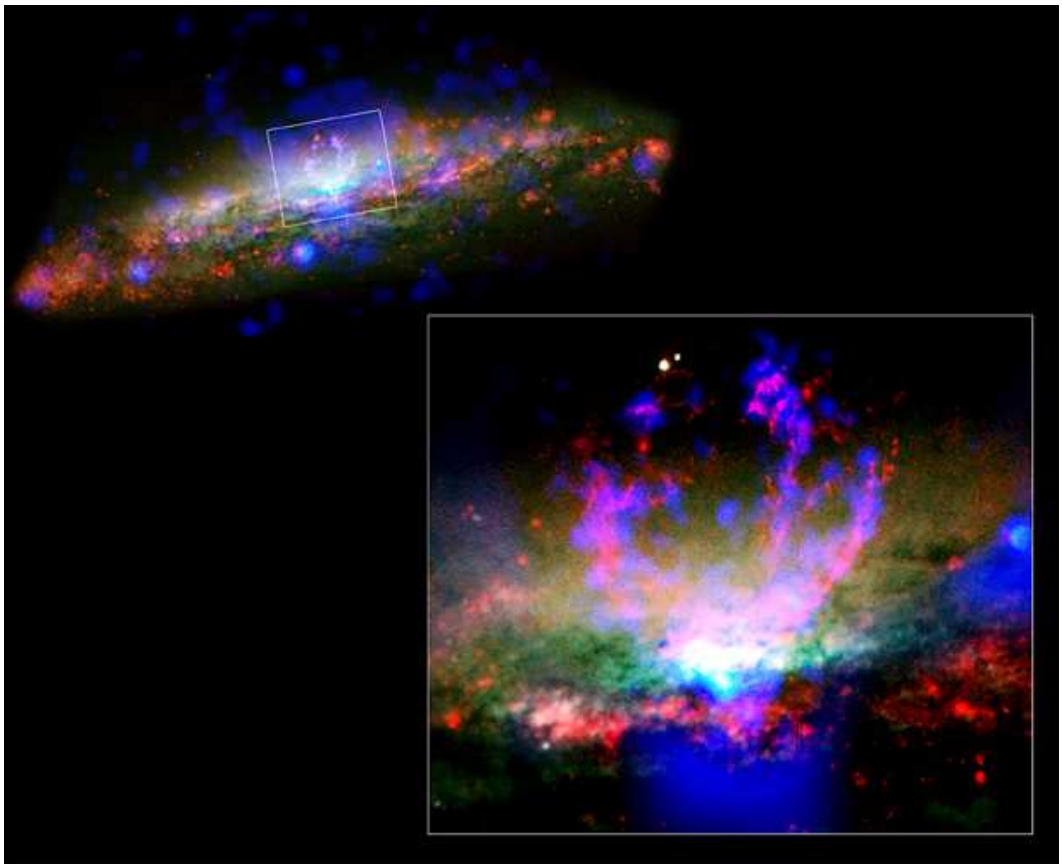

Figure 1.2: Composite image of the active galaxy NGC3079. Enlarged version of the region marked with a box is displayed separately for clearer view. Optical image from HST (yellow-green) showing the stellar disk of the galaxy has been superimposed on the warm and hot gaseous filaments (red) flowing out from the central region of this galaxy in the shape of a bowl. X-ray emission imaged by Chandra (blue) has been superimposed on it. Note that the image has been rotated clock-wise for convenience. See next image along with radio contours for correct orientation of the source in the sky. (Credit: NASA/CXC/STScI/U.North Carolina/G.Cecil)

et al. 2000; Roediger & Bruggen 2006). The ram pressure needed to get the gas in the ISM stripped off the galaxy has to be greater then 2π G Σ_{star} Σ_{gas}, where G is the universal Gravitational constant, Σ_{star} and Σ_{gas} are surface densities of stars and gas of the galaxy. The ram pressure experienced by the gas is ρ_{ICM} v^2 where ρ_{ICM} is the density of the the ICM and v is the relative velocity between the galaxy/gas and ICM. Stars have an extremely small

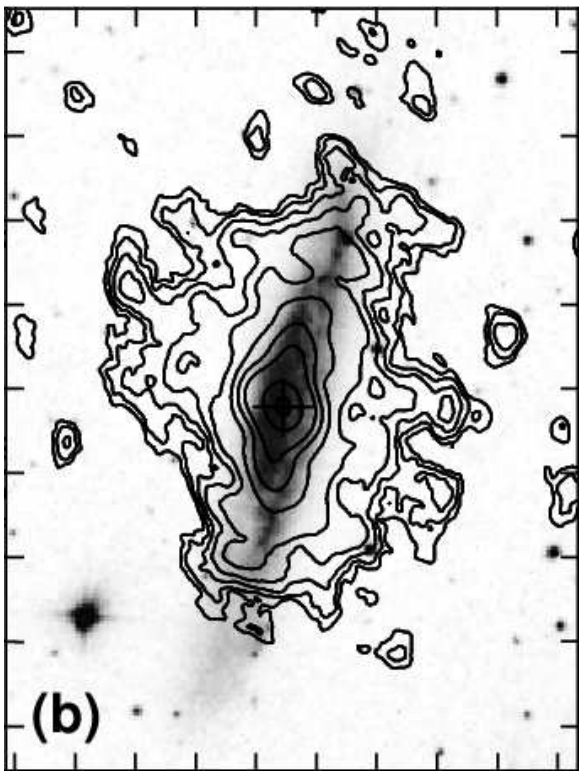

Figure 1.3: Optical image of star light from the galaxy NGC3079 has been superimposed on the 615-MHz radio continuum image in contours taken with the GMRT (Irwin & Saikia 2003). The synchrotron plasma originated from the AGN is seen outflowing perpendicular to the optical disk.

cross-section to the incoming ICM and are practically insensitive to it while the ISM is most susceptible to ram pressure. So the gas swept behind can simply leave a trail of HI, Hα or synchrotron plasma behind it in the cluster medium ((Fig. 1.4, 1.5), Boselli & Gavazzi 2006; Oosterloo & van Gorkom 2005). Apart from this ram pressure stripping there are a few other processes known for gas removal namely tidal stripping, viscous stripping and thermal evaporation. Tidal stripping which occurs during the interaction with another galaxy or with the mean gravitational field of the cluster contributes very little to the gas loss (Boselli & Gavazzi 2006). Viscous stripping is the process in which due to the viscous drag of the fast flowing ICM, ISM gets a

backward push and may get stripped (Nulsen 1982). It would have very similar morphological and kinematic manifestations as ram pressure stripping and difficult to distinguish. Gas loss by thermal evaporation is also possible in a hot cluster medium where gas particles of the ISM in contact with hot ICM gains enough thermal kinetic energy and may escape from the galaxy (Cowie & Songaila 1977). Although all these processes are expected to operate at some level in cluster galaxies, usually the most prominent among them is ram pressure stripping.

The fate of the gas stripped from the galaxy by ram pressure is not well understood. Recently very long tails of the size of 50−125kpc have been discovered such as those in NGC4388 and galaxies in the clusters Abell 1367 and 2115 (Oosterloo & van Gorkom 2005; Gavazzi & Jaffe 1987; Wang et al. 2004). Some are magnetised (synchrotron plasma, emitting in radio continuum), some are million degree hot (detected in X-ray emission), some ionised (Hα emitting gas) and some are neutral (seen in HI emission). Since there are not many examples of long trails arising due to ram pressure stripping, it is worth noting the most prominent cases. The tails emitting radio continuum not only extends up to 75 kpc but can contain up to 50% of the total radio continuum emission of the whole galaxy (Gavazzi & Jaffe 1987). The X-ray emitting tails which can also be similarly 50 to 90 kpc long are found to be cooler than the nearby ICM, possibly due to inter-mixing with the stripped gas (Kim et al. 2004; Fujita et al. 2006; Sun et al. 2006, Sun & Vikhlinin 2005; Wang et al. 2004). There are suggestions that the presence of the magnetic field in the stripped gas helps to preserve them against disruption (Vikhlinin et al. 1997; Asai et al. 2004). The ionised gas in such tails can also extend to large distances of up to 50 to 75 kpc with an estimated mass of a few 10^9 $M_\odot$ (Gavazzi et al. 2001). In some cases galaxies are known to

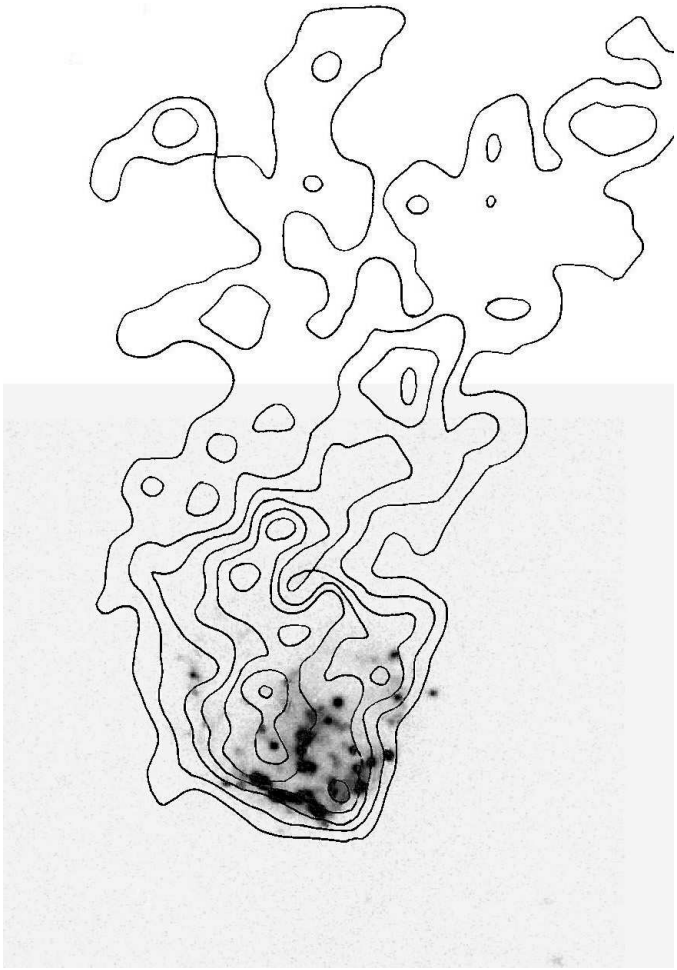

Figure 1.4: This face on galaxy CGCG 97073 in the cluster A1367 is seen to have long radio-continuum tail shown as radio contours. Hα image in gray scale has been superimposed, which shows the bright starforming knots in a bow shape on the up-stream side of the galaxy. (Credit: GOLDmine data base)

have become even 90 % deficient in HI in comparison to field galaxies of the same type and size (Haynes & Giovanelli 1984). The stripped tails can have enough HI mass (few times 10^8 $M_\odot$) which can in principle condense and eventually form dwarf galaxies, inter galactic HII regions or may evaporate and mix with the ICM (Oosterloo & van Gorkom 2005). They enrich the ICM with metals and magnetic fields carried away from the parent galaxy.

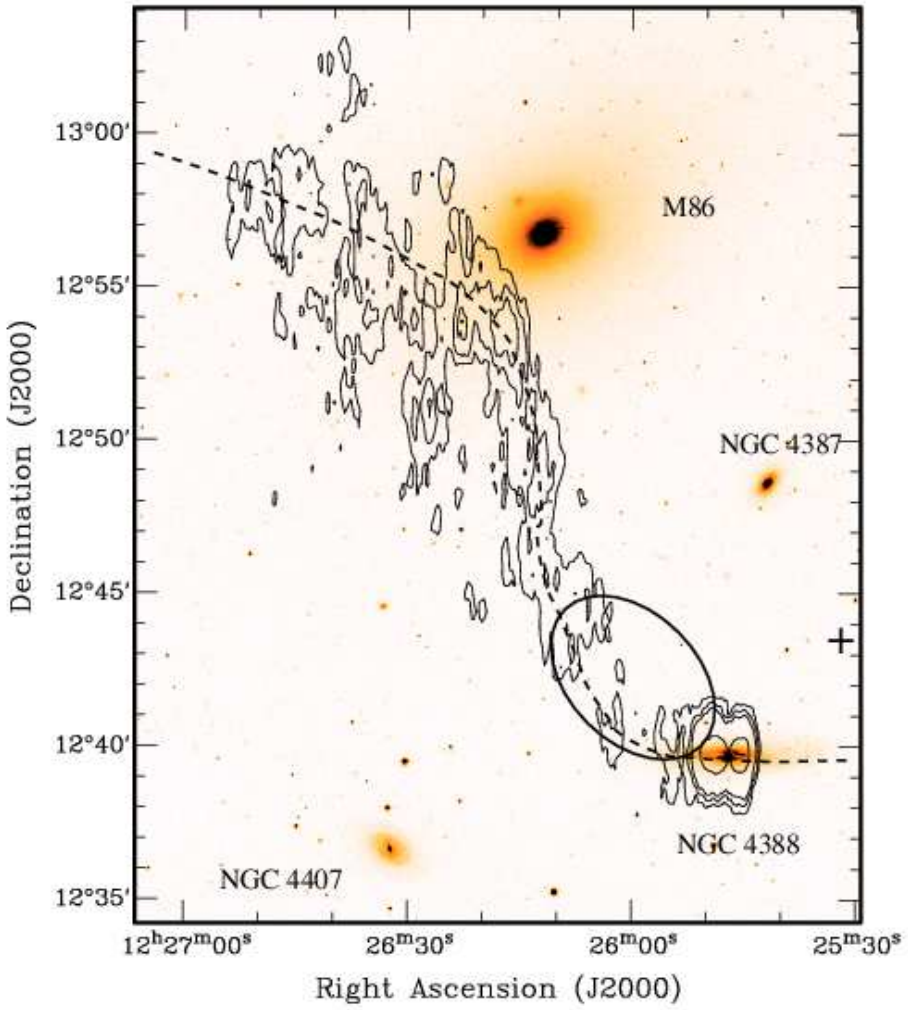

Figure 1.5: The Virgo cluster galaxy NGC4388 shows a long and massive HI tail on the north-eastern side, which has been formed by ram pressure stripping as it moves to the west. The HI contours have been superimposed on the optical image from DSS. (Credit: Oosterloo & van Gorkom, A&A, 2005, 437, L19)

Thus this is an important process by which galaxies seem to lose gas and have a profound effect on their appearance and evolution.

1.5 The approach adopted in the present study

I have studied a few galaxies using both the GMRT and the VLA at a number of radio continuum wavelengths and have also made spectroscopic observations in the 21cm atomic hydrogen (HI) line towards exploring the importance of different processes which may affect their structures and mass loss from the disk in different situations. Such studies are useful not only for studying individual galaxies but also for evolving strategies for studies of large samples to examine dependences on galaxy types, environments and cosmic epoch. The individual galaxies which have been chosen for this study are of different types, show evidence of mass loss and are located in different kinds of environments. These galaxies are described briefly below.

NGC1482: It is an SO galaxy at a distance of 19.6 Mpc which has remarkable hour-glass shaped optical emission line filaments and X-ray emission along the minor axis of the galaxy. The optical emission line gas and X-ray emission extend to $\sim$2 kpc with velocities which range upto $\sim$250$-$350 km s^{-1}. M82 and NGC253, the archetypal starburst galaxies with superwinds, are relatively nearby at distances of 2 and 3 Mpc respectively and have been studied in some detail. NGC1482 is a rather unique and interesting system in being an SO galaxy with a prominent superwind, which has been suggested to be one of the mechanisms for the ISM deficiency in S0 galaxies (Faber & Gallagher 1976; Bregman 1978; Quilis et al. 2000). NGC1482 does not show evidence of an AGN and is an example of a pure starburst driven superwind galaxy. We have imaged the nuclear region with high resolution to study the starburst region as well as identify any nuclear component which may have been missed in observations in different wavebands. Low-resolution radio continuum observations were made to study the

extent of any non-thermal outflow as well as estimate the supernova rate and hence the energy responsible for the outflows seen in other wavebands. The HI observations were made to study the kinematic effects of the starburst on the atomic component of the ISM. The results for this galaxy are presented in Chapter 2.

NGC6764: This radio bright Seyfert galaxy lies at a distance of 20 Mpc and has a nuclear outflow seen at radio wavelengths with an extent of $\sim$2.5 kpc which is smaller then the galaxy size. It is a composite galaxy which has an AGN and its stellar population has been modelled to have undergone two episodes of starburst activity. To understand the interaction of the AGN-driven nuclear outflow with the ISM and any possible wind due to the starburst activity, we observed this galaxy with a range of resolutions in radio continuum and HI. We found that the nonthermal outflow which is seen as two well-defined bubbles on opposite sides of the nucleus shows good correlation with the Hα filaments. We present the results on this galaxy in Chapter 3, where we also explore a possible dependence of extended radio structure on AGN or starburst activity in the nuclear region.

NGC4438: One of the most prominent late-type galaxies in the Virgo cluster, NGC4438, has an AGN and a very disturbed ISM with all phases of it lying on the western side of the main stellar disk. The distribution and kinematics of the extra-planar gas have been suggested to be affected by ram pressure of the ICM, tidal interactions and ISM-ISM collisons with the neighbouring galaxy NGC4435. We studied this galaxy with high resolution at a number of wavelengths to identify the radio nucleus and study the lobes of radio emission which have a total size of $\sim$1 kpc in the central region of the galaxy. The low-resolution continuum observations were used to infer the properties of the more extended radio emission displaced towards the

west, while our HI observations were made to study the distribution and kinematics of the HI gas displaced on the western side as well as any HI gas in the disk of the galaxy. A tail of HI emission with an extent of ∼50 kpc at the distance of the Virgo cluster as well as HI from another cluster member IC3355 were detected during the course of these observations. The results of these observations and the nature of the HI tail are discussed in Chapter 4.

Holmberg 124: One of the reasons for cluster galaxies being predominantly early-type at the present epoch is pre-processing by ram pressure stripping and tidal interactions in groups. We have chosen a nearby group with four galaxies at a distance of 24 Mpc and showing clear evidence of tidal interactions between two of its members, NGC2820 and NGC2814. While NGC2820 is nearly edge-on, NGC2805 is face-on with an arc of star formation towards the south and accumulation of HI towards the north. We have observed this group in both radio continuum and HI to detect any ram pressure stripped gas and study the effects of both ram pressure and tidal interactions. These results are presented in Chapter 5.

Abell 1367: The longest trails of ram pressure stripped gas visible in multiple components of the ISM are seen in the cluster A1367. Three of its galaxies show 50−75 kpc long radio continuum tails with associated Hα emission. Identification and study of such multi-component large tailed systems are important for understanding gas loss processes. We present HI observations of these galaxies and compare these with the Hα and radio continuum tails, as well as models of ram pressure stripping in Chapter 6.

The results of these studies and the concluding remarks are presented in Chapter 7.

1.6 References

Asai N., Fukuda N., Matsumoto R., 2004, JKAS, 37, 575

Baum S.A., O'Dea C.P., Dallacassa D., de Bruyn A.G., Pedlar A., 1993, ApJ, 419, 553

Bregman J.N., 1978, ApJ, 224, 768

Bicknell G.V., Dopita M.A., Tsvetanov Z.I., Sutherland R.S., 1998, ApJ, 495, 680

Boselli A. & Gavazzi G., 2006, PASP, 118, 517

Butcher H. & Oemler A., 1984, ApJ, 285, 426

Capetti A., Axon D.J., Macchetto F., Sparks W.B., Boksenberg A., 1996, ApJ, 469, 554

Cecil G., Bland-Hawthorn J. Veilleux S., Filippenko A.V., 2001, ApJ, 555, 338

Cecil G., Bland-Hawthorn J., Veilleux S.,2002, ApJ, 576, 745

Colbert E.J.M., Baum S.A., Gallimore J.F., O'Dea C.P., Christensen J.A., 1996, ApJ, 467, 551

Condon J.J., 1992, ARA&A, 30, 575

Couch W.J., Sharples R.M., 1987, MNRAS, 229, 423

Cowie L.L., Songaila A., 1977, Nature, 266, 501

Gunn J.E., Gott J. R. III, 1972, ApJ, 176, 1

Dressler A. et al. 1997, ApJ, 490, 577

Elmouttie M., Haynes R.F., Jones K.L., Sadler E.M., Ehle M., 1998, MNRAS, 297, 1202

Faber S.M.& Gallagher J.S., 1976, ApJ, 204, 365

Ferrière K.M., 2001, RvMP, 73, 1031

Fujita Y.; Sarazin C.L., Sivakoff G.R., 2006, PASJ, 58, 131

Gavazzi G., Jaffe W.,1987, A&A, 186, 1L

Gavazzi G., Boselli A., Mayer L., Iglesias-Paramo J., Vlchez J.M., Carrasco L., 2001, ApJ, 563, 23L

Gallimore J.F., Axon D.J., O'Dea C.P., Baum S.A., Pedlar A.,2006, astro-ph/0604219

Greene J., Lim J. & Ho P.T.P., 2004, ApJS, 153, 93

Haynes M.P., Giovanelli R., 1984, AJ, 89, 758

Heckman T.M., Armus L., Miley G.K., 1990, ApJS, 74, 833

Hernquist L. & Mihos J.C., 1995, ApJ, 448, 41

Irwin J.A. & Saikia D.J., 2003, MNRAS, 346, 977

Kim E., Kim D.-W., Fabbiano G., Trinchieri G., 2004, AAS, 204, 1502 Kormendy J. & Richstone D., 1995, ARA&A, 33, 581

Kondratko P.T., Greenhill L.J., Moran J.M., 2005, ApJ, 618, 618

Krolik J.H., 1998, Active Galactic Nuclei: From the Central Black Hole to the Galactic Environment, Princeton University Press

Mirabel I.F. & Sanders D.B., 1988, ApJ, 335, 104

Moorwood A.F.M., 1996, SSRv, 77, 303

Morganti R., Oosterloo T., Tsvetanov Z., 1998, AJ, 115, 915

Nulsen, P.E.J., 1982, MNRAS, 198, 1007

Norman C. & Silk J., 1983, ApJ, 266, 502 Oosterloo T.A., Morganti R., Tzioumis A., Reynolds J., King E., McCulloch P., Tsvetanov Z., 2000, AJ, 119, 2085O

Oosterloo T., van Gorkom J., 2005, A&A, 437, 19L

Quilis V., Moore B. & Bower R., 2000, Science, 288, 1617

Regan M. & Mulchaey J., 1999, AJ, 117, 2676

Roediger E., & Brüggen M., 2006, MNRAS, 369, 567

Rupke D.S., Veilleux S., Sanders D.B., 2005, ApJ, 632, 751

Sanders D.B., Mirabel I.F., 1996, ARA&A, 34, 749

Seaquist E.R., Bell M.B., Bignell R.C., 1985, ApJ, 294, 546

Sun M., Vikhlinin A., 2005, ApJ, 621, 718

Sun M., Jones C., Forman W., Nulsen P.E.J., Donahue M., Voit G.M., 2006, ApJ, 637, 81L

Schwab F.R., 1984, AJ, 89, 1076

Taylor D., Dyson J.E., Axon D.J., Pedlar A., 1989, MNRAS, 240, 487

Ulvestad J.S., Wilson A.S., 1984, 1984, ApJ, 285, 439

Veilleux S., Cecil G., Bland-Hawthorn J., 2005, ARA&A, 43, 769

Wang Q.D., Owen F., Ledlow M., 2004, ApJ, 611, 821

CHAPTER 2

A radio study of the superwind galaxy NGC 1482.

2.1 Abstract

We present multifrequency radio continuum as well as H I observations of the superwind galaxy NGC1482, with both the Giant Metrewave Radio Telescope (GMRT) and the Very Large Array (VLA). This galaxy has a remarkable hourglass-shaped optical emission line outflow as well as bi-polar soft X-ray bubbles on opposite sides of the galactic disk. The low-frequency, lower-resolution radio observations show a smooth structure. From the non-thermal emission, we estimate the available energy in supernovae, and examine whether this would be adequate to drive the observed superwind outflow. The high-frequency, high-resolution radio images of the central starburst region located at the base of the superwind bi-cone shows one prominent peak and more extended emission with substructure. This image has been compared with the infrared, optical red-continuum, Hα, and, soft and hard X-ray images from Chandra to understand the nature and relationship of the various features seen at different wavelengths. The peak of infrared emission is the only feature which is coincident with the prominent radio peak, and possibly defines the centre of the galaxy.

Table 2.1: Basic Data on NGC 1482.[a]

RA[b] (h m s)	DEC[b] (° ′ ″)	Type[c]	a × b[d] (′ × ′)	V_{sys}[e] (km s^{-1})	i[f] (°)	log(L_{FIR})[g] ($L_\odot$)	D[h] (Mpc)
03 54 38.92	−20 30 07.6	SA0/a	2.5 × 1.4	1850±20	58	10.66	24.7

a Taken from the NASA Extragalactic Database (NED), unless stated otherwise.
b The position of radio peak from our high-resolution, VLA A-array, 8460 MHz image in J2000
c Morphological type.
d Optical major and minor axes.
e Heliocentric optical systemic velocity (Veilleux & Rupke, private communication). This is consistent with H I observations of Roth et al. (1991) and those presented in this chapter.
f Inclination angle, from Strickland et al. (2004).
g Log of the far infra-red luminosity (Condon et al. 1990) using the revised distance.
h Distance estimated using the galaxy recessional velocity with respect to the cosmic microwave background radiation and H_0=71 km s^{-1} Mpc^{-1} (Spergel et al. 2003). For this distance 1″=120 pc.

The H I observations with the GMRT show two blobs of emission on opposite sides of the central region. These are rotating about the centre of the galaxy and are located at ∼2.4 kpc from it. In addition, these observations also reveal a multicomponent H I-absorption profile against the central region of the radio source, with a total width of ∼250 km s^{-1}. The extreme blue- and red-shifted absorption components are at 1688 and 1942 km s^{-1} respectively, while the peak absorption is at 1836 km s^{-1}. This is consistent with the heliocentric systemic velocity of 1850±20 km s^{-1}, estimated from a variety of observations. We discuss possible implications of these results.

2.2 Introduction

Galactic-scale outflows along the minor-axes of nearby edge-on galaxies have been observed over a wide frequency range extending from radio continuum to

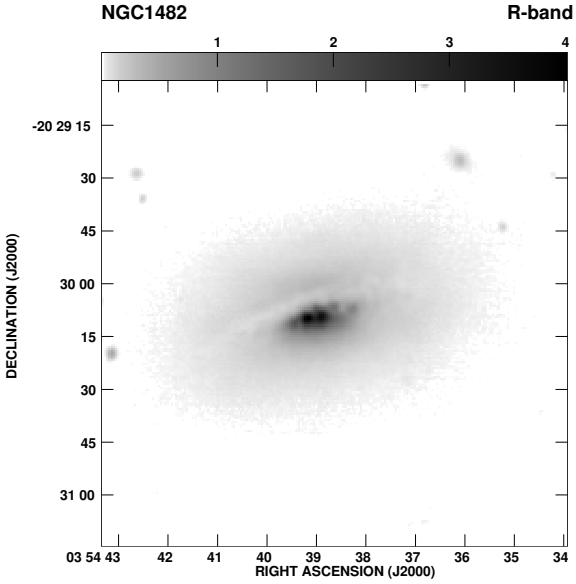

Figure 2.1: An optical R-band image of NGC1482 .

X-ray wavelengths. The more prominent outflows with an outflow mass and kinetic energy of approximately $10^5 - 10^7$ $M_\odot$ and $10^{53} - 10^{55}$ ergs respectively are often referred to as superwinds, and these have been observed over a wide range of redshifts (e.g. Heckman, Armus & Miley 1990; Pettini et al. 2001; Veilleux 2002a, 2003). The superwind could contain different phases of the metal enriched interstellar medium (ISM) such as hot X-ray emitting gas, warm ionized gas emitting ultraviolet (UV) and optical emission lines, synchrotron emitting relativistic plasma and magnetic fields, dust, as well as H I and molecular gas (Dahlem 1997; Strickland 2001). These superwinds play an important role in heating and supplying kinetic energy to the Inter Galactic Medium (IGM) and enriching it with metals. Many of these outflows are interpreted as the combined effect of numerous supernovae and stellar winds in the nuclear starforming region of the parent Seyfert or starburst galaxy. An active galactic nucleus (AGN) or winds from the tori in the

nuclear regions could also contribute to the observed outflows (Heckman et al. 1990; Balsara & Krolik 1993; Baum et al. 1993; Krolik & Kriss 1995; Colbert et al. 1996a,b; Weaver 2001; Veilleux 2002b).

In this chapter we present a detailed radio study of the interesting superwind galaxy NGC1482, which has received relatively little attention. The basic properties of this galaxy are summarised in Table 2.1. In an emission-line survey of early-type spirals Hameed & Devereux (1999) noticed the presence of "filaments and/or chimneys of ionized gas extending perpendicular to the disk". Veilleux & Rupke (2002) imaged the galaxy in Hα and N II and highlighted the remarkable hourglass-shaped optical emission line outflow with a velocity of $\sim$250 km s^{-1}. They estimated the energy in the optical emission-line outflow to be at least 2×10^{53} ergs. The ionization ratios of the gas in the superwind have been interpreted to be due to shock formation in the outflow. More recently, Veilleux et al. (2003 and private communication) have reported an outflow velocity of $\sim$460 km s^{-1} in one of the filaments. The soft X-ray image from the Chandra Observatory also exhibits bipolar emission along a similar axis to that of the optical hourglass-shaped structure (Strickland et al. 2004).

We have studied this galaxy at radio continuum wavelengths ranging from 335 MHz to 14965 MHz as well as in H I using both the GMRT and the VLA. While VLA images at 1.49 GHz have been presented by Condon et al. (1990), continuum observations at lower and higher frequencies as well as H I images have been presented here for the first time. The objectives of the observations were to clarify the radio structure, constrain the energetics and explore evidence of outflow at radio wavelengths. We first briefly describe the observations in Section 2. The large-scale radio structure, its comparison with the images at other wavelengths, and some of the implications are discussed

Table 2.2: Log of the radio observations

Telescope	Freq. MHz	Obs. date	t min	Phase Calib.	$S_{cal.}$ Jy
GMRT	335	2002Aug17	60	0521−207	9.67
GMRT	615	2003Mar07	180	0453−281	2.21
VLA-BnA	1365	2002May20	25	0416−188	2.85
GMRT	1409,H I	2002Nov16	180	0453−281	1.99
VLA-A	4860	2003Jun26	54	0416−188	0.68
VLA-BnA	8460	2002May20	23	0416−188	0.68
VLA-A	8460	2003Jun26	60	0416−188	0.83
VLA-A	14965	2003Jun26	20	0348−278	1.02

in Section 3. The small-scale radio structure and a comparative study of this with features seen at other wavelengths are also presented in Section 3. Section 4 describes the H I observations, where we report the detection of both emission and absorption lines, discuss these results and compare with the spectral information at optical and CO wavelengths. In Section 5 we summarise the conclusions.

2.3 Observations and Data analyses

The observing log for both the GMRT and VLA observations is presented in Table 6.2, which is arranged as follows. Column 1: Name of the telescope where we also list the configuration for the VLA observations. Column 2: The frequency of the observations where H I denotes spectral line observations centred at an observed frequency of ∼1412 MHz. Columns 3 and 4: Dates of the observations and the time, t, spent on the source. Columns 5 and 6: The phase calibrator used and its flux density. A conservative estimate of the error in the flux density is approximately 10% at 335 and and 5% at the higher frequencies.

(a) GMRT

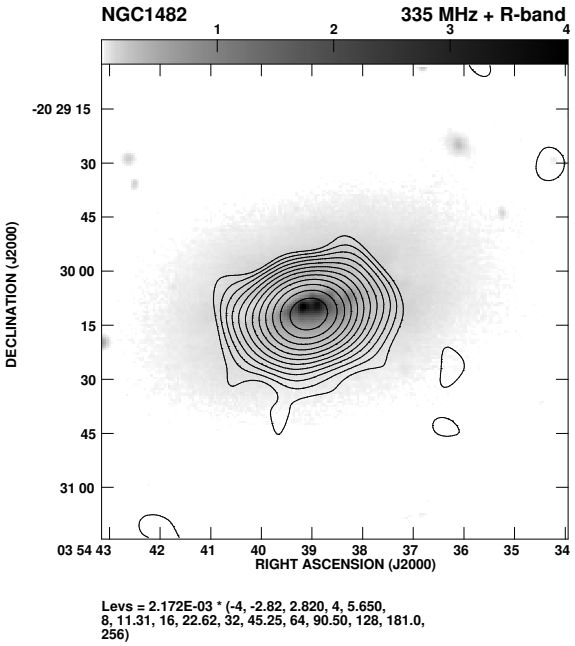

Figure 2.2: The GMRT 335-MHz contour image restored with a circular beam of 11.6 arcsec superimposed on the optical R-band image in grey scale.

The GMRT consists of thirty antennas, each of 45 m diameter, in an approximate 'Y' shape similar to the VLA but with each antenna in a fixed position. Twelve antennas are randomly placed within a central 1 km by 1 km square (the "Central Square") and the remainder form the irregularly shaped Y (6 on each arm) over a total extent of about 25 km. Further details about the array can be found at the GMRT website at `http://www.gmrt.ncra.tifr.res.in`. The observations were made in the standard fashion, with each source observation interspersed with observations of the phase calibrator. The primary flux density calibrator was 3C286 whose flux density was estimated on the Baars et al. (1977) scale, using the latest (1999.2) VLA values. The bandwidth of the continuum observations at 335 and 615 MHz was 16 MHz, while for the L-band observations it was 8

MHz. The data analyses were done using the Astronomical Image Processing System (AIPS) of the National Radio Astronomy Observatory. Since GMRT data is acquired in the spectral-line mode, gain and bandpass solutions were applied to each channel before combining them. The 335 MHz observations were affected by ionospheric phase fluctuations. A significant amount of data had to be edited, and the first round of phase self-calibration was done assuming a point source model. In the subsequent runs of self-calibration the image of the target source was used as the model. The position of the source was determined by aligning its peak with that of the 615 MHz image.

The analyses of the H I observations were also done in the standard way. 3C286 was the primary flux density and bandpass calibrator. The total bandwidth for H I observations was 8 MHz and the spectral resolution was 62.5 kHz, which corresponds to 13.3 km s^{-1} in the centre of the band. We discarded any antennas with more than 3% fluctuations in the bandpass gains during the observations. A few channels in the beginning and approximately ten channels towards the end were also not included in the analyses. The AIPS task UVLIN was used for continuum subtraction and the multi-channel data were then CLEANed using IMAGR.

Some of the observed parameters of the GMRT and the VLA continuum images are presented in Table 6.3 which is arranged as follows. Columns 1 and 2 are similar to that of Table 6.2, except that we also list the parameters from the NRAO VLA Sky Survey (NVSS). Columns 3 to 5: The resolution of the image with the major and minor axes being listed in arcsec and the position angle (PA) in degrees. Column 6: The rms noise in units of mJy/beam. Columns 7 and 8: The peak and total flux densities in units of mJy/beam and mJy respectively. In addition to the rms noise in the image, we also examined the change in flux density by varying the size of the box around

the source. The error in the flux density is approximately 10% at 335 MHz and 5% at the higher frequencies.

(b) VLA

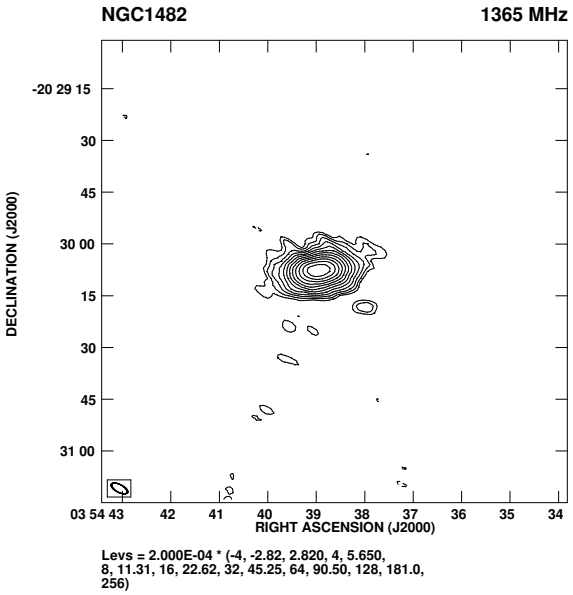

Figure 2.3: The VLA BnA-array image at 1365 MHz with an angular resolution of 5.13×2.23 arcsec along a PA∼62°.

The VLA observations were also made in the standard way with a phase calibrator being observed before and after each scan on a source. The primary flux density calibrator was 3C286. However, since 3C286 is significantly resolved on the longer baselines at 14965, 8460 and 4860 MHz with the VLA A-array, the following procedure was adopted. The flux density of 3C286 was calculated by the AIPS task SETJY. The flux density of the phase calibrator was estimated by comparing its visibility amplitude with those of 3C286 at the shorter baselines, over the *uv* ranges specified in the VLA Calibrator manual. These values of the phase calibrator flux density were incorporated using the task GETJY, and are also listed in Table 6.2. We attempted to

Table 2.3: Observed parameters of radio continuum images

Telescope	Freq.	Beam size			rms	S_{pk}	$S_{tot.}$
	MHz	maj.	min.	PA	mJy	mJy	mJy
		$''$	$''$	$^\circ$	/b	/b	
GMRT	335	11.6	11.6	0	2.24	370	723
GMRT	615	8.24	5.44	178	0.65	140	397
VLA-BnA	1365	5.13	2.23	62	0.17	35	198
NVSS	1400	45.0	45.0	0	0.50	23	224
GMRT	1409	2.96	2.01	25	0.60	21	218
VLA-A	4860	0.64	0.35	12	0.04	1.9	44
VLA-BnA	8460	1.06	0.55	46	0.07	1.3	25
VLA-A	8460	0.36	0.20	9	0.02	0.9	18
VLA-A	14965	0.20	0.11	5	0.09	<0.3	

make self-calibrated images for all the different data sets. However, the A-array images did not improve after self calibration. Therefore, BnA-array images presented here are self-calibrated ones, while the A-array ones are not.

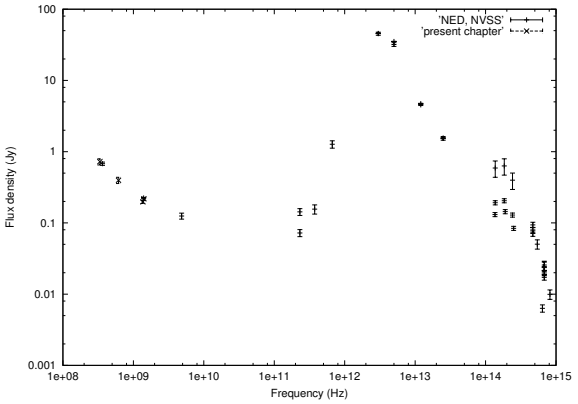

Figure 2.4: The integrated spectrum of NGC1482 using values from NED, NVSS (+)and from the observations presented here (×).

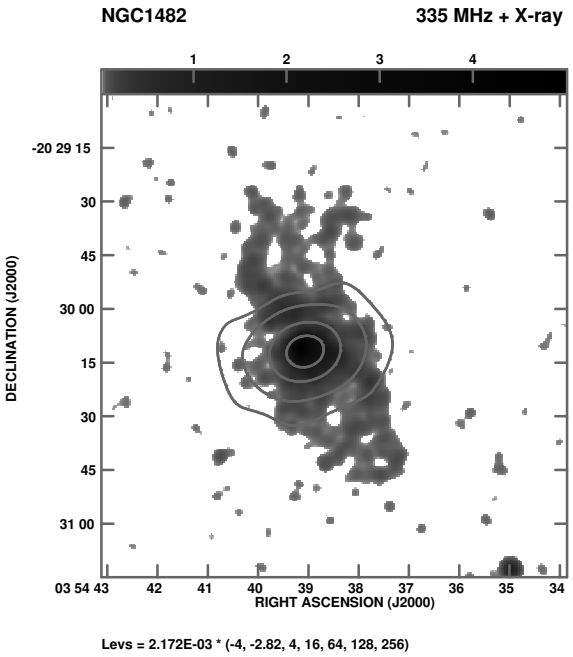

Figure 2.5: The GMRT 335-MHz contour image with an angular resolution of 11.6 arcsec superimposed on the soft X-ray image from Chandra X-ray observatory.

2.4 Radio continuum emission

(a) Large-scale structure

In Fig. 2.1,2.2 and 2.3 we respectively show the optical R-band image of the galaxy (Strickland et al. 2004; and Strickland, private communication), our GMRT 335-MHz contour map superimposed on the optical image and our VLA BnA-array 1365-MHz image. The GMRT 335-MHz image, which has an angular resolution of 11.6 arcsec shows the source to be resolved with a deconvolved angular size of 14×8 arcsec along a PA of 107°. Its angular dimensions are less than that of the optical galaxy, and shows no evidence of a large-scale outflow or halo due to diffusion of cosmic ray particles. This is consistent with the NVSS image where the source appears to be a single source with a 45 arcsec beam. The GMRT 615-MHz image is essentially

similar to the 335-MHz image and is not shown here, although the flux density estimates are listed in Table 6.3. The somewhat higher-resolution VLA 1365-MHz image, which has a lower rms noise than the low-frequency GMRT images, shows the central region to be very clearly extended along a PA$\sim$105°, but again with no evidence of any large-scale diffuse emission.

A comparison of the radio image with the Chandra soft X-ray bubbles of plasma shows that the X-ray emission extends far beyond the radio extent as seen in the 335-MHz image (Fig. 2.5). The non-thermal synchrotron emission appears largely confined to the disk of the galaxy, with no significant emission from the outflowing superwind plasma.

The GMRT images do not appear to have missed significant emission from any diffuse component. A comparison of the GMRT flux densities with the known and reliable flux density measurements listed by NED (Fig. 2.4) shows that these values are consistent with the overall straight, non-thermal spectrum of the source with a spectral index, α, of 0.82 (S$\propto \nu^{-\alpha}$) between 335 and 1400 MHz. We have not attempted to make a spectral index image from the low-resolution images since the number of beamwidths along the source is small.

Adopting the spectral index of 0.82 as the mean value over the region of emission, and assuming the synchrotron emission to have lower and higher cutoffs at 10^7 and 10^{10} Hz respectively, a proton to electron ratio of unity, a filling factor of unity and an oblate spheroidal distribution for the emitting region we estimate the minimum energy density and equipartiton magnetic field to be $\sim 5.9\times10^{-11}$ ergs cm^{-3} and 25 μG respectively. The radiative life time of an electron radiating in this field at 1.4 GHz is $\sim 2.2\times10^6$ yr. These values are similar to estimates for nearby galaxies (e.g. Condon 1992). The proton to electron ratio is not well determined for external galaxies. For a

value of $\sim$50 from studies of cosmic rays in our own Galaxy (e.g Webber 1991), the equipartition magnetic field would increase by a factor of $\sim$2.5.

Since the overall spectral index is steep, the contribution of the thermal fraction to the total emission is expected to be small. Using the expression due to Condon (1992) for the thermal fraction in spiral galaxies, as measured globally, we estimate that only 4, 7 and 11 per cent of the total emission could be due to thermal components at 335, 615 and 1400 MHz respectively. From the non-thermal emission, we estimate the supernova rate in this galaxy to be $\sim$0.14 yr^{-1} (Condon 1992). The supernova rate appears similar to estimates in other starburst galaxies such as $\sim$0.1 yr^{-1} for M82 (e.g. Huang et al. 1994), $\lesssim$0.1 to 0.3 for NGC253 (Ulvestad & Antonucci 1997), $\sim$0.1 yr^{-1} for the clumpy irregular starburst galaxy Mrk 325 (Condon & Yin 1990) and also for the starburst galaxy NGC3448 of the Arp 205 system (Noreau & Kronberg 1987) and $\sim$0.07 yr^{-1} for NGC6951 (Saikia et al. 2002).

We can examine whether the energy the from the estimated supernova rate is adequate to drive the observed superwind outflow. Adopting a value of 10^{51} ergs for the kinetic energy of a supernova, the available energy over the dynamical lifetime of the bubble, $\sim 7.5 \times 10^6$ yr, is $\sim 10^{57}$ ergs. However, the energy which drives the outflow depends on the heating efficiency of the supernovae, i.e. the fraction of supernova energy which is not radiated away. In a classic paper, Larson (1974) estimates that approximately 10 per cent of the explosion energy is effectively transmitted to the gas. There is a wide range of values in the literature, with many of the simulations of galactic winds assuming a heating efficiency of 100 per cent. Melioli & de Gouveia Dal Pino (2004) note that this is often not consistent with the observations, and that the heating efficiency may be time dependent and sensitive to the initial conditions of the system, and cannot be assumed to be 100 per cent.

For our purposes we assume an efficiency of 10 per cent, so that the available energy is $\sim 10^{56}$ ergs. Veilleux & Rupke (2002) estimate the kinetic energy involved in the outflow of the warm ionized gas to be $\gtrsim 2\times10^{53} n_{e,2}^{-1}$ ergs, where $n_{e,2}^{-1}$ is the number density in units of 100 cm^{-3}. They estimate the number density of particles in the entrained material to be $\lesssim$100 cm^{-3} from their [S II]λ6731/6716 line ratios. The total kinetic energy involved in the outflow could be significantly larger. In addition to the optical line-emitting gas and the known X-ray plumes, there could also be cold gas entrained in the flow. For example, for a sample of far-infrared bright, starburst galaxies, Heckman et al. (2000) estimate the kinetic energy in the cool gas to be $\sim 10^{55}$ ergs. In the case of NGC1482, we need a reliable estimate of total energy in the outflow before determining whether the observed supernova rate is adequate to drive the outflow.

(b) Small-scale structure

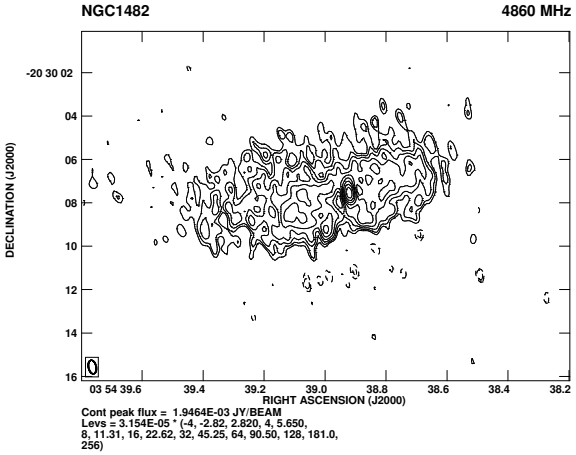

Figure 2.6: VLA A-array image at 4860 MHz with an angular resolution of 0.64×0.35 arcsec along a PA$\sim$12°.

The 4860 MHz, VLA A-array image (Fig. 2.6) shows a prominent peak

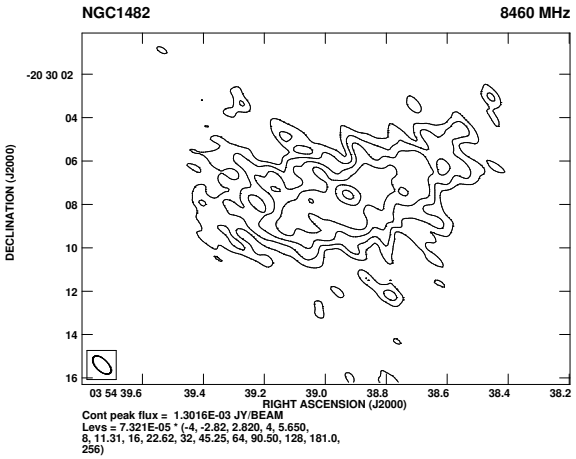

Figure 2.7: VLA snapshot image with the BnA array at 8460 MHz. The angular resolution is 1.06×0.55 arcsec along a PA∼46°.

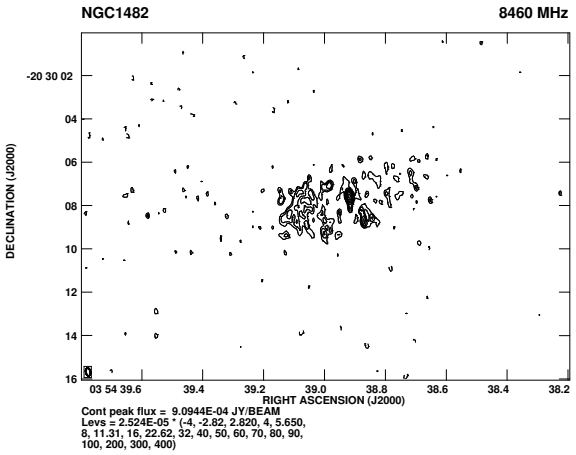

Figure 2.8: VLA A-array image at 8460 MHz with an angular resolution of 0.36×0.20 arcsec along a PA∼9°.

of emission with a brightness of 1.95 mJy/beam and more diffuse emission along a PA of ∼100°, similar to the orientation of the galaxy. The diffuse emission is more prominent on the eastern side of the peak, the total flux density on this side being 27 mJy compared with 15 mJy on the western side. The brightest feature on the eastern side, which we call the secondary peak, is located at RA: 03 54 39.12, Dec: −20 30 08.60 and has a peak brightness of 0.65 mJy/beam. This image shows a sharper boundary on the southern

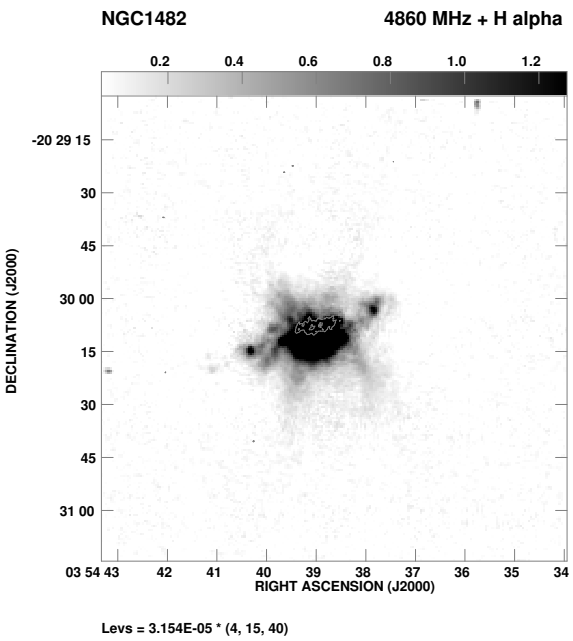

Figure 2.9: The VLA A-array 4860 MHz image, superimposed on the grey scale image of Hα emission. Only three of the radio contours are shown.

side than on the northern one, as is also seen in the VLA BnA-array image at 1365 MHz (Fig. 2.3). The somewhat lower-resolution VLA BnA-array, 8460 MHz snap-shot image (Fig. 2.7) shows basically a similar structure with the peak brightness being 1.30 mJy/beam. Smoothing the 4860 MHz image to that of the BnA array 8460 MHz one yields a peak brightness of 2.38 mJy/beam and a spectral index of $\sim$1 for the prominent peak of emission. The spectral index of the central region between 4860 and 8460 MHz is also $\sim$1, showing that the entire region has a steep radio spectrum.

The expected brightness of this peak of emission at 14965 MHz with a similar resolution to that of the VLA BnA-array image is $\sim$0.7 mJy/beam. Its non-detection with a 3σ upper limit of $\sim$0.3 mJy/beam in the image with a resolution of $\sim$0.15 arcsec is consistent with this. Although its steep spectral index does not suggest it to be an AGN, it is difficult to rule out the possibility of there being a weak AGN with more extended emission associated with it. It

is relevant to note here that from optical spectroscopic observations, Kewley et al. (2000) have classified it to be a starburst galaxy without an AGN. The brightness temperature of the peak of emission, estimated from the 4860 MHz image (e.g. Condon et al. 1991) is only $\sim$630° K making it difficult to use it as a diagnostic to identify whether it is an AGN. The VLA A-array 8460 MHz image with a resolution of $\sim$0.27 arcsec (Fig. 2.8)shows the peak feature to have a possible extension to the south and again more emission on the eastern side of this peak (9 mJy) compared with the western side (6 mJy). The peak brightness here is 0.9 mJy/beam. The brightness temperature estimated for the peak is $\sim$740° K. The linear resolution in the VLA A-array 8460 MHz image is approximately 30 pc, and its peak luminosity is 6.5×10^{19} W Hz^{-1}. The peak luminosity in the other regions of the source is typically 10^{18} W Hz^{-1}. It is of interest to compare this with other galaxies. For example, the median luminosity at 8.4 GHz of the components observed in M82 which is at a distance of 3.4 Mpc is $\sim2\times10^{18}$ W Hz^{-1} (Huang et al. 1994; Allen & Kronberg 1998) when observed with a linear resolution of $\sim$3 pc. Considering a more distant galaxy, the median luminosity for the archetypal starburst galaxy in the southern hemisphere, NGC1808 (distance$\sim$10.9 Mpc), is about 8×10^{18} W Hz^{-1} with a linear resolution of 30 pc (Collison et al. 1994). The luminosities in NGC1482 appear similar to the discrete features in some of the well-known archetypal starburst galaxies.

(c) Comparison with other wavebands

The high-resolution radio images, which define the structure of the circumnuclear starburst region, consist of one prominent peak of emission and several weaker secondary peaks. A superposition of the VLA 4860 MHz image on

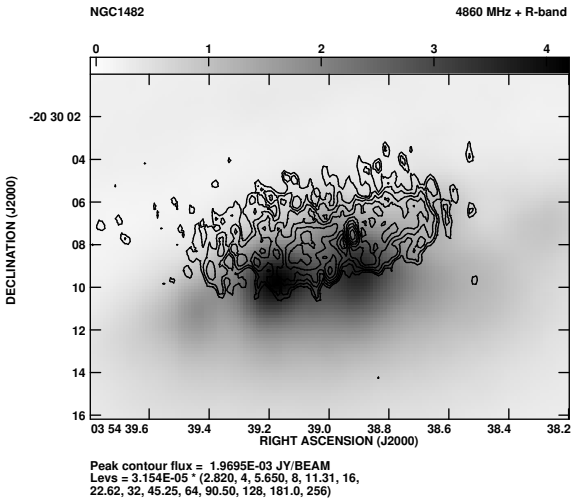

Figure 2.10: The 4860 MHz VLA A-array contour map with an angular resolution of 0.64×0.35 arcsec along a PA∼12° is shown superimposed on an optical R-band image of only the central region of the galaxy.

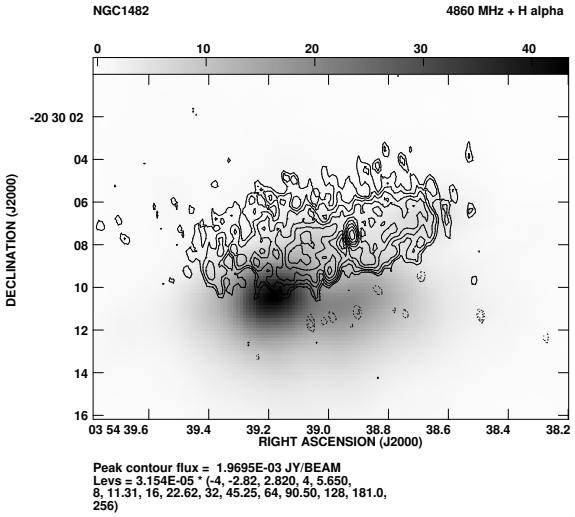

Figure 2.11: The 4860 MHz VLA A-array contour map with an angular resolution of 0.64×0.35 arcsec along a PA∼12° is shown superimposed on a narrow-band Hα image of only the central region of the galaxy.

the optical, hourglass-shaped structure traced by the Hα emission (Fig. 2.9) shows that the starburst region lies at the base of this structure, and possibly provides the energy to drive the outflow. The 4860 MHz image and the two

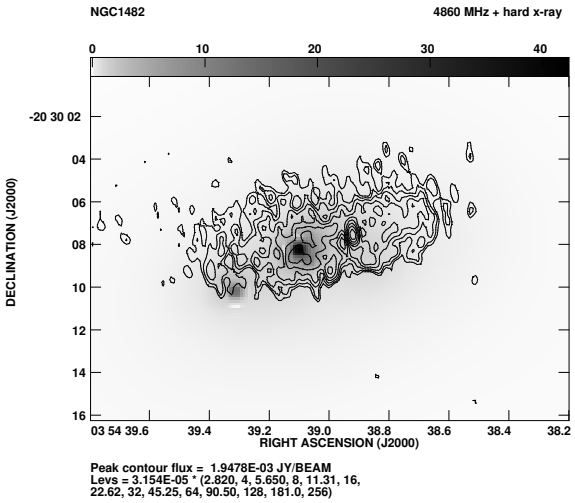

Figure 2.12: The 4860 MHz VLA A-array contour map with an angular resolution of 0.64×0.35 arcsec along a PA∼12° is shown superimposed on the Chandra 2-8 keV hard X-ray image of only the central region of the galaxy.

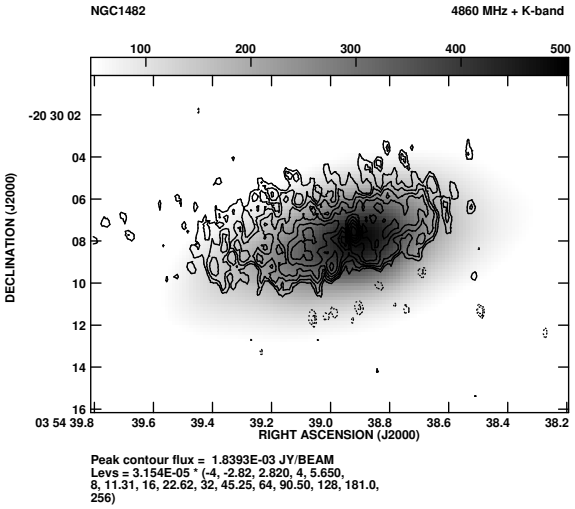

Figure 2.13: The 4860 MHz VLA A-array contour map with an angular resolution of 0.64×0.35 arcsec along a PA∼12° is shown superimposed on the infrared K-band 2MASS image of only the central region of the galaxy.

Hα peaks of emission at the extremeties appear to lie along a line perpendicular to the axis of the outflow. The 4860 MHz image appears displaced

to the north in the central visible Hα region of emission; this apparent displacement could be largely due to obscuration of the northern part by the dust lane.

In order to understand the nature of the prominent radio peak we have compared the 4860 MHz radio image with the optical R-band continuum, Hα, hard X-ray and infrared images (Fig. 2.10, 2.11, 2.12 and 2.13). The positions of the peaks in J2000 co-ordinates at the different wavelengths are listed in Table 2.4. These positions have been estimated from the FITS images kindly provided by Strickland and Veilleux (private communication). The R-band image shows two prominent peaks of emission with the peak brightness of the eastern one being brighter by a factor of $\sim$1.14, and a dust lane to the north. The northern part of the the 4860 MHz image is seen through the dust lane. The R-band peaks possibly arise due to a combination of enhanced emission in the sites of star formation and differential extinction in the circumnuclear region. These peaks skirt the southern edge of the radio continuum image and are not coincident with the radio peak. The Hα image also shows two peaks of emission with the maximum value for the eastern one being brighter than the western one by a factor of $\sim$2. The Hα peaks also lie along the southern boundary of the image, are within $\sim 1.''5$ of the peaks in the R-band image, and are not coincident with the radio peaks.

The 2 to 8 keV hard X-ray Chandra image also shows two compact peaks of emission. Such features have been seen in a number of nearby starburst galaxies such as M82 (Zezas et al. 2001), NGC4038/4039 (Zezas et al. 2002) and NGC3256 (Lira et al. 2002), and are interpeted to be due to X-ray binaries or supernova remnants. In NGC1482, the western hard X-ray peak is within 0.5 arcsec of the secondary radio peak (Fig. 2.12). The point source subtracted hard X-ray image (Strickland et al. 2004), not shown here, reveals

Table 2.4: Nuclear emission peaks at different wavebands

Peaks	RA(J2000)	Dec.(J2000)
Radio 4860 MHz	03 54 38.92	−20 30 07.5
Radio 8460 MHz	03 54 38.92	−20 30 07.6
X-ray West	03 54 39.10	−20 30 08.2
X-ray East	03 54 39.31	−20 30 10.1
Hα West	03 54 39.05	−20 30 11.2
Hα East	03 54 39.18	−20 30 10.5
R-band West	03 54 38.92	−20 30 09.3
R-band East	03 54 39.18	−20 30 09.9

more extended emission coincident with the secondary peak in the 4860 MHz image. These are possibly due to one or more supernova remnants. The eastern hard X-ray peak (see Fig. 2.12) lies at the southern edge of the radio image and does not have any compact component associated with it. No hard X-ray peak is seen at the position of the prominent peak in the radio image.

A superposition of the radio image on the infrared 2MASS (2 Micron All Sky Survey) K-band image (Jarrett et al. 2003) shows the infrared peak to be coincident with the prominent radio peak (Fig. 2.13). The infrared image, which is largely due to a population of old giant stars, also appears asymmetric with more emission on the eastern side than the western one. This asymmetry is similar to what is seen in the radio image, and reflects a greater degree of circumnuclear activity on the eastern side of this peak. The coincidence of the radio and infrared peaks suggest that this is possibly the centre of the galaxy. The centre of the galaxy estimated from the outer isophotes of the R-band image is at RA 03 54 38.91 and Declination −20 30 07.2, which is within an arcsec of the radio peak in the high-resolution images. The geometrical centre of a line joining the peaks of the red- and blue-shifted H I emission blobs (RA: 03 54 38.8 and Dec.: −20 30 10 in

J2000 co-ordinates, Section 4.1) is within 2 arcsec of this position, and hence co-incident with it within the errors.

2.5 H I Observations

The H I spectra towards different regions of the galaxy show significant H I emission from two diametrically opposite regions located at a distance of ∼20 arcsec from the nuclear region, while H I in absorption is seen against the radio continuum source. These observations which have an rms noise of ∼0.6 mJy/beam per channel are described below.

(a) H I emission

The global H I profile from a tapered image with an angular resolution of 8.19×6.52 arcsec along a PA of 36° is shown in Fig. 2.14. This spectrum has been obtained by specifying a box around the visible extent of the galaxy, and there is a hint that it could be double-humped. The heliocentric velocities at zero intensity range from ∼1690 to 2020 km s^{-1}, indicating a systemic velocity of 1855±20 km s^{-1}. The total width is ∼330 km s^{-1}, similar to that of typical spiral galaxies. The published H I spectrum by Roth, Mould & Davies (1991) is very similar and has a central velocity of 1859 km s^{-1} with a velocity resolution of 7.3 km s^{-1}. The total H I flux density estimated from our spectrum is 9±1 Jy km s^{-1}, implying that the total H I mass using the standard expression (e.g. Mirabel & Sanders 1988) is $13.5\pm1.5\times10^8 M_\odot$.

We compare the global H I profile with the CO J=1−0 spectra published by a number of authors (Sanders et al. 1991; Elfhag et al. 1996; Chini et al. 1996). Sanders et al. (1991) find a double-humped profile with the blue-shifted component being narrower and weaker than the redshifted one,

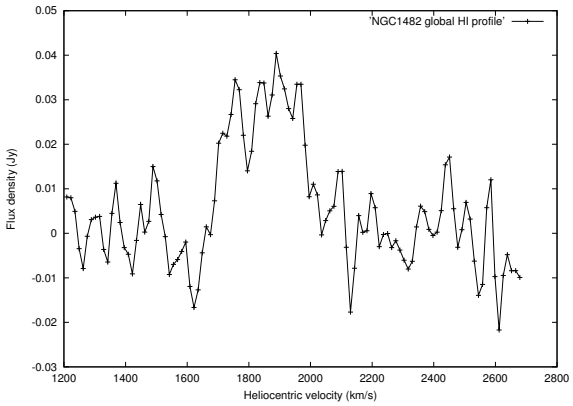

Figure 2.14: The global H I emission profile of NGC1482 obtained from a tapered image with an angular resolution of 8.19×6.52 arcsec along a PA of 36°.

similar to the H I profile. The velocity width at the 20 per cent level of the peak is 325 km s^{-1} . CO J=1−0 spectra published by Elfhag et al.(1996) and Chini et al. (1996) span a similar velocity range, but show significant differences in their CO profiles. Chini et al. have noted the difference and have mentioned that they do not have an explanation.

The estimates of heliocentric systemic velocity from H I observations are consistent with those quoted from CO observations by Young et al. (1995) and Elfhag et al. (1996). They find the values to be 1848 and 1847 km s−1 respectively with spectral resolutions of 10−15 km s^{-1}. These values agree with the estimate of 1850±20 km s^{-1} by Veilleux & Rupke (private communication) from their optical spectroscopic observatinos. The earlier estimate of 1916±39 km s^{-1} obtained by fitting the Hα, Hβ, [O III], [N II] and [S II] lines (Da Costa et al. 1991) appear to be higher. Da Costa et al. note in their paper that Fairall has pointed out that some of their estimates differ from those in the literature by ∼100 km s^{-1}. At present, we adopt the value of 1850±20 km s^{-1} as the heliocentric systemic velocity of the galaxy.

The H I total intensity map has been generated from a MOMENT analysis

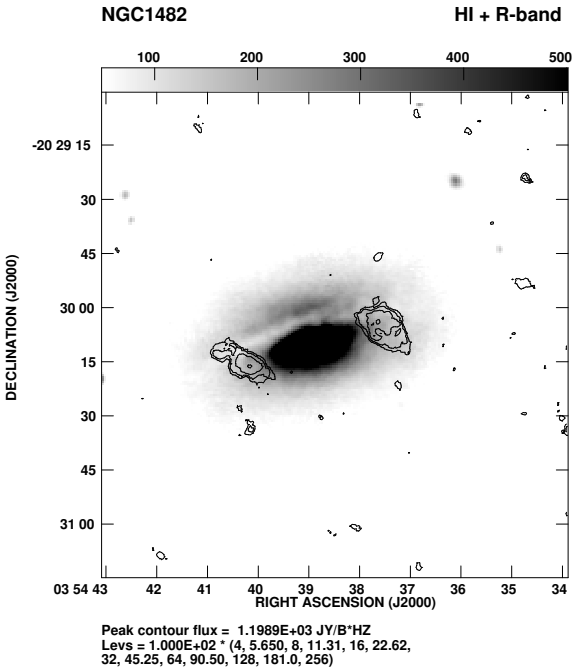

Figure 2.15: H I total-intensity contour map with an angular resolution of 8.19×6.52 arcsec along PA of 36° superimposed on an optical R-band image.

in AIPS by integrating the velocities from 2090 to 1555 km s^{-1} and blanking out points which are below three times the rms noise. A Hanning smoothing along the velocity axis and a Gaussian smoothing in the spatial plane were used for making this image. There are two blobs of emission on opposite sides of the nuclear region, and located about 20 arcsec (2.4 kpc) from it (Fig. 2.15 and 2.16). van Driel (1987) and van Driel & van Woerden (1991) have studied the distribution and kinematics of a sample of lenticulars and early-type disk galaxies and compared their properties with late-type spirals. They note that while most barred spirals have a pronounced central hole in their H I distribution, often as large as the bar itself, non-barred spirals and S0/a galaxies generally show filled H I disks, sometimes with a central depression. Although our results on H I observations of NGC1482, an S0/a galaxy, is broadly consistent with these trends, the depletion appears pronounced,

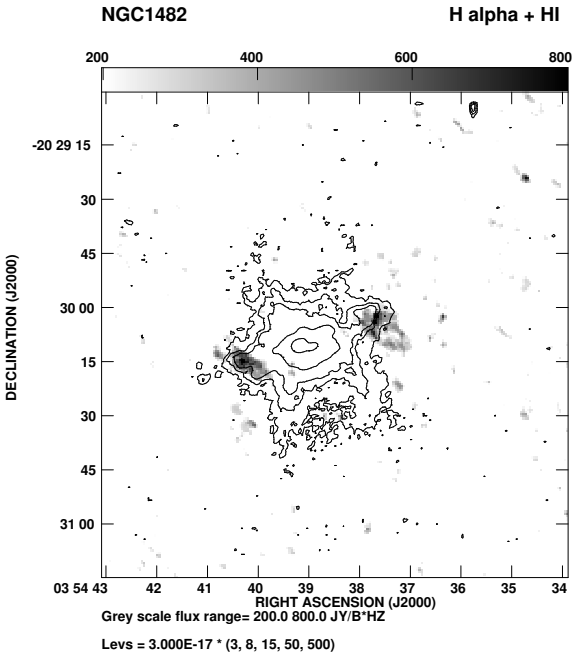

Figure 2.16: The H I total-intensity image in grey with an angular resolution of 6.95×5.17 arcsec along PA of 34° superimposed on the Hα contour map.

possibly due to the nuclear starburst.

At about 20% of the peak intensity in the spectrum (Fig. 2.19), the estimated central velocity is 1835±20 km s^{-1}, consistent with the systemic velocity. The western blob has a maximum red shift of ∼190 km s^{-1} relative to the systemic velocity of 1850 km s^{-1}, while the maximum blue-shift value for the eastern one is ∼220 km s^{-1}. The width of the line towards each blob is ∼250 km s^{-1} at 20 % of the peak intensity. The estimated column density and mass for the western blob are 4.0±0.3×10^{21} atoms cm^{-2} and 15±1×10^{7} M$_{\odot}$ respectively, while the corresponding values for the eastern blob are 3.8±0.3×10^{21} atoms cm^{-2} and 13.5±1×10^{7} M$_{\odot}$ respectively.

The H I total-intensity distribution is shown superimposed on an optical R-band image of the galaxy as well as on the Hα ionization cone in Fig. 2.15 and 2.16. It is clear that the H I blobs of emission lie at the outer edges of the

galaxy close to the edge of the dust lane. It avoids the central region where active star formation is taking place. A comparison of the H I emission blobs with the Hα image (Fig. 2.16) shows that the H I blobs define an axis which is approximately perpendicular to the optical emission-line outflow bicone. The peaks of these two blobs are close to two Hα knots or peaks of emission in the outer edges of the galaxy. The N II to Hα flux density ratios suggest that the two knots are consistent with these being H II regions (Veilleux & Rupke 2002). More sensitive H I observations of higher angular resolution are required to establish reliably the structure and dynamics of the blobs, and the effects of the Hα knots and the circumnuclear startburst on these properties.

(b) H I absorption

In Fig. 2.17, we present the absorption profiles towards different regions of the continuum source with an angular resolution of 6.95×5.17 arcsec along PA of 34°, and an rms noise of 0.6 mJy/beam. A 21-cm continuum image with an angular resolution of 3×2 arcsec along a PA of 28° from the same data set is also shown 2.18. The continuum image shows evidence of two peaks of emission towards the nuclear region. The peak absorption occurs at a heliocentric velocity of 1836±15 km s^{-1}, which is consistent with the heliocentric systemic velocity. An absorption feature at this velocity is seen over most of the source. In addition there is a blue-shifted component at a heliocentric velocity of 1688 km s^{-1} which is prominent on the eastern side. The western side shows a weaker red-shifted shoulder with a heliocentric velocity of ∼1942 km s^{-1}. These features which are seen in the absorption

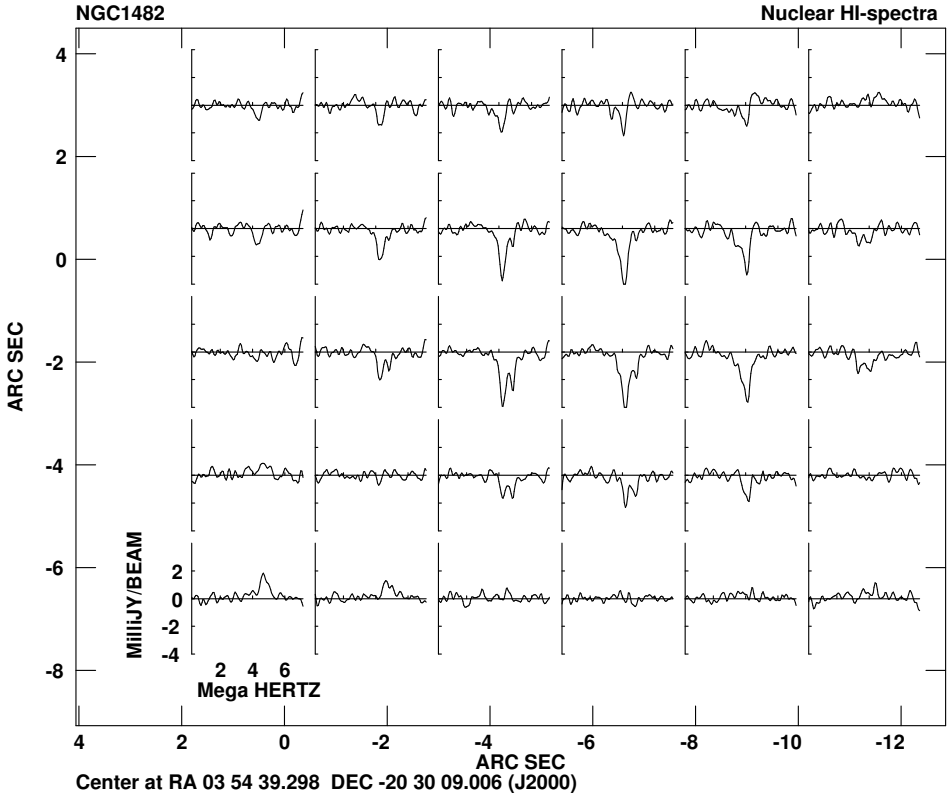

Figure 2.17: Multiple H I absorption spectra against the central radio continuum source with an angular resolution of 6.95×5.17 along PA of 34°.

spectrum against the nuclear region (see Fig. 2.19) taken over a rectangular area of 7×4 arcsec, highlights the possibility that absorption is caused by multiple clouds moving with different velocities. Hydrodynamical simulations of starburst-driven superwinds show that the cool gas could expand laterally in the disk of the galaxy, be carried vertically outwards by the tenuous superwind or be entrained in the interface between the hot, superwind fluid and the cool, dense ISM (e.g. Heckman et al. 1990, 2000). For a systemic velocity of 1850±20 km s^{-1}, there is a suggestion of a mild asymmetry in the absorption profile with the approaching component being blue shifted by 162 km s^{-1} while the receding component is red shifted by 92 km s^{-1}. In addition to galactic rotation, the width of the absorption profile may also be

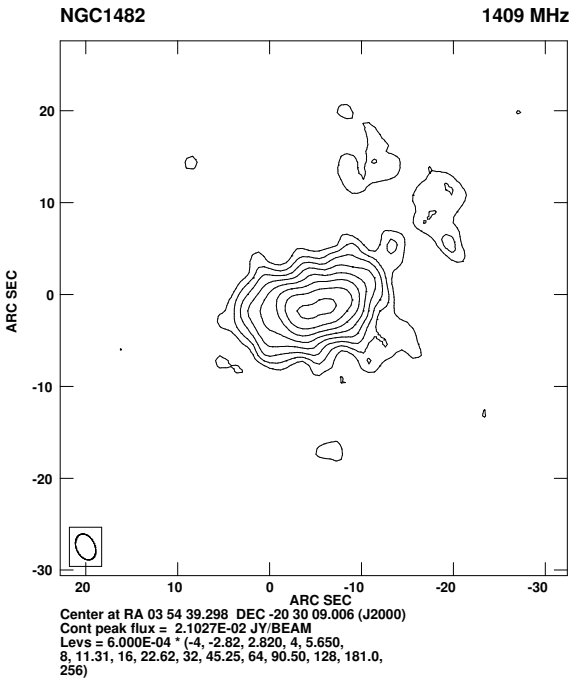

Figure 2.18: The GMRT 1409-MHz continum image against which H I absorption is seen. This image has an angular resolution of 2.96×2.01 arcsec along PA of 25°.

due to cool, HI components which have been hydrodynamically affected by the superwind, but this needs further investigation.

The optical depth in each velocity channel has been calculated using the background continuum flux density of 60 mJy from the area of 7×4 arcsec. The peak optical depth estimated from this spectrum is 0.11. The total column density is $2.8\pm0.1\times10^{21}$ cm^{-2}, which has been estimated in the ususal way (e.g. Heckman, Balick & Sullivan 1978) by integrating the optical depth from 1675 to 1956 km s^{-1}, and assuming a spin temperature of 100° K. The corresponding total mass of the absorbing H I clouds is $6.3\pm0.3\times10^{6}$M$_{\odot}$.

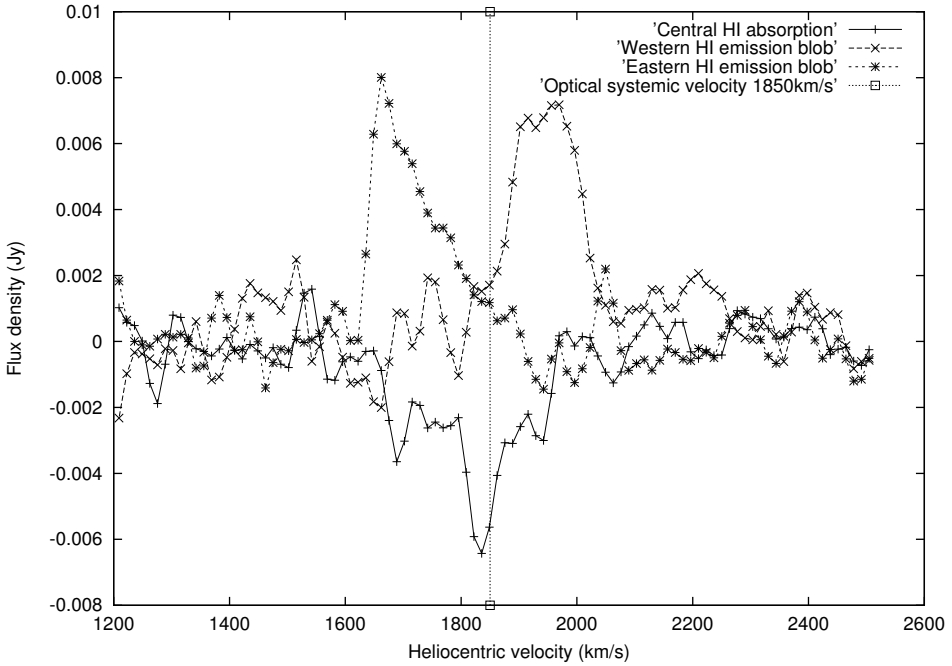

Figure 2.19: The H I emission spectra of the western and eastern blobs, and the H I absorption spectrum against the central radio continuum source. The emission spectra have been obtained from the image with an angular resolution of 8.19×6.52 arcsec along PA of 36°, while the absorption spectrum has been obtained with an angular resolutiion 2.96×2.01 arcsec along PA of 25°. The vertical line indicates the optical systemic velocity of 1850±20 km s^{-1}.

2.6 Summary and concluding remarks

The results of a radio study of the superwind galaxy NGC1482 which has a remarkable hourglass-shaped optical emission line outflow as well as bipolar soft X-ray bubbles of emission, are summarised and discussed briefly here.

1. The low-frequency images trace the relatively smooth non-thermal emission due to relativistic particles generated largely in the starburst. There is no evidence of significant non-thermal emission along the optical hourglass-shaped or X-ray outflows.

2. From radio observations we have estimated the supernova rate and

find it to be similar to other well-known starburst galaxies. We also estimate the available energy in the supernovae, which could be the driving force for the superwind outflow. However, an estimate of the total energy in all the different components of the outflow is required before determining whether the energy in the supernovae is adequate to drive the superwind.

3. The higher resolution 4860 and 8460 MHz images, which trace the circumnuclear starburst region, show a single prominent peak and secondary substructure embedded in the more extended emission. These lie at the base of the optical hourglass-shaped structure and the X-ray outflows.

4. The prominent radio peak in the high-resolution images has a steep radio spectrum between 4860 and 8460 MHz and has not been detected at 14965 MHz. The highest resolution 8460 MHz A-array image shows an extension towards the south. The brightness temperature of the prominent peak in the 8460 MHz A-array image is 740° K, and it is difficult to distinguish whether it is an AGN or non-thermal emission from a compact starburst region. Optical spectroscopic observations by Kewley et al. (2000) show no evidence of an AGN.

5. The prominent radio peak is not coincident with the peaks of emission in the R-band, Hα and hard X-ray images, but is coincident with the peak in the 2MASS K-band image, suggesting that this feature is possibly the centre of the galaxy. The centre of the galaxy estimated from the outer isophotes of the R-band image is within an arcsec of the radio peak. The geometrical centre of a line joining the peaks of the red- and blue-shifted H I blobs of emission is within 2 arcsec of the prominent

radio peak.

6. The H I observations reveal two blobs of emission on opposite sides of the centre of the galaxy. The western blob has a maximum red shift of $\sim$190 km s^{-1} relative to the systemic velocity of 1850$\pm$20 km s^{-1}, while the maximum blue shift for the eastern one is $\sim$220 km s^{-1}. These blobs are located at a distance of $\sim$2 kpc from the centre and have masses of approximately 15 and 13.5$\times$10^7 M$_\odot$ respectively.

7. The H I absorption profile shows multiple components with the deepest absorption feature at 1836 km s^{-1}, consistent with the systemic velocity of the galaxy. The H I mass estimated from the absorption profile is 6.3$\times$10^6 M$_\odot$. Relative to the systemic velocity of 1850$\pm$50 km s^{-1}, there is a suggestion of a mild asymmetry in the absorption profile which could be due to H I clouds hydrodynamically affected by the superwind, in addition to the effects of galactic rotation.

8. Although the distribution of H I gas is consistent with that seen for other S0/a galaxies (van Driel 1987; van Driel & van Woerden 1991), the central depletion is pronounced, possibly due to the nuclear starburst.

References

Allen M.L., Kronberg P.P., 1998, ApJ, 502, 218

Baars J.W.M., Genzel R., Pauliny-Toth I.I.K, Witzel A., 1977, A&A, 61, 99

Balsara D.S., Krolik J.H., 1993, ApJ, 402, 109

Baum S.A., O'Dea C.P., Dallacassa D., de Bruyn A.G., Pedlar A., 1993. ApJ, 419, 553

Chini R., Krügel E., Lemke R., 1996, A&AS, 118, 47

Colbert E.J.M., Baum S.A., Gallimore J.F., O'Dea C.P., Lehnert M.D., Tsvetanov Z.I., Mulchaey J.S., Caganoff S., 1996a, ApJS, 105, 75

Colbert E.J.M., Baum, S.A., Gallimore J.F., O'Dea C.P., Christensen, J.A., 1996b, ApJ, 467, 551

Collison P.M., Saikia D.J., Pedlar A., Axon D.J., Unger S.W., 1994, MNRAS, 268, 203

Condon J.J., 1992, ARA&A, 30, 575

Condon J.J., Helou G., Sanders D.B., Soifer B.T., 1990, ApJS, 73, 359

Condon J.J., Yin Q.F., 1990, ApJ, 357, 97

Condon J.J., Huang Z.-P., Yin Q.F., Thuan T.X., 1991, ApJ, 378, 65

Da Costa L.N., Pellegrini P.S., Davis M., Meiksin A., Sargent W.L.W., Tonry J.L., 1991, ApJS, 75, 935

de Vaucouleurs G., de Vaucouleurs A., Corwin Jr H.G., Buta R.J., Paturel G., Fouqué P., 1991, Third Reference Catalogue of Bright Galaxies, Springer-Verlag

Dahlem M., 1997, PASP, 109, 1298

Elfhag T., Booth R.S., Höglund B., Johansson L.E.B., Sandqvist Aa., 1996, A&AS, 115, 439

Hameed S., Devereux N., 1999, AJ, 118, 730

Heckman T.M., Balick B., Sullivan III W.T., 1978, ApJ, 224, 745

Heckman T.M., Armus L., Miley G.K., 1990, ApJS, 74, 833

Heckman T.M., Lehnert M.D., Strickland D.K., Armus L., 2000, ApJS, 129, 493

Huang Z.P., Thuan T.X., Chevalier R.A., Condon J.J., Yin Q.F., 1994, ApJ, 424, 114

Jarrett T.H., Chester T., Cutri R., Schneider S.E., Huchra J.P., 2003, AJ, 125, 525

Kewley L.J., Heisler C.A., Dopita M.A., Sutherland R., Norris R.P., Reynolds J., Lumsden S., 2000, ApJ, 530, 704

Krolik J.H., Kriss G., 1995, ApJ, 447, 512

Larson R.B., 1974, MNRAS, 169, 229

Lira P., Ward M., Zezas A., Alonso-Herrero A., Ueno S., 2002, MNRAS, 330, 259

Melioli C., de Gouveia Dal Pino E.M., 2004, A&A, 424, 817

Mirabel I.F., Sanders D.B., 1988, ApJ, 335, 104

Noreau L., Kronberg P.P., 1987, AJ, 93, 1045

Pettini M., Shapley A.E., Steidel C.C., Cuby J.-G., Dickinson M., Moorwood A.F.M., Adelberger K.L., Giavalisco M., 2001, ApJ, 554, 981

Roth J., Mould J.R., Davies R.D., 1991, AJ, 102, 1303

Saikia D.J., Phookun B., Pedlar A., Kohno K., 2002, A&A, 383, 98

Sanders D.B., Scoville N.Z., Soifer B.T., 1991, ApJ, 370, 158

Spergel D.N. et al., 2003, ApJS, 148, 175

Strickland D., 2001, in Chemical enrichment of the ICM and IGM, eds Fusco-Femiano R., Matteucci F., ASP Conf. Proc., 253, 387

Strickland D.K., Heckman T.M., Colbert E.J.M., Hoopes C.G., Weaver K.A., 2004, ApJS, 151, 193 (astro-ph/0306592)

Tully R.B., 1988, Nearby Galaxies Catalogue, Cambridge University Press

Ulvestad J.S., Antonucci R.R.J., 1997, ApJ, 488, 621

van Driel W., 1987, PhD Thesis, University of Groningen

van Driel W., van Woerden H., 1991, A&A, 243, 71

Veilleux S., 2002a, in Galaxies: The Third Dimension, eds Rosado M., Binette L., Arias L., ASP Conf. Series, 282, 293

Veilleux S., 2002b, in Extragalactic Gas at Low Redshift, eds Mulchaey J.S., Stocke J., ASP Conf. Series, 254, 313

Veilleux S., 2003, astro-ph/0309119

Veilleux S., Rupke D.S., 2002, ApJ, 565, L63

Veilleux S., Shopbell P.L., Rupke D.S., Bland-Hawthorn J., Cecil G., 2003, AJ, 126, 2185

Weaver K.A., 2001, in The Central Kiloparsec of Starbursts and AGN: The La Palma Connection, eds Knapen J.H., Beckman J.E., Shlosman I., Mahoney T.J., SP Conf. Proc., 249, 389 Webber W.R., 1991, in The interpretation of modern synthesis observations of spiral galaxies, eds Duric N., Crane P.C., ASP Conf. Series, 18, 37

Young J.S. et al., 1995, ApJS, 98, 219

Zezas A., Fabbiano G., Prestwich A., Ward M., Murray S., 2001, in Central kpc of starburst and AGN, eds Knapen J.H., Beckman J.E., Shlosman I., Mahoney T.J., ASP Conf. Ser., 249, 425

Zezas A., Fabbiano G., Rots A.H., Murray S., 2002, ApJ, 577, 710

CHAPTER 3

Radio bubbles in the composite AGN-starburst galaxy NGC 6764.

3.1 Abstract

We present multi-frequency radio continuum as well as H I observations of the composite galaxy NGC 6764, which has a young, circumnuclear starburst and also harbours an active galactic nucleus (AGN). These observations have been made at a number of frequencies ranging from ∼600 MHz to 15 GHz using both the Giant Metrewave Radio Telescope (GMRT) and the Very Large Array (VLA). They reveal the structure of the bipolar bubbles of non-thermal, radio emission which are along the minor axis of the galaxy and extend up to ∼1.1 and 1.5 kpc on the northern and southern sides respectively. Features in the radio bubbles appear to overlap with filaments of Hα emission. The high-resolution observations reveal a compact source, likely to be associated with the nucleus of the galaxy, and a possible radio jet towards the south-west. We have compiled a representative sample of galaxies with bubbles of non-thermal radio emission and find that these are found in galaxies with an AGN.

The H I observations with the GMRT show two peaks of emission on both the ends of the stellar-bar and depletion of H I in the central region

Table 3.1: Basic data on NGC 6764.[a]

RA [b] (h m s)	DEC [b] (° ′ ″)	Type[c]	a × b[d] (′ × ′)	V_{sys}[e] (km s^{-1})	i[f] (°)	$\log(L_{FIR})$[g] ($L_\odot$)	D[h] (Mpc)
19 08 16.428	50 55 59.47	SB(s)bc	2.3 × 1.3	2416 ±4	44.5	10.31	34.0

a Taken from the NASA Extragalactic Database (NED), unless stated otherwise.
b The position of radio peak from our high-resolution, VLA A-array, 8460-MHz image in J2000.
c Morphological type.
d Optical major and minor axes.
e Heliocentric systemic velocity.
f Inclination angle from HI study by Wilcots, Turnbull & Brinks (2001).
g Log of the far infra-red luminosity (Condon et al. 1996) revised for a distance of 34.0 Mpc.
h Distance estimated using the galaxy recessional velocity and H_0=71 km s^{-1} Mpc^{-1} (Spergel et al. 2003) using the web-based cosmology calculator of Ned Wright. For this distance 1″=163 pc.

of the galaxy. We also detect H I in absorption against the central radio peak at the systemic velocity of the galaxy. The H I-absorption spectrum also suggests a possible weak absorption feature blue-shifted by ∼120 km s^{-1}, which requires confirmation. A similar feature has also been reported from CO observations, suggesting that the circumnuclear activity affects the kinematics of the atomic and molecular gas components, in addition to the ionised gas seen in Hα and [NII].

3.2 Introduction

Galactic-scale outflows or galactic winds play an important role in heating and supplying kinetic energy to the intergalactic medium (IGM) and enriching it with metals (e.g. Heckman, Armus & Miley 1990; Veilleux, Cecil & Bland-Hawthorn 2005 for a review). These outflows can be driven either by a circumnuclear starburst or an active galactic nucleus (AGN), although it

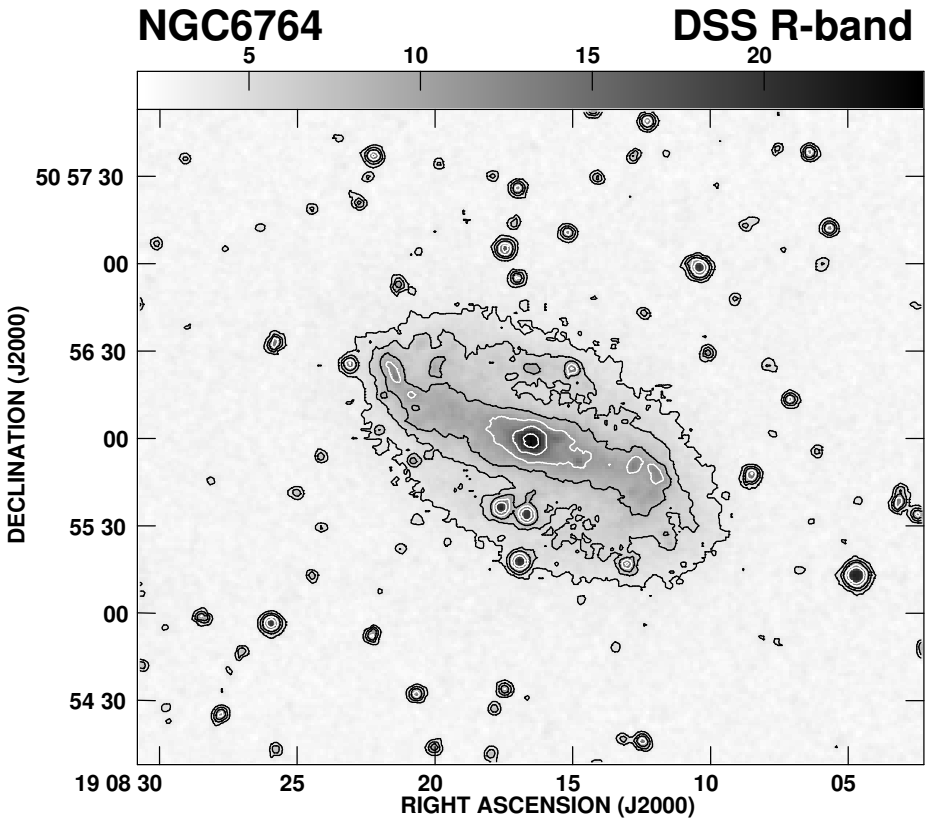

Figure 3.1: An optical R-band image of NGC 6764 from the Digitized Sky Survey (DSS). Contour levels are in arbitrary units.

is often likely to be due to a combination of both these processes. The conditions for an AGN, such as a deep potential well and a supply of gas, could also lead to a circumnuclear starburst and trigger a starburst-driven galactic wind. Observationally, about a half of nearby Seyfert 2 galaxies are found to host a nuclear starburst, with the proportion being larger for infra-red selected objects (e.g. Cid Fernandes et al. 2001; Veilleux 2001 and references therein). Also in some cases, such as in NGC3079, there is strong evidence that starburst-driven winds co-exist with the AGN-driven outflows (Cecil et al. 2001; Irwin & Saikia 2003). Although it is not usually straightforward

to disentangle the contributions to the galactic-scale outflows from the AGN and the starburst, the galactic winds from starbursts tend to be oriented along the minor axes of their parent galaxies, while the outflows from AGN show no preferred orientation (e.g Ulvestad & Wilson 1984; Kinney et al. 2000; Gallimore et al. 2006 and references therein).

In this chapter, we present radio continuum and HI observations of the S-shaped spiral galaxy, NGC6764, which hosts an AGN and also exhibits evidence of a recent, intense starburst. It has been classified as a Seyfert 2 galaxy (Rubin, Thonnard & Ford 1975) and also as a low-ionization nuclear emission line region or LINER (Osterbrock & Cohen 1982; Schinnerer, Eckart & Boller 2000; Eckart et al. 1991, 1996). X-ray observations exhibit evidence of variability by a factor of $\sim$2 over a time scale of 7 days, consistent with the existence of an AGN (Schinnerer et al. 2000). The basic properties of the galaxy are summarised in Table 6.1. It is strongly barred and has a compact nuclear region, bright in both optical emission lines (Eckart et al. 1996) and radio continuum (Baum et al. 1993). There is a very prominent 466 nm Wolf-Rayet (W-R) emission feature from the nucleus (Osterbrock & Cohen 1982; Schinnerer et al. 2000), suggestive of recent star formation (Armus, Heckman & Miley 1988; Conti 1991). There is a dense concentration of molecular gas in the central region (Eckart et al. 1991, 1996; Kohno et al. 2001) with $T_{kin} >$ 20K in the circumnuclear region and $\lesssim$10K towards the spiral arms (Eckart et al. 1991). Interferometric observations show molecular cloud complexes with an asymmetric velocity field which is blue-shifted relative to the systemic velocity. The distribution of the 2.12 μm H_2 line flux is orthogonal to the stellar bar and also indicates possible outflow from the circumnuclear region (Eckart et al. 1996). The radio emission is extended roughly orthogonal to the major axis, forming bubbles of emission on opposite sides. There is also

an extended X-ray component similar in extent to that of the radio emission (Schinnerer et al. 2000).

The new radio continuum observations presented here were made with the Very Large Array (VLA) and the Giant Metrewave Radio Telescope (GMRT) at a number of frequencies ranging from ∼600 MHz to 15 GHz. These observations reveal the structure of the bubbles of non-thermal emission extending up to ∼7 and 9 arcsec on the northern and southern sides respectively, as well as that of the circumnuclear region, in far greater detail. We present spectral index images of these features, compare NGC6764 with other sources with bubbles of non-thermal plasma and discuss the possible origin of these features. The HI observations were made with the GMRT to examine the distribution of HI clouds with higher resolution and also possible kinematic effects of the circumnuclear starburst on the HI clouds via HI-absorption spectra. We describe the observations in Section 2, and present the observational results from our radio continuum and HI observations in Sections 3 and 4 respectively. These are discussed in Section 5 while the conclusions are summarised in Section 6.

3.3 Observations and Data analysis

The observing log for both the GMRT and VLA observations is presented in Table 6.2, which is arranged as follows. Column 1: Name of the telescope where we also list the configuration for the VLA observations. In addition to our own data, we have also analysed some of the relevant archival VLA data on this galaxy, which are listed separately in Table 6.2. Column 2: The frequency of the observations where H I denotes spectral line observations. Columns 3 and 4: Dates of the observations and the time, t, spent on the

Table 3.2: Observation log

Telescope	Freq. MHz	Obs. date	t min	Phase Calib.	$S_{cal.}$ Jy
GMRT	598	2004Jan04	180	2023+544	0.80
VLA-A	1400	2003Aug12	27	2023+544	1.11
GMRT	1408,H I	2004Jan26	240	2023+544	1.03
VLA-A	4860	2003Aug12	50	2023+544	1.08
VLA-A	8460	2003Aug12	60	2023+544	0.99
VLA-A	14965	2003Aug12	10	2023+544	0.87
Archival					
VLA-B[1]	4985	1985May25	45	1927+612	0.55
VLA-C[2]	8435	1999July26	16	1944+548	0.66
VLA-B[3]	8460	2002	9	1944+548	0.65
VLA-C[3]	14964	2002	16	1824+568	1.68

Programme code: [1]: VH17; [2]: AL490; [3]: AC624

source in minutes. For the archival data the dates have been taken from the image headers. However, for the observations in 2002, the precise dates seem inconsistent with the array configurations; hence only the year is listed. The project codes for the archival data are indicated below the Table. Columns 5 and 6: The phase calibrator used and its flux density estimated from our observations.

The observations with the GMRT, which is described on the website `http://www.gmrt.ncra.tifr.res.in`, as well as with the VLA were made in the standard fashion, with each source observation interspersed with observations of the phase calibrator. The primary flux density calibrator was 3C286 whose flux density was estimated on the Baars et al. (1977) scale, using the 1999.2 VLA values. The bandwidth of the continuum observations with GMRT at 598 MHz was 16 MHz, while for the L-band observations it was 8 MHz. The bandwidth for all the VLA observations was 50 MHz. The VLA data from both the IFs were combined to make the final images. The data analysis was done using the Astronomical Image Processing System

(AIPS) of the National Radio Astronomy Observatory. Since GMRT data is acquired in the spectral-line mode with 128 spectral channels, gain and bandpass solutions were applied to each channel before combining them.

The analysis of the H I observations were also done in the standard way. 3C286 was the primary flux density and bandpass calibrator. The total bandwidth for H I observations was 8 MHz and the spectral resolution was 62.5 kHz, which corresponds to 13.5 km s^{-1} in the centre of the band. We discarded a few antennas with more than 3% fluctuations in the bandpass gains during the observations. One channel in the beginning and eight channels towards the end were also not included in the analysis. The AIPS task UVLIN was used for continuum subtraction and the multi-channel data were then CLEANed using IMAGR. To estimate the overall properties of the galaxy, we made images by tapering the data to different uv distances.

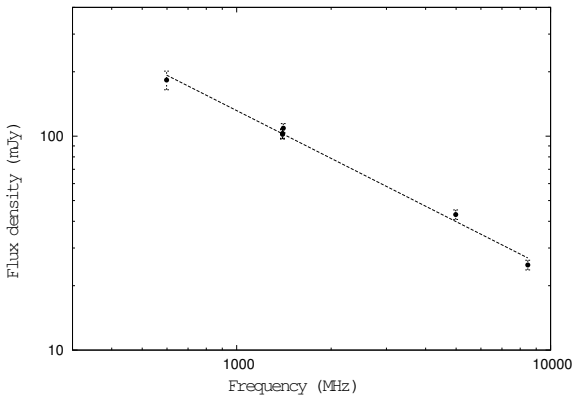

Figure 3.2: The radio spectrum of the central region of NGC 6764. The dashed line represents the linear least-squares fit to the data points.

We have made self-calibrated images for all the different data sets. The GMRT images and the archival VLA B- and C-array 8460-MHz images showed significant improvement after self calibration. For these data sets two cycles of phase and one cycle of amplitude self calibration were applied.

For the remaining data sets, we have presented the un-selfcalibrated images. Some of the observed parameters of the GMRT and the VLA continuum images are presented in Table 6.3 which is arranged as follows. Columns 1 and 2 are similar to that of Table 6.2, except that we also list the NRAO VLA Sky Survey (NVSS). Columns 3 to 5: The resolution of the image with the major and minor axes being listed in arcsec and the position angle (PA) in degrees. Column 6: The rms noise in units of mJy/beam. Columns 7 and 8: The peak and total flux densities in units of mJy/beam and mJy respectively. These have been estimated by specifying a polygon around the source. The total error in the flux density is approximately 5%.

3.4 Radio continuum emission

(a) The radio bubbles

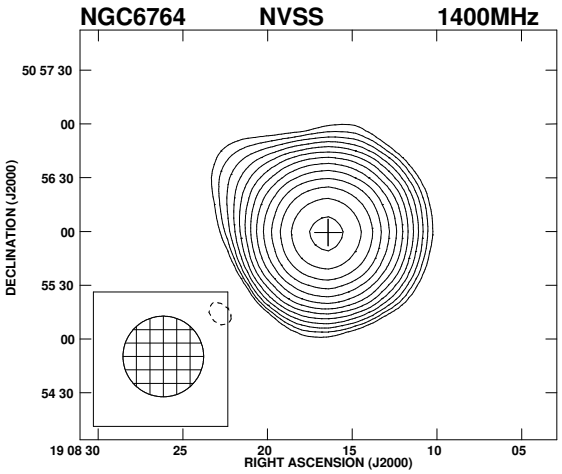

Figure 3.3: NVSS image of the same region with an angular resolution of 45 arcsec. Contour levels are $0.50\times(-4, -2.82, 2.82, 4, 5.65, 8 \ldots)$ mJy/beam. All contour levels are in steps of $\sqrt{2}$, unless otherwise specified.

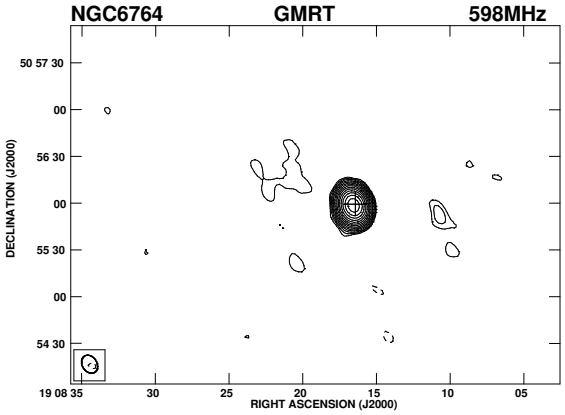

Figure 3.4: GMRT 598-MHz image of the same region of the sky with an angular resolution of ∼11 arcsec. Contour levels are 0.40×(−4, −2.82, 2.82, 4, 5.65, 8 ...) mJy/beam. The cross denotes the position of the optical nucleus from Clements (1981) in all the images except Fig. 11, where the radio nucleus is marked.

We show the optical DSS R-band image of the galaxy, the NVSS image with an angular resolution of 45 arcsec and the GMRT 598-MHz contour map with an angular resolution of ∼11 arcsec in Fig. 3.1, 3.3, 3.4 respectively. The R-band image shows a strong stellar bar and peaks of emission which are likely to be HII regions. The Hα continuum-subtracted image of the galaxy (Zurita, Rozas & Beckman 2000) shows clearly the large number of HII regions and also the filamentary-like structure extending beyond the circumnuclear region, defined here to be within ∼0.5 kpc from the radio nucleus. At radio frequencies, the NVSS image appears somewhat extended with a deconvolved angular size of 15×14 arcsec^2 along a PA of 36°, but well-within the optical extent of the galaxy. The GMRT 598-MHz image shows the emission to be dominated by the central radio source, with possible weak emission from the bar. The spectral index of the central radio source (Fig. 3.2) using our measurements between 598 and 8460 MHz is −0.74±0.02 (S $\propto \nu^{\alpha}$), showing the source to be clearly dominated by non-thermal emission.

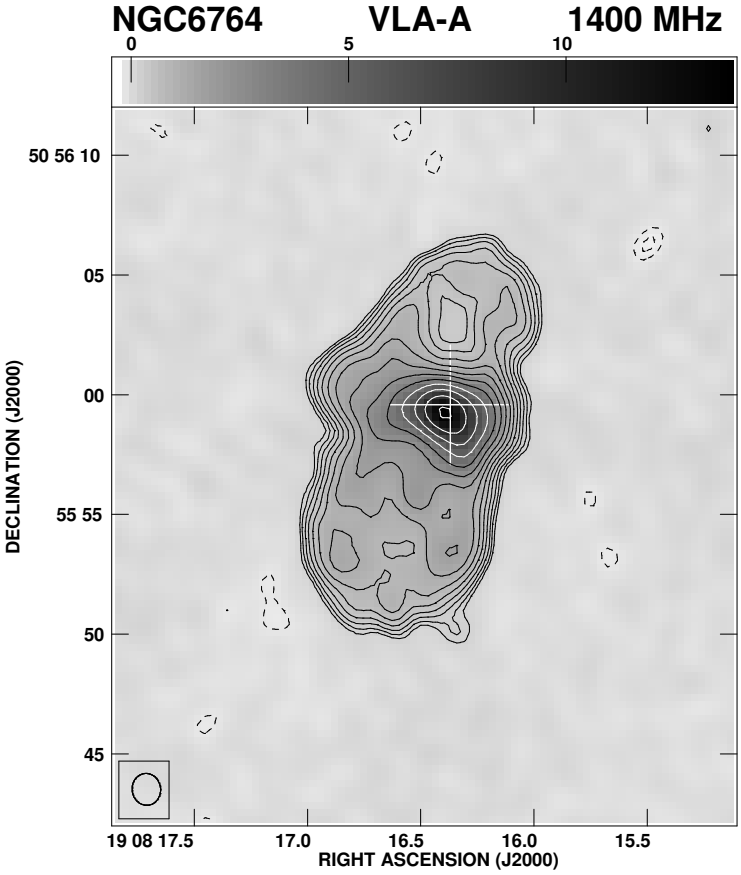

Figure 3.5: VLA A-array image of the radio bubbles at 1400 MHz with an angular resolution of ∼1.3 arcsec. Contour levels are 0.052×(−4, −2.82, 2.82, 4, 5.65, 8 . . .) mJy/beam in steps of $\sqrt{2}$.

Published radio images of the central region of the galaxy (Wilson & Willis 1980; Ulvestad, Wilson & Sramek 1981; Condon et al. 1982; Baum et al. 1993) have shown a 'bright resolved peak at the location of the optical nucleus and diffuse emission on both sides of the nucleus' (cf. Baum et al. 1993). Our images of the extended emission with higher sensitivity using the VLA A-array at 1400 MHz and VLA B-array at 4985 MHz clearly show a bubble-like structure with a drop in brightness towards the centre of each

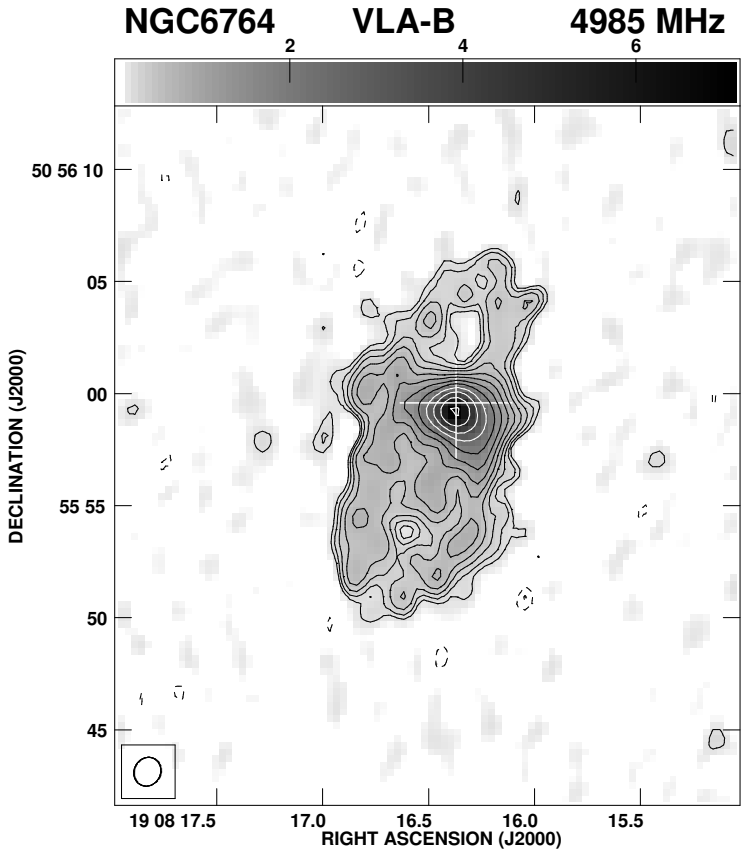

Figure 3.6: VLA B-array image of the same region at 4985 MHz with an angular resolution of ∼1.2 arcsec. Contour levels are 0.054×(−4, −2.82, 2.82, 4, 5.65, 8 . . .) mJy/beam.

bubble, located on opposite sides of the nucleus (Fig. 3.5, 3.6). These images have been made with angular resolutions of ∼1.3 and 1.2 arcsec respectively. The extents of the bubbles are ∼7 and 9 arcsec (1.1 and 1.5 kpc respectively) on the northern and southern sides respectively, while the flux densities at 1400 MHz are 42 mJy and 62 mJy respectively. In addition to the asymmetry in the extents of the bubbles along the minor axis of the galaxy, the radio emission in the circumnuclear region which is roughly orthogonal to this axis is also asymmetric relative to the radio peak or the position of the optical

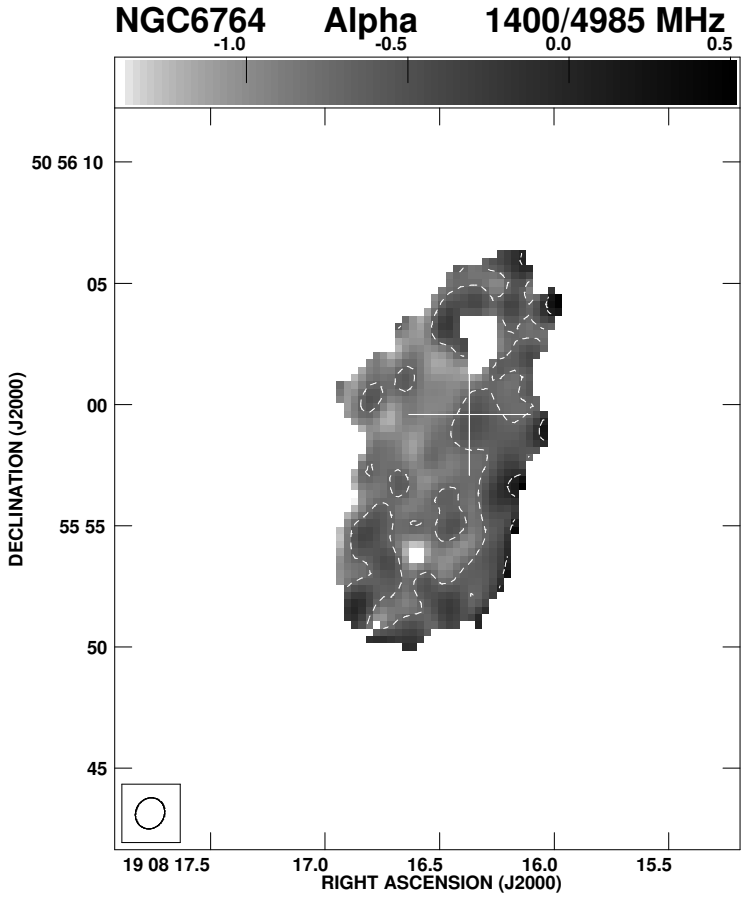

Figure 3.7: Spectral index map of the region obtained by smoothing the 4985-MHz image to the same resolution as that of the 1400-MHz image. The contour level of -0.7 demarcates the regions of flatter and steeper spectral indices.

nucleus, which is marked with a + sign. The emission on the eastern side extends for $\sim$5 arcsec (0.8 kpc) from the radio peak compared with 2.5 arcsec (0.4 kpc) on the western side. At a somewhat lower resolution of 2.7 arcsec, our GMRT image at 1408 MHz and the VLA archival image at 8460 MHz with the same resolution (Fig. 3.8, 3.9) show the bubbles to have similar asymmetric morphologies.

A spectral index image between 1400 and 4985 MHz (Fig. 3.7) made by

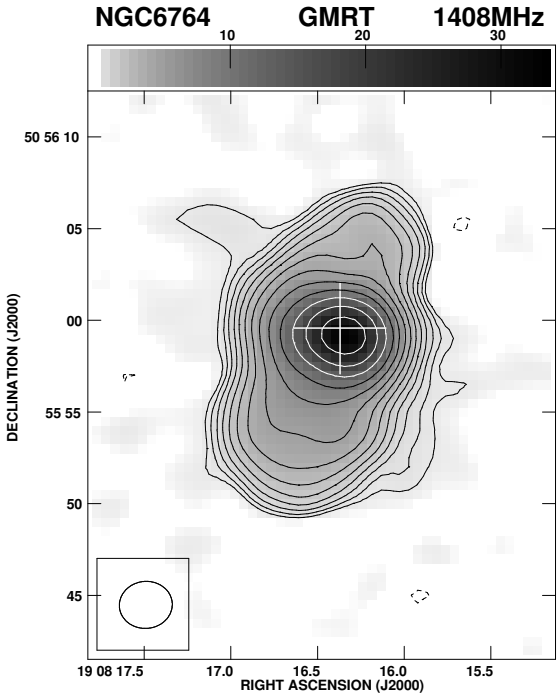

Figure 3.8: GMRT image of the radio bubbles in NGC 6764 at 1408 MHz with an angular resolution of ∼2.7 arcsec. Contour levels are 0.15×(−4, −2.82, 2.82, 4, 5.65, 8 . . .) mJy/beam.

smoothing the 4985-MHz image to the resolution of the 1400-MHz image and using only those pixels which are over 3 times the rms noise, shows that the mean spectral index is ∼−0.72. The western side appears to have a somewhat flatter spectral index, with a mean value of ∼−0.56, compared with ∼−0.77 for the rest of the source. The spectral index image between 1408 and 8460 MHz (Fig. 3.10) shows a mean spectral index of ∼−0.85. This spectral index map also shows a similar trend of a flatter spectral index on the western side. The lateral or east-west asymmetry which is seen in the circumnuclear region is also apparent in parts of the bubbles, as seen in the VLA A-array image shown in Fig. 3.5. If this structural asymmetry, where the western side appears closer to the peak or the axes of the bubbles, and spectral

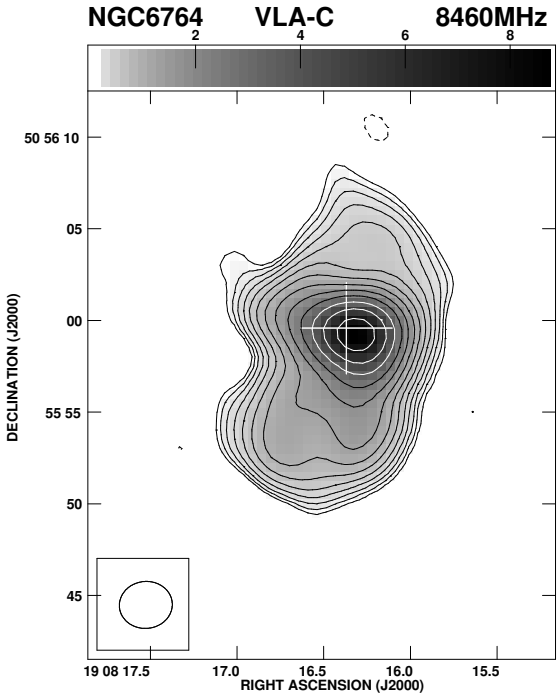

Figure 3.9: VLA C-array image of this region at 8460 MHz with the same resolution as that of the GMRT image. Contour levels are $0.039\times(-4, -2.82, 2.82, 4, 5.65, 8 \ldots)$ mJy/beam.

asymmetry are related, it could be due to an asymmetric distribution of thermal gas. This gas could be probed by high-resolution X-ray observations. Although the ROSAT HRI image (Schinnerer et al. 2000) shows extended X-ray emission in addition to the nuclear source, the resolution is inadequate. High-resolution X-ray observations with Chandra are required to study the detailed distribution of this gas.

Adopting the spectral index of -0.74 as the mean value over the region of emission, and assuming the synchrotron emission to have lower and higher cut-offs at 10^7 and 10^{10} Hz, respectively, a proton-to-electron energy ratio of unity, a filling factor of unity and an oblate spheroidal distribution for the emitting region ($17'' \times 9'' \times 9''$), we estimate the minimum energy density

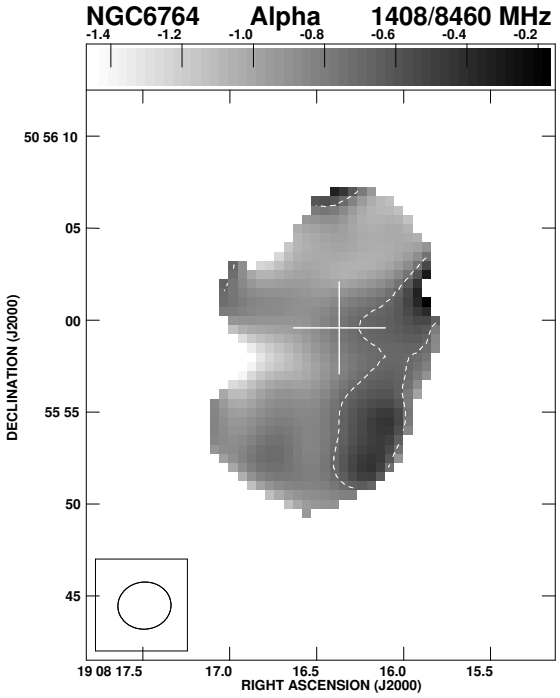

Figure 3.10: Spectral index map of the region generated from these two images. The contour level of -0.7 demarcates the regions of flatter and steeper spectral indices.

and equipartition magnetic field to be 6.5×10^{-12} erg cm^{-3} and 8.4 μG, respectively. The radiative lifetime of an electron radiating in this field at 1.4 GHz is $2.5{\times}10^7$ yr. These values are similar to estimates for nearby galaxies (e.g. Condon 1992). The proton-to-electron ratio is not well determined for external galaxies. For a value of 50 from studies of cosmic rays in our own Galaxy (e.g Webber 1991), the equipartition magnetic field would increase by a factor of 2.5.

(b) The circumnuclear region

The full-resolution VLA-A array images of the circumnuclear region, which is taken to be within $\sim$0.5 kpc from the radio nucleus, are presented in Fig.

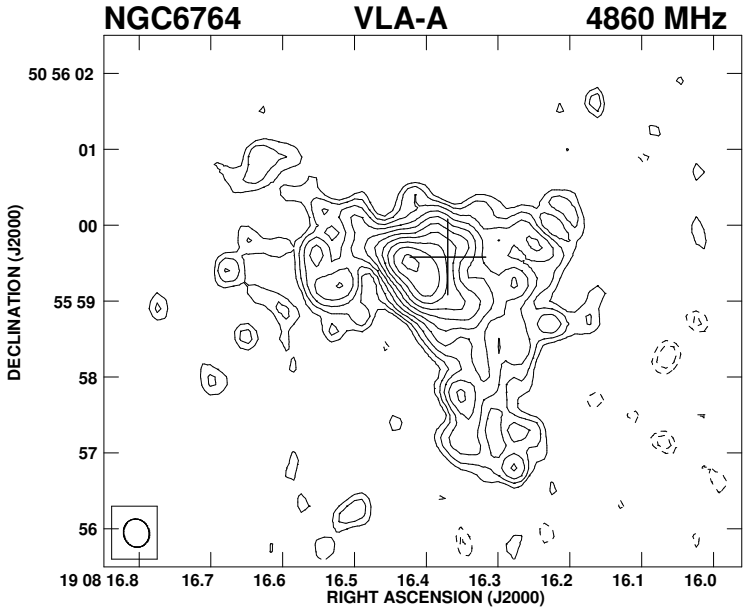

Figure 3.11: VLA A-array image of the circumnuclear region at 4860 MHz with an angular resolution of ∼0.35 arcsec. Contour levels are 0.023×(−4, −2.82, 2.82, 4, 5.65, 8 . . .) mJy/beam.

3.11, 3.12. These images at 4860 and 8460 MHz with angular resolutions of ∼0.35 and 0.19 arcsec respectively reveal the structure to be somewhat complex. In the lower-resolution 4860-MHz image, the emission on the western side of the peak is more prominent and is triangular shaped, extending for about 3 arcsec (∼ 0.5 kpc) towards the south and 2 arcsec (0.3 kpc) towards the west. The emission on the eastern side is more diffuse, faint and shorter in extent and contributes only 3.7 mJy of the total flux density of 17 mJy visible in the image.

The higher-resolution 8460-MHz image reveals two extensions from the radio peak, one along a PA of −90° and extending for ∼1 arcsec (0.16 kpc) and the other which is more prominent and slightly longer extending for ∼1.2 arcsec (0.2 kpc) along a PA of −135°. Given Bridle & Perley's (1984)

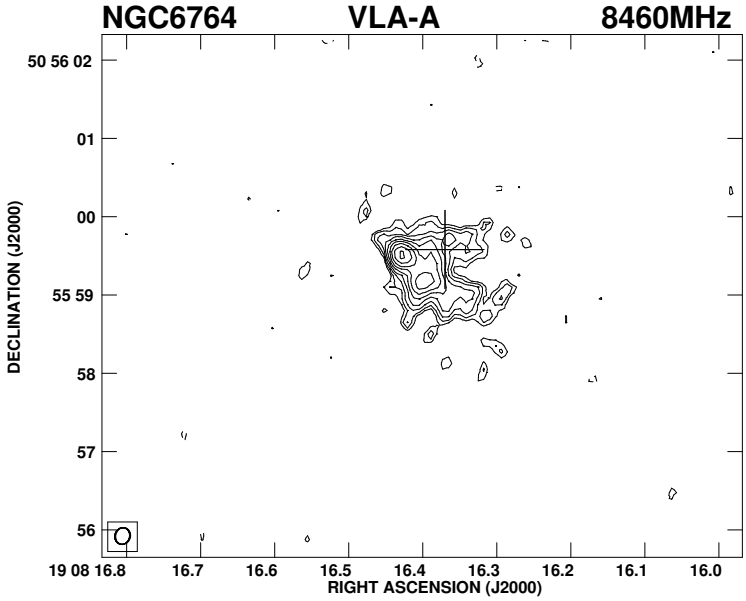

Figure 3.12: VLA A-array image of the circumnuclear region at 8460 MHz with an angular resolution of ∼0.19 arcsec. Contour levels are 0.016×(−4, −2.82, 2.82, 4, 5.65, 8 . . .) mJy/beam.

definition of a radio jet, the south-western feature could be classified as a possible jet which connects the radio nucleus with more diffuse emission which is oriented along a PA of ∼180° and smoothly joins on to the ridge of emission on the western side of the southern bubble (Figs. 3.11, 3.12). However, this feature could also be a resolved structure at the base of the bubble. The extensions to the east and west could also form the base of the bubbles seen in Fig. 3.5, 3.6.

The nuclear source

The position of the radio peak determined from the VLA-A array 8460-MHz image is RA: $19^h\ 08^m\ 16.^s428$, Dec 50° 55′ 59.″47 in J2000 co-ordinates (see

Table 3.3: Observed parameters of radio continuum images

Telescope	Freq.	Beam size			rms	S_{pk}	$S_{tot.}$
	MHz	maj.	min.	PA	mJy	mJy	mJy
		$''$	$''$	$^\circ$	/b	/b	
GMRT	598	12.4	9.4	33	0.39	136	183
NVSS	1400	45.0	45.0	0	0.50	102	113
VLA-A	1400	1.33	1.19	7	0.05	14	103
GMRT	1408	2.89	2.56	−85	0.14	33	109
VLA-A	4860	0.37	0.33	17	0.023	1.6	17
VLA-A	8460	0.21	0.18	−16	0.016	0.8	5.9
VLA-A	14965	0.13	0.11	43	0.221	<0.7	<0.7
VLA-B	4985	1.31	1.18	−28	0.054	7.1	43
VLA-C	8460	2.89	2.56	−85	0.039	8.7	25
VLA-B	8460	1.53	1.29	−68	0.069	5.2	20
VLA-C	14939	2.32	1.06	−82	0.166	4.1	14

Table 6.1). This is ∼0.04 arcsec from the peak in the VLA-A array 4860-MHz image (Fig. 3.11), but is ∼0.55 arcsec from the position of the optical nucleus (RA 19 08 16.370; Dec: +50 55 59.58 in J2000 co-ordinates with an uncertainty of 0.22 arcsec) determined by Clements (1981). This difference between the radio and optical peaks may be due to higher extinction close to the nucleus of this galaxy. Similar differences have been seen in other galaxies as well, such as in NGC1482 (Hota & Saikia 2005; Chapter 2). Although the radio peak is likely to be associated with the AGN, it is undetected in our VLA-A array 14940-MHz image, the 3σ upper limit being ∼0.7 mJy. This is only marginally lower than the flux density of 0.8 mJy/beam at 8460 MHz, suggesting that the spectrum could still be flat. A more sensitive VLA-A array 14940-MHz image is required to detect the possible nuclear source at higher frequencies and determine its spectrum.

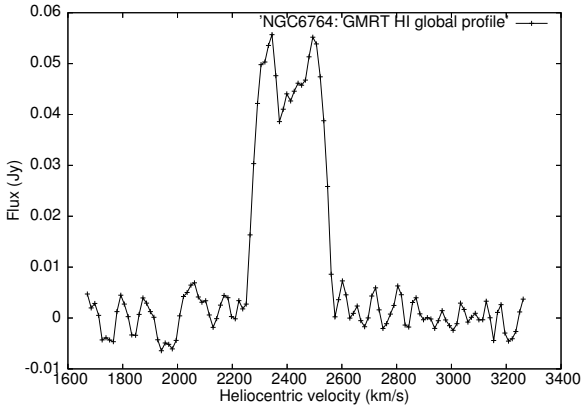

Figure 3.13: GMRT HI-emission global profile of NGC 6764 mapped with a resolution of 37″.76×33″.36 along PA ∼6° and smoothed to 27 km s^{-1}.

3.5 HI observations

HI observations of NGC6764 have been reported earlier with an angular resolution of ∼54 arcsec (8.8 kpc) using the VLA-D array (Wilcots, Turnbull & Brinks 2001). We observed this source with the GMRT with higher resolution to (i) identify any kinematic effects of the AGN and starburst activity on the circumnuclear HI gas via HI 21-cm absorption lines towards the central continuum source, (ii) study the distribution of HI gas relative to the HII regions, and (iii) further investigate the nature of the observed depression in HI column density towards the centre of the galaxy. Wilcots et al. noted this depression but with the relatively coarse resolution of their observations were unable to test the proposition that this might be due to absorption against the central continuum source. The results of our observations, which have an rms noise of 0.6 mJy beam^{-1} per channel in the full-resolution images, are described below.

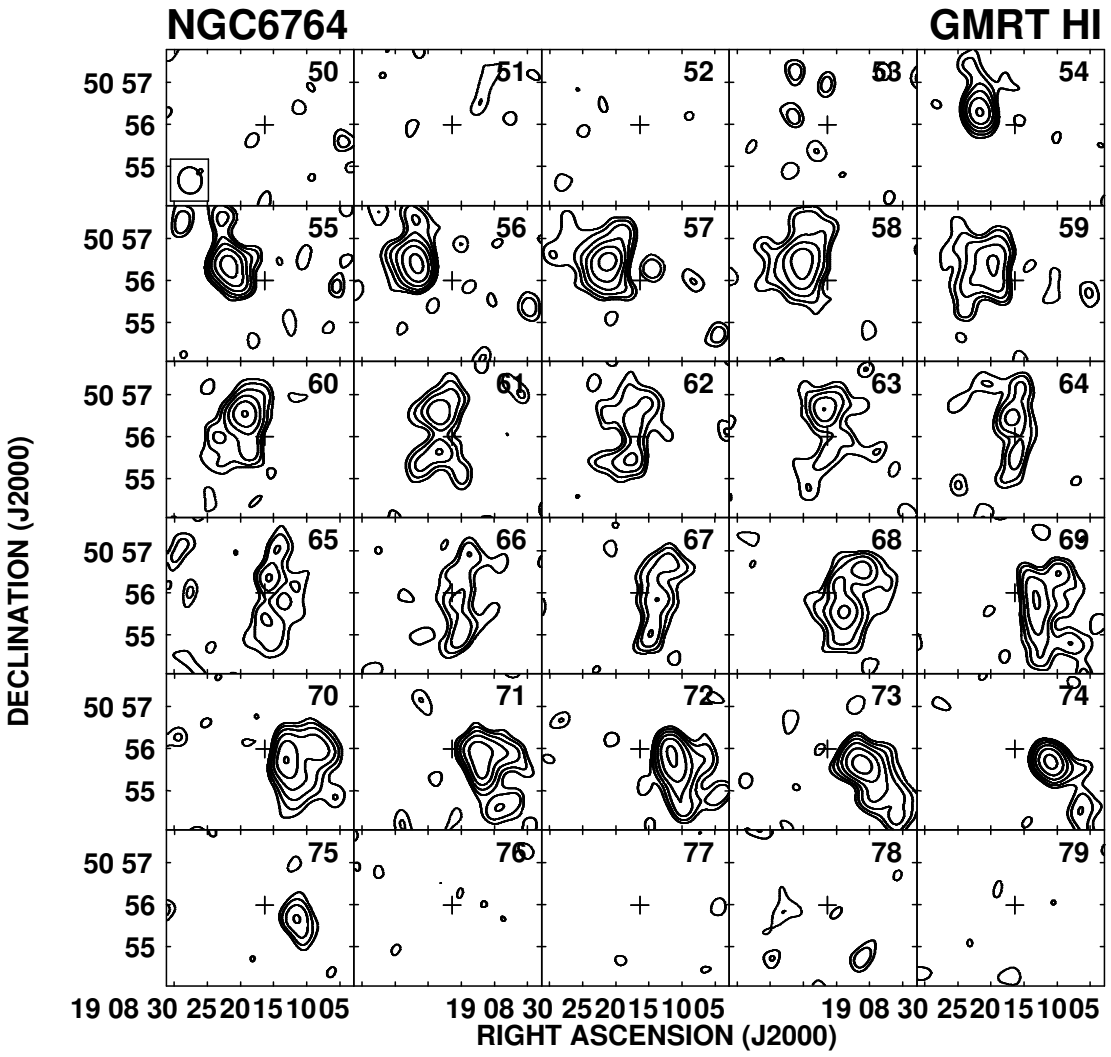

Figure 3.14: NGC 6764 HI-emission channel maps made with a resolution of $37''.76 \times 33''.36$ along PA $\sim 6^{\circ}$. Channel 50 corresponds to a heliocentric velocity of 2602 km s^{-1}, while channel 79 corresponds to a heliocentric velocity of 2211 km s^{-1}. The systemic velocity of 2416 km s^{-1} corresponds to channel 64. The velocity separation between adjacent channels is 13.48 km s^{-1}. The crosses in all the images denote the position of the optical nucleus. Peak flux: 19.8 mJy/beam. Contour levels are -4, -2.82, 2.82, 4, 5.65, 8 ... mJy/beam.

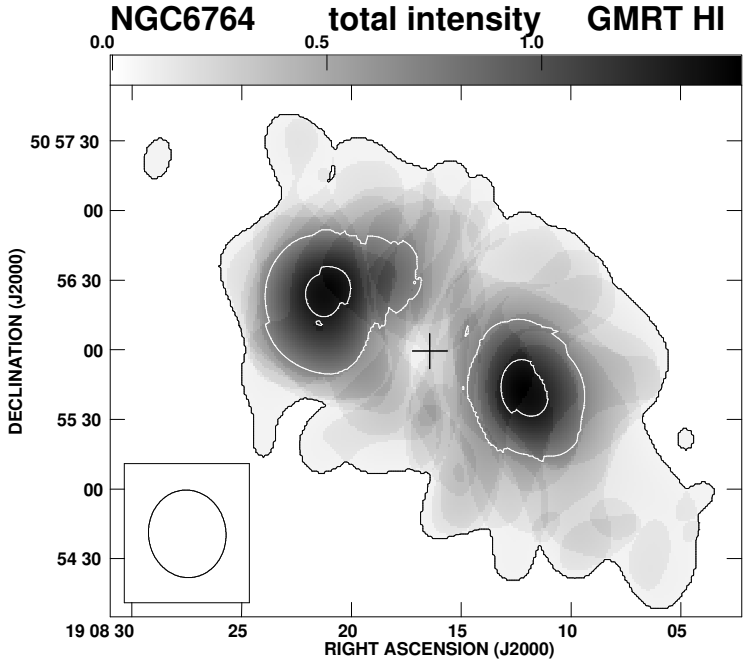

Figure 3.15: GMRT total intensity HI contour as well as gray scale map of NGC 6764 made with a resolution of $37''.76 \times 33''.36$ along PA$\sim 6^{\circ}$. The contour levels correspond to HI-column densities of 5, 71 and 132 $\times$ 10^{19} atoms cm^{-2}.

(a) HI emission

In Fig. 3.13, we show the global profile obtained by tapering the data to 4 kλ and making the channel maps which have an rms noise of $\sim$1 mJy/beam and an angular resolution of $\sim$35 arcsec (Fig. 3.14). In the channel maps, we confirm the extensions to the north (channel=55; 2515 km s^{-1}) and south (channel=74; 2258 km s^{-1}) noted by Wilcots et al., which is clearly seen in our data. The total HI mass calculated from the global profile over the velocity range 2225 to 2562 km s^{-1} is 3.6 $\times$ 10^9 M$_{\odot}$. The total HI mass detected by Wilcots et al. (2001) is (5.9$\pm$1)$\times 10^9$ M$_{\odot}$ (revised for a distance of 34 Mpc), which implies that in our higher-resolution images we have resolved out some of the diffuse extended HI-gas of the galaxy. Moment maps were generated

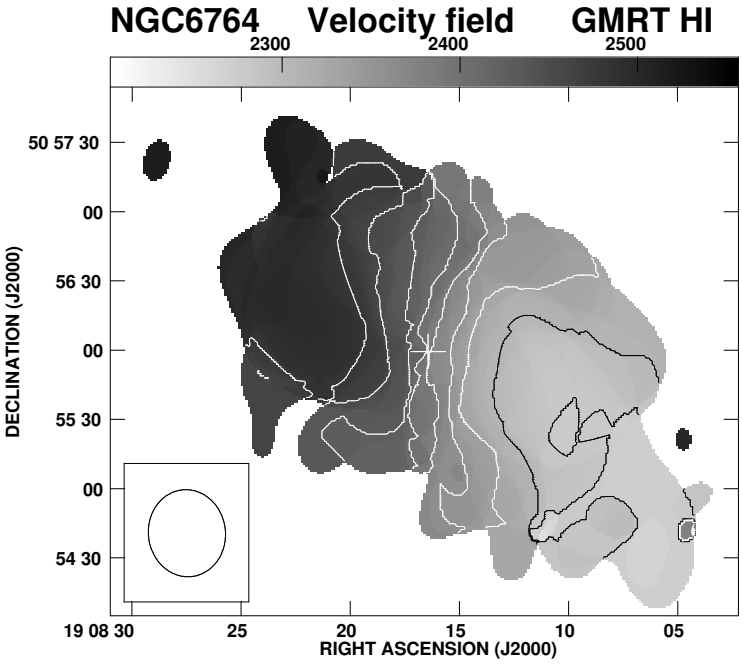

Figure 3.16: The HI-velocity field (Moment-1) generated from the same data set. The velocity contours from west to east are 2300, 2325, 2350, 2375, 2400, 2425, 2450, 2475 and 2500 km s^{-1}. The systemic velocity is 2416 km s^{-1}.

by blanking each channel of this data cube at the 5σ level. The HI column density image and the velocity field are shown in Fig. 3.15, 3.16. The velocity field is similar to that published by Wilcots et al. (2001). The iso-velocity contours show evidence of non-circular motions due to the existence of a bar in NGC6764. We also see the velocity field being slightly distorted on the north-eastern and the south-western edges of the disk, as seen by Wilcots et al. (2001). The Moment-2 map shows the velocity width of the gas being slightly higher in the inner region than that in the outer region (Fig. 3.17).

To study the HI properties with higher resolution, we generated moment maps by tapering the data to 10 kλ and blanking each channel of this data cube at the 5σ level. The total HI column density image with an angular

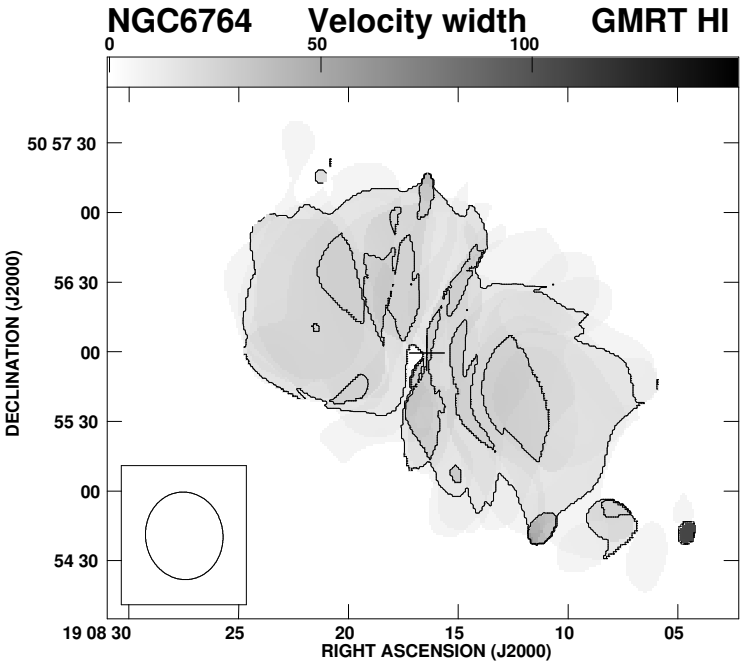

Figure 3.17: HI-velocity width map of NGC 6764 from the same data set. The contour levels are 13 and 26 km s^{-1}.

resolution of ∼15 arcsec shows the structure of the two well-resolved blobs of emission which are located on opposite sides of the circumnuclear region (Fig. 3.18). A superposition of the HI column density image on the DSS R-band image of the optical galaxy (Fig. 3.19) shows that the HI line-emitting gas is located in the outer regions of the galaxy, and there appears to be no significant HI emission towards the centre of the galaxy which harbours the young starburst and the AGN. This is unlikely to be due to absorption against the central continuum source, which extends for only ∼15 arcsec, similar to the resolution of these images, and contributes almost the entire continuum flux density seen in the NVSS image. The depression in the HI column density in the central region extends for $\gtrsim$50 arcsec.

A comparison of the HI column-density image with the Hα image of the

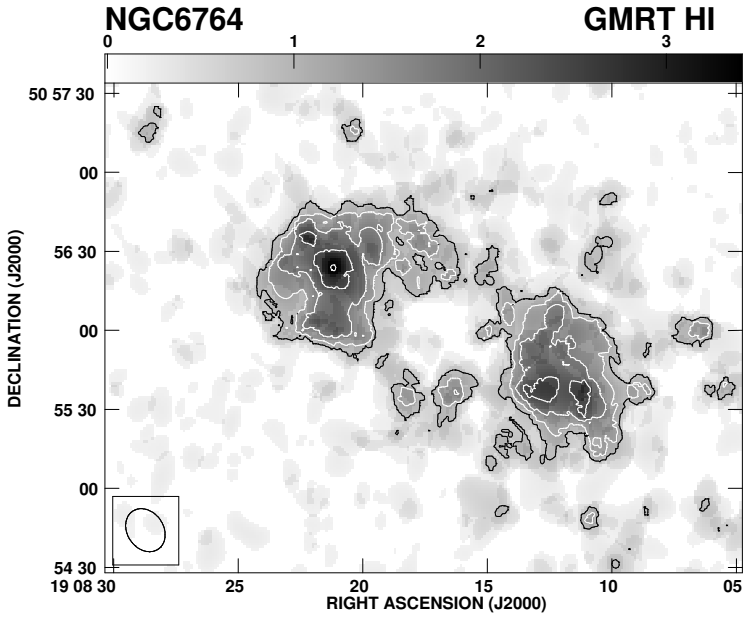

Figure 3.18: HI contour map and gray-scale image of NGC 6764 made with a resolution of $17''.37 \times 13''.77$ along PA $\sim 34°$. The contour levels correspond to $1.21 \times (8, 11.31, 16, 22.62, 32..)$ in units of 10^{20} atoms cm^{-2}.

galaxy (Zurita et al. 2000) shows that the most prominent region in Hα is the central starburst source which has no significant HI gas. Although close to the circumnuclear region this could be due to ionisation by the central starburst and AGN, the depletion of HI at larger distances could be due to an ISM phase transition from atomic to molecular hydrogen. As mentioned earlier, there is a concentration of molecular gas extending for $\sim$2.3 kpc along the bar of the galaxy (Eckart et al. 1991, 1996; Kohno et al. 2001; Leon et al. 2003).

The next most prominent regions of Hα emission are at the ends of the bar, with weaker emission along the bar and spiral arms. The peaks of HI emission in the south-western blob appear displaced from the Hα peaks while in the northern lobe they appear to be roughly coincident at this resolution

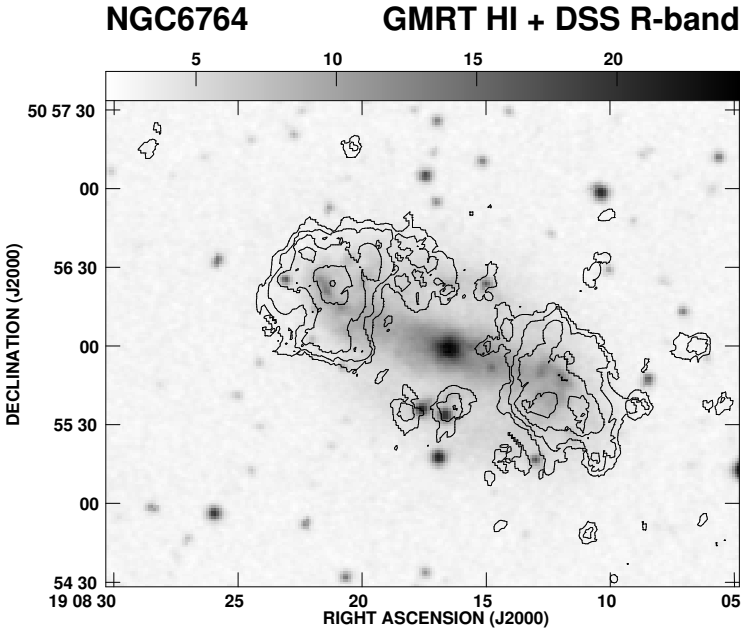

Figure 3.19: The HI contour map with the same resolution superimposed on the DSS Red-band image.

(Fig. 3.20).

(b) HI absorption

In Fig. 3.21, we present the HI absorption profile towards the peak of the central continuum source (Fig. 3.5) with an angular resolution of ∼2.7 arcsec and an rms noise of 0.6 mJy beam^{-1}. No absorption is observed towards any other part of the radio source. The peak absorption occurs at a heliocentric velocity of 2426 km s^{-1}, which is consistent with the heliocentric systemic velocity 2416 km s^{-1}. In addition there is a weak blue-shifted component at a heliocentric velocity of ∼2300 km s^{-1}, which corresponds to a blue shift of ∼120 km s^{-1} relative to the systemic velocity. Although this feature is very weak ($\sim 2\sigma$) and requires confirmation from more sensitive observations, it is

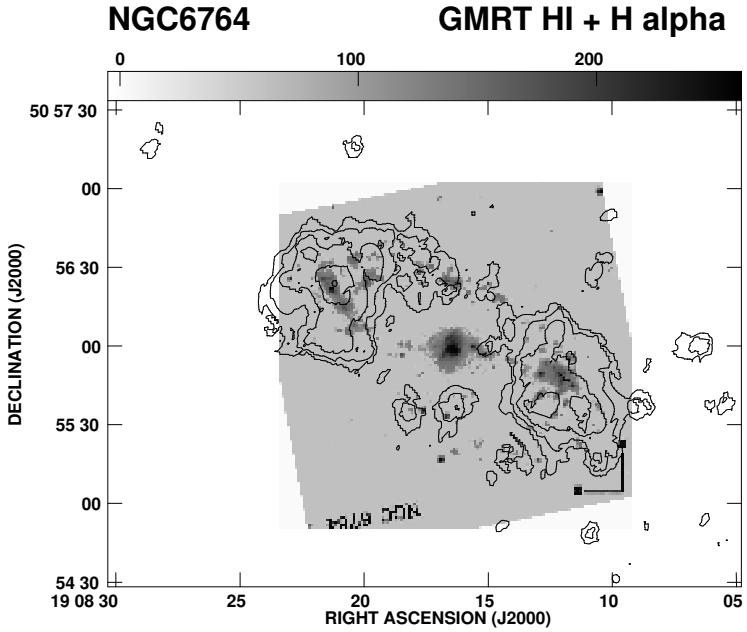

Figure 3.20: The HI contour map superimposed on the Hα image of Zurita et al. (2000).

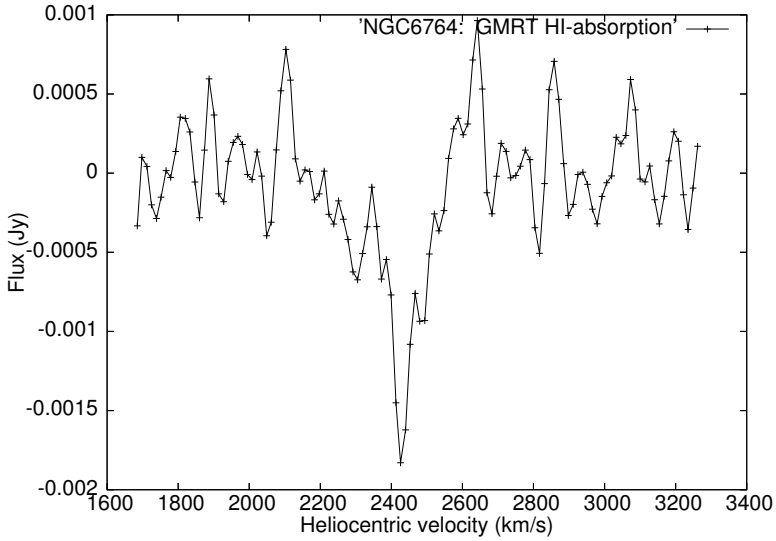

Figure 3.21: GMRT HI-absorption spectrum taken from a $3''\times3''$ region around the radio continuum peak of NGC 6764. The spatial resolution of the data cube is $2''.90\times2''.55$ along PA $\sim$-87°; the spectrum has been smoothed to 27 km s^{-1}.

likely to be real since it is seen in both the Stokes RR and LL data sets and it extends over a few channels. It is interesting to note that mm-wavelength observations of CO have shown molecular gas towards the circumnuclear region which is blue shifted by ∼140 km s^{-1} relative to the systemic velocity (Leon et al. 2003).

The peak optical depth, calculated using the background peak continuum flux density of 33 mJy from the area of 9 $arcsec^2$ against the peak is 0.06. The total optical depth, calculated with data points over the full width at zero intensity (2184−2548 km s^{-1}) is 0.5. Assuming a spin temperature of 100 K this corresponds to a total $N_{Hi} \sim 1.23 \times 10^{21}$ cm^{-2}. The total mass of the absorbing HI clouds is $2.35 \times 10^6 M_\odot$. The blue-shifted component spread over 2184−2346 km s^{-1} has an optical depth of 0.13 which corresponds to an $N_{Hi} \sim 3.1 \times 10^{20}$ cm^{-2}. Although the blue shift could be due to non-circular motions due to the barred potential, such shifts may also be caused by gas clouds driven outwards by the circumnuclear starburst or AGN. In the latter scenario, the outflowing (∼120 kms^{-1}) HI cloud, which has an estimated mass of $5.9 \times 10^5 M_\odot$, assuming the cloud to have an area of 9 $arcsec^2$, has a kinetic energy of 8.5×10^{52}ergs.

3.6 Discussion

(a) Radio bubbles

At radio continuum wavelengths, the most striking features are the bubbles of non-thermal plasma with a size of ∼1.1 and 1.5 kpc on the northern and southern sides respectively of the circumnuclear region, and oriented roughly orthogonal to the stellar bar and the major axis of the galaxy (Fig.3.22).

Table 3.4: Comparision with other radio-bubble galaxies

Table 1: Comparision with other radio-bubble galaxies

Galaxy name (1)	Morph. class (2)	AGN type (3)	Dist. Mpc (4)	Size $''$ (5)	Size kpc (6)	$S_{b+n}(1.4)$ mJy (7)	$L_{1.4}$ (10^{20}) W/Hz (8)	$\log(L_{FIR}/L_{\odot})$ (9)	Refs. (10)
NGC1068	SAb	Sy1,Sy2	16.0	14	1.0	4221	1296	10.98	1,2
NGC2782	SABa	Sy1,SB	36.0	14	2.4	107	166	10.44	3,4
NGC2992	SA,pec	Sy1,Sy2	32.5	8	1.2	168	213	10.26	5,6
NGC3079	SBc	Sy2,L	15.7	45	3.4	409	121	10.53	7,8
NGC3367	SBc	Sy,L	42.7	75	15.3	51	112	10.49	9,10
NGC4051	SABbc	Sy1.5	9.9	10	0.4	20	2.3	9.47	11,12
M51	SAbc,pec	HII,Sy2.5,L	8.4	15	0.6	45	3.8	10.38	13,14
NGC5548	SA0/a	Sy1.5	72.3	10	3.4	23	147	9.98	12,15
NGC6764	SBbc	Sy2,L	34.0	16	2.6	106	147	10.31	16,17
Circinus	SAb	Sy2	6.1	270	8.1	-	-	$\sim$10.45	18,19

1 Cecil, Bland & Tully 1990; 2 Pogge 1988; 3 Jogee, Kenney & Smith 1998; 4 Yoshida, Taniguchi & Murayama 1999; 5 Chapman et al. 2000; 6 Veilleux, Shopbell & Miller 2001; 7 Cecil et al. 2001; 8 Irwin & Saikia 2003; 9 García-Barreto, Franco & Rudnick 2002; 10 García-Barreto et al. 2005; 11 Christopoulou et al. 1997; 12 Baum et al. 1993; 13 Cecil 1988; 14 Ford et al. 1985; 15 Wilson et al. 1989; 16 This paper; 17 Zurita, Rozas & Beckman 2000; 18 Elmouttie et al. 1998a; 19 Elmouttie et al. 1998b.

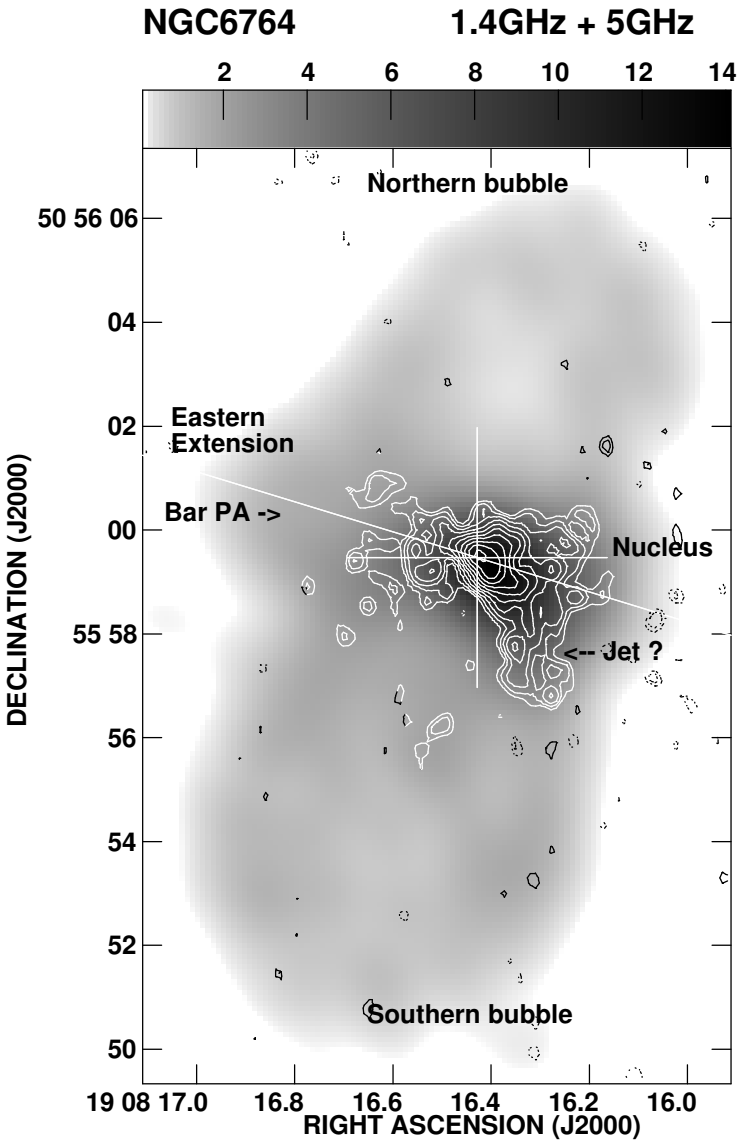

Figure 3.22: Contour map of the radio-continuum emission from the circumnuclear region of NGC6764 at 4860 MHz with the VLA A-array (Fig. 3.5) is superimposed on the gray scale image of the radio bubbles at 1400 MHz with the VLA A-array (Fig. 3.11). The bubbles, the eastern extension and a possible jet are labelled. The cross marks the position of the radio nucleus. The line at a PA of 73° shows the orientation of the stellar bar.

There also appears to be an extension on the eastern side extending beyond the base of the bubbles. In addition, smaller-scale structure with a size of $\sim$0.5 kpc but asymmetric in extent relative to the radio nucleus is seen oriented roughly along the stellar bar. There is also a jet-like structure starting from the nucleus along an initial PA of -135° which appears to connect the nucleus to more extended emission towards the south-west. These features are shown in Fig. 3.22 where the smaller-scale structure is shown superimposed on the larger-scale bubbles.

We first discuss the origin of these structures in this composite galaxy which harbours both a young starburst and an AGN. It is worth noting here that the activity in this galaxy does not appear to be triggered by interaction with any companion galaxy, since there is no evidence of any nearby galaxy within a distance of $\sim$160 kpc (Wilcots et al. 2001). However, the HI observations do show evidence of a weak perturbation but this is unlikely to significantly affect the starburst and AGN activity seen in this galaxy.

In order to understand the nature of these bubbles, we have compiled a representative sample of nearby galaxies with similar structures from the literature. A bubble is defined to be one whose width is larger than approximately half the size of its length. This working definition has been adopted to distinguish it from jets or jet-like features and normal lobes of radio emission formed by these jets whose axial ratios are usually more than $\sim$2 (e.g. Leahy, Muxlow & Stephens 1989). The sample of nearby galaxies with bubbles is listed in Table 3.4, along with some of their properties. The Table is arranged as follows. Column 1: name of the galaxy; column 2: galaxy classification from NED; column 3: classification of the AGN from NED where Sy denotes a Seyfert galaxy, L a LINER galaxy, SB a starburst and HII a galaxy with

prominent HII regions; column 4: distance to the galaxy in Mpc; columns 5 and 6: total extent of the bubbles in arcsec and kpc respectively. Columns 7 and 8: flux density and radio luminosity at 1.4 GHz of the bubbles and any core or jet emission. These have been estimated from the FIRST images, except for NGC2992 for which we have used the NED image (Ulvestad & Wilson 1989) and NGC6764 for which we have used the results presented in this chapter. The flux density of the bubbles and any core or jet emission has been estimated by specifying a polygon around this region. The flux density value for the bubbles in Circinus is not available. Column 9: The FIR luminosity of the galaxies. Except for Circinus, for which we have estimated the value from Elmouttie et al. (1998b), these have been taken from Condon et al. (1990, 1998) and scaled to the distances listed in column 4. Column 10: References for the radio, X-ray and/or Hα images.

It can be seen that the total extents of the bubbles range from $\sim$0.4 to 15 kpc, with a median value of $\sim$2.5 kpc, similar to that of NGC6764. While some bubbles lie within the scale-height of the interstellar medium (ISM) of the parent galaxy, others extend beyond it. In these radio bubbles, the ionised gas seen in optical emission lines such as Hα or [OII] tend to be spatially related to the radio emission. The radio luminosity of the bubbles and any core or jet emission ranges from $\sim 2.3\times10^{20}$ to $\sim 1.3\times10^{23}$ W Hz^{-1} with a median value of $\sim 1.4\times10^{22}$ W Hz^{-1}, while the infrared luminosity of the galaxies ranges from 9.47 to 10.98 in units of $\log(L_{FIR}/L_{\odot})$ with a median value of $\sim$ 10.3. Although the galaxies are luminous at infrared wavelengths, their luminosity is well below the threshold for defining these as ultra-luminous infrared galaxies.

In Table 3.4, it is striking that all the sources with non-thermal bubbles of radio emission have an AGN associated with it. It is worth comparing

this with archetypal starburst galaxies such as M82 and NGC253, whose infrared luminosities of 10.38 and 10.26 in units of $\log(L_{FIR}/L_{\odot})$ respectively, are comparable with the sources in the sample of galaxies with bubbles. These two galaxies are dominated by the circumnuclear starburst with no clear evidence of an AGN, although there have been attempts to identify one (Wills et al. 1999; Mohan et al. 2002). High-resolution radio images of the nuclear regions of these two galaxies reveal a large number of compact radio components (Muxlow et al. 1994; McDonald et al. 2002 and references therein; Collison et al. 1994; Ulvestad & Antonucci 1997 and references therein) which are a mixture of HII regions and supernova remnants, while lower-resolution observations reveal a more extended halo of emission (Seaquist & Odegard 1991; Reuter et al. 1992; Carilli et al. 1992). Although outflows along the minor axes are visible in both these two galaxies in X-rays and Hα (Strickland et al. 2004), there are no bubbles of non-thermal plasma similar to those seen in our sample of galaxies. The archetypal starburst galaxy in the southern hemisphere, NGC1808, which is also dominated by a starburst with no unambiguous identification of an AGN (Forbes et al. 1992; Jiménez-Bailón et al. 2005), has extended non-thermal emission with no clear bubbles of radio emission (e.g. Dahlem et al. 1990). The small-scale radio structure is dominated by a number of compact components (Saikia et al. 1990; Collison et al. 1994). Also, in a recent study of the superwind galaxy NGC1482, which has a remarkable hourglass-shaped optical emission-line outflow as well as bipolar soft X-ray bubbles of emission (Veilleux & Rupke 2002; Strickland et al. 2004), there is no non-thermal radio emission or bubbles associated with the superwind although radio emission is seen associated with the disk of the galaxy (Hota & Saikia 2005; Chapter 2). Its infrared luminosity of log L_{FIR}=10.66 is similar to the sources with bubbles listed in

Table 3.4. Although the high-resolution radio observations of the nuclear region of NGC1482 show a peak of emission with a steep radio spectrum, and more diffuse emission with secondary peaks, it is not clear if this feature could be associated with an AGN (Hota & Saikia 2005; Chapter 2). It is relevant to note here that, from optical spectroscopic observations, Kewley et al. (2000) have classified it to be a starburst galaxy without an AGN. Considering these aspects, it is tempting to speculate that the formation of bubbles is closely linked to the existence of an AGN. It is interesting to note that Colbert et al. (1996) have highlighted similar differences in the radio structures between Seyfert and starburst galaxies.

Thus although the AGN possibly gives rise to the bubbles of non-thermal radio emission, these would interact with the external environment in the host galaxy. A galactic wind generated by a starburst (cf. Veilleux et al. 2005) along with effects of buoyancy (Gull & Northover 1973; Stone, Wilson & Ward 1988) could lead to the bubbles of plasma being oriented along the minor axis of the galaxy. In this case, the radio jet close to the nucleus could be misaligned with the minor axis, as seen in NGC6764 as well as in the well-studied galaxy NGC3079 (cf. Irwin & Seaquist 1988; Kondratko et al. 2005). Using the formalism of Stone et al. (1988), we estimate the time scale for the bubbles to reach the observed distances due to buoyancy to be $\sim$35 Myr. This is likely to be an upper limit because of the presence of an AGN as well as galactic wind. The extended X-ray emission from a region similar to that of the radio bubbles (Schinnerer et al. 2000) and the velocity structure in the Hα gas (Rubin et al. 1975) suggests the presence of a galactic wind in this starburst galaxy. Estimating an outflow velocity of $\sim$80 km s^{-1} for the ionised gas observed by Rubin et al., the dynamical time scale for the Hα gas to reach distances of $\sim$1.5 kpc is $\sim$20 Myr. For

comparison, the circumnuclear star formation history suggests two starbursts with ages of 3−5 Myr and between 15 and less than 50 Myr (Schinnerer et al. 2000), suggesting that both episodes of star formation could have affected the detailed structure of the bubbles.

(b) Kinematic effects on the ISM

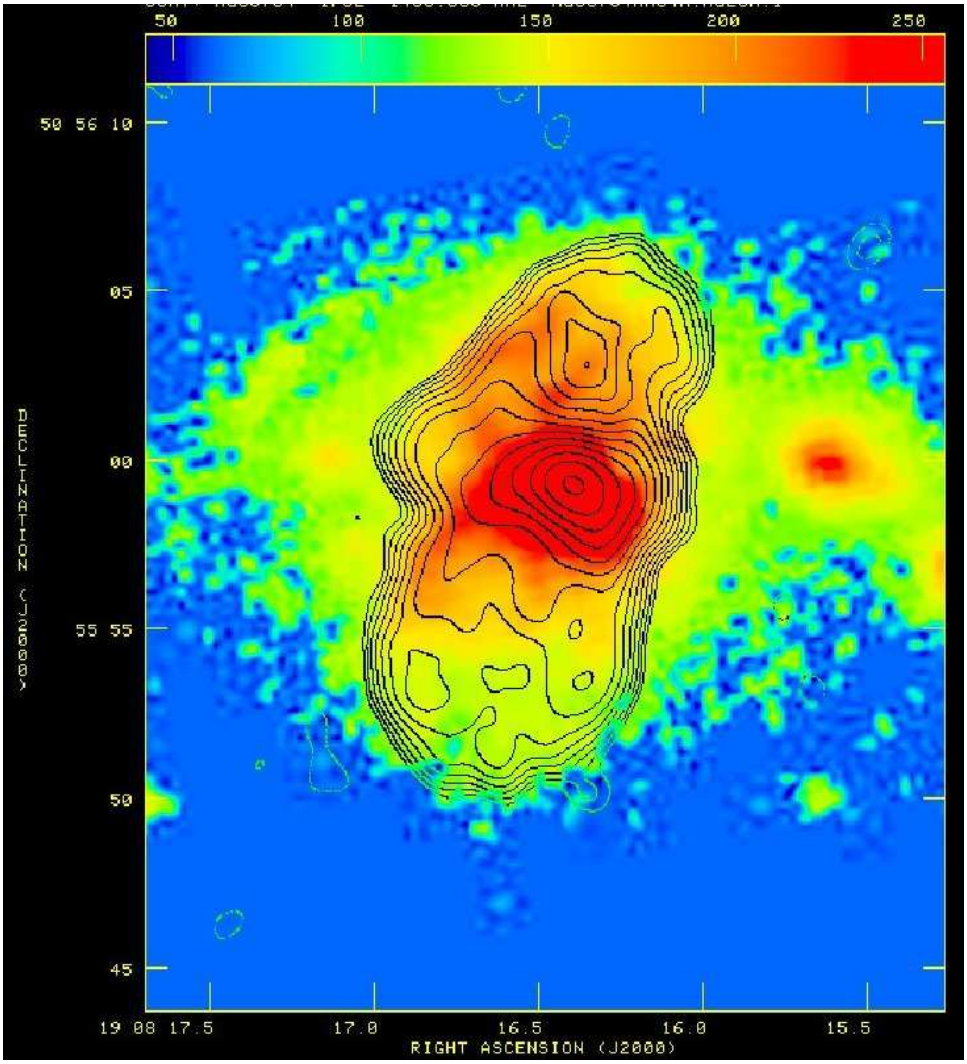

Figure 3.23: Contour map of the radio bubble at 1400 MHz with the VLA A-array (Fig. 3.5) is superimposed on the same Hα image in colour showing (in red) the Hα-filaments. The Hα image is taken from Zurita et al. (2000).

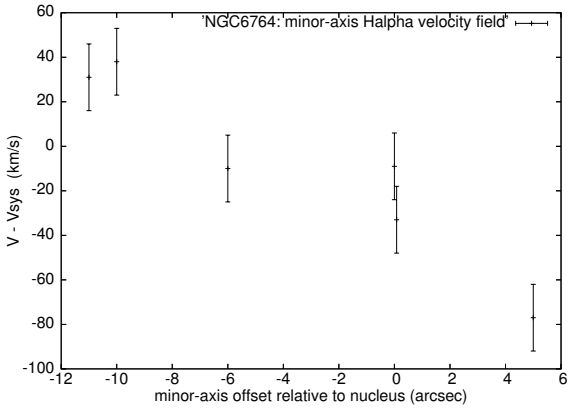

Figure 3.24: The Hα and [NII] velocity field measured along the minor-axis of the bubbles. Data plotted from the measurements of Rubin et al. (1975).

Interaction of radio jets and bubbles, as well as the galactic wind with the ambient medium could affect the kinematic properties of the ISM. However, in the case of NGC6764 the radio features are likely to play a relatively smaller role. The total minimum energy in the radio features is only $\sim 4.8\times10^{54}$ ergs, which corresponds to a pressure of 2.2×10^{-12} dynes cm^{-2}, similar to values for the ISM in the Milky Way. The total energy in the radio features of NGC6764 are significantly smaller than typical values for the total energy in the outflows. Although the total energy in the various components in the outflow in NGC6764 is not known, the kinetic energy in the outflow of only the warm ionised and the neutral gas components in typical galaxies with galactic winds are $\sim 10^{53}$ to 10^{56} and $\sim 10^{56}$ to 10^{60} ergs respectively (Veilleux et al. 2005).

A continuum-subtracted Hα image of the central region of the galaxy (Zurita et al. 2000) shows a number of filamentary structures, reminescent of those seen in galaxies with galactic winds. We have determined the positional information of this Hα image by comparing the pixel positions of three stars which are visible in the Hα image with their positions determined from the

DSS image. A superposition of the radio continuum image at 1400 MHz with an angular resolution of 1.2 arcsec (0.2 kpc) on the Hα image (Fig. 3.23) shows some correlation of the radio emission with the Hα features, which are possibly driven outwards by a galactic wind.

Spectroscopic observations of NGC6764 by Rubin, Thonnard & Ford (1975) showed that along the axis of the bubbles, the ionised gas appears red-shifted on the northern side and blue-shifted on the southern side by up to $\sim$80 km s^{-1} relative to the systemic velocity of the galaxy (Fig. 3.24). These motions are likely to be caused by a bi-polar outflow due to the circumnuclear starburst.

In addition to the ionised gas component, the outflow due to the circumnuclear starburst could also affect the molecular and atomic gas components in the galaxy. For example, interaction of the bubbles with the molecular gas can give rise to CO gas compression and also affect their kinematic properties. Such effects have been seen in detailed studies of individual starburst galaxies. For example, in the starburst galaxy NGC253, Sakamoto et al. (2006) find that the circumnuclear molecular disk harbouring the starburst is highly disturbed on small scales by individual young clusters and supernovae and globally by the well-known superwind. In the map of NGC6764 published by Eckart et al. (1991), the line ratio CO(2-1)/CO(1-0) shows higher values of $\sim$0.9 along the orientation of the bubbles but smaller values of $\sim$0.5 near the arms. Such higher values of the line ratio are expected when CO gas is compressed. Leon et al. (2003) find evidence of CO gas which is blue shifted by $\sim$140 km s^{-1} and have a very high line ratio of $\sim$2 for CO(2-1)/CO(1-0). As discussed earlier (Section 4.2) our HI absorption spectrum shows a possible feature at a blue-shifted velocity of $\sim$120 km s^{-1}, which is similar to that of the molecular gas observed in CO. A similar blue-shifted feature was also

noted in the superwind galaxy NGC1482 by Hota & Saikia (2005; Chapter 2), which was also interpreted to be due to the circumnuclear starburst.

Hydrodynamical simulations of starburst-driven winds show that the cool gas could expand laterally in the disc of the galaxy, be carried vertically outwards by the tenuous superwind or be entrained in the interface between the hot, superwind fluid and the cool, dense ISM (e.g. Heckman et al. 1990; Heckman et al. 2000). The kinematic and physical properties of the different components discussed above are broadly consistent with the results of these simulations of winds.

3.7 Summary and concluding remarks

We have presented radio continuum and HI observations of NGC6764, which has a young starburst as well as a Seyfert nucleus. The results are briefly summarised here.

1. The low-resolution GMRT image at 598 MHz with an angular resolution of ∼11 arcsec (1.8 kpc) shows that almost all the radio emission from the galaxy comes from the central region of the source, with very little emission from the disk of the galaxy. The VLA A-array image at 1400 MHz with an angular resolution of ∼1.3 arcsec accounts for more than 90 per cent of the flux density visible in the NVSS image. This central source has a non-thermal spectrum with a spectral index of -0.74 ± 0.02 between ∼600 MHz and 8 GHz.

2. With an intermediate resolution of 1.3 arcsec (0.2 kpc), the central source is resolved into two bubbles of non-thermal radio emission which are shell-like with a depression in the centre. The ridges of emission

appear to overlap with Hα filaments seen in a continuum-subtracted optical image of the galaxy. The bubbles are oriented along the minor axis of the galaxy with a total extent of $\sim$2.6 kpc. The western edge of the bubbles tend to have a flatter spectral index than the rest of the bubbles.

3. The images at 4860 MHz with resolutions of 0.35 arcsec (0.05 kpc) show emission along the major axis of the galaxy as well as extensions which appear to connect to the ridges of emission in the bubbles.

4. Our highest-resolution images (0.19 arcsec; 0.03 kpc) reveal a compact source, which is possibly associated with the nucleus of the galaxy, and is slightly offset ($\sim$0.55 arcsec) from the position of the optical nucleus determined by Clements (1981). In addition there is a possible radio jet along a PA of -135° which appears to connect to more extended emission towards the south.

5. A compilation of a representative sample of ten galaxies with non-thermal bubbles, shows that these are all associated with an AGN. However, the detailed radio and optical structures, as well as the distribution of atomic and molecular gas, could be affected by a galactic wind due to a starburst in addition to any AGN activity. Prominent starburst galaxies such as M82, NGC253, NGC1482 and NGC1808 have similar infrared luminosity, but do not exhibit such bubbles of radio emission, suggesting that these are not usually caused by the circum-nuclear starburst.

6. The H I observations, which are of higher resolution than those reported earlier by Wilcots et al. (2001), show that the two main peaks of

emission are roughly coincident with the ends of the bar. There is a depletion of HI towards the central region. Although this is likely to be due to the circumnuclear starburst and AGN close to the nucleus, at larger distances it could be due to phase transition in the ISM from atomic to molecular hydrogen.

7. The peak absorption feature in the HI-absorption profile has an optical depth of $\sim$0.06 and a heliocentric velocity of 2426 km s^{-1}, consistent with the systemic velocity of the galaxy. The H I mass estimated from the absorption profile is $\sim 2.4\times10^6$ M$_\odot$. There is a suggestion of a weak absorption feature at a blue-shifted velocity of 120 km s^{-1}, which requires confirmation from more sensitive observations. A feature with a similar blue-shifted velocity has also been reported from CO observations, suggesting that the circumnuclear activity may have affected the kinematics of the atomic and molecular gas components of the ISM in the host galaxy, in addition to the ionised gas seen in Hα and [NII].

References

Armus L., Heckman T.M., Miley G.K., 1988, ApJ, 326L, 45

Baars J.W.M., Genzel R., Pauliny-Toth I.I.K, Witzel A., 1977, A&A, 61, 99

Baum S.A., O'Dea C.P., Dallacassa D., de Bruyn A.G., Pedlar A., 1993. ApJ, 419, 553

Bridle A. H., Perley R. A., 1984, ARA&A, 22, 319

Carilli C.L., Holdaway M.A., Ho P.T.P., de Pree C.G., 1992, ApJ, 399L, 59

Cecil G., 1988, ApJ, 329, 38

Cecil G., Bland J., Tully R.B., 1990, ApJ, 355, 70

Cecil G., Bland-Hawthorn J., Veilleux S., Filippenko A.V., 2001, ApJ, 555,

338

Chapman S.C., Morris S. L., Alonso-Herrero A., Falcke H., 2000, MNRAS, 314, 263

Christopoulou P. E., Holloway A. J., Steffen W., Mundell C. G., Thean A. H. C., Goudis C. D.,

Meaburn J., Pedlar A., 1997, MNRAS, 284, 385

Cid Fernandes R., Heckman T., Schmitt H., Delgado R. M. G., Storchi-Bergmann T., 2001, ApJ, 558, 81

Clements E.D., 1981, MNRAS, 197, 829

Colbert E.J.M., Baum, S.A., Gallimore J.F., O'Dea C.P., Christensen J.A., 1996, ApJ, 467, 551

Collison P.M., Saikia D.J., Pedlar A., Axon D.J., Unger S.W., 1994, MNRAS, 268, 203

Condon J.J., 1992, ARA&A, 30, 575

Condon J.J., Condon M. A., Gisler G., Puschell J. J., 1982, ApJ, 252, 102

Condon J.J., Helou G., Sanders D.B., Soifer B.T., 1990, ApJS, 73, 359

Condon J.J., Helou G., Sanders D. B., Soifer B. T., 1996, ApJS, 103, 81

Condon J.J., Yin Q.F., Thuan T.X., Boller Th., 1998, AJ, 116, 2682

Conti P.S., 1991, ApJ, 377, 115

Dahlem M., Aalto S., Klein U., Booth R., Mebold U., Wielebinski R., Lesch H., 1990, A&A, 240, 237

Eckart A., Cameron M., Jackson J. M., Genzel R., Harris A. I., Wild W., Zinnecker H., 1991, ApJ, 372, 67

Eckart A., Cameron M., Boller Th., Krabbe A., Blietz M., Nakai N., Wagner S. J., Sternberg A., 1996, ApJ, 472, 588

Elmouttie M., Koribalski B., Gordon S., Taylor K., Houghton S., Lavezzi T., Haynes R., Jones K., 1998a, MNRAS, 297, 49

Elmouttie M., Haynes R. F., Jones K. L., Sadler E. M., Ehle M., 1998b, MNRAS, 297, 1202

Forbes D.A., Boisson C., Ward M.J., 1992, MNRAS, 259, 293

Ford H. C., Crane P. C., Jacoby G. H., Lawrie D. G., van der Hulst J. M., 1985, ApJ, 293, 132

Gallimore J.F., Axon D.J., O'Dea C.P., Baum S.A., Pedlar A., 2006, AJ, in press (astro-ph/0604219)

Garc´ia-Barreto J.A., Franco J., Rudnick L., 2002, AJ, 123, 1913

Garc´ia-Barreto J. A., Scoville N. Z., Koda J., Sheth K., 2005, AJ, 129, 125

Gull S.F., Northover K.J.E., 1973, Nature, 244, 80

Heckman T.M., Armus L., Miley G.K., 1990, ApJS, 74, 833

Heckman T.M., Lehnert M.D., Strickland D.K., Armus L., 2000, ApJS, 129, 493

Hota A., Saikia D.J., 2005, MNRAS, 356, 998 (Chapter 2)

Irwin J.A., Saikia D.J., 2003, MNRAS, 346, 977

Irwin J.A., Seaquist E.R., 1988, ApJ, 335, 658

Jiménez-Bailón E., Santos-Lleó M., Dahlem M., Ehle M., Mas-Hesse J.M., Guainazzi M.,

Heckman T.M., Weaver K.A., 2005, A&A, 442, 861

Jogee S., Kenney J. D. P., Smith B.J., 1998, ApJ, 494, L185

Kewley L.J., Heisler C.A., Dopita M.A., Sutherland R., Norris R.P., Reynolds J.,

Lumsden S., 2000, ApJ, 530, 704

Kinney A. L., Schmitt H. R., Clarke C. J., Pringle J. E., Ulvestad J. S., Antonucci R. R. J., 2000, ApJ, 537, 152

Kohno K., Matsushita S., Vila-Vilaró B., Okumura S. K., Shibatsuka T., Okiura M.,

Ishizuki S., Kawabe R., 2001, in The Central Kiloparsec of Starbursts and AGN: The La Palma Connection, eds Knapen J.H., Beckman J.E., Shlosman I., Mahoney T.J., ASP Conf. Proc., 249, 672

Kondratko P.T., Greenhill L.J., Moran J.M., 2005, ApJ, 618, 618

Leahy J.P., Muxlow T.W.B., Stephens P.W., 1989, MNRAS, 239, 401

Leon S., Eckart A., Laine S., Schinnerer E., 2003, in Active Galactic Nuclei: from Central Engine to Host Galaxy, eds S. Collin, F. Combes and I. Shlosman., ASP Conf. Proc., 290, 395

McDonald A.R., Muxlow T.W.B., Wills K.A., Pedlar A., Beswick R.J., 2002, MNRAS, 334, 912

Mohan N.R., Anantharamaiah K.R., Goss W.M., 2002, ApJ, 574, 701

Muxlow T.W.B., Pedlar A., Wilkinson P.N., Axon D.J., Sanders E.M., de Bruyn A.G., 1994, MNRAS, 266, 455

Osterbrock D. E., Cohen R. D., 1982, ApJ, 261, 64

Pogge R.W., 1988, ApJ, 328, 519

Reuter H.-P., Klein U., Lesch H., Wielebinski R., Kronberg P.P., 1992, A&A, 256, 10

Rubin V. C., Thonnard N., Ford W. K., Jr., 1975, ApJ, 199, 31

Saikia D.J., Unger S.W., Pedlar A., Yates G.J., Axon D.J., Wolstencroft R.D., Taylor K.,

Gyldenkerne K., 1990, MNRAS, 245, 397

Sakamoto K., et al., 2006, ApJ, 636, 685

Schinnerer E., Eckart A., Boller Th., 2000, ApJ, 545, 205

Seaquist E. R., Odegard N., 1991, ApJ, 369, 320

Spergel D.N. et al., 2003, ApJS, 148, 175

Stone J.L. Jr., Wilson A.S., Ward M.J., 1988, ApJ, 330, 105

Strickland D.K., Heckman T.M., Colbert E.J.M., Hoopes C.G., Weaver K.A.,

2004, ApJS, 151, 193

Ulvestad J.S., Antonucci R.R.J., 1997, ApJ, 488, 621

Ulvestad J.S., Wilson A.S., 1989, ApJ, 343, 659

Ulvestad J.S., Wilson A.S., 1984, ApJ, 285, 439

Ulvestad J.S., Wilson A.S., Sramek R.A., 1981, ApJ, 247, 419

Veilleux S., 2001, in Starburst Galaxies: Near and Far, eds Tacconi L., Lutz D., Springer-Verlag, Heidelberg, p. 88

Veilleux S., Rupke D.S., 2002, ApJ, 565, L63

Veilleux S., Shopbell P. L., Miller S. T., 2001, AJ, 121, 198

Veilleux S., Cecil G., Bland-Hawthorn J., 2005, ARA&A, 43, 769

Webber W.R., 1991, in The interpretation of modern synthesis observations of spiral galaxies, eds Duric N., Crane P.C., ASP Conf. Series, 18, 37

Wilcots E.M., Turnbull M.C., Brinks E., 2001, ApJ, 560, 110

Wills K.A., Pedlar A., Muxlow T.W.B., Stevens I.R., 1999, MNRAS, 305, 680

Wilson A.S., Willis A. G, 1980, ApJ, 240, 429

Wilson A.S., Wu Xuening, Heckman T. M., Baldwin J. A., Balick B., 1989, ApJ, 339, 729

Yoshida M. Taniguchi Y., Murayama T., 1999, AJ, 117, 1158

Zurita A., Rozas M., Beckman J. E., 2000, A&A, 363, 9

CHAPTER 4

NGC 4438 and its environment at radio wavelengths.

4.1 Abstract

We present multi-frequency radio continuum and HI observations of NGC4438, the highly-disturbed, active galaxy in the Virgo cluster, with the Very Large Array (VLA) and the Giant Metrewave Radio Telescope (GMRT). High-resolution observations of the central 1 kpc with the VLA at 4860 and 8460 MHz show the presence of an inverted-spectrum radio nucleus located between the highly asymmetric lobes of radio emission. This demonstrates that these lobes which are seen in radio continuum, Hα and X-ray wavelengths and are located at $\sim$230 and 730 pc from the nucleus arise due to an active galactic nucleus (AGN) rather than a compact nuclear starburst. The low-frequency radio continuum observations made with the GMRT detect the diffuse extended emission on the western side of the galaxy whose spectral index is flatter at higher frequencies and suggests that it is a mixture of thermal and non-thermal emission.

The HI observations made with the GMRT show an elongated structure which is displaced by $\sim$4.1kpc on the western side of NGC4438 and exhibits systematic rotation, consistent with earlier observations. The VLA D-array

full-resolution HI observations show that the elongated structure extends further to the south and has a size of ∼9.8 kpc and a mass of $1.8\times10^8 M_\odot$. These observations also show HI emission from the disk of the galaxy with a mass of $1.2\times10^8 M_\odot$. A tapered, lower-resolution D-array image reveals more gas located primarily on the western side of the galaxy and rotating about a velocity of ∼110 km s^{-1}. This is significantly higher than the systemic velocity of 71 km s^{-1} for the galaxy. The iso-velocity contours appear to curve outwards close to the disk, while at larger distances from the disk the contours curve inwards, as seen in the ram-pressure stripped galaxy in the Virgo cluster NGC4522. We detect a faint HI-tail towards the north of NGC4438 close to a stellar tail seen earlier in deep optical observations. This HI-tail has a total extent of ∼50 kpc and a mass of 1.4×10^8 $M_\odot$ assuming it to be at a distance similar to that of NGC4438. The velocity of the HI tail is ∼−10 km s^{-1} similar to that of HI emission from IC3355. There appears to be two velocity systems towards IC3355, namely ∼−10 and 162 km s^{-1}, the former being similar to HI emission from IC3355 and the HI tail. We discuss the different structures in the light of different models which have been suggested for this disturbed galaxy, namely ram pressure stripping, tidal and ISM-ISM interactions.

4.2 Introduction

The galaxy, NGC4438 (VV188, Arp 120), which is located only about 1° (∼350 kpc) from the centre of the Virgo cluster, is highly inclined (80°) and has a very disturbed disk with various components of the interstellar medium (ISM) being visible on the western side of the disk. High-resolution X-ray observations with the Chandra telescope show emission from a ∼700

Table 4.1: Basic data on NGC 4438.[a]

RA[b] (h m s)	Dec[b] (° ′ ″)	Type[c]	a × b[d] (′ × ′)	PA[e] °	i[f] °	V_{sys}[g] (km s^{-1})	D[h] (Mpc)	H I[i] def.
12 27 45.67	+13 00 31.5	SA(s)0/a pec	8.5 × 3.2	29	80	71±3	17	>1.0

a Taken from the NASA Extragalactic Database (NED) unless stated otherwise.
b The position of radio nucleus from our high-resolution, VLA A-array image at 8460 MHz in J2000.
c Morphological type.
d Optical major and minor axes.
e Kenney et al. (1995)
f Inclination angle from Kenney et al. (1995)
g Heliocentric systemic velocity.
h Vollmer et al. (2005). For this distance 1″=82 pc.
i Cayatte et al. (1994)

pc nuclear region, a ∼2.3 kpc spherical bulge and a network of filaments extending 4−10 kpc to the west and south-west of the galaxy (Machacek, Jones & Forman 2004). These regions are well correlated with similar features seen in Hα (Kenney & Yale 2002; Chemin et al. 2005). Diffuse extended radio emission at 1.4 GHz has been seen extending up to ∼10 kpc on the western side of the galaxy. Some have suggested that these features on the western side might be due to interactions with the intracluster medium (ICM) of the Virgo cluster since the relative velocity of NGC4438 is ∼1000 km s^{-1}. A tidal encounter with the SB0 galaxy NGC4435 at a projected distance of ∼4.3 arcmin (∼20 kpc) is also likely to affect NGC4438. Kenney et al. (1995) have suggested that most of the features of the disturbed ISM are likely to be due to a high-velocity ISM-ISM collision between NGC4438 and 4435. Numerical simulations suggest that the nuclei of these two galaxies have passed within 5−10 kpc of each other ∼10^8 yr ago (Vollmer et al. 2005). Radio continuum observations of the nuclear region by by Hummel & Saikia (1991) have shown two lobes of radio emission which are highly asymmetric

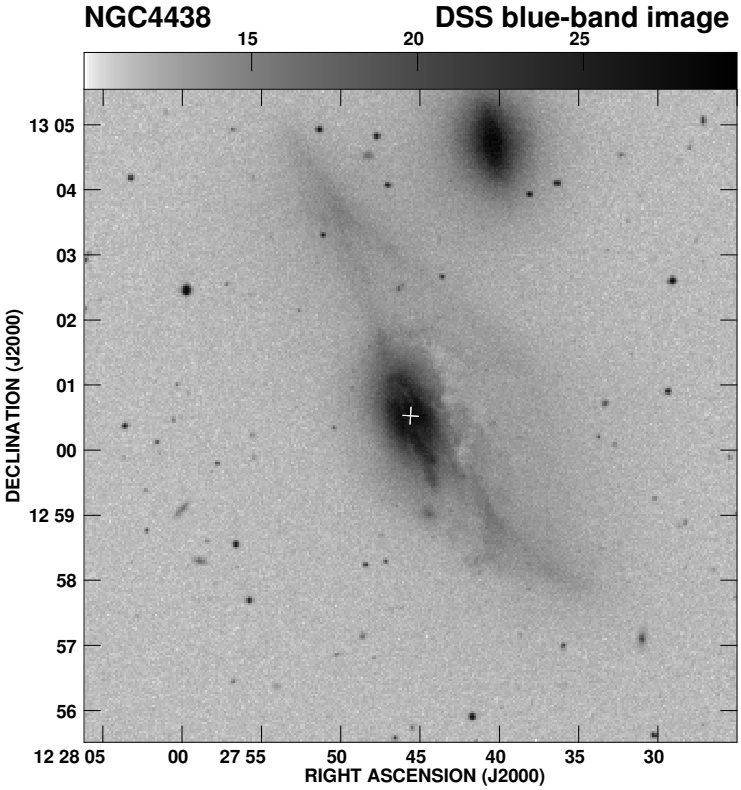

Figure 4.1: The DSS blue-band image of NGC4438 and its companion NGC4435. The + sign marks the position of the radio nucleus discussed in this chapter.

with the north-western one being much brighter than the south-eastern one. X-ray and Hα+[NII] emission are also seen from these two lobes which exhibit a bubble-like structure and similar asymmetry in location, brightness and size at these wavelengths (Kenney & Yale 2002; Machacek et al. 2004).

In this chapter, we first present our results of radio continuum observations of the nuclear region and diffuse extended emission on the western side (Section 3). We then present the results of H I observations with the GMRT and the VLA D-array (Section 4). This is followed by a brief discussion and a summary of the results (Section 5).

4.3 Observations and data analysis

The observing log for both the GMRT and VLA observations as well as some of the observed parameters of the continuum images are presented in Table 6.2 which is arranged as follows. Column 1: Name of the telescope where we also list the configuration for the VLA observations. In addition to our own data we have also analysed many sets of archival VLA data on this galaxy. Column 2: The frequency of the observations; columns 3 and 4: dates of the observations and the time, t, spent on the source in minutes. Columns 5 and 6: The phase calibrator used and its flux density estimated from the observations; columns 7, 8 and 9: the major and minor axes of the restoring beam in arcsec and its position angle (PA) in degrees; column 10: the rms noise in the continuum image in units of mJy/beam; columns 11 and 12: the peak and total intensity in units of mJy/beam and mJy for the continuum images. The total error in the flux density is approximately 5% for frequencies higher than 1 GHz and ∼10% at 617 MHz. The information for the HI observations are presented in Table 4.4 where we have also listed the spectral resolution in units of km s^{-1} (column 6), the rms noise in the channel maps in units of mJy/beam (column 10), the rms noise in the spectrum in units of mJy (column 11) and the HI flux density in units of Jy km s^{-1} (column 12).

The radio continuum observations with the GMRT as well as with the VLA were made in the standard fashion with each source observation interspersed with observations of the phase calibrator. The primary flux density calibrator was 3C286 or 3C147 whose flux density was estimated on the Baars et al. (1977) scale using the 1999.2 VLA values. The bandwidth of the continuum observations with GMRT at 617 MHz was 16 MHz, while for the L-band

Table 4.2: Observation log and observed parameters of the continuum images

Telescope	Freq.	Obs.	t	Phase	$S_{cal.}$	Beam size			rms	S_{pk}	$S_{tot.}$
	MHz	date	min	Calib.	Jy	maj.	min.	PA	mJy	mJy	mJy
						$''$	$''$	$^\circ$	/b	/b	
(1)	(2)	(3)	(4)	(5)	(6)	(7)	(8)	(9)	(10)	(11)	(12)
GMRT	617	11Jan02	300	1120+057	3.57	46	23	149	4	151	311
VLA-A	1490	24May86	236	1252+119	0.98	1.50	1.50		0.04	19	87
VLA-B	4860	20Jul86	177	1252+119	0.62	1.50	1.50		0.03	7.3	33
VLA-A	4860	24May86	44	1252+119	0.62	0.41	0.36	114	0.04	0.5	12
VLA-A	8460	13May98	23	1236+077	0.71	0.21	0.19	176	0.03	0.4	7.8
VLA-AB	14939	05Dec91	13	1252+119	0.52	0.57	0.43	127	0.19	1.0	8.9

observations it was 8 MHz. The bandwidth for all the VLA continuum observations was 50 MHz. The data analysis was done using the Astronomical Image Processing System (AIPS) of the National Radio Astronomy Observatory. Since GMRT data is acquired in the spectral-line mode with 128 spectral channels, gain and bandpass solutions were applied to each channel before combining them. Self-calibration was applied to all the GMRT and VLA data sets. The low-resolution 617-MHz map was made with the 3-D cleaning option in CLEAN using 16 fields. The self calibrated gains were applied to this data set correcting only for phase and rejecting all the failed solutions. For all the VLA data sets two cycles of phase and one cycle of amplitude self calibration were applied except for the VLA A-array 8460-MHz data where only two cycles of phase self calibration were applied. The analysis of the H I observations were also done in the standard way. 3C286 was the primary flux density and bandpass calibrator. The total bandwidth for GMRT H I observations was 8 MHz and the spectral resolution was 62.5 kHz, which corresponds to a velocity resolution of 13.2 km s^{-1}. The total bandwidth for the VLA D-array H I observations was 6 MHz and the spectral resolution was 97.7 kHz, which corresponds to a velocity resolution of 20.7 km s^{-1}. The details of the HI observations are listed in Table 6.2. The AIPS

task UVLIN was used for continuum subtraction specifying sets of line-free channels. The GMRT data was cleaned using the self-calibrated gains from the continuum data analysis. For the VLA data analysis, the bright continuum source M87 was subtracted using UVSUB, before the multi-channel data was continuum subtracted and CLEANed using IMAGR.

4.4 Radio continuum emission

(a) A mini double-lobed radio source

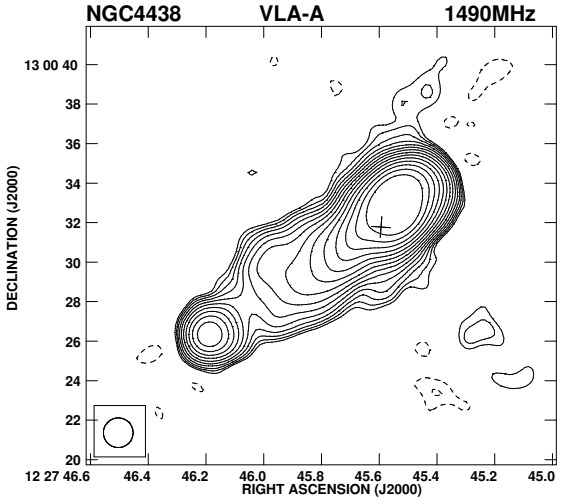

Figure 4.2: The VLA A-array image at 1490 MHz with an angular resolution of 1.5 arcsec. Contours: 0.037×(−4, −2.82, 2.82, 4, 5.65, 8 . . .) mJy/beam.

The VLA A-array image at 1490 MHz and the VLA B-array image at 4860 MHz with an angular resolution of 1.5 arcsec (Fig. 4.2, 4.3) show the well-known double-lobed structure of the radio source in the nuclear region (Hummel & Saikia 1991). The double-lobed source has a total extent of ∼12 arcsec (960 pc), with the western lobe being separated from the nucleus

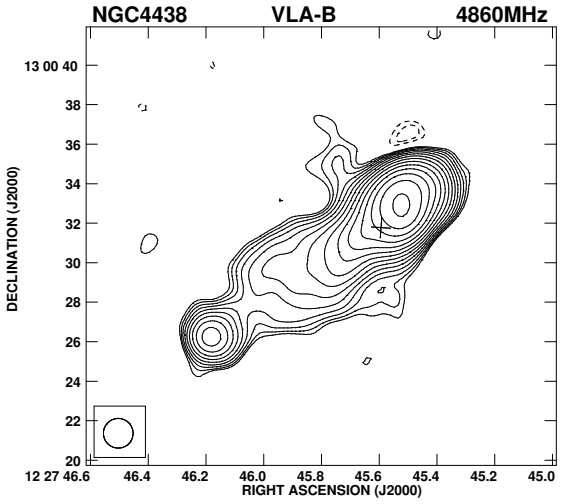

Figure 4.3: VLA B-array image at 4860 MHz with an angular resolution of 1.5 arcsec. Contours: 0.026×(−4, −2.82, 2.82, 4, 5.65, 8 . . .) mJy/beam.

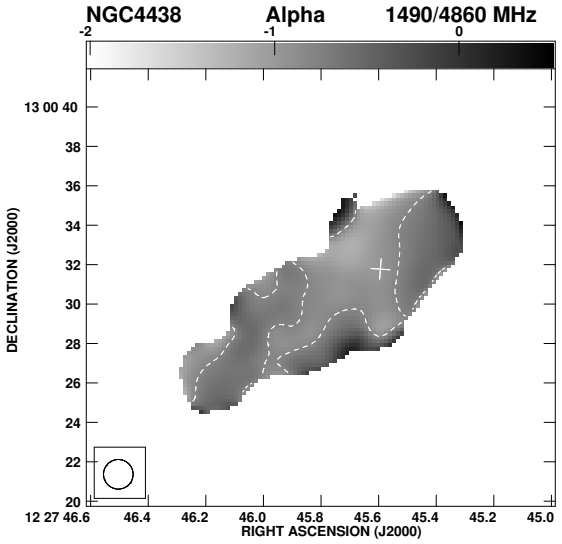

Figure 4.4: Spectral index image between 1490 and 4860 MHz. The contour is at −0.8. The + sign marks the position of the radio nucleus in all the images.

discussed in Section 3.2 by 2.9 arcsec (230 pc) compared with 8.9 arcsec (730 pc) for the eastern lobe. The spectral index image made from these

scaled-array VLA images by considering only those pixels which are 5 times above the rms noise is also shown in Fig. 4.4. The spectral index, defined as S$\propto \nu^{\alpha}$, varies from -1.5 to $+0.5$, while the error in the spectral index is $\sigma_{\alpha} = 0.08$. The mean value of spectral index for the western lobe, the diffuse central region and the eastern lobe are -0.78, -0.84 and -0.61 respectively, the spectral index being steepest between the lobes.

Given the steepness of α, the emission is clearly strongly dominated by synchrotron emission. However, it is important to quantify what, if any, contribution a thermal component might make. The latter would flatten the spectral index from a steeper value, α_{NT}, to the flatter value, α, that is observed. In particular, we ask what the thermal contribution would have to be in order to flatten the spectral index by an amount that is significantly outside of our error bar in the spectral index map. We use the measured flux densities of the two maps shown in Fig. 4.2, 4.3, cut off to the same 5σ level as the spectral index map. These values are $S_{1.5\,GHz} = 86.3$ mJy and $S_{4.86\,GHz} = 32.5$ mJy, giving an observed total spectral index of $\alpha = -0.825$. If the true non-thermal spectral index is $\alpha_{NT} = -0.825 - 2\sigma_{\alpha} = -0.985$, then (following Lee et al. 2001) we find that the thermal flux required to alter the spectral index by this much is $S_{1.5\,GHz}(th) = 8.2$ mJy. This corresponds to a required average electron density of $n_e = 7.2$ cm^{-3} over a region whose equivalent spherical radius is 700 pc. While there may be regions smaller than a beam within which the density is higher than this (e.g. Kenney & Yale 2002), it is very unlikely that the electron density is this high, on average, over the observed region. Indeed, Machacek et al. (2004) find a mean density of $n_e \approx 0.03$ cm^{-3} for the hot gas component over a roughly equivalent volume. We therefore conclude that the thermal contribution to these maps are negligible and continue with the minimum energy calculations

under the assumption that $\alpha \approx \alpha_{NT}$.

The minimum energy parameters

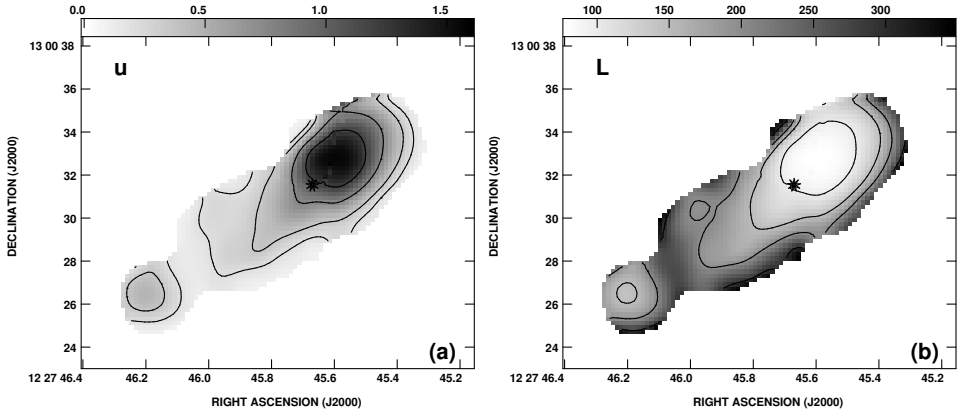

Figure 4.5: Maps of the minimum energy parameters of the mini double-lobed radio source, made from Fig. 4.2, 4.3, assuming a heavy particle to electron energy ratio of k=40. In each case, black denotes the *highest* values. (a) The cosmic ray energy density. Contours are 200, 350, 750, and 1200 eV cm^{-3} and the peak value is 1.58 $\times$ 10^3 eV cm^{-3} . (b) Diffusion length. Contours are 100, 150, 200 and 300 pc and the peak is 347 pc.

The VLA images, which have the same spatial resolution and similar signal-to-noise (S/N) ratios, along with the spectral index map (Fig. 4.2, 4.3) can be used to compute the following minimum energy parameters (see Pacholczyk 1970; Duric 1991): the cosmic ray energy density u_{CR}, the cosmic ray electron diffusion length L_D, the magnetic field strength B, and the particle lifetime t. In addition, we compute the This calculation can be done on a pixel-by-pixel basis from some geometry, as previously described in Irwin & Saikia (2003).

In the case of the doubel-lobed source, we use a geometry in which the line-of-sight depth is taken to be the measured average width of the mini double-lobed source, i.e. $4.21'' = 344$ pc with unity filling factor. The

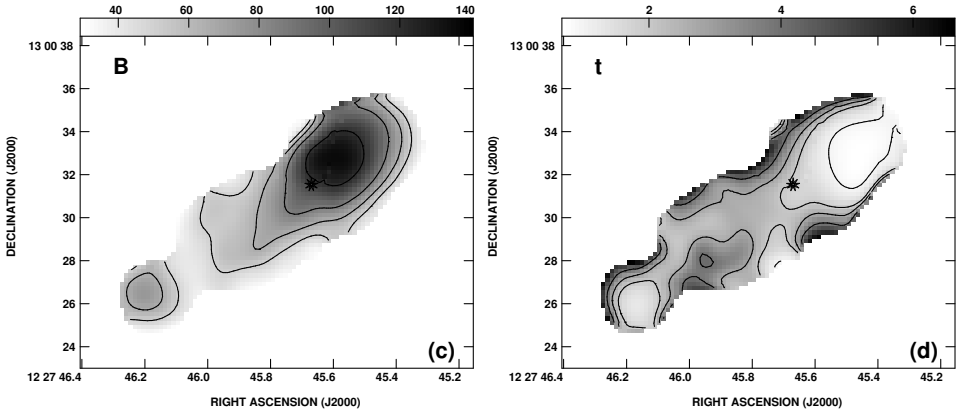

Figure 4.6: Maps of the minimum energy parameters of the mini double-lobed radio source, made from Fig. 4.2, 4.3, assuming a heavy particle to electron energy ratio of k=40. In each case, black denotes the *highest* values. (c) Magnetic field strength. Contours are 50, 65, 85, and 120 μG and the peak is 136 μG. (d) Lifetime of the particles. Contours are 1, 2, 2.75, and 4 Myr and the peak is 6.59 Myr.

lower- and higher-frequency cut-offs of the spectrum are ν_1=10^7 and ν_2=10^{11} Hz, respectively, and we adopt two different values for the heavy-particle energy to the electron energy, k=40, and k=100. The results are shown in Fig. 4.5,Fig. 4.6, Fig. 4.7 and averages over these maps are given in Table 4.3. We have found that changes in the choice of line of sight distance and upper frequency cutoff make relatively small changes in the results in comparison to the choice of k (e.g. Irwin & Saikia 2003). For the large range in adopted value of k, the results, overall, are within a factor of $\approx$ 1.5 of each other. Note also, that this choice affects only the absolute scale of the maps and not the point-to-point variations.

In Fig. 4.7, we also show a map of power, P=U/t, where U is the cosmic ray energy density u_{CR} integrated along a line of sight and t is the particle lifetime. The result is identically P= (1 +k)L, where L is the observed luminosity at a point. Thus the map of P closely resembles the map of total

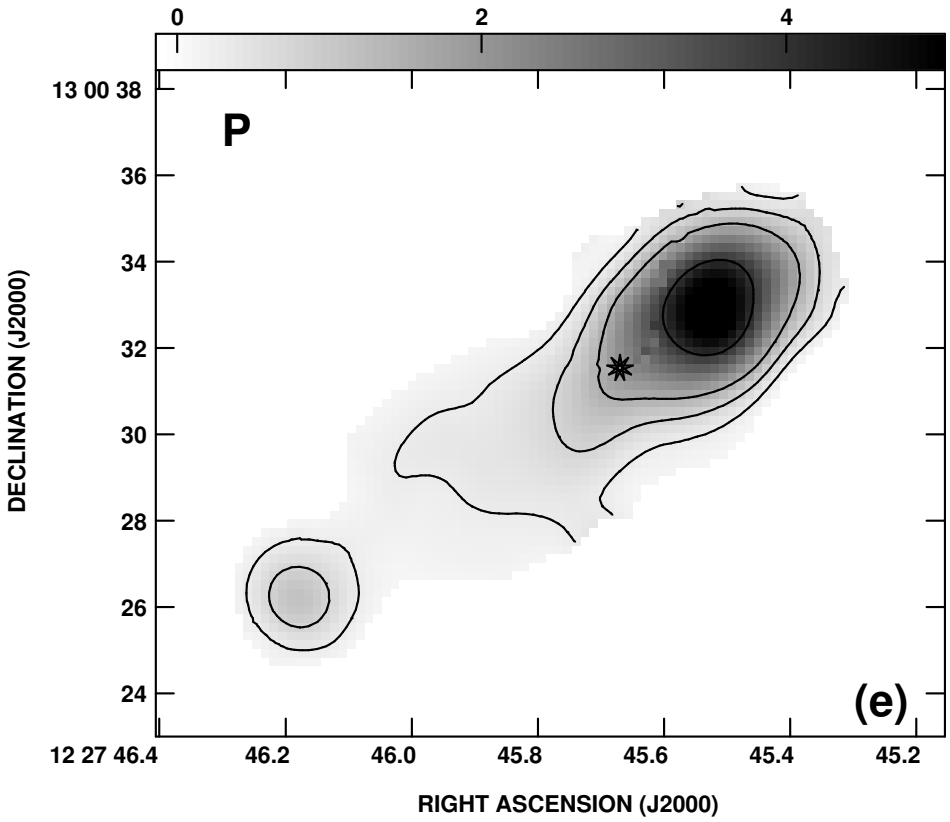

Figure 4.7: Maps of the minimum energy parameters of the mini double-lobed radio source, made from Fig. 4.2, 4.3, assuming a heavy particle to electron energy ratio of k=40. In each case, black denotes the *highest* values. (e) Cosmic ray power. Contours are 0.33, 0.75, 1.5, and 4 $\times 10^{39}$ ergs s^{-1} and the peak is 5.57 $\times$ 10^{39} ergs s^{-1}.

flux density but does not match it exactly because the computation of L requires an integration over frequency which is dependent on spectral index, and the spectral index is different at different points in the map. The map of P represents the rate at which cosmic rays must be accelerated in order to maintain equilibrium. As indicated in the Table 4.3, the total power in the cosmic ray component is a few 10^{42} ergs s^{-1} and the total energy in cosmic rays is 10^{56} ergs.

Table 4.3: Minimum energy parameters.[a]

Model[b]	$\bar{u}_{CR}{}^c$ (eV cm^{-3})	$\bar{L}_D{}^d$ (kpc)	B^e (μG)	t^f (Myr)	$U_{CR}{}^g$ (10^{55} ergs)	$P_{CR}{}^h$ (10^{42} ergs s^{-1})
k=40	463	178	68.6	2.46	8.75	1.72
k=100	775	137	88.8	1.67	14.6	4.24

a See Pacholczyk (1970), Duric (1991), or Irwin & Saikia (2003).
b A line of sight distance of 344 pc is adopted. k is the ratio of heavy particle to electron energy.
c Cosmic ray energy density, averaged over the source. The total cosmic ray plus magnetic field energy density is 7/4 times these values.
d Average diffusion length.
e Average magnetic field strength.
f Average particle lifetime.
g Total cosmic ray energy integrated over the source volume.
h Total power, $P_{CR} = (1 + k)\, L$, where L is the luminosity radiated by the electron component (see text).

The eastern and western lobes/shells

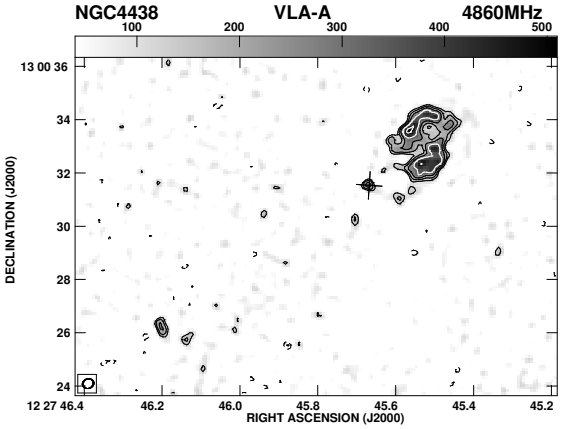

Figure 4.8: The VLA A-array image at 4860 MHz with an angular resolution of ∼0.38 arcsec. Contours: 0.042×(−4, −2.82, 2.82, 4, 5.65, 8 ...) mJy/beam.

The VLA A-array images at 4860 and 8460 MHz reveal the prominent shell-like structure in the western lobe, noted earlier by Hummel & Saikia (1991), and also regions of emission from the eastern lobe (Fig. 4.8, 4.9).

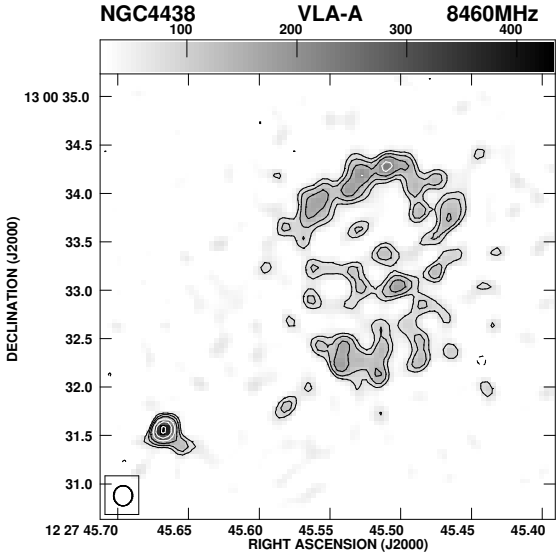

Figure 4.9: The VLA A-array image at 8460 MHz with an angular resolution of ∼0.19 arcsec showing only the nucleus and the western shell. Contours: 0.025×(−4, −2.82, 2.82, 4, 5.65, 8 . . .) mJy/beam.

The shell on the eastern side is smaller with a radius of ∼0.5 arcsec (40pc), compared with a radius of 1.0 arcsec (80pc) for the western one. The structure of the western lobe, which is seen more clearly here than in the image of Hummel & Saikia shows two main ridges of emission on the northern and southern side with the peak of emission being on the northern ridge rather than the outer edge of the bubble. Both the lobes exhibit a shell-like structure in Hα and X-ray wavelengths (Machacek et al. 2004; Kenney & Yale 2002). Although there is a close correspondence between the shells seen at radio and Hα and X-ray wavelengths there are also significant differences. For example while the eastern shell appears more complete at Hα and ring-like at X-ray wavelengths the radio emission seen in the high-resolution image (Fig. 4.8) arises from only parts of the shell. On the western side the shell appears more filled in at radio and X-ray wavelengths while Hα and [NII] emission

are seen in the outer parts of the shell. Both Hα and X-ray emission peak close to the nucleus which is weak at radio wavelengths.

(b) The radio nucleus

VLA A-array images at 4860 and 8460 MHz with angular resolutions of $\sim$0.38 and 0.19 arcsec respectively show clearly a compact radio source which is consistent with the position of the optical and infrared positions of the nucleus (Clements 1983; Keel & Wehrle 1993; Falco et al. 1999). The J2000 position of the infrared peak which is likely to be least affected by extinction is RA 12^h 27^m $45.^s67$, Dec $+13^\circ$ $00'$ $31.''54$ (Keel & Wehrle 1993) and is consistent with the measurements at optical wavelengths. The position of the compact radio source is RA 12^h 27^m $45.^s67$, Dec $+13^\circ$ $00'$ $31.''54$ at 4860 MHz, which agrees well with the position of RA 12^h 27^m $45.^s66$ Dec $+13^\circ$ $00'$ $31.''53$ determined from the 8460-MHz image as well as the position from infrared observations. The peak flux densities of the compact radio source estimated from our two images are 0.29 mJy/beam at 4860 MHz and 0.43 mJy/beam at 8460 MHz which yields an inverted radio spectrum with a spectral index of +0.69. The spectrum could be even more inverted if there is any contamination of the flux density at 4860 MHz by any extended emission. The highly inverted spectrum of this compact component confirms it to be the nucleus of NGC4438. It would be interesting to re-observe it for any possible signs of variability.

(c) The western diffuse radio emission

We have imaged the diffuse continuum emission on the western side of the disk which was initially reported by Allen et al. (1973) and Kotanyi, van

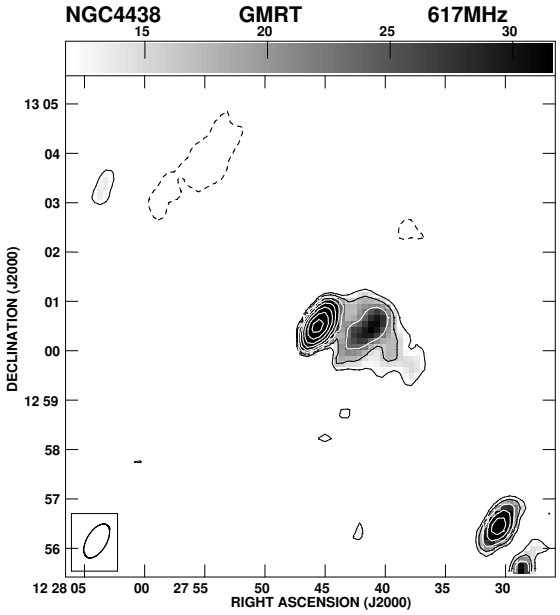

Figure 4.10: The GMRT image of NGC4438 and 617 MHz with an angular resolution of 33arcsec. Contours: $4\times(-4,\ -2.82,\ 2.82,\ 4,\ 5.65,\ 8\ \ldots\ )$ mJy/beam.

Gorkom & Ekers (1983) with the GMRT at 617 MHz. The rms noise in the image is 4 mJy/beam which is on the higher side due to the presence of the strong radio source M87. This is also possibly responsible for the significant variations in the total flux density values of NGC4438 which have been reported in the literature. For example the total flux density values at $\sim$5000 MHz range from 70$\pm$10 mJy determined using the NRAO 300$'$ telescope (Becker et al. 1991) to 97$\pm$9 mJy measured by Vollmer et al. (2004a) using the Effelsberg telescope. Vollmer et al. (2004a) have systematically tried to determine the radio continuum spectra of galaxies in the Virgo cluster and quote a spectral index of -0.67 for the total emission using a number of measurements between 600 and 10550 MHz.

Subtracting the flux densities of the nuclear double-lobed source for which

we have reliable measurements of the total flux density (Table 6.2; Hummel & Saikia 1991) from the measurements of total flux density by Vollmer et al. (2004a) we can estimate the spectral index of the more extended emission. The total flux density at 1400 MHz reported by Vollmer et al. is 149 mJy which is consistent with the value of 150 mJy reported by Kotanyi et al. (1983), while the value at 5000 MHz is 97 mJy. The flux densities for the nuclear double is 87 and 33 mJy at 1400 and 4860 MHz (see Table 6.2), giving flux densities of 62 and 64 mJy for the extended emission at these two frequencies. This yields a flat spectral index of $\sim$0 for the diffuse extended emission, even flatter than the value of ~-0.5 reported by Kotanyi et al.(1983). Adopting the value of 70 mJy for the total flux density at 5000 MHz gives us a flux density of 37 mJy and a spectral index of ~-0.4 for the extended emission. The western diffuse radio emission is visible in the 10550 MHz image of Niklas, Klein & Wielebinski (1995) possibly due to its flat spectrum. Estimating the flux density of the nuclear emission at 10550 MHz by extrapolating it to higher frequencies and subtracting it from the total flux density also yields a similar flat spectral index of ~-0.4 between 1400 and 10550 MHz.

At low-frequencies the total flux density of 324$\pm$30 mJy at 600 MHz reported by Vollmer et al. is consistent with our estimate of 311$\pm$30 mJy at 617 MHz with an angular resolution of $46''\times24''$ arcsec^2 along a PA of 149°. Identifying the peak flux density of 151 mJy in the GMRT image at 617 MHz with the nuclear double gives a flux density of $\sim$167 mJy for the extended emission. The peak flux density of 151 mJy is consistent with the extrapolated flux density of $\sim$179 mJy at 617 MHz for the nuclear double using our VLA measurements. This yields a spectral index of ~-1.1 for the extended

Table 4.4: Observation log and observed parameters of the HI-images

Tel.	Obs. date	t min	Phase calib.	S_{cal} Jy	Vel res. km /s	Beam size maj. ″	min. ″	PA °	map rms mJy /b	spec. rms mJy	HI flux Jy km/s
(1)	(2)	(3)	(4)	(5)	(6)	(7)	(8)	(9)	(10)	(11)	(12)
GMRT	14Apr02	300	1254+116	0.79	13.2	38	35	178	1.2	5.8	2.9
VLA	02Jul88	330	1252+119	0.92	20.7	58	48	0	0.9	2.0	4.0
						127	124	84	1.2	4.6	6.5

emission between 600 and 1400 MHz significantly steeper than the high-frequency spectrum. This suggests that the low-frequency spectral index is dominated by non-thermal emission, while at high-frequencies contributions from thermal emission become important. This is a clear demonstration of both thermal and non-thermal radio-emitting material exisiting in the extra-planar gas. It is relevant to note that a flat spectral index of ~ -0.5 for extended extra-planar radio emission may also be due to re-acceleration of particles (e.g. Bell 1978) as has been suggested for the Virgo cluster galaxy NGC4522 (Duric 1986, 1998; Vollmer et al. 2004b). However, the difference in spectral index discussed above suggests that this is not the explanation for NGC4438.

4.5 HI observations

HI observations of NGC4438 have been reported earlier with an angular resolution of 23×118 arcsec^2 along PA=0° using the Westerbork telescope by Kotanyi (1981), and more recently with an angular resolution of ∼40 arcsec (3.3 kpc) using the VLA-D array by Cayatte et al. (1994) and again with the VLA D-array by Li & van Gorkom (2001). We observed this source with the GMRT to determine the structure of HI in emission with higher

resolution, and also to detect HI in absorption towards the central compact source to identify any kinematic effects of the nuclear activity on the HI gas. We have also analysed VLA D-array archival data to detect and study the disk emission, which has not been seen earlier, with high surface brightness sensitivity and also detect and understand the properties of more extended HI gas. Unlike the observations reported by Li & van Gorkom (2001) the phase centre of this archival data set was NGC4438.

(a) HI emission

GMRT observations

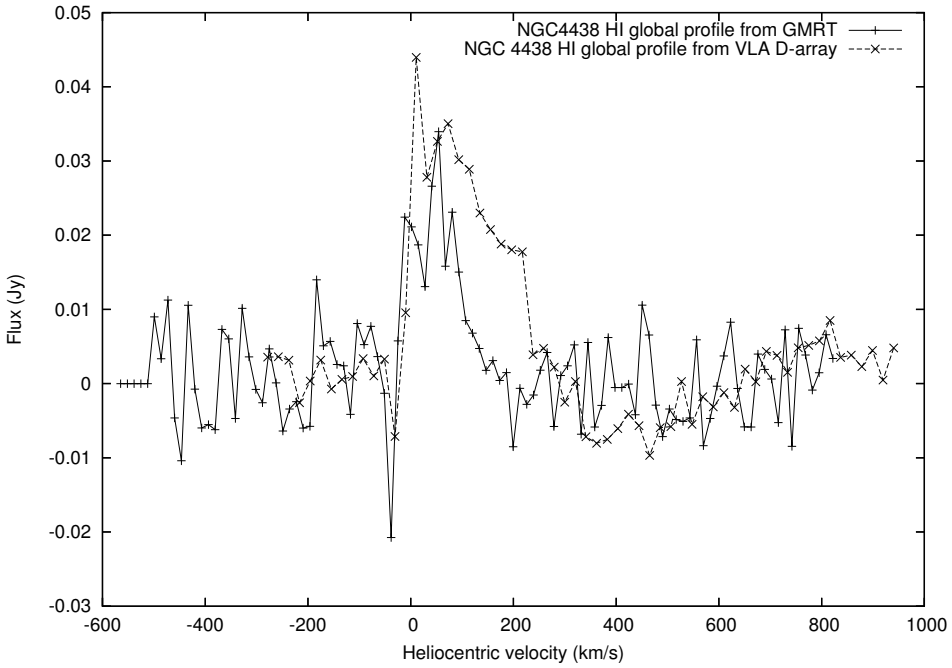

Figure 4.11: The global profile of HI emission from the GMRT observations with an angular resolution of ∼36 arcsec (continuous line) and VLA D-array observations tapered to an angular resolution of ∼125 arcsec (dashed line).

We present here the global profile (Fig. 4.11) and the total-intensity HI image from the GMRT observations (Fig. 4.12). These observations

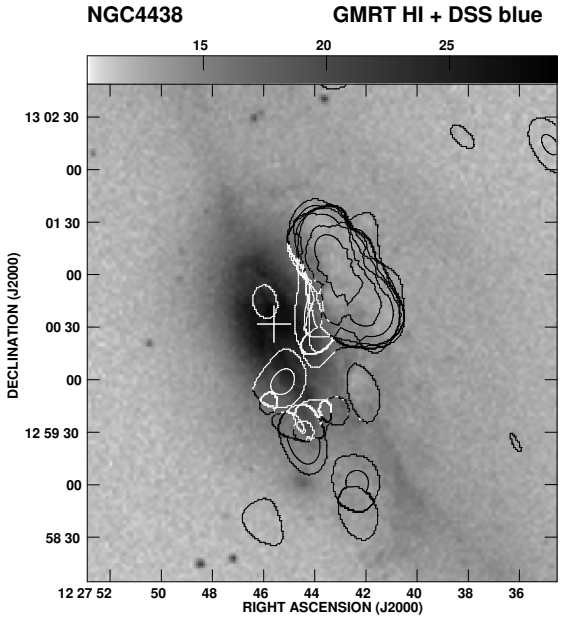

Figure 4.12: The moment zero image from the GMRT observations with an angular resolution of ∼36 arcsec superimposed on the DSS blue-band image. Contour levels are 5.67, 8.0, 11.3 ..... 10^{19} atoms cm^{-2}, in the steps of multiples of $\sqrt{2}$.

clearly show an elongated structure along a PA of ∼35° which is very similar to the PA of 29° for the central stellar disk measured from molecular line observations (Kenney et al. 1995). This elongated structure extends for ∼6.5 kpc in our GMRT image. It is roughly parallel to the stellar disk and ∼4.1 kpc away from its mid plane. Earlier HI images (e.g. Kotanyi et al. 1983; Cayette et al. 1994; Li & van Gorkom 2001) show the displacement of HI gas on the western side of the stellar disk but the detailed structure was not apparent in these observations. In addition to this elongated structure there are weak blobs of HI emission towards the south.

The HI mass of the elongated feature is 1.5×10^{8}M$_{\odot}$, while the total H I mass estimated from the global profile (Fig. 4.11) obtained from the GMRT

observation is $\sim 2\times10^8 M_\odot$. The global profile exhibits a possible absorption feature at ~ -40 km s^{-1} with a width of $\sim$15 km s^{-1}. Although most of the H I gas appears red-shifted with respect to the systemic velocity of the galaxy (71 km s^{-1}), the blobs towards the south appear blue shifted. The velocity gradient of the elongated structure shows that the north-eastern side is receding with a maximum heliocentric radial velocity of 107 km s^{-1} while the south-western side is approaching with a minimum radial velocity of -28 km s^{-1}. These velocities are consistent with the Westerbork observations reported by Kotanyi (1981). The middle point of the radial velocity range of the elongated feature from our observations is $\sim$40 km s^{-1}. The maximum line width in this elongated HI emission structure is $\sim$40 km s^{-1}. The observed sense of rotation of this feature is similar to that of CO emission seen in the stellar disk of the galaxy (Combes et al. 1988; Kenney et al. 1995; Vollmer 2005), and lies close to the position of the extra-planar CO(1-0) emission along a PA$\sim$20° (Vollmer et al. 2005). The extent of the extra-planar CO emission is very similar to that of the HI feature seen here, although the peak of the CO emission lies slightly to the north-west while that of the HI-elongated structure towards the centre of the feature. In this region the DSS blue band image shows the presence of dust plumes which appear very similar in nature to those seen in the Virgo cluster galaxy NGC4402 (Crowl et al. 2005).

VLA observations

We first present the results of the VLA D-array full-resolution observations with an angular resolution of 58×48 arcsec^2 along a PA of 0°. Moment maps were made with a cutoff at 4σ and integrated in velocity from -133 to velocity +340 km s^{-1} (Fig. 4.13, 4.14,4.15, 4.16). With a higher surface brightness

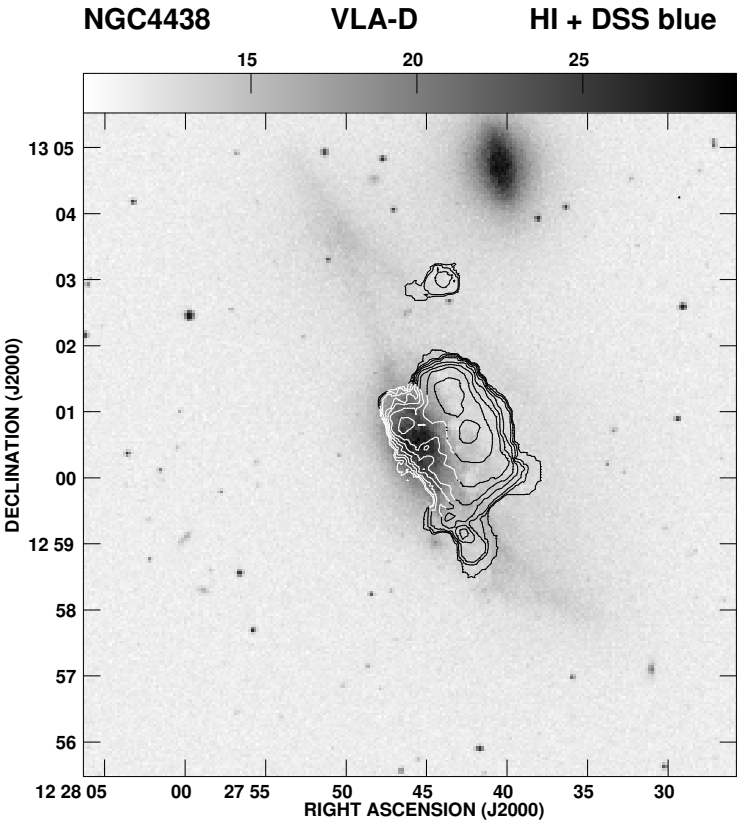

Figure 4.13: The moment zero image from the VLA D-array observations with an angular resolution of ∼53 arcsec superimposed on the DSS blue-band image. Contour levels: 3.84,5.45,7.69 ... 10^{19} atoms cm^{-2} in steps of multiples of $\sqrt{2}$.

sensitivity than the GMRT observations, the total-intensity contours of HI emission show that the elongated feature extends further south with a total size of $\sim 2'$ (9.8 kpc) along a similar orientation to that of the elongated feature seen in the GMRT observations. There is also HI emission from the optical disk of the galaxy with the emission having a sharper edge towards the north and extending further towards the south with a similar total extent $\sim 2'$ (9.8 kpc). There is a clump of HI emission at the southern end of the disk emission with velocities in the range of ~ -20 to $+20$ km s^{-1}. The moment 0

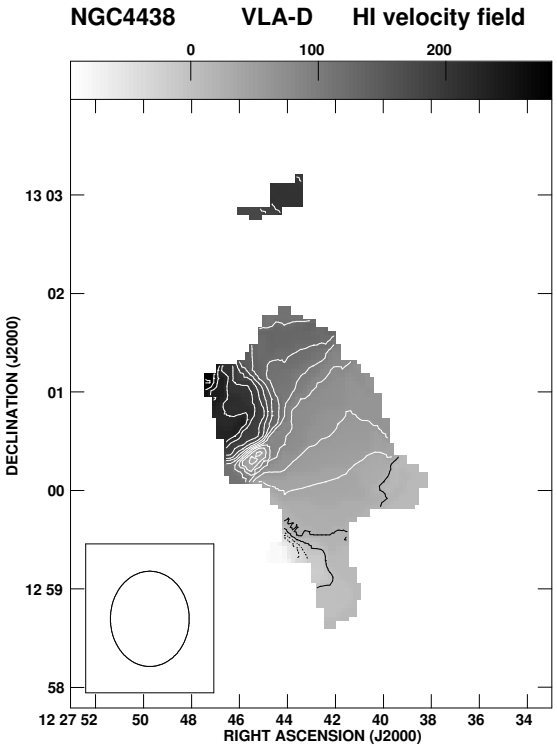

Figure 4.14: The corresponding moment one image showing the velocity field. Contour levels from south to north are -40, -20, 0, 20, 40, 60, 80... km s^{-1} in steps of 20 km s^{-1}.

map also shows a clump of HI emission towards the north between NGC4438 and NGC4435 with heliocentric velocities ranging from +176 to +217 km s^{-1}.

The velocity field of NGC4438 in this VLA D-array map is complex. In the central region of the disk within ∼10 arcsec of the nucleus the isovelocity contours are orthogonal to the central stellar disk with velocities ranging from 40 km s^{-1} on the southern side to 240 km s^{-1} on the northern side, yielding a gradient of 10 km s^{-1} $arcsec^{-1}$. At larger distances from the nucleus the isovelocity contours along the disk of the galaxy range from −80 near the southern clump to 280 km s^{-1} on the northern edge giving a velocity gradient

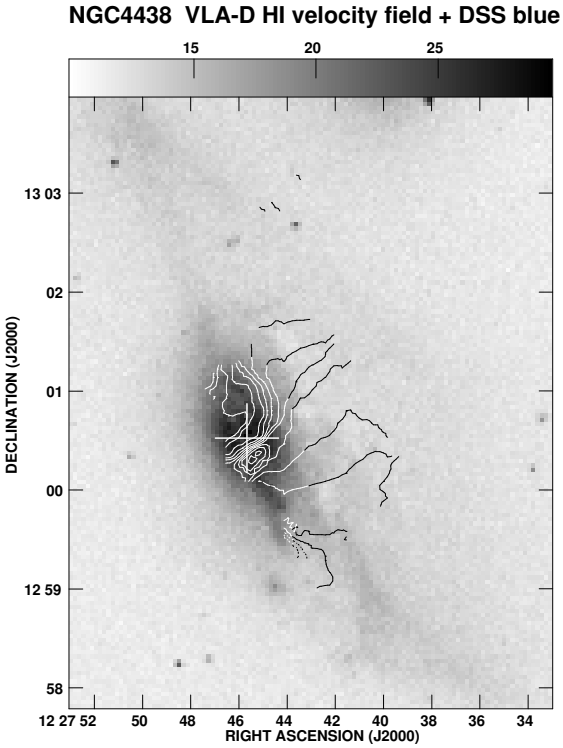

Figure 4.15: The corresponding moment one image showing the velocity field, superimposed on the DSS blue band image. Contour levels from south to north are -40, -20, 0, 20, 40, 60, 80... km s^{-1} in steps of 20 km s^{-1}.

of 3 km s^{-1} $arcsec^{-1}$. The isovelocity contours appear to be curving away in the interface between the disk and the extra-planar gas. This is reminescent of NGC4522 which is at a similar orientation and undergoing interaction with the ICM of the Virgo cluster. The extra-planar gas in NGC4438 has a smoother velocity field ranging from +10 on the southern side to 130 km s^{-1} on the northern side giving a lower velocity gradient of 1 km s^{-1} $arcsec^{-1}$ over a similar length scale. It is worth noting that the blue-shifted velocities of -28 km s^{-1} in the southern side of the elongated feature seen in the GMRT and Westerbork observations is not apparent in the D-array image, suggesting that observations with different resolutions pick up sub structures

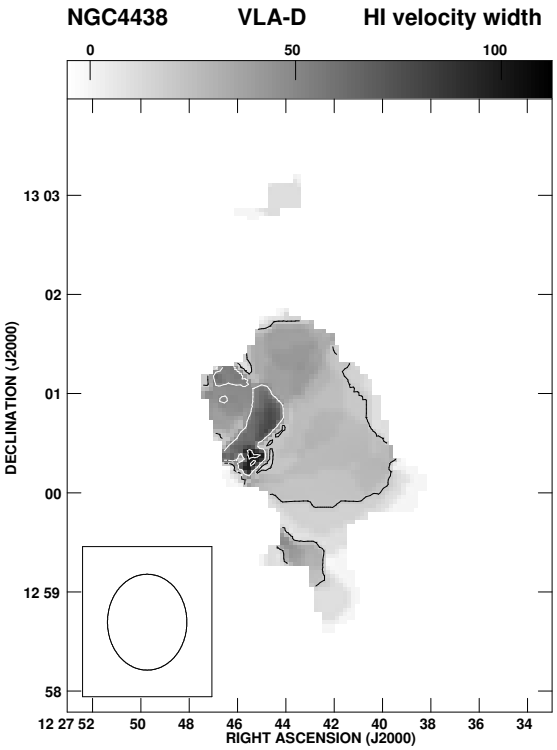

Figure 4.16: The corresponding moment two map showing the velocity dispersion. Contour levels: 20, 50 and 100 km s^{-1}.

with different velocities.

Approximately 15 arcsec south of the nucleus centred approximately at RA 12 27 45.4, Dec 13 00 20, there is a small region of 15×10 $arcsec^2$ along a PA∼130° where the iso-velocity contours are closed and have values ranging from 40 to 80 km s^{-1}. These contours represent gas which is approaching us relative to the gas in its vicinity. The moment 2 map shows that the velocity dispersion in this region is high with values in the range of 90−115 km s^{-1}. The moment 2 map also shows that towards the north of this region, the velocity dispersion is typically 50−80 km s^{-1} over a total extent of ∼3.7 kpc approximately orthogonal to the PA of the disk. For the rest of the galaxy and the extra-planar emission the line widths are in the range of 20−50 km

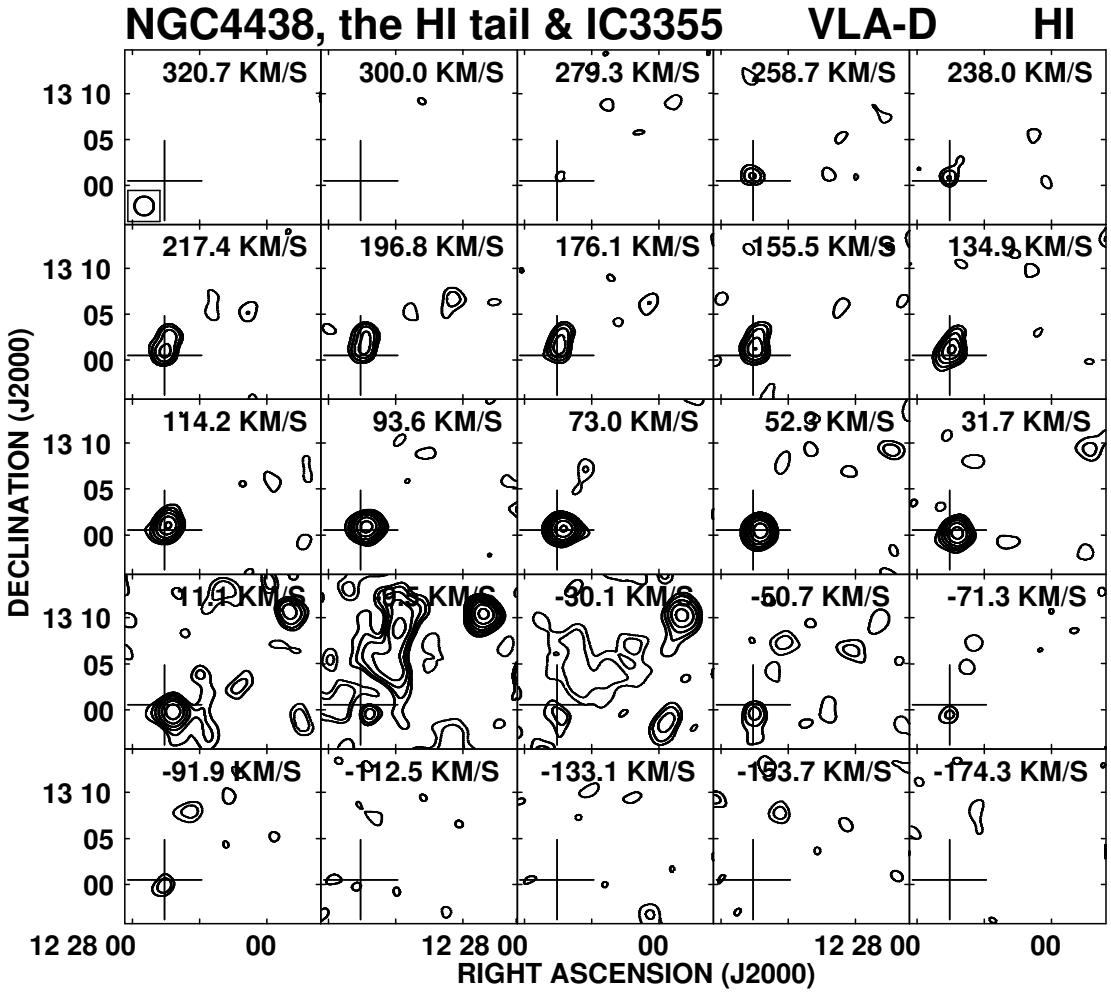

Figure 4.17: HI-emission channel maps made with a resolution of $37''.76 \times 33''.36$ along PA $\sim 6°$. The systemic velocity of NGC4438 is 71 km s^{-1}. The velocity separation between adjacent channels is 20.7 km s^{-1}. The crosses in all the images denote the position of the radio nucleus of NGC4438.

s^{-1} with the line widths being larger on the northern side.

The VLA D-array data were also imaged with a 1kλ taper (resolution of $\sim$ 125 arcsec) which shows more HI gas primarily on the western side. The global profile (Fig. 4.11) superimposed on the one from the GMRT

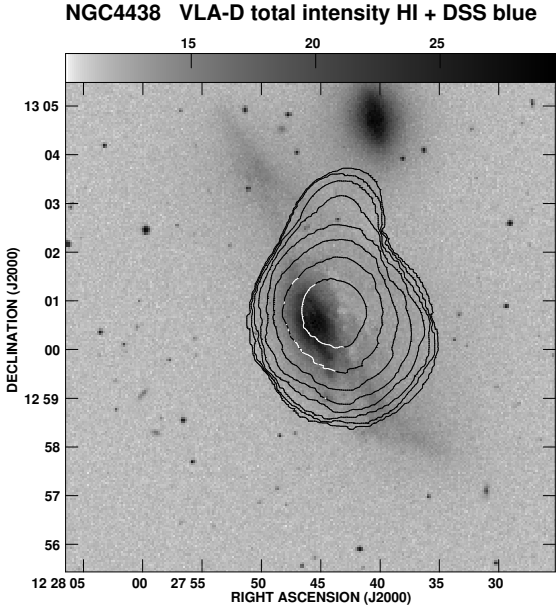

Figure 4.18: The moment zero image from the VLA D-array observations tapered to an angular resolution of ∼125 arcsec superimposed on the DSS blue-band image. Contour levels: 2.26, 3.22, 4.54 10^{19} atoms cm^{-2} in steps of multiples of $\sqrt{2}$.

higher resolution observations shows that there is indeed more HI gas towards the red-shifted side. The VLA spectrum also shows a sharp cut off on the blueward side of the spectrum as seen in the GMRT global profile. The total HI flux density is 6.5 Jy km s^{-1} which is consistent with that of Arecibo mesurements by Giovanardi, Krumm & Salpeter (1983) who quote a line flux density of 6.1±0.6 Jy km s^{-1}. Our VLA mesurements correspond to a total HI mass of 4.4×10^8 M$\odot$ which is ∼2 times larger than that estimated from the GMRT spectrum. The channel maps obtained with a spatial resolution of ∼ 125 arcsec (Fig 4.17) also shows clearly the presence of diffuse, extended HI emission. Apart from NGC4438 HI emission is also seen at the position of the irregular galaxy IC3355 towards the north-west and a tail of HI emission

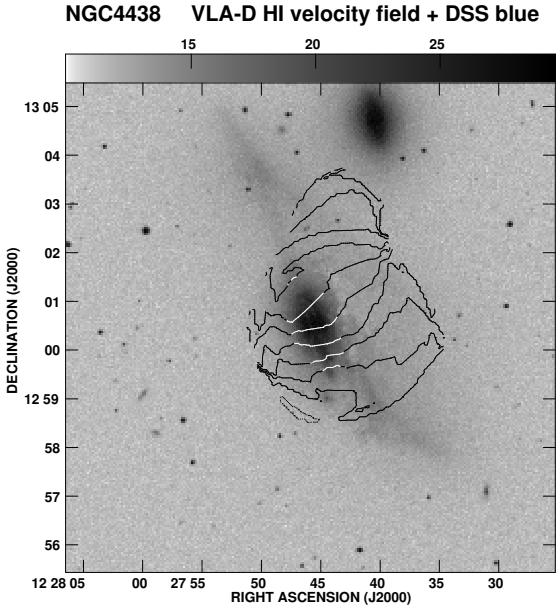

Figure 4.19: The corresponding moment one image showing the velocity field. Contour levels from south to north are -5, 20, 40, 60, 80, 100, 120, 140, 160, 180 and 190 km s^{-1}.

is detected which is most prominent in the velocity channel of $\sim$−9.5 km s^{-1}.

Moment maps of NGC4438 were made with a cutoff at 4σ and integrated in velocity from 238 to −71 km s^{-1} (Fig. 4.18, 4.19, 4.20). The HI total-intensity image with an angular resolution of 127×124 $arcsec^2$ looks resolved with an extension towards the north. The northern clump seen in the full-resolution D-array image is coincident with this extension. In the tapered image the disk emission, the extra-planar elongated structure and the southern and northern clumps appear blended with more diffuse HI gas. The iso-velocity contours appear to exhibit an interesting pattern with the contours on the southern side of the diffuse extra-planar emission being curved upwards while those on the northern side being curved downwards. The velocity contours in the southern side of the disk are approximately parallel

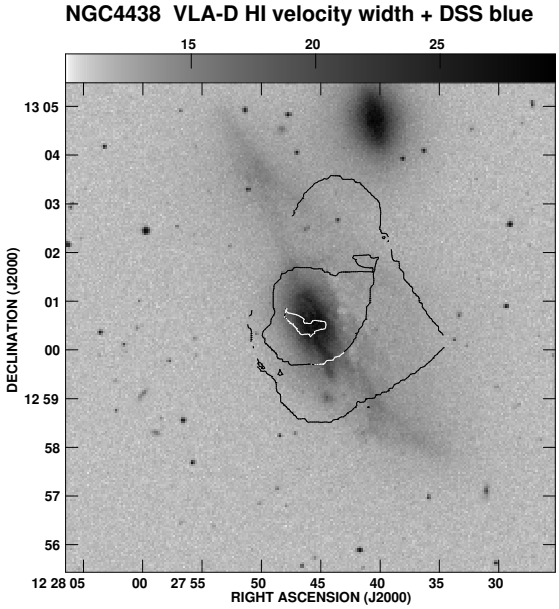

Figure 4.20: The corresponding moment two map showing the velocity dispersion. Contour levels are 20, 55 and 70 km s^{-1}.

to each other along a PA of $\sim -80°$ while those on the northern side are oriented along a PA of $\sim -45°$. The velocity in the disk ranges from +20 to 140 km s^{-1} with a velocity gradient of 0.9 km s^{-1} arcsec^{-1}. The extra-planar gas including the the northern extension has velocities ranging from $\sim$20 to $\sim$190 km s^{-1} yielding an average velocity gradient of $\sim$0.5 km s^{-1} arcsec^{-1}. At this resolution the HI gas in the disk as well as the extended emission on the western side are rotating about a heliocentric velocity of $\sim$110 km s^{-1} about an axis which is at a PA of $-48°$. The isovelocity contours of the extra-planar gas seen in this tapered image appear to symmetrically curve inwards about this axis, while in the full-resolution image they appear to diverge closer to the interface between the disk and the extra-planar gas. In a detailed study of the galaxy NGC4522 in the Virgo cluster which has been affected by ram-pressure stripping the HI observations (Kenney, van

Gorkom & Vollmer 2004) show a similar divergence of the isovelocity contours, which could be due to the extra-planar gas rotating slower than the disk. Kenney et al. also notes that the iso-velocity contours curve inwards in the south-western side at larger distances from the disk. Some evidence of similar diverging iso-velocity contours are also seen in the galaxy NGC2820, which is affected by ram pressure stripping due to the intra-group medium (Kantharia et al. 2005; Chapter 5). The moment 2 map shows that the width of the HI line changes from ∼20 km s^{-1} in the outer regions to ∼87 km s^{-1} near the centre of the galaxy.

IC3355

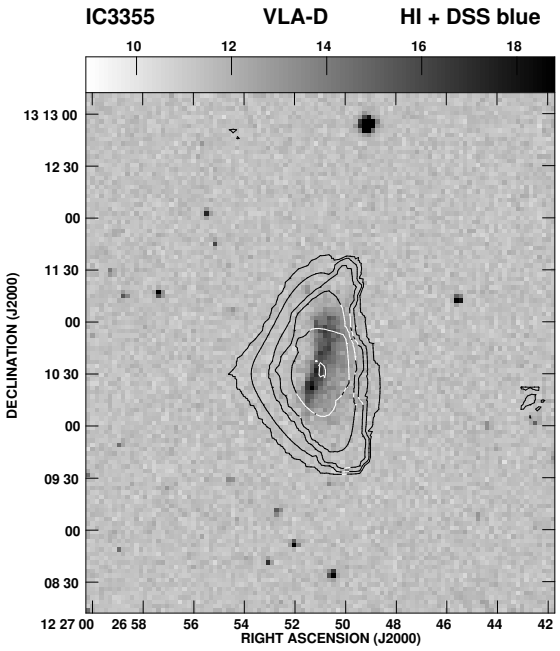

Figure 4.21: The total-intensity HI emission contour of IC3355, observed with the VLA D-array with an angular resolution of ∼53 arcsec has been superimposed on the DSS blue-band image. Contour levels: 3.84,5.45,7.69 ... 10^{19} atoms cm^{-2} in steps of multiples of $\sqrt{2}$.

IC3355 (VV 511, DDO 124, VCC 0945) is an irregular galaxy which is listed in the atlas of interacting galaxies by Vorontosov-Velyaminov (1977) who also note the presence in its tail of '3 diffuse companions in a blue haze'. The B-band image shows a number of compact star-forming regions towards the eastern side of the galaxy. Spectroscopic observations at both radio and optical wavelengths listed in NED, the HyperLeda (http://leda.univ-lyon1.fr; Paturel et al. 2003) and GOLDmine (http://goldmine.mib.infn.it; Gavazzi et al. 2003) data bases and available information in the literature show the presence of two systems, one with a heliocentric velocity of $\sim$−10 km s^{-1} and the other at a heliocentric velocity of $\sim$162 km s^{-1} (de Vaucouleurs, de Vaucouleurs & Nieto 1979; Sulentic 1980; Haynes & Giovanelli 1986; Hoffman et al. 1987; Cayatte et al. 1990; Huchra 1995; Gavazzi et al. 2004). At radio wavelengths Haynes & Giovanelli (1986) report the detection of a weak feature at 162 km s^{-1} and note that the 'spectrum in severely blended with local HI emission'. They have however proposed a detection because 'no emission at the velocities associated with the galaxy is seen in frequency switched spectra taken at 10′ offsets'. Hoffman et al. (1987) and Cayatte et al. (1990) have reported the detection of HI emission at a heliocentric velocity of −9 and −12 km s^{-1} respectively.

The channel maps (Fig. 4.17) from the VLA D-array data clearly show the detection of HI emission at a position of RA 12^h 26^m $51.^s1$, Dec +13° 10′ 33″, which is coincident with the position of the optical galaxy: RA 12^h 26^m $51.^s13$, Dec +13° 10′ 32.″6 (Yasuda, Ohamura & Fukugita 1995). In Fig. 4.17 HI emission is detected in the channels with velocities of 11.1, −9.5 and −30.1 km s^{-1}, but no emission is detected in the channels with velocities of 176.1 and 155.5 km s^{-1}, which are closest to the velocity system at 162 km s^{-1}.

At this resolution of ∼125 arcsec the primary beam corrected total HI flux density is 5.47 Jy km s^{-1} estimated from the global profile (Fig. 4.11) and corresponds to a total mass of 3.72×10^8 $M_\odot$ for IC3355. A full-resolution VLA D-array image of IC3355 (Fig 4.21) shows the emission to be elongated approximately in the north-south direction, similar to that of the galaxy and consistent with the structure reported by Cayatte et al.(1990) with an angular resolution of 21×17 $arcsec^2$ along a PA of 75° obtained by combining VLA C- and D-array data. The western side of the HI gas a sharp gradient but with the emission on the northern and southern extremeties bending marginally towards the west. The image presented by Li & van Gorkom (2001) detects extended emission on the western side which is not seen in either our image or that of Cayatte et al., possibly due to lower sensitivity. The detailed structure of the HI gas is possibly due to a combination of ram pressure and tidal interactions if IC3355 along with NGC4438, NGC4406 (M86) and NGC4402 constitute a small group of galaxies falling into the Virgo cluster (see Kotani & Ekers 1983; Elmegreen et al. 2000) and the two optical velocity systems represent two interacting galaxies.

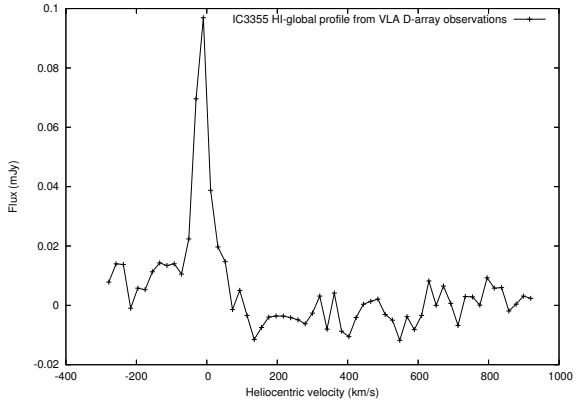

Figure 4.22: The Primary beam corrected HI emission spectra of IC3355

An HI-tail

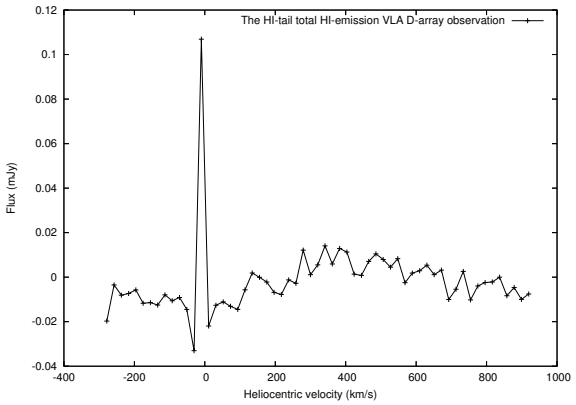

Figure 4.23: The Primary beam corrected HI emission spectra of the possible HI tail.

The channel maps at -9.5 and -30.1 km s^{-1} show extended diffuse emission which is seen most prominently at -9.5 km s^{-1} and appears like a tail of HI emission extending for $\sim$15 arcmin. It is of interest to note that the HI emission from the galaxy IC3355 is also strongest in the velocity channel of -9.5 km s^{-1} which is close to its optical velocity of -10 km s^{-1}. This suggests that the tail of HI emission is likely to be of extragalactic origin rather than being Galactic foreground emission. Also, deep optical images of the sources around NGC4438 (Phillips & Malin 1982; Katsiyannis et al. 1998) show a stellar tail extending towards the north west. The north-western stellar tail is similar in extent and location to the HI tail we have imaged, although there is an offset of $\sim 1'$ between the positions of the stellar and HI tails. Such offsets have been noted in the HI images of interacting galaxies by Hibbard, Vacca & Yun (2000) who attribute such differences to ram pressure by the ICM and/or ionisation by the stellar tail or extinction by the gas.

The HI tail could be debris of tidal interaction, ram pressure stripped gas or intergalactic HI in the Virgo cluster medium (see Bekki, Koribalski

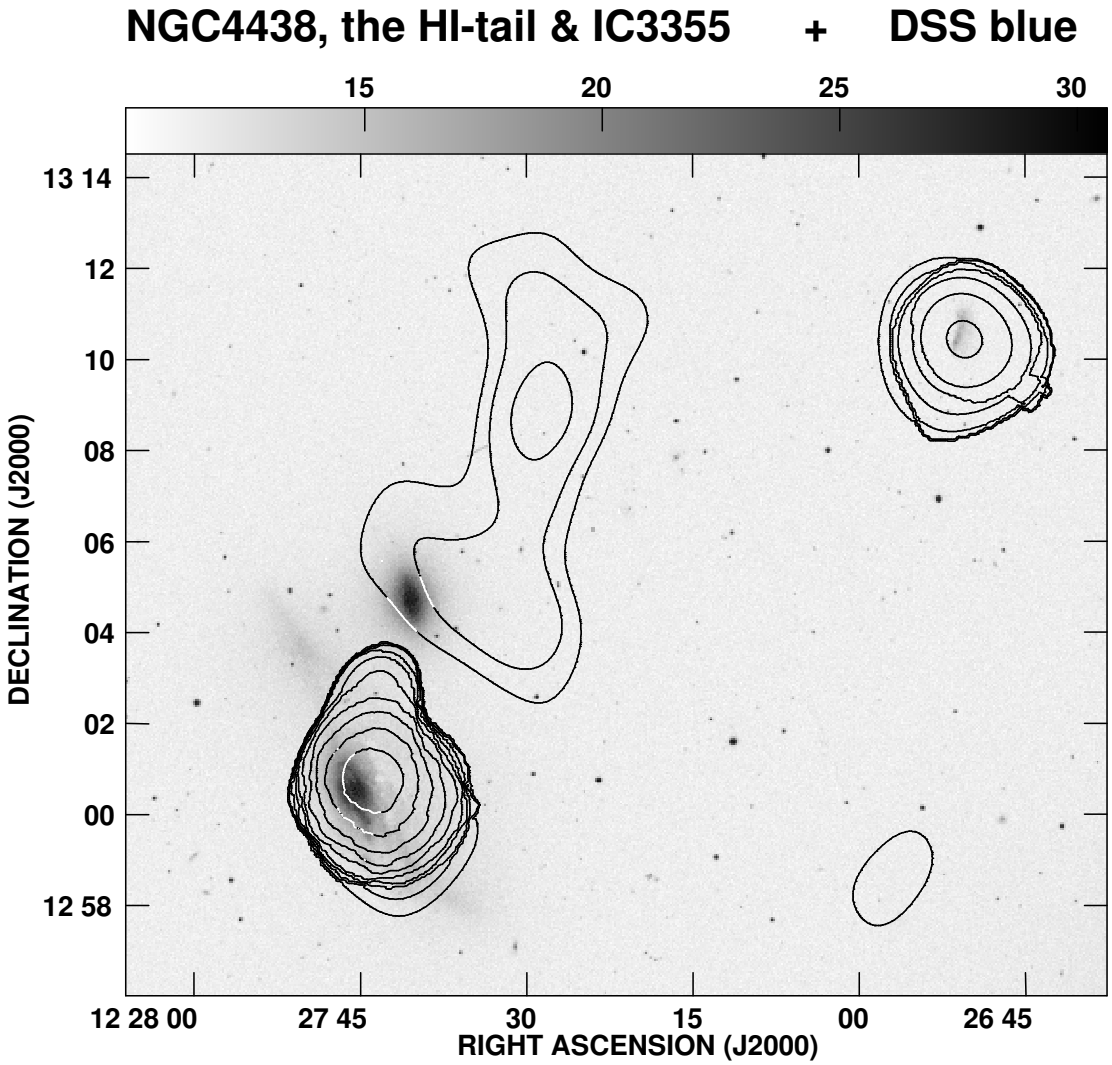

Figure 4.24: The total-intensity contours of HI emission the possible tail and the galaxies NGC4438 and IC3355. Contours levels are 1.13, 1.60 and 2.27 ... 10^{19} atoms cm^{-2} in steps of multiple of $\sqrt{2}$.

& Kilborn 2005). For a distance of 17 Mpc for the Virgo cluster, the total length of 15 arcmin implies that the linear size of the tail is ∼75 kpc, which is somewhat smaller than the tail of HI emission in NGC4388 which extends

for ∼110−125 kpc (Oosterloo & van Gorkom 2005). For a transverse velocity of 1200 km s^{-1} and a length of 75 kpc, the dynamical time scale of the tail is ∼60 Myr compared with ∼100 Myr for the tail of NGC4388. The line flux of the tail in the velocity channel of −9.5 km s^{-1} is 2 Jy km s^{-1} yielding a mass of $\sim 1.36\times10^{8}$ $M_{\odot}$.

4.6 Discussion and concluding remarks

(a) The double-lobed radio source

Our detection of an inverted-spectrum nuclear component confirms that the small double-lobed radio source with a scale size of ∼1 kpc is due to an AGN rather than a starburst, consistent with earlier suggestions from X-ray observations (Machacek et al. 2004). From a compilation of the structures of nearby galaxies with a starburst or/and an AGN, Hota & Saikia (2006; Chapter 3) have suggested that such bubble- or lobe-like radio structures are likely to be seen in sources with an AGN rather than a starburst. One of the most striking aspects of the structure on scales of ∼1 kpc is the shell-like structures seen also in Hα and X-ray wavelengths on opposite sides of the nucleus, closely related to the radio structure. The Hα and X-ray emission possibly arise in regions where the bubbles of synchrotron-emitting plasma interact with the surrounding ISM.

The radio lobes are very asymmetrically located with the ratio of separations of the eastern lobe from the nucleus to that of the western one being ∼3, while the corresponding flux density ratio is ∼0.60 and 0.57 at 1.4 and 5 GHz respectively. A higher density on the western side where the ISM of

NGC4438 appears displaced could provide a viable explanation of the asymmetry in location relative to the nucleus. The lobe on the denser side is also expected to be more luminous due to a higher efficiency of conversion of beam energy into radio emission, and better confinement of the radio lobe (cf. Eilek & Shore 1989). However, this simple scenario does not provide a natural explanation for the western lobe which is nearer and brighter to be also larger in size by a factor of $\sim$2.

A possible solution to this inconsistency comes from the results of numerical simulations of propagation of jets. Hydrodynamic simulations of light, large-scale jets in a decreasing density profile, which have also been examined by Carvalho & O'Dea (2002), show that the jet bow shock undergoes two phases, first a nearly spherical one and secondly the well-known cigar-shaped one (Krause 2002; Krause & Camenzind 2002). The shell-like structure of the western lobe is suggestive of the first phase of the development of the bow-shock. In this scenario, the western jet has not yet entered the cigar phase, and deposits its radio-emitting plasma in a bigger part of the bubble, almost filling the region within the bounds of the bow shock. On the other hand, the eastern jet appears to be in the cigar phase and should therefore have a fairly regular backflow around it, which flows back into the central parts diffusing and mixing with the shocked external gas.

For a galaxy moving with a velocity of $\sim$1000 km s^{-1} through the Virgo cluster ram pressure could also affect the observed structure of the source. Using plausible values from Combes et al. (1988) and Vollmer et al. (2005) the ram pressure is approximately few times 10^{-11} dynes cm^{-2}. For comparison the pressure in the eastern and western lobes are $\gtrsim 10^{-10}$ dynes cm^{-2} significantly larger than the ram pressure, while the pressure in the interlobe

region is comparable to that of ram pressure. The lobes of emission are unlikely to be significantly affected by ram pressure due to the motion of the galaxy.

(b) The HI gas

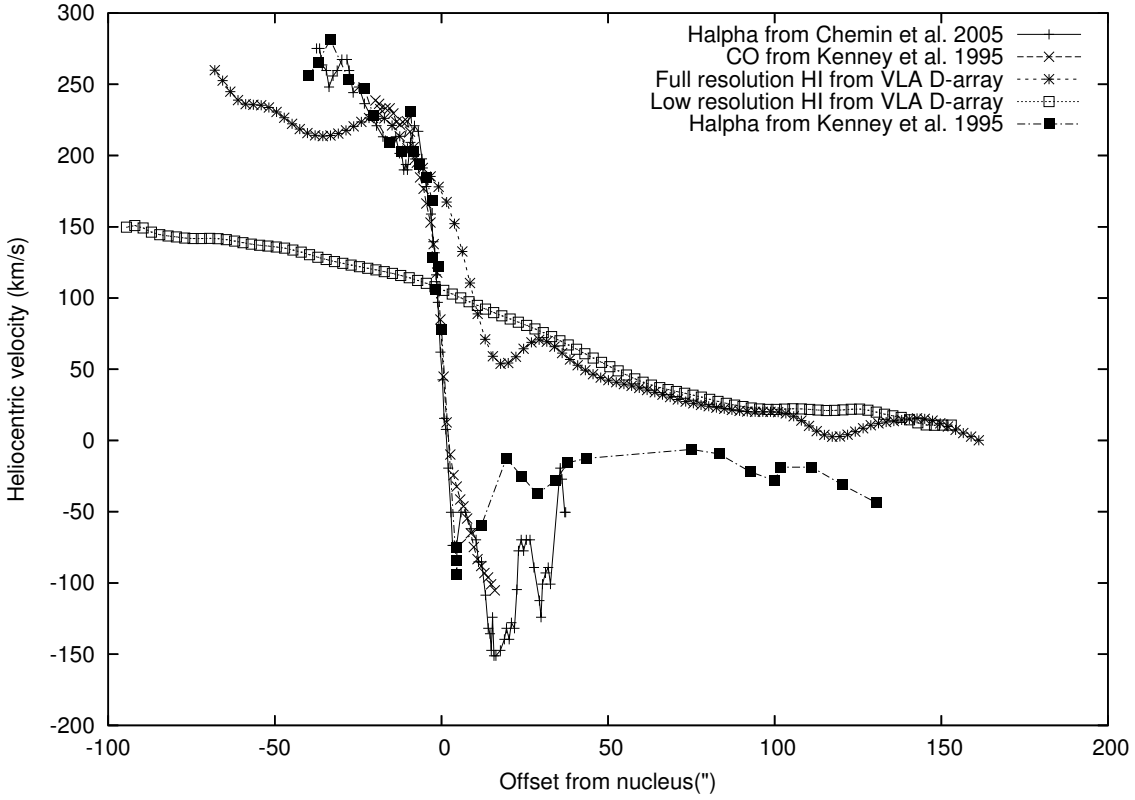

Figure 4.25: The velocity curves along the disk for CO and Hα emission from Kenney et al. (1995) and Hα emission from Chemin et al. (2005) compared with the values for HI emission from our observations with angular resolutions of $\sim$60 and 120 arcsec. The PA for CO emission is along 27° while for the Hα and Hsc i emission the PA is along 29°.

The GMRT and VLA observations show the structure of HI emission from both the disk and extra-planar gas associated with NGC4438, HI emission from IC3355 and a 'tail' of HI gas extending for $\sim$15′ which is possibly in

the Virgo cluster rather than being foreground Galactic emission. The extra-planar HI gas in NGC4438 has an approximately linear structure with a total size of ∼9.8 kpc and displaced from the disk by ∼4.1 kpc. The elongated HI structure overlaps with the CO extra-planar emission but has a larger length than the CO feature which has been reproduced in simulations involving both tidal interactions and ram pressure stripping by the ICM of the Virgo cluster with ISM-ISM interactions between NGC4438 and NGC4435 playing a relatively minor role (Vollmer et al. 2005). The isovelocity contours in the extra-planar gas appear to initally diverge while at larger heights they curve inwards. These features are somewhat similar to that of the galaxy NGC4522 also in the Virgo cluster, which has been interpreted to be due to ram-pressure stripping. The VLA D-array full-resolution image shows a region of closed velocity contours where the gas appears to deviate from the overall rotation and approaches us. A similar feature is also seen in the Hα observations at a similar location but with a much higher approaching velocity (Chemin et al. 2005). There is an X-ray source at this location and it is tempting to speculate that the outflowing gas may be related to energy released from the X-ray source. The high velocity dispersion of the HI gas in this location would be consistent with such an interpretation.

The HI emission in the direction of the disk appears to be rotating more slowly than the CO and Hα emission A comparison of the HI velocity field along a PA of 29° and passing through the nucleus of the galaxy with that of CO and Hα emission along PAs of 29° and 27° respectively (Kenney et al. 1995) are presented in Fig. 4.25. The CO and Hα axes considered by Kenney et al. also pass through the nucleus of the galaxy estimated from optical and infrared observations (Clements 1983; Keel & Wehrle 1993) whose position is within 1 arcsec of the radio nucleus. It is relevant to note that

these observations are of significantly different angular resolutions with the optical observations having a seeing of 1.5−2 arcsec, the CO observations having an angular resolution of ∼6 arcsec while the HI images have angular resolutions of ∼60 and 120 arcsec for the full-resolution and tapered images respectively. In Fig. 4.25 we have also shown the velocities of the Hα gas obtained by Chemin et al. (2005) along a PA of 29° from Fabrey-Perot spectroscopic observations. As noted by Kenney et al. the CO and Hα velocities are symmetric and in good agreement within a galactocentric radius of ∼10 arcsec. Beyond this distance, the velocities become asymmetric with the CO velocities on the north-eastern side increasing to ∼240 km s^{-1} at ∼20 arcsec from the nucleus while the Hα velocities increase to ∼275 km s^{-1} at ∼40 arcsec from the nucleus. On the south-western side the CO extends to ∼15 arcsec with a minimum blue-shifted velocity of −105 km s^{-1} but the Hα gas seen by Kenney et al. extends up to ∼130 arcsec with a nearly constant velocity of ∼−20 km s^{-1}. The velocities obtained by Chemin et al. (2005) are very similar to those of Kenney et al. on the north-eastern side, but goes to significantly higher blue-shifts of ∼−150 km s^{-1} approximately 15 arcsec south-west of the nucleus. The HI data with a full-resolution of ∼60 arcsec exhibits a somewhat similar pattern but with significantly different velocities particularly on the south-western side. The velocity of the HI gas on the north-eastern side is ∼260 km s^{-1} at ∼70 arcsec from the nucleus, while on the south-western side it decreases slowly from ∼70 km s^{-1} at ∼30 arcsec to ∼0 at 160 arcsec from the nucleus. It is seen that the HI velocities on the south-western side are systematically higher typically by ∼50 km s^{-1}. On the north-eastern side the difference in velocity between HI and Hα is less pronounced with the HI being lower by a maximum value of ∼50 km s^{-1} at ∼30 arcsec from the nucleus. Tapering the HI data to an angular

resolution of 120 arcsec makes no major difference to the velocity on the south-western side but decreases the velocity on the north-eastern side by $\sim$100 km s^{-1}. These velocity curves show that the velocity range seen in HI is significantly smaller than what has been observed in CO and Hα, with the difference being even more marked when one considers the tapered HI image. These observations suggest that the observed HI gas is rotating more slowly than the Hα and CO gas. The significant drop in the HI velocity on the north-eastern side with coarser resolution is due to extra-planar gas which has lower velocities than the disk emission, is stronger and not resolved from the disk HI emission.

References

Allen R.J., Ekers R.D., Burke B.F., Miley G.K., 1973, Nature, 241, 260

Bell A.R., 1978, MNRAS, 182, 147

Baars J.W.M., Genzel R., Pauliny-Toth I.I.K, Witzel A., 1977, A&A, 61, 99

Becker R.H., White R.L., Edwards A.L., 1991, ApJS, 75, 1

Bekki K.; Koribalski B.S., Kilborn V.A., 2005, MNRAS, 363, 21L

Boselli A., et al., 2005, ApJ, 623L, 13

Carvalho J.C., O'Dea C.P., 2002, ApJS, 141, 371

Cayatte V., Kotanyi C., Balkowski C., van Gorkom J. H., 1994, AJ, 107, 1003

Cayatte V., van Gorkom J. H., Balkowski C., Kotanyi C., 1990, AJ, 100, 604

Chemin L., et al., 2005, A&A, 436, 469

Clements E.D., 1983, MNRAS, 204, 811

Combes F., Dupraz C., Casoli F., Pagani L., 1988, A&A, 203L, 9

Crowl H.H., Kenney J.D.P., van Gorkom J.H., Vollmer B., 2005, AJ, 130, 65

Duric N., 1986, ApJ, AJ, 115, 1603

Duric, N., 1991, in Duric N., Crane P., eds, ASP Conf. Ser Vol. 18, The Interpretation of Modern Synthesis Observations of Spiral Galaxies. ASP., San Francisco, p. 17

Duric N., Irwin J., & Bloemen H., 1998, A&A, 331, 428

de Vaucouleurs G., de Vaucouleurs A. & Nieto J.-L., 1979, AJ, 84, 1811

Eilek J.A., Shore S.N., 1989, ApJ, 342, 187

Elmegreen D.M., Elmegreen B.G., Chromey F.R., Fine M.S., 2000, AJ, 120, 733

Falco, E.E. et al., 1999, PASP, 111, 438

Gavazzi G., Zaccardo A., Sanvito G., Boselli A., Bonfanti C., 2004, A&A, 417, 499

Giovanardi C., Krumm N. & Salpeter E.E., 1983, AJ, 88, 1719

Gavazzi et al., 2003, astro-ph/0401636

Haynes M.P., & Giovanelli R., 1986, ApJ, 306, 466

Hoffman G.L., Helou G., Salpeter E.E., Glosson, J., Sandage A., 1987, ApJS, 63, 247

Hota A., Saikia D.J., 2005, MNRAS, 356, 998 (Chapter 2)

Hota A., Saikia D.J., 2006, MNRAS, (in press; Chapter 3)

Huchra, John P.; Geller, Margaret J., Corwin H.G. Jr., 1995, ApJS, 99, 391

Irwin J.A., Saikia D.J., 2003, MNRAS, 346, 977

Hibbard J.E., Vacca W.D., Yun M.S., 2000, AJ, 119, 1130

Hummel E., Saikia D.J., 1991, A&A, 249, 43

Irwin J.A., 1991, in The Interpretation of Modern Synthesis Observations of Spiral Galaxies; ASP Conf. Proc., 18, 591

Kantharia N.G., Ananthakrishnan S., Nityananda R., Hota A., 2005, A&A, 435, 483 (Chapter 5)

Katsiyannis A.C., Kemp S.N., Berry D.S., Meaburn J., 1998, A&AS, 132, 387

Keel W. C., Wehrle A. E., 1993, AJ, 106, 236

Kenney J. D. P., Rubin V. C., Planesas P., Young J. S., 1995, ApJ, 438, 135

Kenney J. D. P., Yale E. E., 2002, ApJ, 567, 865

Kenney J.D.P., van Gorkom J.H., Vollmer B., 2004, AJ, 127, 3361

Kotanyi C.,van Gorkom J. H., Ekers R. D., 1983, ApJ, 273L, 7

Kotanyi C.G., Ekers R.D., 1983, A&A, 122, 267

Krause M., 2002, A&A, 386, 1L

Krause M., Camenzind M., 2002, in Collin S., Combes F., Shlosman I., Active galactic nuclei: from central engine to host galaxy, ASP conference series, 290, 42

Lee, S.-W. et al. 2001, A&A, 377, 759

Li Y., van Gorkom J.H., 2001, in Gas and Galaxy Evolution, eds J.E. Hibbard, M. Rupen and J.H. van Gorkom, ASP Conf. Proc., 240, 637

Machacek M. E., Jones C., Forman W. R., 2004, ApJ, 610, 183

Niklas S., Klein U., Wielebinski R., 1995, A&A, 293, 56

Phillips M.M. & Malin D.F., 1982, MNRAS, 199, 905

Stone J.L. Jr., Wilson A.S., Ward M.J., 1988, ApJ, 330, 105

Sulentic J.W., 1980, ApJ, 241, 67

Vollmer B., Thierbach M., Wielebinski R., 2004a, A&A, 418, 1

Vollmer B., Beck R., Kenney J.D.P., van Gorkom J.H., 2004b, AJ, 127, 3375

Vollmer B., Braine J., Combes F., Sofue Y., 2005, A&A, 441, 473

Vollmer B., Soida M., Otmianowska-Mazur K., Kenney J.D.P., van Gorkom J.H., Beck R., 2006, astro-ph/0603854

Yasuda N., Okamura S., Fukugita M., 1995, ApJS, 96, 359

CHAPTER 5

GMRT observations of the group Holmberg 124: evolution by tidal forces and ram pressure?

5.1 Abstract

A radio study of the group Holmberg 124 (Ho 124) comprising four late type galaxies, namely NGC2820, Mrk 108, NGC2814 and NGC2805, using the GMRT was initiated by Ananthakrishnan, Kantharia & Nityananda (2003) as part of an ongoing study of radio emission from disk galaxies. This work was extended upon and later reported by Kantharia, Ananthakrishnan, Nityananda & Hota (2005). This chapter presents the results reported by Kantharia et al. (2005) where my contribution has been mainly on the interpretation of the observations. The galaxies, NGC 2820, Mrk 108 and NGC 2814 have clearly undergone tidal interactions. We also note various features in the group members which might be due to ram pressure.

In this chapter, four interesting results emerging from these observations are described: **a)** detection of the tidal radio continuum bridge at 330 MHz connecting the galaxies NGC 2820+Mrk 108 with the galaxy NGC 2814. The radio bridge was discovered at 1465 MHz by van der Hulst & Hummel (1985). The radio bridge has a fairly steep spectrum with a spectral index α ($S \propto \nu^{\alpha}$) of $-1.8^{+0.3}_{-0.2}$ which is much steeper than the -0.8 quoted by van

der Hulst & Hummel (1985). **b)** Detection of other tidal features like the tilted HI and radio continuum disk of NGC 2814, a HI streamer and a radio continuum tail arising from the south of NGC 2814. We also report the detection of a possible tidal dwarf galaxy in HI. **c)** Sharp truncation in the HI distribution in the south of NGC 2820 and in the HI and radio continuum distribution in the north of NGC 2814. The optical disks in both the cases look undisturbed. As pointed out by Davis et al (1997), ram pressure affects different components of the ISM in varying degrees. Simple estimates of pressure in different components of the interstellar medium (radio continuum, Hα and HI) in NGC 2820 indicate that ram pressure will significantly influence HI. **d)** Detection of a large one-sided HI loop to the north of NGC 2820. No radio continuum emission or Hα emission is associated with the HI loop. We discuss various scenarios for the origin of this loop including a central starburst, ram pressure stripping and tidal interaction. We do not support the central starburst scenario since it is not detected in ionized gas. Using the upper limit on X-ray luminosity of Ho 124 (Mulchaey et al. 2003), we estimate an upper limit on the IGrM density of 8.8×10^{-4} cm^{-3}. For half this electron density, we estimate the ram pressure force of the IGrM to be comparable to the gravitational pull of the disk of NGC 2820. Since tidal interaction has obviously influenced the group, we suggest that the loop could have formed by ram pressure stripping if tidal effects had reduced the surface density of HI in NGC 2820.

From the complex observational picture of Ho 124 and the numerical estimates, we suggest that the evolution of the Ho 124 group may be governed by both tidal forces due to the interaction and the ram pressure due to motion of the member galaxies in the IGrM and that the IGrM densities should not be too low (i.e. $\geq 4 \times 10^{-4}$). However this needs to be verified by other

observations.

5.2 Introduction

In an ongoing project of studying the radio emission from disk galaxies using the GMRT, the poor group of galaxies known as Ho 124 has been observed. Ho 124 consists of four galaxies: an inclined SBc galaxy, NGC 2820 (UGC 4961), a Markarian galaxy, Mrk 108 (NGC 2820a), an IO galaxy, NGC 2814 and an almost face-on Sc galaxy, NGC 2805 (UGC 4936). Since the first three galaxies lie within a few arc minutes of each other, we refer to them as the triplet in the chapter. NGC 2805 lies about $8'$ to the south-west of the triplet.

This group is an interesting multiple interacting system. It was the first system in which a radio continuum bridge was detected (van der Hulst & Hummel 1985). Although HI bridges and optical bridges had long before been detected, no radio continuum emission had been detected leading to the belief that magnetic fields play little role in confining the bridges. Since then many other interacting galaxies have shown the presence of radio bridges, e.g. the Taffy galaxies (Condon et al. 1993). Bridges, tails and arcs have been detected from many other interacting systems. Following Toomre & Toomre (1972), two long tails are expected if two galaxies of comparable masses interact A bridge extending from one galaxy to other is expected if one galaxy is massive and the other has a fraction of mass of the massive partner

Many of the interacting systems occur in groups of a few galaxies, also known as poor groups. Moreover, although the gravitational interaction and

ram pressure stripping of gas in members of clusters has been fairly well-studied, less is known about these processes in groups. The IGrM densities are at least an order of magnitude lower than the intracluster medium (ICM). Hence, processes like ram pressure stripping and galaxy harrassment which play an important role in the cluster evolution are not expected to be important in groups (Mulchaey 2004). The first X-ray detection of the IGrM was made only a decade ago by Mulchaey et al. (1993). A more extensive X-ray survey of groups using ROSAT data was carried out by Mulchaey et al. (1996) from which emerged the result that groups with at least one early-type galaxy have higher X-ray luminosities than groups with only late-type galaxies. Mulchaey et al. (1996) gave some possible reasons including that the IGrM of groups with only late-type members had either lower temperatures or lower densities. In this chapter, we present radio continuum observations at 240, 325, 610 and 1280 MHz and HI 21 cm observations using GMRT of one such group Ho 124 which consists of only late-type galaxies. No X-ray emission was detected from this group by Mulchaey et al. (1996, 2003). We show that the IGrM densities in the group Ho 124 consistent with this upper limit could still be sufficient to determine the evolution of the members via ram pressure stripping.

Additionally, we report the detection of a tidal bridge connecting the triplet in radio continuum at 325 MHz and marginal detection at 240 MHz and 610 MHz. We also detect HI 21 cm emission from the bridge and a large one-sided HI loop to the north of NGC 2820. Bosma et al. (1980) have studied this group in radio continuum, 21cm HI and in the optical band whereas Artamonov et al. (1994) have studied the group using UBV photometry. Optical properties of the group members can be found in Table 1 of Bosma et al. (1980) and in Table 1 of Artamonov et al. (1994).

The plan of the chapter is as follows. In Section 2, we discuss the observations, data analysis and results. In Section 3, we discuss the various morphological features in the group which we believe are due to the tidal interaction and in Section 4, discuss various possible scenarios for the origin of the HI loop in NGC 2820. In Section 5, we present a discussion of our results and in Section 6 we present a summary.

Bosma et al. (1980) have used a distance of 24 Mpc to the group based on the mean heliocentric radial velocity of 1670 $\mathrm{km\,s^{-1}}$ and a Hubble constant of 75 $\mathrm{km\,s^{-1}\ Mpc^{-1}}$. At this distance, $1'$ corresponds to 7 kpc. We use the Bosma et al. (1980) values in the chapter.

5.3 Observations, data analysis and results

(a) Radio continuum

The multi-frequency radio observations at 240, 330, 610 and 1280 MHz were conducted using the GMRT (Swarup et al. 1991, Ananthakrishnan & Rao 2002) which consists of 30 antennas of 45m diametre each scattered over a 25 km region. The observational details are listed in the first four columns of Table 5.1. These observations followed the sequence of interspersing 20 minutes on-source scans by a 5 minutes scan on the phase calibrator. The bandpass-cum-amplitude calibrator (3C 147) was observed in the beginning and at the end for half an hour each.

The data was imported as a FITS file to NRAO AIPS software for further analysis. The general procedure followed at all bands included editing out corrupted data, gain calibration of one spectral channel data, bandpass calibration and channel averaging to obtain the continuum database. These

Table 5.1: Observation details

Table 1: Observation Details

Parameter	1280 MHz	610 MHz	330 MHz	240 MHz	HI
Date of observation	16/7/2002	6/9/2002	19/8/2002	6/9/2002	28/10/2003
On-source telescope time	4 hrs	2.5 hrs	3.3 hrs	2.5 hrs	5 hrs
Effective bandwidth	9.3 MHz	4 MHz	9.3 MHz	4 MHz	64 kHz
Phase calibrator	0834+555	0834+555	0834+555	0834+555	0834+555
Flux density of ph cal	8.4 ± 0.13 Jy	8.05 ± 0.15 Jy	9.36 ± 0.25 Jy	9.1 ± 0.3 Jy	7.01 ± 0.25 Jy
Synthesized beam[1]	$19.9'' \times 14.1''$ & $6.5'' \times 4.7''$	$21.9'' \times 13''$	$19.9'' \times 14.1''$	$32.9'' \times 14''$	$16.2'' \times 15.2''$
PA	$49°.1$ & $46°.2$	$69°.9$	$49°.1$	$82°.1$	$25°.8$
Continuum/line rms	0.09 mJy/b & 0.08 mJy/b	0.4 mJy/beam	1 mJy/beam	1.9 mJy/beam	0.2 mJy/beam

[1] this is the effective beamwidth of the images used in the paper and in most cases is larger than the best achievable.

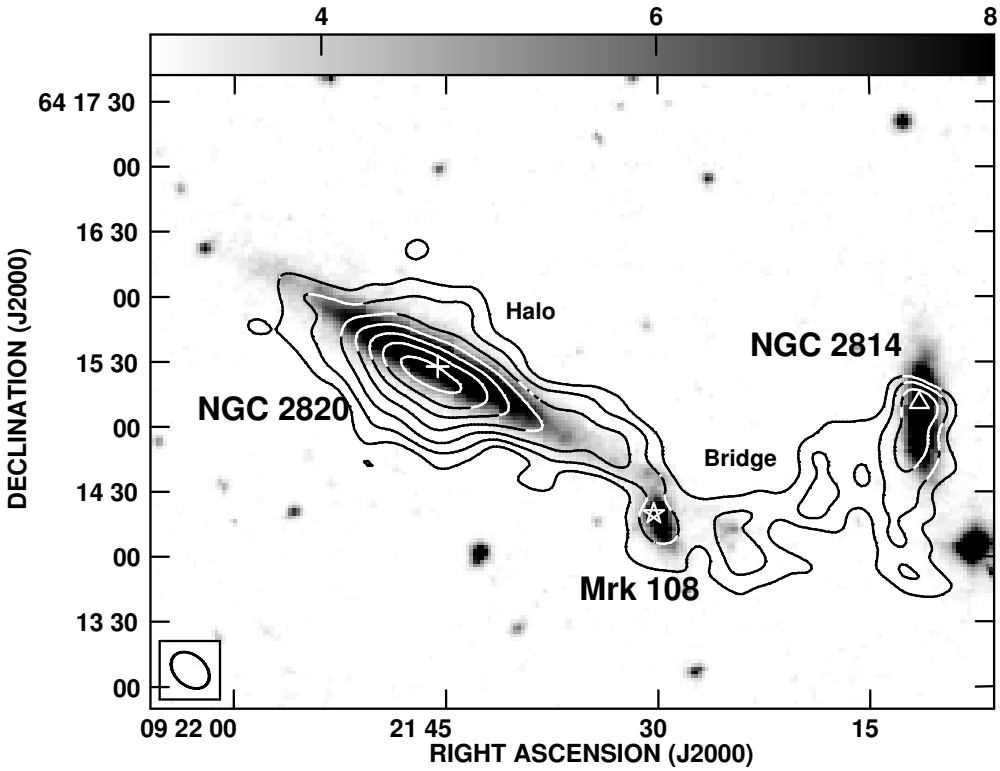

Figure 5.1: **(a)** 330 MHz radio continuum contours superposed on the DSS grey scale image. Note the bridge connecting the triplet and the halo emission. The angular resolution of the image is $19.9'' \times 14.2'', PA = 49°.1$ and rms noise is 1 mJy/beam. The first contour is plotted at 3 mJy/beam and then contours increase in steps of $\sqrt{2}$. The optical centres of the three galaxies are marked by a symbol.

were then imaged and CLEANed to obtain the final image. Wide-field imaging was used at 610, 330 and 240 MHz. We divided the primary beam into 9 facets for 610 MHz, and into 25 facets at 330 MHz and 240 MHz. The data were also 3-d self-calibrated. We used a uv taper of $12k\lambda$ and a uv range of $15k\lambda$ with robust weighting (ROBUST=0). Natural weighting did not seem to improve the image quality at these three frequencies, but degraded the beam and hence was not used. The 330 MHz and 240 MHz images are dynamic range limited. We have obtained a dynamic range of 2500 at 330 MHz. At 1280 MHz, a maximum uv baseline of 60 $k\lambda$ was used with natural weighting. We expect the flux density errors at all frequencies to be less than 10 %. All the images have been corrected for the gain of the primary beam.

The low resolution image at 330 MHz clearly showing the bridge and the high resolution image at 1280 MHz showing fine structure in the galaxies are shown in Fig 5.1. The images at 240 and 610 MHz look fairly similar to the 330 MHz map and hence are not presented. We have used maps of similar resolution at 610 MHz and 330 MHz for estimating the spectral index.

We have detected the triplet in radio continuum at all the observed frequencies. Additionally, a bridge connecting the triplet is also detected at 330 MHz. This bridge was first reported by van der Hulst and Hummel (1985) at 1465 MHz. We have marginal detection of the bridge at 610 and 240 MHz. We have verified that although some short spacings are missing at 1280 MHz, this does not completely resolve out the bridge. However, alongwith the low brightness sensitivity, this made it difficult to detect the bridge with the present data. Faint radio emission is detected at 330 MHz from NGC 2805 (see Fig 5.5 (b)). This emission bears little resemblance to the optical emission (see Fig 5 (b)).

The radio centre of NGC 2820, an almost edge-on galaxy with inclination

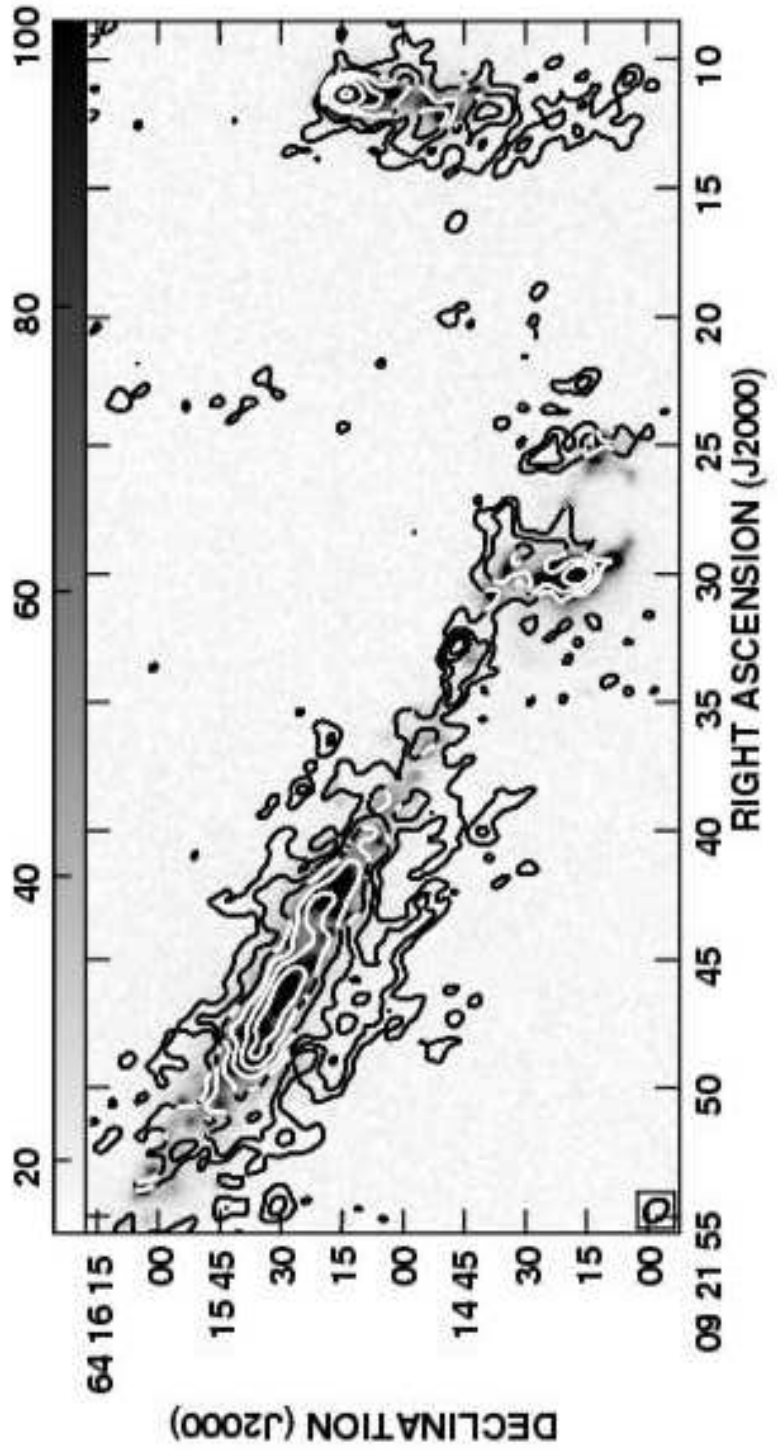

Figure 5.1: **(b)** High resolution image of the group at 1280 MHz in contours is superposed on the Hα emission represented by the grey scale. The angular resolution of the radio image is $6.54'' \times 4.70''$, PA $= 46.21^\circ$ and rms noise is 80μJy. The first contour is at 0.27 mJy/beam and then contours increase in steps of $\sqrt{2}$. The Hα image is from Gil de Paz et al. (2003).

Table 5.2: Radio flux densities of the triplet

	Galaxy	S mJy at ν MHz			α_{610}^{330}
		1280[1]	610	330	
1	NGC 2820+	35	116	227	−1.06
	Mrk 108		(4)	(4)	
2	NGC2820		19.9	27	−0.5
	peak		(0.7)	(1)	
3	NGC 2814	6.7	19	42	−1.25
		(1.6)	(4)	(6)	
4	NGC 2814		5.2	7.5	−0.6
	peak		(0.7)	(1)	

[1] the flux density of NGC 2820 at 1280 MHz that we find is lower than the value quoted by others. Hummel & van der Hulst (1989) estimate a flux density of 60 ± 5 mJy at 1.465 GHz with the VLA whereas Bosma et al. (1980) have estimated a flux density of 48 ± 5 mJy at 21cm using the WSRT. Condon et al. (1990) find a flux density of 64.2 mJy at 1.49 GHz. Since the flux density, we estimate, is lower we do not quote the image errors which are comparatively insignificant.

$\sim 84^\circ$ (Hummel & van der Hulst 1989), coincides with the optical centre within $5''$ (see Fig 5.1 (a)). The flux densities of the galaxies at different frequencies and the galaxy-integrated spectral index between 330 and 610 MHz are listed in Table 5.2.

Halo emission is detected around NGC 2820 at all the observed frequencies and is prominent at 330 MHz (see Fig 5.1 (a)) which is our most sensitive low frequency. In their study of radio emission from six edge-on galaxies, Hummel & van der Hulst (1989), found that NGC 2820 had a radio halo with the largest z-extent (10% peak height of about 3.4 kpc) which they attributed to gravitational interaction with its companions. We find the 10% peak flux level z-extent of the radio halo is 4.2 kpc. The half power thickness of the halo is 2.2 kpc which is double the typical value. We estimated the spectral index between 330 and 610 MHz (from similar angular resolution maps) at a few positions in the halo and find it to be −1.5.

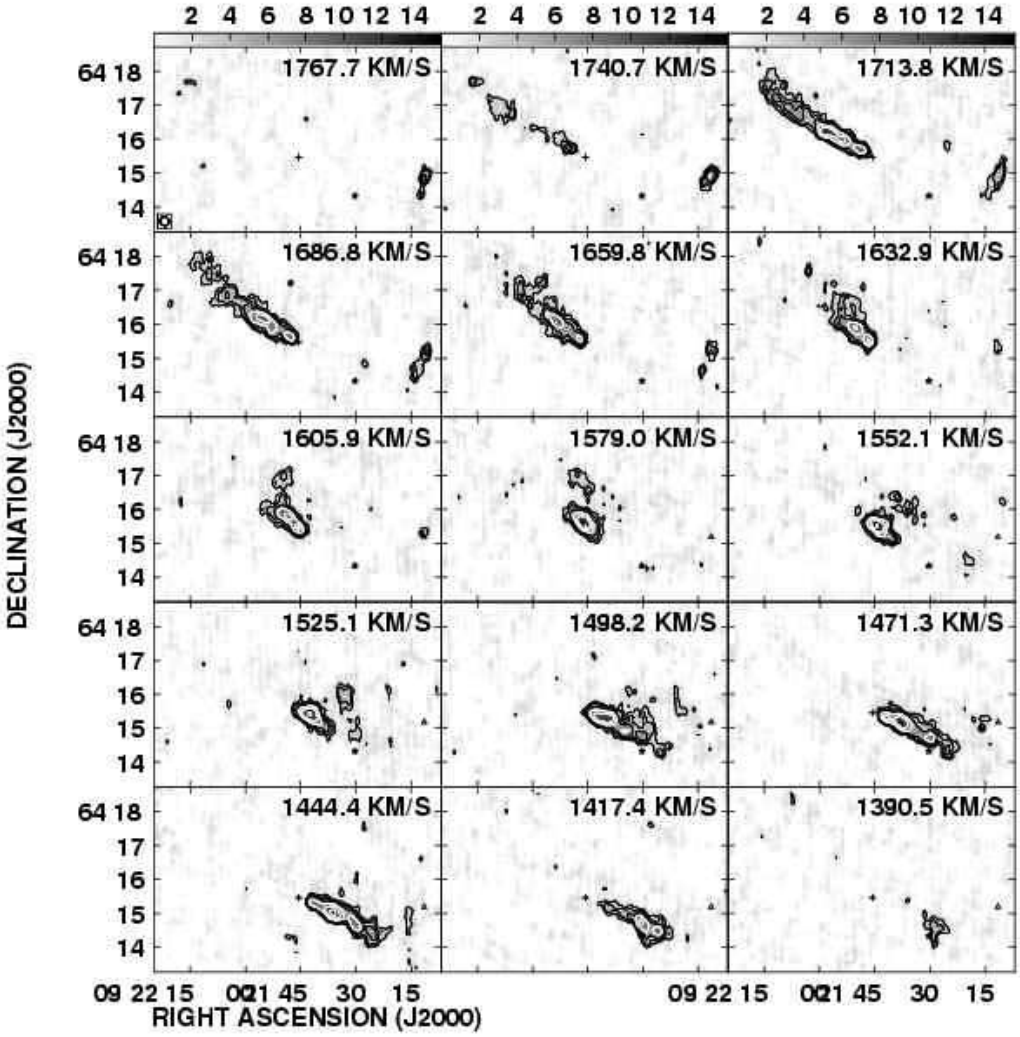

Figure 5.2: HI emission detected at different velocities is shown in the panels. The beam is plotted in the bottom left corner of the first panel. The first contour is at 2.4 mJy/beam and then it increases in steps of $\sqrt{2}$. The grey scale is from 0.1 to 15 mJy/beam. Note that the HI in NGC 2814 is moving at velocities between 1660 to 1767 $\mathrm{km\,s^{-1}}$ whereas the HI gas in Mrk 108 is moving at velocities between 1417 and 1444 $\mathrm{km\,s^{-1}}$. HI is detected from the bridge. The optical positions of NGC 2820, Mrk 108 and NGC 2814 are shown by a cross, star and triangle respectively. The cube has been smoothed in the velocity axis and every alternate channel is plotted here.

NGC 2814 shows halo emission which is tilted with respect to the stellar disk traced by the DSS optical image (see Fig 5.1(a)). We find that the global spectral index of the galaxy is -1.25 whereas that of the radio peak is -0.6 (see Table 5.2). It is difficult to separate the halo emission from the disk emission for this relatively small galaxy.

The radio power of NGC 2820 is 1.2×10^{22} Watt-Hz^{-1} and that of NGC 2814 is 2.6×10^{21} Watt-Hz^{-1} (estimated at 330 MHz). We also estimated the q factor which gives the ratio of FIR flux density to the radio continuum flux density at 1.4 GHz for NGC 2820 following Helou et al. (1985). We find that q = 2.02 for NGC 2820. This value is consistent with the quoted value for spiral galaxies of q = 2.3 with a rms scatter of 0.2 (Condon 1992). Thus, NGC 2820 follows the FIR-radio correlation.

(b) 21 cm HI

The details of the 21cm HI observations are listed in Table 5.1. These data were initially analysed in a way similar to the continuum data sans self calibration. The continuum emission from the line data was removed and spectral channels imaged to generate a cube. We used a uv taper of $12k\lambda$ and uv range of $15k\lambda$ with robust weighting (ROBUST = 0) to obtain the final cube. The beamwidth is $16.2'' \times 15.2''$ with a PA= 25.7° which greatly improves on the arcmin resolution of Bosma et al. (1980).

We detected HI from all members of the group. The channel maps showing HI line emission detected at different velocities for the triplet are shown in Fig 5.2. The column density map of the group (estimated assuming HI is optically thin along the line of sight) is shown in Fig 5.3. A zoomed-in HI column density map for the triplet is shown in Fig 5.4 (a). The first and

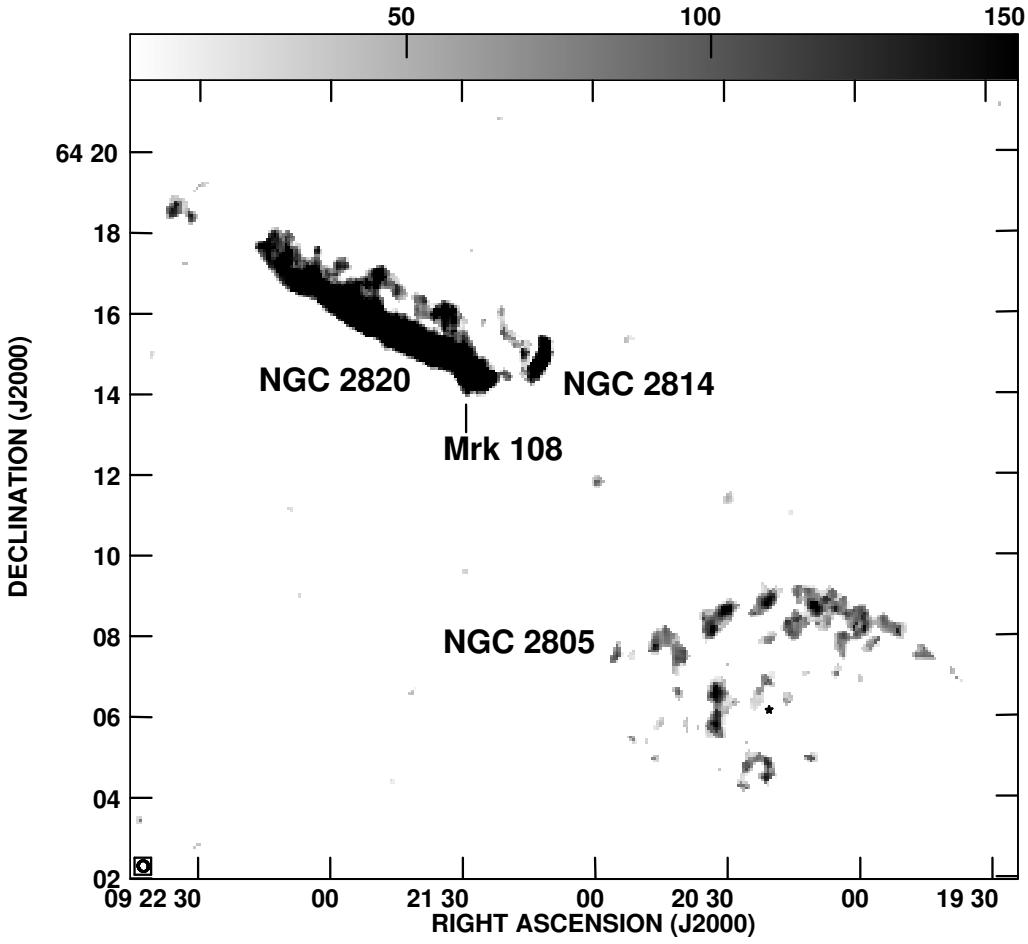

Figure 5.3: The HI moment zero map of the group Holmberg 124. The triplet comprising of NGC 2820, Mrk 108 and NGC 2814 lies in the north-east whereas NGC 2805 is the face-on member seen in the south-west. Note that NGC 2805 was close to the half power point of the primary beam at 21 cm.

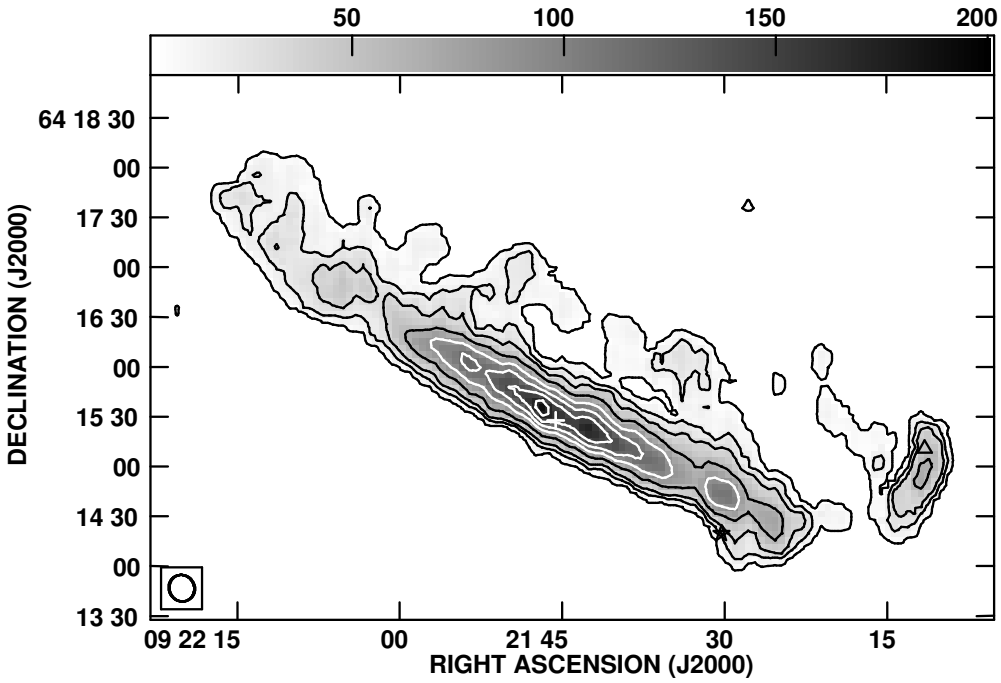

Figure 5.4: **(a)** Column density map of the triplet obtained from the moment zero map. The lowest contour is 0.44×10^{20} cm^{-2}. The next two contours are at an inverval of 1.4×10^{20} cm^{-2} and then the contours increase in steps of 2.8×10^{20} cm^{-2}. The grey scale ranges from 0.4×10^{20} cm^{-2} to 20×10^{20} cm^{-2}

.

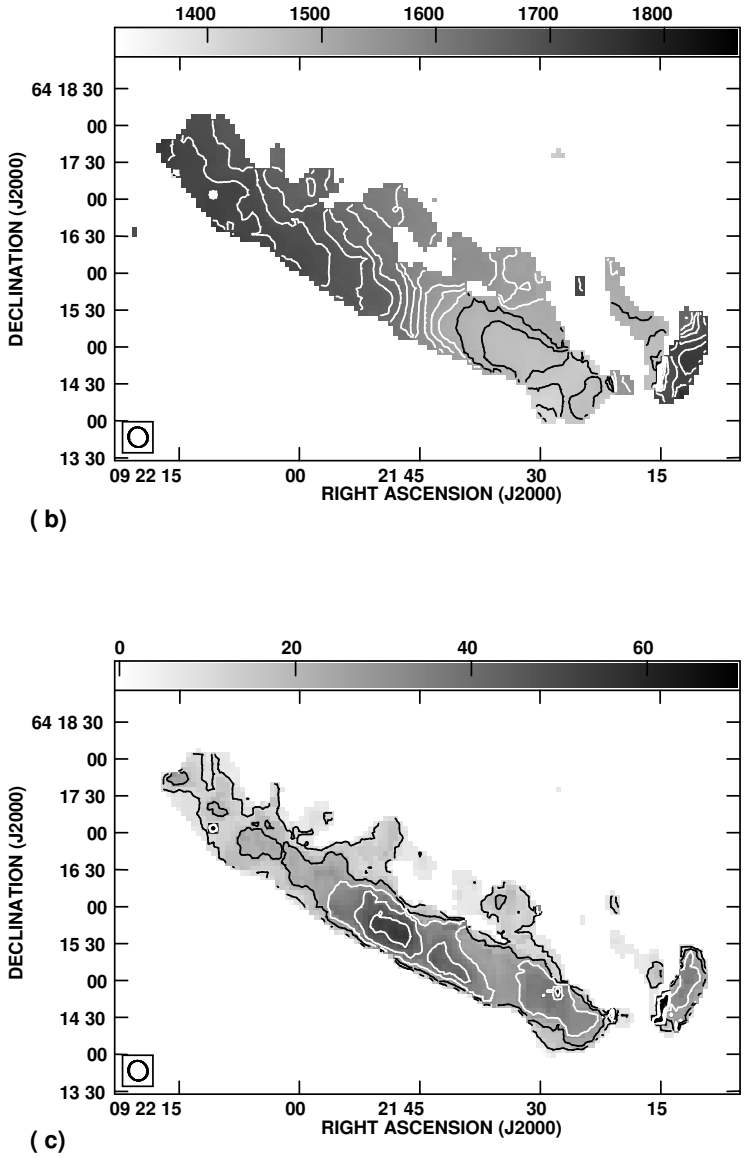

Figure 5.4: **(b)** (top panel) First moment map of the HI emission showing the velocity field in the triplet. The grey scale ranges from 1323 km s^{-1} to 1862 km s^{-1}. The contours are plotted from 1410 km s^{-1} (black contour) to 1730 km s^{-1} in steps of 20 km s^{-1}. Note the distinct velocity field of Mrk 108. **(c)** Second moment map of the HI emission showing the line widths in the triplet. The grey scale ranges from 0 to 70 km s^{-1}. The contours are plotted from 10 to 50 km s^{-1} in steps of 10 km s^{-1}.

second moment maps of HI for the line emission are shown in Figs 5.4 (b) and (c).

The channel maps (see Fig 5.2) clearly show the rotation in the disk of NGC 2820. The HI disk extends more to the northeast than in the southwest. The velocity of the gas in NGC 2820 varies from ~ 1710 km s^{-1} in the northeast to ~ 1445 km s^{-1} in the southwest (see Fig 5.4 (b)). Since the systemic velocity of the galaxy is 1577 km s^{-1}, this gives a difference velocity of 133 km s^{-1} in the northeast and 134 km s^{-1} in the southwest. The rotation speed of the gas is fairly symmetric over the centre unlike what Bosma et al. (1980) found. This is probably because the velocity of the HI gas in Mrk 108, which we can clearly distinguish in our maps (see Fig 5.2 - last two panels) due to our higher angular resolution is around 1410 km s^{-1} and was presumably included within the Bosma et al. (1980) beam. It is of interest to note the nature of the isovelocity contours. In Fig 5.4 (b), it is seen that the contours in the northeast are different from those in the southwest and appear to be kinematically disturbed. It appears that the HI gas in the northeast has been affected by the interaction more than in the southwest. A ring of HI surrounds the optical center (see Fig 5.4 (a)). HI condensation is also seen near Mrk 108 and it is likely associated with a star forming region seen in the Hα image (see Fig 5.7 (c)), possibly triggered by the interaction.

HI is detected from the bridge except for a small region. The mean HI column density in the bridge is $\leq 4.4 \times 10^{19}$ atoms cm^{-2}.

HI emission shows interesting extraplanar features in NGC 2820. Large ammount of HI is seen displaced to the north-west from the peak Hα emission knots. The isovelocity contours of the extraplanar HI also look diverging away from the minor-axis of the galaxy. This is similar to the the case of disk HI in NGC4438 which is undergoing tidal interaction as well as ram

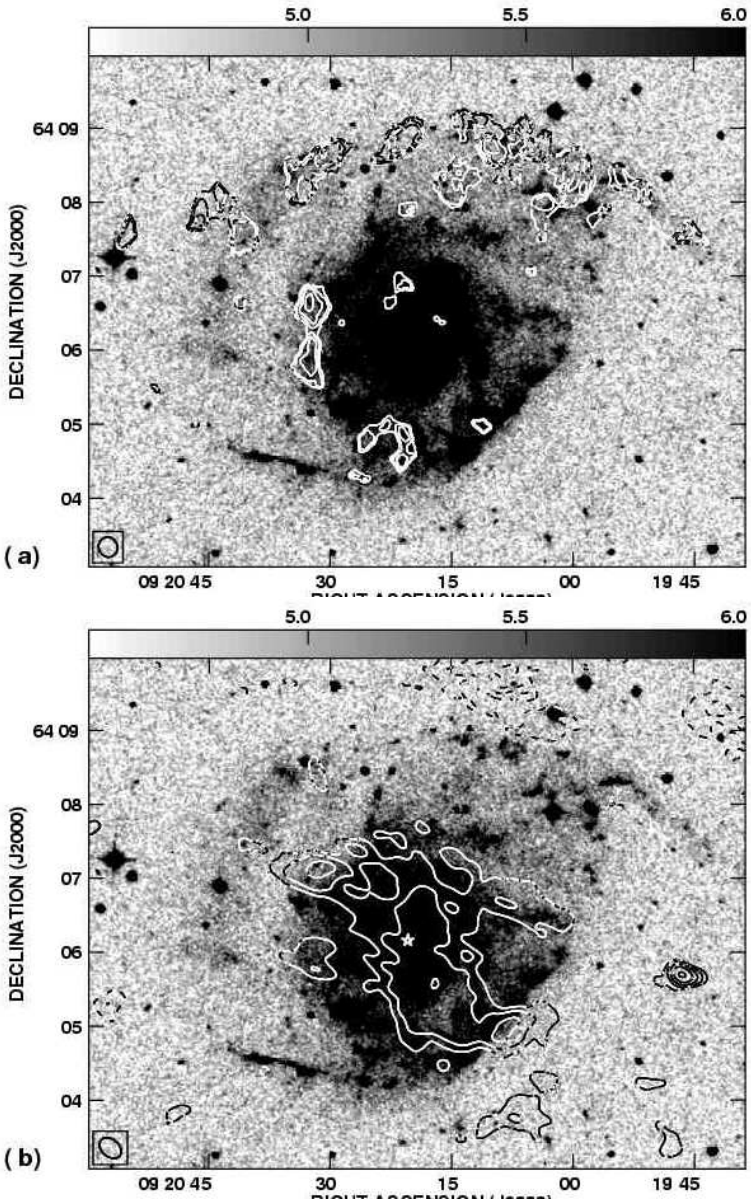

Figure 5.5: **(a)** (top panel) Contours of the zero moment map of HI emission superposed on the grey scale image of DSS blue band image of NGC 2805. Note the ridge of HI emission in the north which coincides with a disturbed spiral arm seen in the optical. Note that HI is confined to the optical disk of the galaxy. Since this galaxy lies close to the half power point of the GMRT primary beam, we do not trust the HI column densities. However the morphology except for the extended disk emission roughly follows what Bosma et al. 1980 had reported. **(b)** Contours of 330 MHz radio emission superposed on the grey scale DSS blue band image of NGC 2805. Note the ridge of star formation and sharp cutoff in the south-west visible in the DSS image. The star marks the optical centre of the galaxy.

pressure stripping by the Virgo cluster medium (Hota, Saikia & Irwin 2006; Chapter 4). A symmetric HI loop is observed to the north of the galaxy - the channel maps (Fig 5.2) between 1633 $\mathrm{km\,s^{-1}}$ and 1525 $\mathrm{km\,s^{-1}}$ clearly show the presence of extraplanar features. The loop opens at the top giving it an appearance of an outflow and then seems to turn back as if the HI gas is falling back towards the disk. The loop has enormous dimensions with a width parallel to the galactic disk of about 17.5 kpc ($\sim 2.5'$) and a height of about 4.9 kpc ($\sim 0.7'$). No detectable radio continuum emission is associated with the HI loop. Moreover there are a couple of other protrusions visible to the east of the large HI loop. Interestingly, no HI filaments or protrusions are observed arising from the southern side of NGC 2820 and the HI shows a smooth boundary. Similarly, we find that the HI disk and radio continuum disk of NGC 2814 are sharply truncated in the north of the galaxy whereas the optical emission extends beyond. The HI disk of NGC 2814, like the radio continuum disk, is inclined to the optical disk. A high velocity streamer is seen emerging, almost perpendicularly, from the south of NGC 2814. This streamer is fairly long, extending to the northeast. The heliocentric velocity of NGC 2814 is 1707 $\mathrm{kms^{-1}}$ whereas the streamer has a line of sight velocity range of $\sim$ 1452 $\mathrm{kms^{-1}}$ to 1510 $\mathrm{kms^{-1}}$. The velocity difference between the streamer and NGC 2814 is more than 200 $\mathrm{kms^{-1}}$. The streamer velocity is more in tune with the velocity field seen in the southern parts of NGC 2820.

The HI distribution of NGC 2805 (see Fig 5.5 (a)) is asymmetric with larger column densities and higher radial velocities in the northern regions as compared to the southern parts. Since this galaxy was close to the half power point of the GMRT primary beam in our 21cm HI image, we cross checked the observed morphology with the Bosma et al. (1980) images. We find the two maps correlate well and the paucity of HI in the southern

Table 5.3: Galaxy parameters from HI data. A distance of 24 Mpc to the group has been used. The systemic velocities of Mrk 108, NGC 2814, NGC 2805, the streamer and the HI blobs have been determined by fitting a gaussian to the source-integrated HI profile.

Parametre	N2820	Mrk108	N2814	N2805	streamer	blobs	Loop
Heliocentric velocity (km/s)	1577	1417	1707	1745	1493	1725	1566
Half-power width (km/s)	350	52	136	99	72	42	137
Rotation velocity (km/s)	175	-	-		-	-	-
Inclination (°)	74	-	-	20[1]	-	-	-
Position angle (°)	66	-	-		-	-	-
Linear size (kpc)	47.6	3	10.4	60	12.7	3.5	17.5
HI mass M_{Hi} ($10^9 M_\odot$)	6.6	0.061	0.34	5.3[2]	0.13	0.11	0.6
Dynamical mass[3] M_{dyn} ($10^9 M_\odot$)	170	0.94	22	584	-	1.4	-
M_{Hi}/M_{dyn} (%)	3.9	6.5	1.5	-	-	7.9	-

[1] From Bosma et al. (1980). This value is used in estimating the HI mass and dynamical mass

[2]This estimate is much less than the value of 12×10^9 $M_\odot$ of Bosma et al. (1980) and is likely because the galaxy is close to the half power points of the GMRT primary beam.

[3]The J2000 position of the dynamical centre is 09h21m45.6s +64d15m31s

parts is real and not an artifact of the primary beam cutoff. However we are insensitive to the large scale HI emission seen from the face-on disk by Bosma et al. (1980).

Global HI line profiles were obtained for all the galaxies and HI features. A gaussian function was fitted to the observed profiles (except for NGC 2820 which shows a classical double-humped HI profile with a sharp fall-off) and the resultant parameters were used to derive various physical quantities (Table 5.3). The systemic velocity, rotation velocity, inclination and dynamical centre of NGC 2820 are results from running the task, GAL in AIPS on the velocity field of the galaxy. We model the observed data with a Brandt curve purely as a fit; it reproduces the solid body rotation in the central regions fairly well. We obtain a rotation velocity of 175 $\mathrm{km\,s^{-1}}$ for NGC 2820. The rotation curve is shown in Fig 5.8. The HI mass was calculated from the

velocity-integrated line strength whereas the dynamical mass was estimated using rv^2/G. We find that the rotation curve fit gives an inclination of 74° and position angle of 66° for NGC 2820. The optical heliocentric velocity of NGC 2820 is 1577 $\mathrm{km\,s^{-1}}$ which is in good agreement with the value of 1574 ± 10 $\mathrm{km\,s^{-1}}$ quoted by Bosma et al. (1980). About 4% of the total mass of NGC 2820 is in HI whereas 6.5% mass of Mrk 108 appears to be in the form of HI (Table 5.3). For the HI blobs, we find that about 8% of its dynamical mass is seen in the form of HI. We find that NGC 2805 is massive with a total dynamical mass of 5.8×10^{11} $\mathrm{M_\odot}$.

The position-velocity (PV) curves plotted along and parallel to the major axis of NGC 2820 are shown in Fig 5.9. Fig 5.9(a) shows that the gas in the central 5.8 kpc of NGC 2820 exhibits solid body rotation. Some asymmetry is visible between 1600 and 1650 $\mathrm{km\,s^{-1}}$. The HI blob, NGC 2814 and the streamer are shown in the PV diagram (see Fig 5.9 (b)) of a slice parallel to the major axis of the galaxy. The streamer is seen to be kinematically independent of NGC 2814.

5.4 Tidal effects

NGC 2820 appears to have had a retrograde interaction with NGC 2814 and the two galaxies presently have a relative radial velocity of 130 $\mathrm{km\,s^{-1}}$. Various morphological signatures which are likely due to the tidal interaction between NGC 2820, Mrk 108 and NGC 2814 are seen in our HI moment zero and radio continuum maps. The dominant signatures in HI are the streamer apparently emerging from NGC 2814 (but showing a different velocity field), the inclined disk of NGC 2814, the bridge between NGC 2820 and NGC 2814 and the detection of HI blobs to the north-east of NGC 2820. Star formation

seems to have been triggered in the disk of NGC 2820 close to Mrk 108, in Mrk 108 and in a small tail of NGC 2814 by the tidal interaction as can be identified on the Hα image of the triplet (see Fig 5.7 (c)). Moreover, Artamonov et al (1994) from their UBV photometric observations, report enhanced star formation in Ho 124 due to tidal interaction. The tidal features which are readily discernible in the 330 MHz map are the steep spectrum radio bridge, the tilted radio disk of NGC 2814 and a radio tail issuing from NGC 2814 and extending southwards. However, the tidal origin of HI features like the HI loop arising from the northern side of NGC 2820 and the small HI protrusions is not clear. We discuss the origin of the loop in the next section.

In this section, we briefly elaborate on some of the clear signatures of tidal interaction discernible in our images.

(a) Tidal bridge

van der Hulst & Hummel (1985) were the first to detect a radio continuum bridge connecting the triplet in Ho 124 at 1465 MHz. Since then radio bridges have been detected in many other systems; a famous one being the Taffy galaxies (Condon et al. 1993) in which one-half the total radio synchrotron emission of the system arises in the bridge.

As shown in Fig 5.1(a), we have detected the bridge connecting the triplet at 330 MHz. Using the 1465 MHz result of van der Hulst and Hummel (1985) along with our data at 330 MHz we estimate a spectral index of $-1.8^{+0.3}_{-0.2}$ for the bridge. This spectral index is much steeper than the value of -0.8 quoted by van der Hulst and Hummel (1985) which might possibly have been corrupted by disk emission at their lower frequency. At 610 MHz and 240 MHz, we report marginal detection of the bridge and the brightness of the

bridge is consistent with the estimated spectral index.

We estimated the size of the bridge from our 330 MHz image. The projected linear extent of the bridge is 5.4 kpc. Our estimate of the projected length of the bridge is less than what van der Hulst & Hummel (1985) estimated. This is likely because we have not included the source west of Mrk 108 which we believe is part of the disk of NGC 2820 and not the bridge. The width of the bridge in the sky plane is 2.1 kpc. We assumed a similar extent for the bridge along the line-of-sight. Using equipartition and minimum energy arguments, we estimated a magnetic field of $\sim 3.4\mu$G, and a minimum energy density of 1.1×10^{-12} ergs cm^{-3}. The minimum energy in the bridge is 7.7×10^{53} ergs. The magnetic pressure of the bridge is about 2600 K cm^{-3}. We have assumed that there is 100 times more energy in protons than electrons for the above calculations. A few possible scenarios for confining the bridge were described in Ananthakrishnan et al. 2003.

We detected HI in the bridge except for a small region (see Fig 5.4 (a)). This HI is moving at a line-of-sight velocity of about 1545 km s^{-1} which is different from the HI in the disk of NGC 2820 nearest to the extension of 1445 km s^{-1} (see Fig 5.4 (b)). However the velocity of HI in the bridge is closer to the systemic velocity of NGC 2820. If the gas in the bridge is moving with a velocity of 100 km s^{-1} (ie. $1545 - 1445$ km s^{-1}) with respect to the gas in NGC 2820, then the kinematic age of the bridge is 46 million years. If the gas is moving with a velocity larger than 100 km s^{-1}, the kinematic age will be lower. The mean column density in the bridge is $\leq 4.4 \times 10^{19}$ cm^{-2}. Using a line-of-sight depth of 2.1 kpc for the bridge, we find that the atomic density in the bridge is < 0.006 cm^{-3}. If we assume a kinetic temperature of 5000 K, the thermal pressure of the gas in the bridge would be only 30 K cm^{-3} which is much less than the magnetic pressure of the bridge. We obtain a result

similar to van der Hulst & Hummel (1985) in that the magnetic field and relativistic particles moving in it seem to dominate the bridge energetics. It appears likely that the bridge is confined by an ordered magnetic field. No Hα emission is detected from the bridge (Gil de Paz et al. 2003) (see Fig 5.7 (c)) indicating that star formation has not been triggered in the bridge. This is not surprising since the column density of neutral atomic matter in the bridge is fairly low. Little molecular gas is therefore likely to be present in the bridge.

(b) Tidal effects on NGC 2814

The disk of NGC 2814 has obviously been affected by tidal forces in its encounter with NGC 2820. The optical disk is aligned almost north-south whereas the radio continuum and HI disks are inclined towards the bridge clearly showing that they have been affected by tidal forces (see Fig 5.1(a) and Fig 5.7(a)) Also note the 'comma'-shaped HI disk and Hα emission of NGC 2814. The Hα image of NGC 2814 (see Fig 5.7 (c)) shows enhanced star formation in a small tail which is likely triggered by the tidal interaction. Star formation, triggered by the tidal interaction is also observed in and close to Mrk 108. A tail is observed in the radio continuum issuing and extending to the south of NGC 2814 (see Fig 5.1 (a)). The spectral index of this tail is ~ -1.6 and the tail is likely a result of the tidal interaction.

(c) Tidal streamer

A HI streamer is observed to arise from the southern end of NGC 2814 and extend towards the north-east (see Fig 5.4 (a)) but which is kinematically distinct from the galaxy. The different velocities (difference of about 200

kms^{-1}) support a projection effect. A velocity gradient of about 5.3 km s^{-1} kpc^{-1} is observed along the streamer. We note that the velocity field seen in the streamer matches the velocities seen on the closer side of NGC 2820 and intriguingly the shape of the tail matches the outer edge of NGC 2820. We believe that the streamer is HI gas which has been stripped off NGC 2820 during the tidal interaction. Since we do not see an extra radial velocity that the streamer might have picked up during the tidal encounter, it might be in motion in the sky plane. If we assume that the streamer was dislocated from NGC 2820 and picked up a velocity of 100 km s^{-1} due to the tidal interaction, then it would have taken about 40 million years for the streamer to be at its current position. The average column density in the streamer is 4.4×10^{19} cm^{-2} and the mass is $\sim 9.1 \times 10^7 M_\odot$. The length of the streamer in the sky plane is about 12.6 kpc.

(d) A tidal dwarf galaxy ?

The HI blobs (see Fig 5.6 (a)) detected to the north-east of NGC 2820 contain about $10^8 M_\odot$ of HI. One possibility to explain these blobs is that it is a tidal dwarf galaxy. It would be interesting to obtain a deep Hα image of this region and check this possibility. The spectrum integrated over the blobs is shown in Fig 5.6(b). No rotation is discernible in the blobs. We do not find any optical counterparts to the blobs in the DSS images. The HI velocity field of the blobs is a continuation of the velocity field seen in the north-east tip of NGC 2820 probably indicating its origin. The blobs are located about 11.5 kpc away from the north-east tip of NGC 2820.

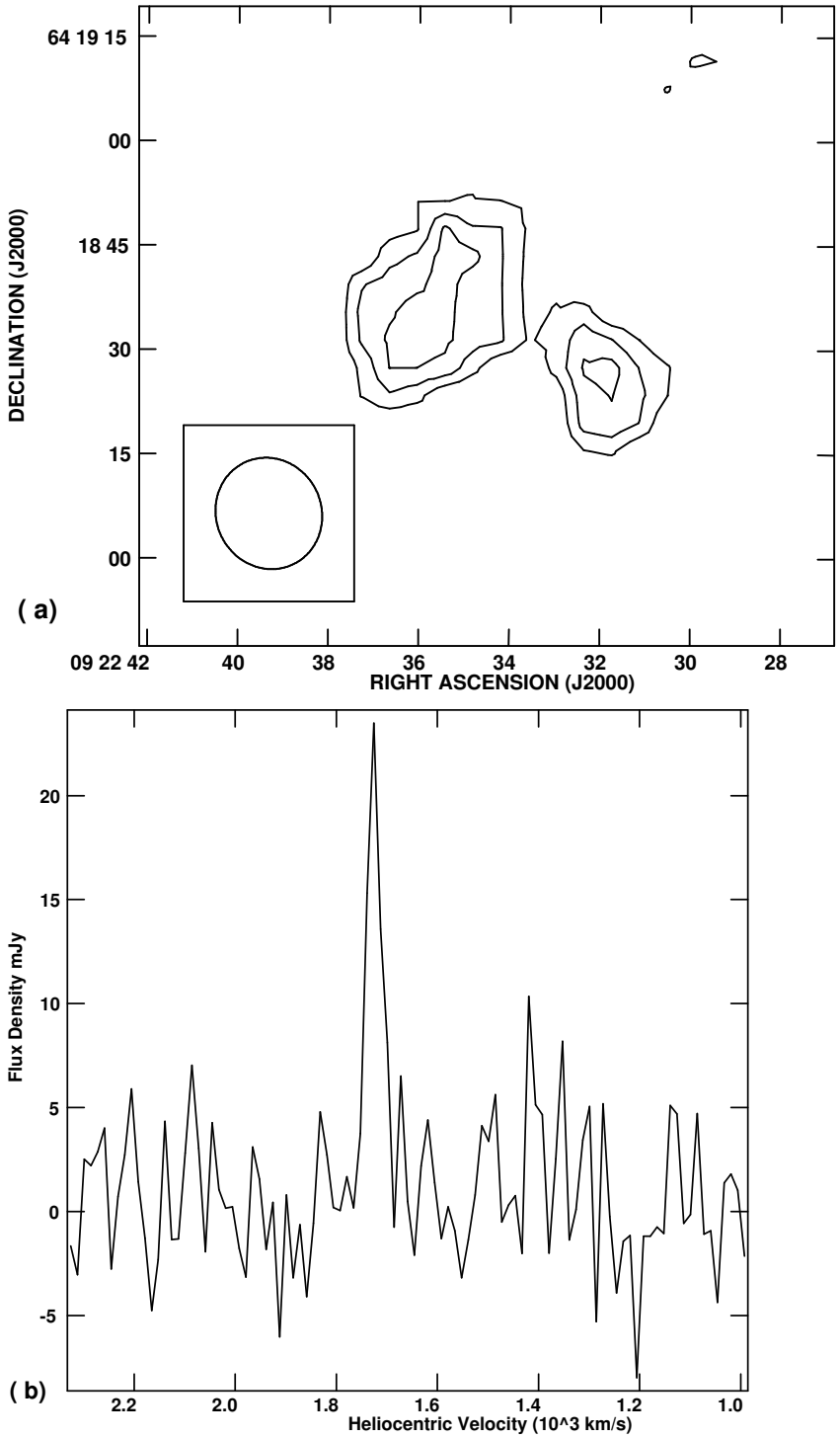

Figure 5.6: **(a)** HI moment zero map of the HI 'blobs' which might be a tidal dwarf. The contours outline column densities of 4.4×1019 cm^{-2},8.8×10^{19} cm^{-2} nd 13.2×10^{19} cm^{-2}. **(b)** The HI profile integrated over the HI 'blobs'.

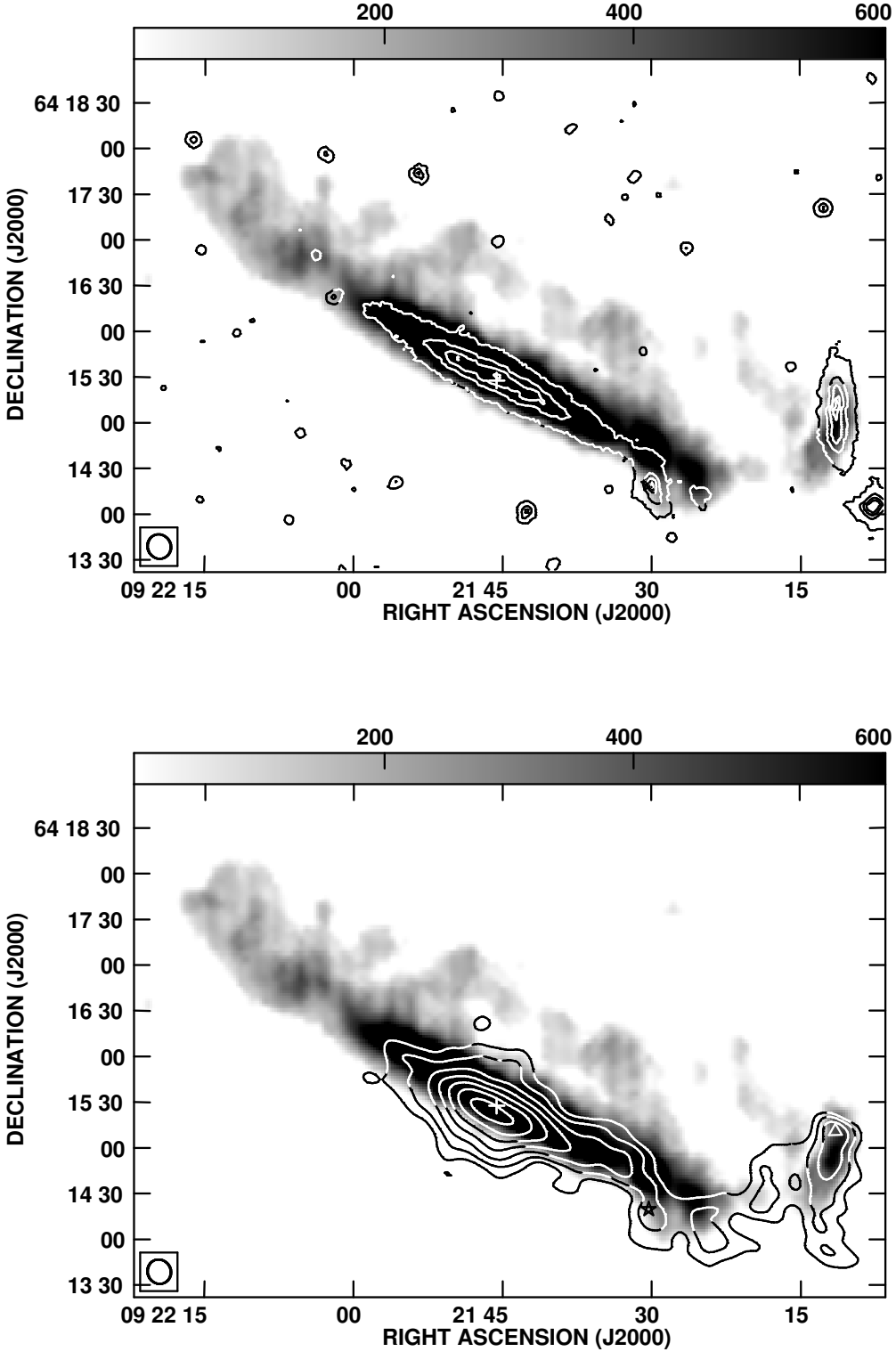

Figure 5.7: **(a)** Grey scale of the HI column density superposed on the DSS optical map (contours). Note the extent of the compared to the optical continuum. **(b)** HI zero moment map (grey) superposed on the 330 MHz radio continuum map.

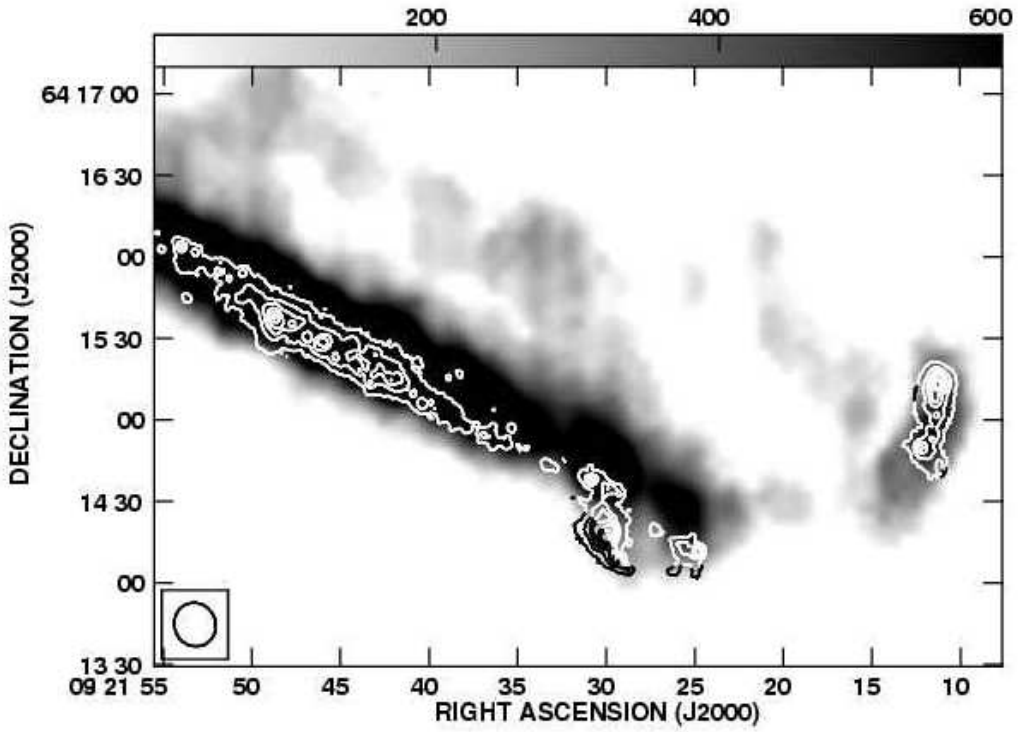

Figure 5.7: **(c)** Hα contours superposed on the moment zero map of HI in grey scale. Note the lack of Hα emission in the bridge and in the loop. The Hα image is from Gil de Paz et al. (2003).

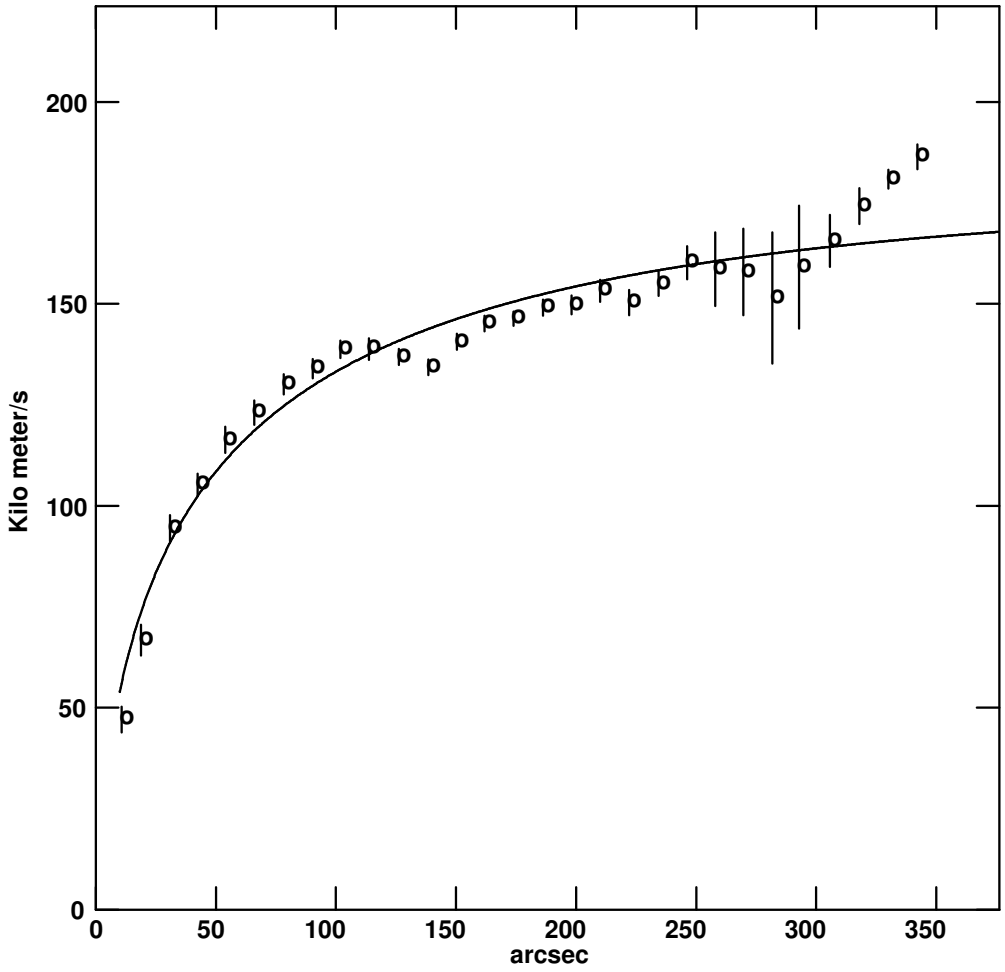

Figure 5.8: Rotation curve of NGC 2820. The solid line is the Brandt model fit to the data, results from which are noted in Table 5.3.

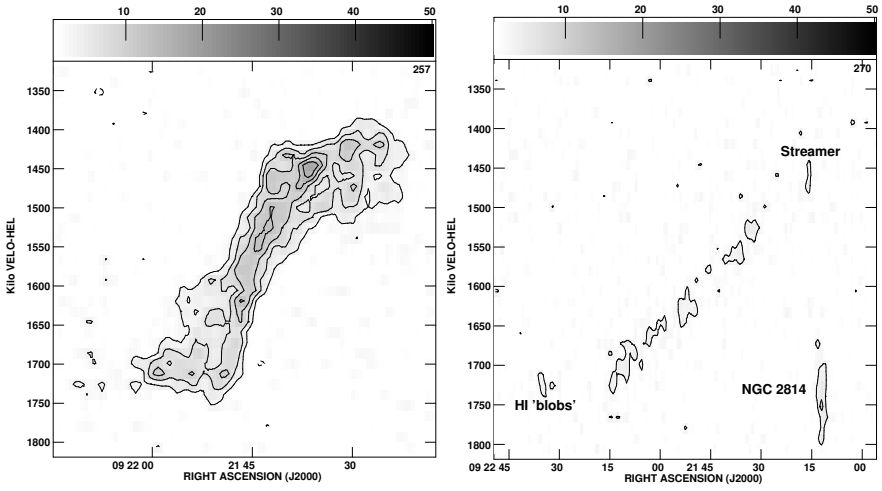

Figure 5.9: **(a)** PV curve along the major axis of NGC 2820. Solid body rotation is seen in the central 50". The grey scale ranges from 1 to 50 mJy/beam whereas the contours are plotted for 3,6,9,12,15 mJy/beam. **(b)** PV diagram along an axis parallel to the major axis passing through the northern loop, the HI blob located off the eastern edge of NGC 2820, the streamer emerging from NGC 2814 and NGC 2814. The streamer and NGC 2814 although positionally coincident, are kinematically distinct. The grey scale and contour levels are the same as (a).

5.5 The HI loop

A large one-sided HI loop is detected to the north of NGC 2820. The loop extends out to about 4.9 kpc along the rotation axis of the galaxy and has a lateral dimension of about 17.5 kpc. No counterpart is detected in the south of the galaxy. Moreover, we do not detect any radio continuum from the loop and no Hα emission is seen to be associated with the loop. In this section, we examine three possible scenarios for the origin of the HI loop, namely a) starburst driven superwind b) ram-pressure stripped HI and c) tidally stripped HI. We look for an origin which can explain the observed constraints: 1) the absence of Hα and radio continuum in the loop 2) the one-sided nature of the loop 3) the symmetry of the loop about the rotation axis. Study of the velocity field of the HI loop gives the following inputs to the above scenarios: 1) The HI loop is trailing the disk rotation. The radial velocity at the top of the loop is close to the systemic velocity of the galaxy (see Fig 5.4 (b)). 2) The line width increases along the loop and is largest at the top of the loop (see Fig 5.4 (c)). 3) The global HI profile and the HI profile of the loop are centred on the systemic velocity of the galaxy and show no tail-like feature indicating that no gas is moving along the line of sight.

(a) Starburst driven superwind

Gas is driven out of the disk by the underlying starburst to tens of kpc from the disk along the minor-axes and is known as superwind. Superwind cones are commonly observed in X-rays, radio continuum and Hα but infrequently in HI. In case of NGC 253, HI has been observed to be confined within the optical disk and to outline the superwind cone of ionized gas in one half of

the galaxy (Boomsma et al. 2004). Another study has shown that significant amounts of HI is observed to be in the halos of spiral galaxies with active star formation Fraternali et al. (2001). In case of NGC 2820, the HI halo is not observed to be significantly larger than the optical disk (see Fig 5.7(a)). Anyway, here, we examine the possibility of the large HI loop that we observe in NGC 2820 being a superwind and estimate its energetics.

The mass of the HI loop is $5.5 \times 10^8 M_\odot$ and the full width at zero intensity of the HI line is 160 $\mathrm{km\,s^{-1}}$. Assuming HI to be flowing along the surface of a superwind bi-cone of half angle 45°, the deprojected outflow velocity is 113 $\mathrm{km\,s^{-1}}$. The kinetic energy contained in the outflowing HI is 7×10^{55} ergs and the dynamical age of the outflow is 34.7 million years.

We compare this with the energy contained in the supernovae in NGC 2820 to examine the feasibility of this scenario. We follow Condon (1992) and use the non-thermal radio continuum emission from the central parts of NGC 2820 to estimate a supernovae rate of ~ 0.007 per year. This rate is fairly low compared to typical superwind galaxies e.g. 0.1 supernovae per year in NGC 1482, M82 and 0.1 to 0.3 in NGC 253.

If the kinetic energy imparted to the interstellar medium by a single supernova explosion is 10^{51} ergs, then the kinetic energy available during the dynamical age of the outflow is 3.4×10^{56} ergs. However, note that the starburst would also drive other phases of the interstellar medium into the halo and hence only about $1 - 10\%$ of the estimated kinetic energy will be seen in HI. In this case, the energy available in the supernovae is at best comparable to the kinetic energy of the HI loop. We arrive at a kinetic energy within a factor of few higher from the above if we include the energy due to the stellar winds from massive young stars. This was estimated from the total FIR luminosity of NGC 2820 following the method by Heckman et

al. (1990).

Even if the energetics just about satisfy the starburst-driven origin of the loop, we note several reasons below why we do not favour this scenario: (a) No Hα emitting gas is found along the HI loop unlike superwind galaxies. (b) NGC 2820 is not classified as a starburst galaxy and does not show any obvious signatures of being a starburst galaxy. (c) No HI loop of such large dimensions appears to have been observed in any superwind galaxy. (d) The HI loop is one-sided. The starburst process which can drive such a large loop in one direction should be energetic enough to drive it in the other direction also.

(b) Ram pressure stripping

In this subsection, we examine the scenario of the observed HI loop as being the stripped HI from NGC 2820 due to ram pressure (Gunn & Gott 1972) exerted by the IGrM. The reason we examine this possibility is the presence of a few interesting features in the group members. Firstly the southern edge of NGC 2820 shows a sharp cutoff in HI whereas the radio continuum extends beyond this cutoff (see Fig 5.7 (b)). Secondly the northern part of NGC 2814 shows a sharp cutoff both in radio continuum and HI whereas the optical disk does not show any such effect. Since ram pressure is expected to distort the various disk components differently (Davis et al. 1997) and the sharp edges can be caused by swept-back material due to ram pressure, we tend towards interpreting the above features to be a signature of ram pressure of the IGrM.

Thus it appears that ram pressure could have played an important role in the evolution of the group. Hence, we examine the case of the HI loop

seen to the north of NGC 2820 being a result of ram pressure stripping. We compare the pressure due to the IGrM as the galaxy moves in it and the gravitational pressure of the disk of NGC 2820. The relevant equation given by Gunn & Gott (1972) is

$$\rho\, v^2 \;\geq\; 2\pi\, G\, \Sigma_*\, \Sigma_{gas} \quad (\mathrm{kg\,m^{-1}\,s^{-2}})$$

where ρ is the IGrM mass density, v is the velocity dispersion of the group, G is the gravitational constant, Σ_* is the surface mass density of stars, Σ_{gas} is the surface mass density of gas. The line of sight velocity dispersion (Osmond & Ponman 2004) of this group is 162 ± 73 km s^{-1}. No X-ray emission has been detected from this group and the upper limit on the bolometric X-ray luminosity is 2.88×10^{40} erg s^{-1} (Mulchaey et al. 2003). If we assume that the temperature of the IGrM in this late-type group is 2×10^6 K (Mulchaey et al. 1996b) and the medium is distributed over a sphere of radius 50 kpc, then we arrive at upper limits on the electron density of 8.8×10^{-4} cm^{-3} and mass of 1.15×10^{10} M$_\odot$. We assume a IGrM density of 4×10^{-4} cm^{-3} (well within the upper limit) and using $\mathrm{v}^2 = 3 * \sigma^2$ (Sarazin 1986) we calculate a ram pressure of $\sim 6 \times 10^{-14}$ kg m^{-1} s^{-2}.

We find an average stellar mass density of 133 $M_\odot$ pc^{-2} in the central 10 kpc region of NGC 2820 using the inclination-corrected total B-band magnitude and the average γ_B (light to mass ratio) factor given by Binney and Merrifield (1998). For $N_H = 4.4 \times 10^{19}$ cm^{-2}, the surface mass density of HI is 0.32 $M_\odot$ pc^{-2}. These give the gravitational pressure of the disk to be to be $\sim 8 \times 10^{-14}$ kgm^{-1}s^{-2}. This is comparable to the ram pressure acting on the system. If we estimate the gravitational pressure of the disk in the outer regions by using the stellar mass density at the 25 mag-asec^{-2} diametre (15.25 M$_\odot$ pc^{-2}), which is close to where the loop is seen to emerge from the

disk, then we find that the ram pressure exceeds the gravitational pressure of the disk by a factor of few. However this does not take into account the influence of dark matter in the outer regions.

Mulchaey et al. (1996, 2003) have concluded from their X-ray observations of many poor groups that the X-ray luminosity of the IGrM of groups with only late-type galaxies is lower than if the group has at least one early-type member. They infer that the late-type-only groups might have a lower temperature or a lower density. Our results seem to indicate that the IGrM should have densities that are almost sufficient to morphologically influence NGC 2820. Thus, the densities should not be too low ($<< 4 \times 10^{-4}$) to be inconsequential.

Assuming ram pressure has played a role in giving rise to the loop, we outline two possible ways in which the loop could have formed.

Model 1: NGC 2820 has been classified as a barred galaxy (Bosma et al. 1980). Many barred galaxies show concentration of HI at the edge of the bar and the loop like structure could be due to the neutral gas from this region being stripped off in its interaction with the IGrM. In this scenario, the stripped HI lies well within the disk, just below the loop. The rotation of the disk causes a twist in the flow. Since HI in this region is likely to be strongly bound to the disk, this model requires extensive help from tidal effects in reducing the surface density of the neutral gas. The kinematic features can be explained as: the trailing velocity field could be due to a combination of vertical motion of gas stripped from different regions in the disk combined with twisting due to galactic rotation. The wider lines at the top of the loop could be because of gas acquiring higher random motions. The central hole in the loop is expected since ram pressure cannot strip the

high density neutral gas in the central regions.

Model 2: The alternate scenario is that HI has been stripped from the edges of the outermost spiral arms - one towards us and the other away from us. Since NGC 2820 is an almost edge-on galaxy, this model is not distinguishable from the above. This model can also explain the observed kinematic features of the loop. The trailing velocity field will be due to the rotation velocity of the gas in the outer spiral arms which might not be the tangent points for those lines of sight. The large line widths would again result from increased random motion as the stripped gas meets the IGrM. However given sufficient time, the central hole in HI should get filled up in this model.

With the present data, we cannot distinguish between the two models.

We estimate a velocity width of about 80 $\mathrm{km\,s^{-1}}$ along the loop. This radial velocity is possibly dominated by rotation since NGC 2820 is a highly inclined galaxy. However, if we assume this to be the outflow velocity then for a loop height of 4.9 kpc, this translates to an age of 60 million years.

Notice that the HI after reaching a certain height seems to be falling back towards the disk (see Fig 5.4 (a)). Vollmer et al. (2001) in their simulations for investigating the role of ram pressure stripping in the Virgo cluster have found that ram pressure can cause a temporary increase in the central gas surface density and in some cases even lead to a significant fraction of the stripped off atomic gas to fall back onto the disk. Such a process could be active in the case of NGC 2820.

(c) Tidal stripping

Interaction usually creates irregular morphology and tidal tails that can stretch the spiral arms. The shape of the parent galaxy and the tidal tails can assume a variety of shapes after the interaction (for example, see simulations by Toomre & Toomre 1972, Barnes 1988, Howard et al. 1993). The members of Ho 124, especially the triplet, have undergone close encounters which is evident from the numerous tidal features seen in the system as described in section 5.4. However it is not clear how tidal interaction alone can give rise to the HI loop as observed in NGC 2820. If one assumes that all the HI features seen to the north of the disk of NGC 2820 ie. the warped extension, the small protrusions, the loop and the streamer are parts of a tidal tail, it is difficult to explain the origin of such a large distortion (stripped HI mass $> 7 \times 10^8$ $M_\odot$) due to a retrograde interaction with a galaxy (NGC 2814) whose HI content is less than that in the HI loop. Moreover no such tail is visible in the opposite direction which such a strong tidal interaction should have produced. Thus, it appears unlikely that the loop is a result of tidal interaction alone. But on the other hand evolution of the system has obviously been affected by tidal interactions e.g. Artamonov et al. 1994 note enhanced star formation due to the tidal interaction. Hence any model that explains the HI loop should include tidal interaction. However it is beyond the scope of this chapter to make any quantitative estimates of the tidal interaction which require detailed simulations.

We suggest that the loop could have been created by the combined effect of ram pressure and tidal forces acting on NGC 2820.

5.6 Discussion

In this chapter, we have described four main results arising from our observations, (i) the steep radio continuum bridge between the triplet, (ii) the sharp cutoffs in different galactic constituents observed in three members of the group, (iii) one-sided HI loop in NGC 2820 and (iv) various signatures left behind by the tidal interaction. HI is detected from the bridge with a mean column density of 4.4×10^{19} cm^{-2}. The bridge has a steep synchrotron spectrum with a spectral index of $-1.8^{+0.3}_{-0.2}$ and hence has large energy losses caused by synchrotron and/or inverse Compton processes or a steep electron spectrum. From equipartition arguments, we find that relativistic particles and magnetic field dominate the bridge evolution. It contains a small fraction of the total sychrotron emission in the system and it is interesting to contrast it with the Taffy galaxies in which the bridge emission constitutes half of the total synchrotron emission in the system (Condon et al. 1993).

A sharp cutoff in HI (see Fig 5.3 & Fig 5.5 (a)), radio continuum (see Fig 5.1 (a)) or optical blue band (see Fig 5.5) is clearly evident in three members of Ho 124. The fourth member (Mrk 108) is small and too tidally disrupted. The above is schematically summarized in Fig 5.10. We suggest that the sharp boundaries are caused by motion of the galaxies in the IGrM. In the case of NGC 2814, the optical disk appears to be viewed edge-on with zero position angle and the compression in radio continuum and HI is seen to be perpendicular to the major axis of the disk in the north in the sky plane. Moreover the radio continuum and HI are confined to well within the optical disk. In NGC 2820, the HI in the southern side is sharply truncated. The interaction between the triplet appears to have left behind a trail of tidal debris like the streamer, the HI blobs and the radio continuum tail of NGC

2814. The HI loop could be a result of both tidal effects and ram pressure. If the tidal effects have reduced the surface density of HI in the disk of NGC 2820, then ram pressure of the IGrM should have been able to strip the outlying HI giving rise to the HI loop. The solid arrows near NGC 2820 and NGC 2814 in Fig 5.10 indicate the direction of motion of those galaxies as we can deduce in the sky plane from the sharp truncations. However, the ambiguity of the sharp cutoff in HI in the north and the enhanced star formation in the south of NGC 2805 makes its direction of motion in the IGrM ambiguous. If we interpret the star formation ridge to be due to the interaction with IGrM, then NGC 2805 appears to be moving towards the south-west. If this is true then the three galaxies seem to be moving in different directions. However if we interpret the sharp HI boundary in the north of NGC 2805 as due to ram pressure, then the galaxy is moving towards the north. In short, we cannot comment on the direction of motion of NGC 2805 from the existing observations.

We compared the ram pressure and the equivalent pressure in the different phases of the interstellar medium in NGC 2820 to examine its effect on different constituents of the medium which show distinct morphologies and hence understand the observational picture sketched in Fig 5.10. Assuming a typical particle density of 4×10^{-4} cm^{-3} for the IGrM, we estimated a ram pressure of 4170 cm^{-3} K for the IGrM. We estimate a magnetic pressure $\sim$ 5000 cm^{-3} K in the radio continuum halo. The two pressures are comparable. For the Hα seen in the extended-diffuse ionized gas (e-DIG), Miller & Veilleux (2003) estimate an emission measure of about 8 pccm^{-6} and a size of 2 kpc. If we assume a filling factor of 0.1 (see Fig 10 in Miller & Veilleux (2003)) for e-DIG then for a temperature of 10^4 K, the pressure in the gas is 2000 cm^{-3} K and the difference by a factor of two could easily be due to an incorrect

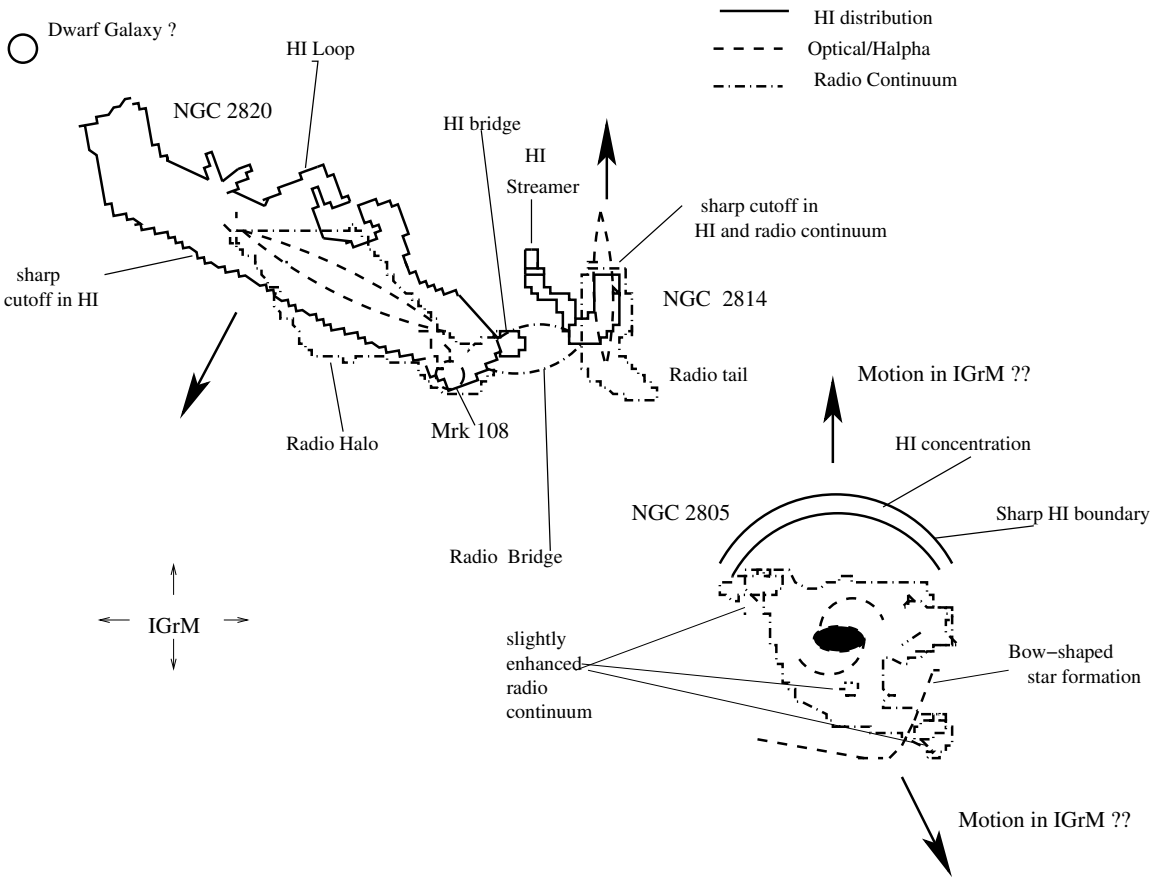

Figure 5.10: A Schematic of the group Holmberg 124. The solid line represents the observed HI 21cm distribution, the dashed line is for DSS optical distribution and the dash-dotted line is for the radio continuum distribution in the group. The thick arrows show the direction of motion of the galaxies in the group as inferred from the sharp edge. Note the ambiguity in the direction of motion of NGC 2805. Please note that the figure is not to scale.

filling factor assumed by us. The pressure in the e-DIG is also comparable to the ram pressure. Lastly we estimate the pressure in the HI gas. Since the sharp edge in HI is unresolved by our beam, we used a column density of 3.2×10^{20} cm^{-2} (the second contour) to estimate an atomic density of 0.02 cm^{-3} for a volume filling factor of 0.4 (taken from our Galaxy for warm neutral medium). If we use a temperature of 5000 K which is typical of the warm neutral medium in our Galaxy, then the pressure is 100 cm^{-3} K. The HI pressure is significantly lower than the ram pressure due to the IGrM. Thus we can understand the observed picture where HI has a swept-back appearance in the south of NGC 2820 which could be due to ram pressure affecting whereas the radio continuum and Hα seem to extend out beyond HI and are either expanding or in pressure equilibrium with the IGrM. For this the galaxy should be in motion along the south-west as shown by the solid arrow in Fig 5.10.

The HI distribution in NGC 2805 is asymmetric with enhanced column densities in clumps towards the north (see Fig 5.5 (a)). The HI is extended east-west along the highly-disturbed northern optical spiral arm and is confined to the optical disk. The radio continuum emission in NGC 2805 is fairly weak (see Fig 5.5 (b)), with localised peaks in the south and northeast, and bearing little resemblance either to the optical or to the HI distribution. The central region of the galaxy is bright in the JHK near-IR bands and in the optical band but faint in radio continuum (Fig 5.5 (b)) which is intriguing. In short, this massive galaxy appears to be highly disturbed, the reason for which is not clear from existing observations.

Thus, we end with a picture (somewhat speculative) of this group as derived from the present and other existing observations as shown in Fig 5.10. NGC 2820 has probably undergone a retrograde tidal encounter with

NGC 2814 which has left behind a trail of tidal debris. A HI streamer probably detached from NGC 2820 is seen projected onto NGC 2814 (see Fig 5.10) but is kinematically distinct from NGC 2814. The interaction has also probably given rise to a bridge connecting the two galaxies and a tail of radio continuum emission in the south of NGC 2814. Star formation has been triggered in south-west parts of the disk of NGC 2820, in Mrk 108 and in the southern parts of NGC 2814 (see Fig 5.7 (c)). Using about half the upper limit on the electron density estimated from the upper limit on the X-ray emission (Mulchaey et al. 2003), we estimate the ram pressure force of the IGrM to be comparable to the gravitational pull of the disk of NGC 2820. Since tidal interaction has obviously influenced the group, we suggest that the loop could have formed by ram pressure stripping if tidal effects had reduced the surface density of HI in NGC 2820. We suggest that the HI loop which is several kpc high and across could have been produced by the combined effects of ram pressure and tidal forces. Moreover we find sharp truncations to the HI in some of the group members which we believe supports the ram pressure explanation. If we assume that this is true then NGC 2814 is probably moving towards the north and NGC 2820 towards moving in the south-east direction (solid arrows in Fig 5.10). From the existing observations there is ambiguity in the direction of motion of NGC 2805. Considering all this, we suggest that the group evolution is being influenced by both tidal forces due to the mutual interactions and ram pressure due to the motion of the galaxies in an IGrM.

Since the IGrM is not detected in X-rays (Mulchaey et al. 2003) but we tend to believe shows detectable effect on the galaxies in Ho 124, we suggest that the IGrM densities in this group should not be too low. Mulchaey et al. (1996, 2003) have suggested that the non-detection of X-rays in late-type

groups could be due to lower temperatures or densities. The detection of a 0.2 keV (Wang & McGray 1993) IGrM in the Local group which is a late-type group indicates that such groups do have a IGrM. It is more difficult to detect lower temperature gas in groups for several reasons like the enhanced absorption of such soft X-rays by galactic HI and the increased strength of the X-ray background. One clearly needs to explore other avenues of detecting this gas.

5.7 Summary and concluding remarks

- We detect the faint radio continuum bridge at 330 MHz connecting NGC 2820+Mrk 108 with NGC 2814 which was first detected by van der Hulst & Hummel (1985) at 1465 MHz. The bridge has a a spectral index of $-1.8^{+0.3}_{-0.2}$ which is steeper than the -0.8 quoted by van der Hulst & Hummel (1985). HI is detected from most of the bridge at a velocity close to the systemic velocity of NGC 2820 and has a mean column density of 4.4×10^{19} cm^{-2}. No Hα emission is associated with the bridge.

- We detect radio contiuum from all the members of the group. A radio halo is clearly detected around NGC 2820 in the radio continuum with a 10% peak flux density extent of 4.2 kpc at 330 MHz and a spectral index of -1.5. A radio halo is also detected around NGC 2814. The radio continuum at 330 MHz from NGC 2805 is fairly weak bearing little resemblance to either the HI distribution or the optical emission. The centre of the galaxy is intriguingly faint.

- HI is detected from all the galaxies in the group. The heliocentric

systemic velocity of NGC 2820 is 1577 $\mathrm{km\,s^{-1}}$ and its rotation velocity is 175 $\mathrm{km\,s^{-1}}$. The linear extent of the HI disk of NGC 2820 is about 48 kpc and its HI mass is 6.6×10^9 $\mathrm{M_\odot}$. The HI emission associated with Mrk 108 is clearly detected at 1417 $\mathrm{km\,s^{-1}}$ and it encloses a HI mass of 6.1×10^7 $\mathrm{M_\odot}$.

- We detect various tidal features close to NGC 2814. The radio continuum disk and HI disk of NGC 2814 are tilted with respect to the optical disk. A HI streamer is seen to emerge from the south of NGC 2814 but the two are are kinematically distinct. The velocity field of the streamer is similar to parts of NGC 2820 close to it. The streamer has a sky plane extent of 12.6 kpc and encompasses an HI mass of 1.3×10^8 $\mathrm{M_\odot}$. A tail emerging from the south of NGC 2814 and extending westwards is detected in the radio continuum. The tail has a spectral index of -1.6.

- We detect HI gas located about 11.5 kpc to the north-east of NGC 2820 whose dynamical mass is 1.4×10^9 $\mathrm{M_\odot}$ and which might possibly be a tidal dwarf galaxy. However, deep Hα observations are required to confirm this. The velocity of this gas is similar to the velocity field of the part of NGC 2820 closest to it.

- We observe a sharp cutoff in HI on the southern rim of NGC 2820 and a sharp truncation in HI and radio continuum to the north of NGC 2814. Iso-velocity contours of the extraplanar HI in NGC2820 seems to diverge away from the minor axis of the galaxy suggesting that extraplanar HI is possibly trailing the disk rotation. We suggest that these features could be a result of ram pressure due to motion of the galaxies in the IGrM along the solid arrows shown in Fig 5.10 since

simple estimates of pressure in different components of the interstellar medium in NGC 2820 suggest that ram pressure exceeds the pressure in HI by a factor of many. However this needs to be verified.

- We report detection of a gigantic HI loop arising to the north of NGC 2820. The loop is $\sim$ 17.5 kpc across and rises up to $\sim$ 4.9 kpc. It encompasses an HI mass of 6×10^8 $M_\odot$. No radio continuum or Hα emission is associated with this loop. We present possible origin scenarios which include a central starburst, ram pressure stripping and tidal stripping. We do not favour a central starburst mainly because of the absence of detectable ionized gas in the loop. We tend to favour the ram pressure scenario. Using the upper limit on the X-ray luminosity from Ho 124 (Mulchaey et al. 2003), we estimate an upper limit on the electron density of 8.8×10^{-4} cm^{-3}. Our calculations using half this electron density show that ram pressure force of the IGrM is comparable to the gravitational pull of the disk. Hence we suggest that this loop could have been formed due to ram pressure stripping if tidal forces had reduced the surface density of HI in NGC 2820.

- The group under study exhibits multiple signatures of tidal interaction and possibly ram pressure. Thus, we suggest that the evolution of Ho 124 may be governed by both tidal interaction and ram pressure due to the motion of the galaxies in the IGrM.

5.8 References

Ananthakrishnan S., Kantharia N.G., Nityananda R., 2003, BASI, 31, 421

Ananthakrishnan S., & Rao A.P. 2002, Multicolour Universe. In International conference on Multi Colour Universe, ed. R. Manchanda & B. Paul, 233

Artamonov B.P., Bruevich V.V., Popravko G.V., 1994, A Rep, 38, 597 Barnes J.E., 1988, ApJ, 331, 699

Binney J. & Merrifield M., 1998, Galactic Astronomy, Princeton University Press

Boomsma R., Osterloo T.A., Fraternali F., van der Hulst J. M., Sancisi R., 2004, astro-ph/0410055.

Bosma, A., Casini, C., Heidmann, J., van der Hulst, J. M., van Woerden, H. 1980, A&A, 89, 345, astro-ph/0406169

Condon, J. J. 1992, ARA&A, 30, 575

Condon, J. J., Helou, G., Sanders, D. B., Soifer, B. T. 1990, ApJS, 73, 359

Condon, J. J., Helou, G., Sanders, D. B., Soifer, B. T. 1993, AJ, 105, 1730

Davis, D. S., Mulchaey, J. S., Henning, P. A., 1997, AJ, 114, 613 Fraternali, F., Oosterloo, T. A., Sancisi, R., van Moorsel, G. 2001, ApJ, 562, L47

Gil de Paz, A., Madore, B. F., Pevunova, O., 2003, ApJS, 147, 29

Gunn, J. E., & Gott III, J. R. 1972, ApJ, 176,1

Heckman, T. M., Armus, L., Miley, G. K., 1990, ApJS, 74, 833

Helou, G., Soifer, B. T., Rowan-Robinson, M. 1985, ApJ Lett., 298, L7

Howard, S., Keel, W. C., Byrd, G., Burkey, J. 1993, ApJ, 417, 502

van der Hulst, J. M., & Hummel, E. 1985, A&A, 150, l7

Hummel, E., & van der Hulst, J. M. 1989, A&AS, 81, 51

Kantharia, N. G., Ananthakrishnan, S., Nityananda, R., Hota, A. 2005,

A&A, 435..483

Miller, S. T. & Veilleux, S. 2003, ApJS, 148, 383

Mulchaey, J. S., David, D. S., Mushotzky, R. F., Burstein, D. 1993, ApJ, 404, L9

Mulchaey, J. S., David, D. S., Mushotzky, R. F., Burstein, D. 1996, ApJ, 456, 80

Mulchaey, J. S., Mushotzky, R. F., Burstein, D., David, D. S. 1996b, ApJ, 456, L5

Mulchaey, J. S., David, D. S., Mushotzky, R. F., Burstein, D. 2003, ApJS, 145, 39

Mulchaey, J. S. 2004, in Clusters of Galaxies: Probes of Cosmological Structure and Galaxy Evolution from the Carnegie Observatories Centennial Symposia, Carnegie Observatories Astrophysics Series, Vol 3 ed: J. S. Mulchaey, A. Dressler, A. Oemler, Cambridge Univ. Press, 354

Osmond, J. P. F., & Ponman, T., 2004, MNRAS, 350, 1511

Sarazin, C. L. 1986, Revs of Mod Phys, 58, 96

Swarup, G., Ananthakrishnan, S., Kapahi, V., Rao, A.P., Subrahmanya, C.R., Kulkarni, V.K., 1991, Current Science, 60, 95

Toomre, A., & Toomre, J. 1972, ApJ, 178, 623

Vollmer, B., Cayatte, V., Balkowski, C. 2001, ApJ, 561, 708

Wang, Q. D. & McCray, R. 1993, ApJ, 409, L37

CHAPTER 6

HI—study of of three long-tailed irregular galaxies in Abell 1367.

6.1 Abstract

We present the results on the distribution and kinematics of H*i* gas with higher sensitivity and in one case of higher spectral resolution as well than reported earlier, of three irregular galaxies CGCG 09773, 09779 and 09787 (UGC06697) in the cluster Abell 1367. These galaxies are known to exhibit long (50−75 kpc) tails of radio continuum and optical emission lines (Hα) pointing away from the cluster centre and arcs of starformation on the opposite sides of the tails. These features as well as the HI properties, with two of the galaxies (CGCG 09773 and 09779) exhibiting sharper gradients in HI intensity on the side of the tails, are consistent with the HI gas being affected by the ram pressure of the intracluster medium. However the HI emission in all the three galaxies extends to much smaller distances than the radio-continuum and Hα tails, and are possibly still bound to the parent galaxies.

Table 6.1: Basic data on these three galaxies.[a]

Galaxy[a] CGCG	RA[b] h m s	DEC[b] ° ′ ″	Type[c]	a×b[d] ′ × ′	V_{sys}[e] km /s	D[f] Mpc	S_{Hi}[g] Jy km/s	S[h] mJy
097073	11 42 56.4	+19 57 58	SAcd, pec	0.5×0.5	7275±6	86	1.0	25
097079	11 43 13.4	+20 00 17	Irr	0.5×0.4	7000±9	86	0.8	15
097087	11 43 49.1	+19 58 06	Im	1.9×0.3	6725±2	86	3.5	60

a Taken from the NASA Extragalactic Database (NED), unless stated otherwise.
b Optical position of the galaxy from NED in J2000.
c Morphological type.
d Optical major and minor axes.
e Heliocentric systemic velocity.
f Assumed distance to the object from Gavazzi et al. (2001b). For this distance 1″=417 pc.
g Total HI line flux density taken from Arecibo measurements by Gavazzi (1989)
h Total 1.4 GHz radio continuum flux density from the VLA D-array observations of Gavazzi (1989).

6.2 Introduction

Clusters of galaxies, which are the most massive gravitationally bound systems in the Universe, provide us with an opportunity to study the effects of the local environment on the structure, evolution and star formation history of its constituent galaxies (e.g. Gunn & Gott 1972; Dressler 1980; Boselli & Gavazzi 2006). Besides interactions with neighbouring galaxies, the hot intracluster medium (ICM) is also likely to play an important role in influencing the observed properties of the galaxies. Simulations of stripping of spirals falling into a cluster by the ram pressure of the ICM have shown this to have a range of manifestations (Abadi et al. 1999; Quillis et al. 2000; Vollmer et al. 2001; Schulz & Struck 2001; Bekki & Couch 2003; Roediger & Brüggen 2006). For example, while the galactic interstellar medium (ISM) may be largely stripped in a high ICM density region leading to a suppression

of star formation, the star formation rate may be enhanced in a less dense ICM region where the ISM is only compressed rather than being completely stripped. In addition to these effects, clusters of galaxies also provide us with important insights towards understanding the formation of large-scale structures in the Universe (e.g. West et al. 1991; Katz & White 1993). Many of these clusters have sub-structures, suggesting that these are dynamically young systems still in the process of formation.

The rich cluster Abell 1367 is an interesting nearby system at a distance of ∼86 Mpc where three subgroups containing a number of star-forming galaxies are falling into the core of the cluster (see Cortese et al. 2004). The cluster lies at the intersection of two filaments and has been suggested to be a prototype of a dynamically young cluster (e.g. Cortese et al. 2004). Optical and radio observations of individual galaxies by Gavazzi et al. (1995, 2001a,b) also suggest infall of galaxies into the cluster core. Gavazzi & Jaffe (1987) reported the discovery of extended tails of radio continuum emission associated with three irregular galaxies in the north-west region of A1367, namely CGCG 97073, 97079 and 97087 (UGC6697). Tails of Hα emission associated with the radio tails have also been reported by Gavazzi et al. (2001a,b). We have listed the basic properties of these three galaxies in the Table 6.1. All the three galaxies have an asymmetric radio structure with a 'head' in the up-stream side roughly towards the cluster centre and a 'tail' on the opposite down-stream side with the size of the radio emission exceeding the size of the optical galaxy (e.g. Gavazzi 1978; Gavazzi & Jaffe 1987). The galaxies CGCG 97073 and 97079 also exhibit an arc of HII regions suggesting star formation on their leading edges approximately towards the cluster centre (Gavazzi et al. 1995, 2001a,b). These features are consistent with the paradigm where ram pressure due to the ICM is significantly affecting

the observed properties of the galaxies. Observations of the atomic HI and molecular CO and H_2 gas are also consistent with the ram pressure paradigm. Gavazzi (1989) found the galaxies to be deficient in HI compared with field galaxies from observations with the Arecibo telescope. The reported interferometric observations of HI which only plotted the locations of the peaks of emission in a few channels showed the gas to be displaced in the direction of the radio tails (Gavazzi 1989; Dickey & Gavazzi 1991; hereafter referred to as DG91), while the molecular gas content of the galaxies appeared to be normal with the distribution exhibiting no strong asymmetries (Boselli et al. 1994).

In this chapter we present the detailed distribution and velocity field of HI gas in all the three galaxies, CGCG 97073, 97079 and 97087 (UGC6697), with better sensitivity and in one case, CGCG 97079, with higher spectral resolution as well, using archival Very Large Array (VLA) data with both the C- and D-configurations. These observations reveal new details which we compare with observations at other wavelengths and simulations of ram pressure stripping.

6.3 Observations and data analysis

The observing log for the observations is presented in Table 6.2, which is arranged as follows. Column 1: Name of the telescope where we list the configuration for the observations. The program code for the observations in 1988 is AG264 while for those in 1999 it is AB900. Columns 2 and 3: Dates of the observations and the time, t, spent on the source in hours. Column 4: The channel separation in units of kHz and km s^{-1}; column 5: the bandwidth of the observations in units of MHz and km s^{-1}.

Table 6.2: H I Observation log

Telescope Array	Obs. date	time hrs	Ch. sp. kHz, km/s	band width MHz, km/s
VLA-D	26Mar1999	9	98, 22	3.1, 650
VLA-C	02Apr1988	8	391, 86	12.5, 2600
VLA-D	25Jul1988	3	391, 86	12.5, 2600

Table 6.3: Observational parameters and some results from the HI images

VLA	Vel res. km /s	Beam size maj. ″	min. ″	PA °	map rms mJy /b	spec. rms mJy	S 73 Jy km/s	S 79	S 87	Δv 73 km /s	Δv 79	Δv 87
(1)	(2)	(3)	(4)	(5)	(6)	(7)	(8)	(9)	(10)	(8)	(9)	(10)
D	22	43.2	41.8	−51.3	0.33	0.4		0.38			190	
CD	86	22.5	19.9	71.8	0.30	0.7	0.92	0.52	2.67	170	170	600

The observations were made in the standard fashion, with each source observation interspersed with observations of the phase calibrator. The primary flux density and bandpass calibrator was 3C286 whose flux density was estimated on the Baars et al. (1977) scale using the 1999.2 VLA values. The data analysis was done using the Astronomical Image Processing System (AIPS) of the National Radio Astronomy Observatory. The AIPS task UVLIN was used for continuum subtraction and the multi-channel data were then CLEANed using IMAGR.

6.4 Observational results

The VLA C− and D−array data which has a velocity resolution of 86 km s^{-1} were combined to create a data cube with a spatial resolution of ∼21″ for all the three galaxies, while the VLA D-array data with a velocity resolution of 22 km s^{-1} was used to image the galaxy CGCG 097079. The observational parameters and some results from the HI images are presented in Table 6.3

which is arranged as follows. Columns 1 and 2: The configuration of the VLA observations and the spectral resolution in units of km s^{-1}; columns 3, 4 and 5: the major and minor axes of the restoring beam in arcsec and its position angle in deg.; columns 6 and 7: the rms noise in the image and the spectrum in units of mJy/beam and mJy respectively; columns 8, 9 and 10: the total HI flux density in units of Jy km s^{-1} for the galaxies CGCG 097073, 097079 and 097087 respectively.

(a) CGCG 097073

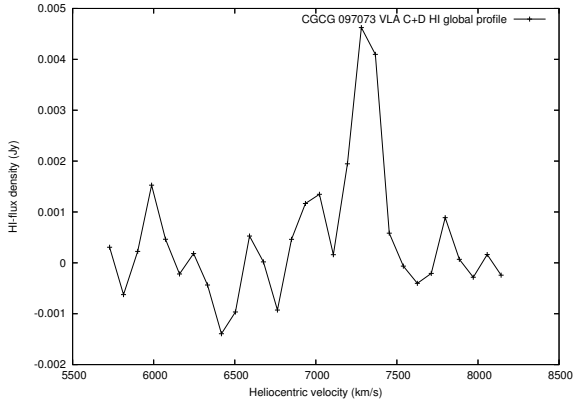

Figure 6.1: CGCG 097073: HI global profile of the galaxy observed with a spatial and spectral resolution of $\sim 21''$ and 86 km s^{-1}.

The global profile obtained from the combined VLA C− and D−array data with a spatial resolution of $\sim 21''$ and a velocity resolution of 86 km s^{-1} does not show any significant asymmetry, consistent with the spectrum obtained with the Arecibo telescope (Gavazzi 1989). Significant emission is seen in three channels whose velocities cover a range of $\sim$200 km s^{-1}. The width of the HI spectrum obtained with the Arecibo telescope is 294 km s^{-1}. Both these values are significantly larger than the velocity width of 85 km s^{-1} estimated from the Tully Fisher relation and inclination of the optical disk by

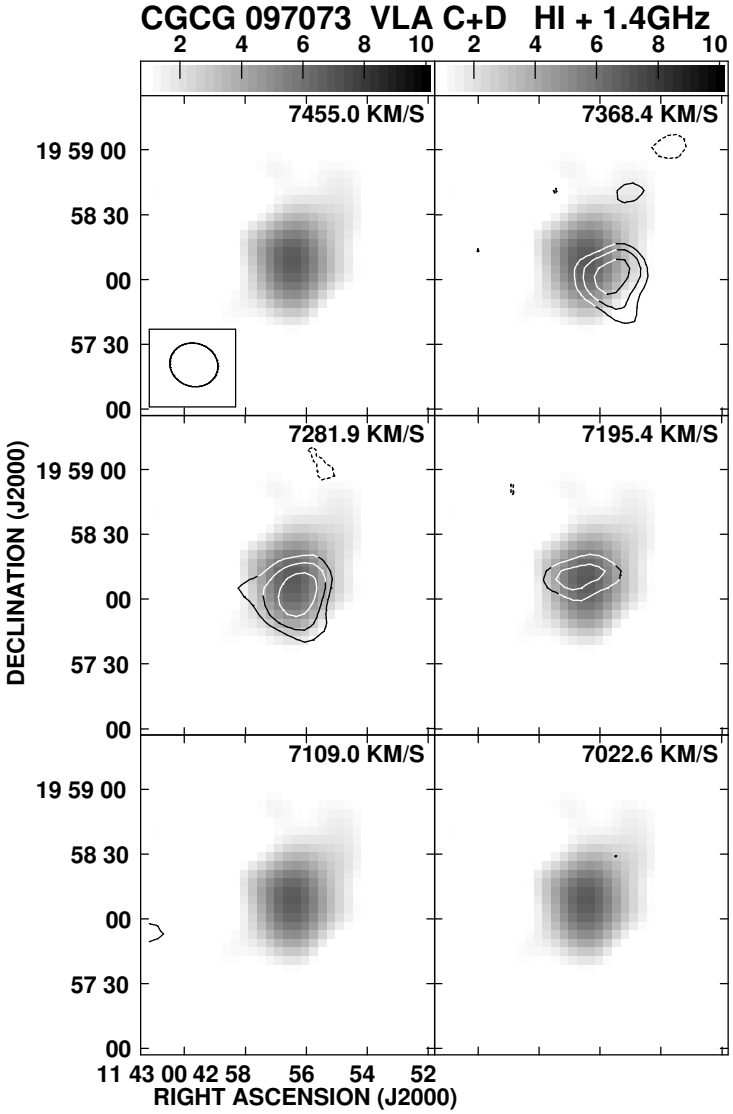

Figure 6.2: CGCG 097073: The HI channel maps in contours have been superimposed on the gray scale single channel continuum image obtained from the same data with a resolution of $\sim 21''$. The contour levels are 0.3 $\times$ (-4, -2.82, 2.820, 4, 5.65 ...) mJy/beam.

Gavazzi (1989), suggesting strong kinematic effects leading to non-circular motions in the ISM. The total HI mass estimated from the global profile

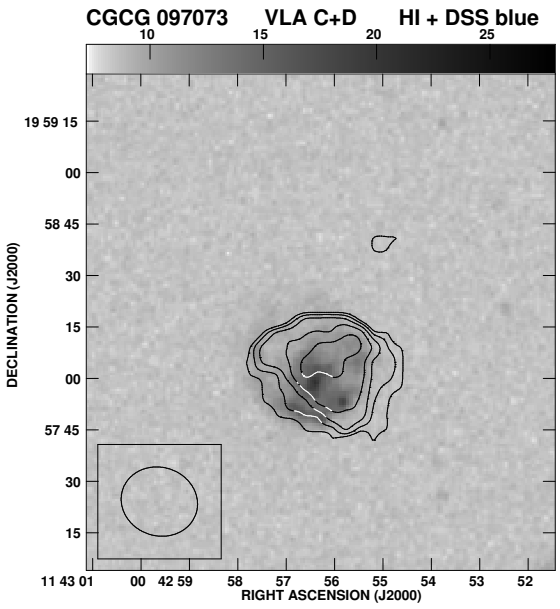

Figure 6.3: CGCG 097073: Total intensity HI contour map with a resolution of $\sim 21''$ has been superimposed on the DSS blue-band image. The contour levels are 2.358×10^{20} cm^{-2} or 1.89 M$_\odot$ pc^{-2} in steps of multiples of $\sqrt{2}$.

is 1.6×10^9 M$_\odot$. The peak of the HI emission is consistent with the optical systemic velocity of 7225 km s^{-1}. The HI emission channel maps in contours are shown superimposed on the radio-continuum, single channel gray scale image in Fig. 6.2. It is clear that the position of the peak of HI emission varies from channel to channel. DG91 reported HI emission at 7282 and 7196 km s^{-1} with the lower velocity detection towards the northern edge of the optical image. We clearly see these two features but also emission at 7368 km s^{-1} towards the south-western part of the optical image. We have not been able to confirm the possible weak component towards the north-west with a velocity of 7109 km s^{-1} noted by DG91.

A moment map generated from these three channels with a 3σ cut off is presented in the Fig. 6.3. The total intensity HI (moment 0) map is

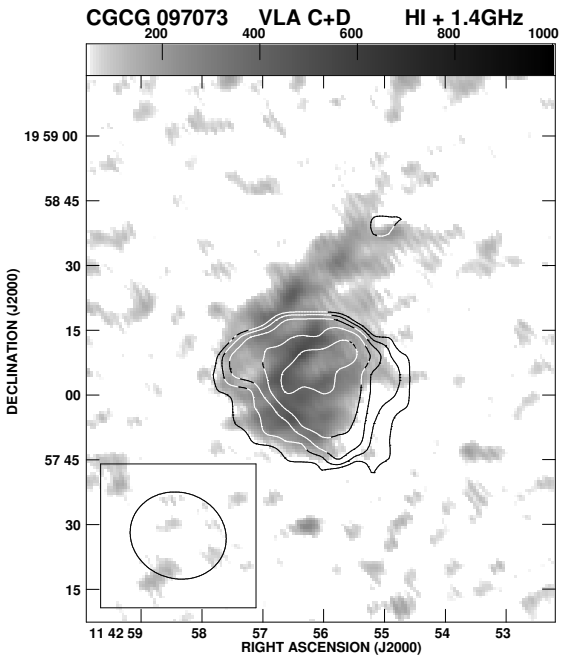

Figure 6.4: CGCG 097073: Same HI map on the 1.4-GHz radio continuum image made with a resolution of $\sim 4''$. The contour levels are $2.358 \times 10^2 0$ cm^{-2} or 1.89 M$\odot$ pc^{-2} in steps of multiples of $\sqrt{2}$.

shown superimposed on the DSS blue-band optical image of the galaxy. On the southern edge of the optical disk the stellar arc is visible with the HI contours having a relatively sharper edge on the northern side. This sharper HI contours on the opposite side of the optical starforming arc is also visible in the galaxy NGC2805, a member of the group Ho 124 (Bosma et al. 1980 ; Kantharia et al. 2005; Chapter 5). Coincidentally NGC2805 is also seen nearly face on and the galaxies in that group show evidence of ram pressure stripping and galaxy interactions. The accumulation of gas in the down-stream region can be qualitatively understood as follows. In the region where the gravitational pull and the ram pressure come to a balance and gas which is still bound to the galaxy may just travel tangentially. Here, the rotating gas

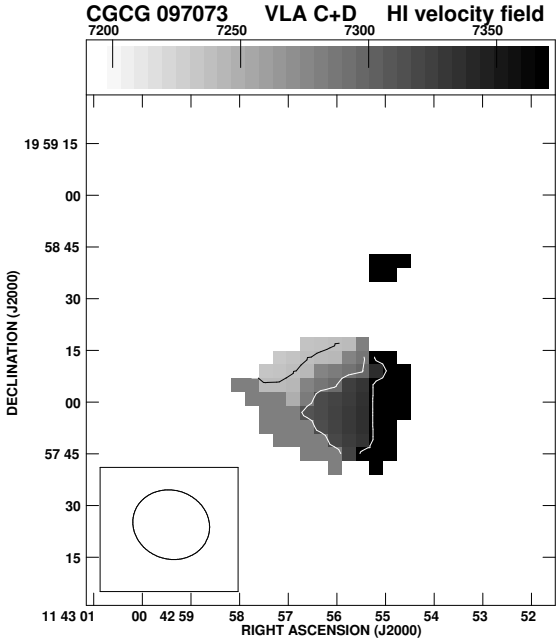

Figure 6.5: CGCG 097073: The intensity weighted HI velocity field made from the same image cube with a spatial and spectral resolution of $\sim 21''$ and 86 km s^{-1} respectively. The contours are 7240, 7300 and 7360 km s−1 from east to west.

following the ram pressure will reach the down-stream region faster while the gas rotating against the ram pressure direction will face a greater resistance and thus spending a longer time on the down-stream region. Due to ram pressure one would expect the up-stream side to get compressed and trigger star formation. Although at optical wavelengths there is an arc of HII regions possibly triggered by compression of gas due to ram pressure, the HI intensity contours do not appear to be particularly edge-brightened.

The moment 0 image is also shown superimposed on a radio-continuum image at 1.4 GHz with an angular resolution of $\sim 4''$ made from archival VLA AB-array data. At this resolution there is no clearly defined peak of radio continuum emission. The southern arc-shaped region seen in radio continuum

is also slightly offset from the southern most peak of the arc seen at optical wavelengths. Although this higher resolution image shows the orientation of the tail to the north-west, a larger-scale image with lower angular resolution shows that the tail extends almost to the north (Gavazzi & Jaffe 1987). We can see that on the northern side there is no correspondence of the HI and radio continuum emission in the tail. Hence it is possible that we do not detect HI from the stripped tail but the HI gas is still largely rotating about the centre of the galaxy. Although the moment-one image shows evidence of rotation, observations of higher spectral resolution are required to determine the velocity field.

(b) CGCG 097079

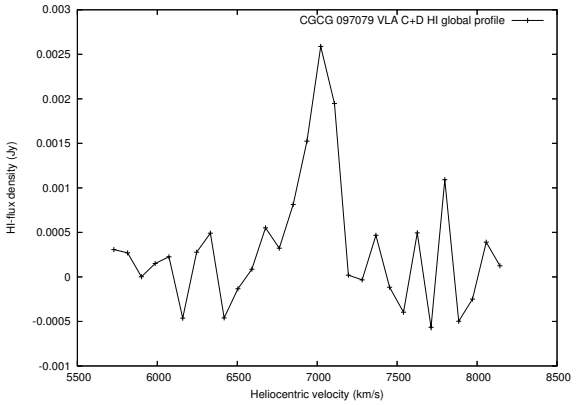

Figure 6.6: CGCG 097079: Global HI profile of the galaxy made with a spatial and spectral resolution of $\sim$21$''$ and 86 km s^{-1} respectively.

The global profiles of HI emission made from the combined VLA C-and D-array data with a spectral resolution of $\sim$86 km s^{-1} and the VLA D-array data with a spectral resolution of $\sim$22 km s^{-1} are shown in Fig. 6.6, 6.7 and 6.8. The total mass estimated from the global spectra is 0.9×10^9 M$_\odot$. In Fig. 6.9 we present the higher spatial resolution channel maps showing

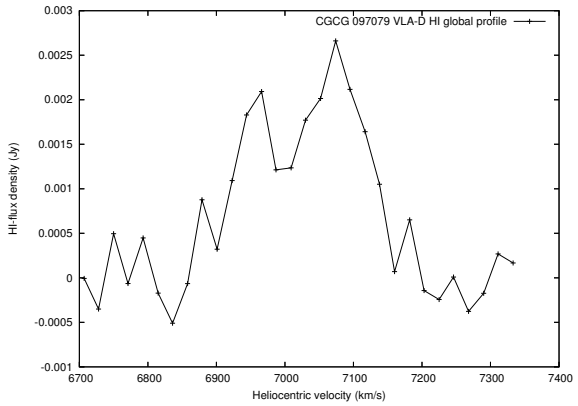

Figure 6.7: CGCG 097079: Global HI profile of the same galaxy made with a spatial and spectral resolution of $\sim 42''$ and 22 km s^{-1} respectively.

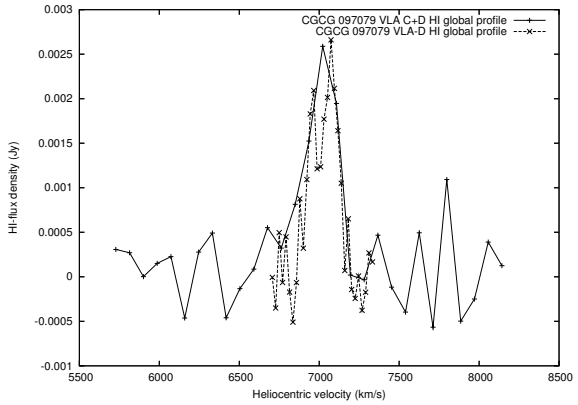

Figure 6.8: CGCG 097079: Global HI profile of the above two plots plotted together.

the HI intensity superimposed on the single-channel radio-continuum image shown in gray scale. The HI emission is seen in three channels with velocities of 7109, 7023 and 6936 km s^{-1} with the emission peak shifting from north-west to south-east as we go lower in velocities. DG91 also reported HI at two velocities one having a peak to the north-west with a velocity of 7023 km s^{-1} and the other tentative detection on the western boundary of the optical disk at a velocity of 7109 km s^{-1}. We detect the emission in a third channel at a velocity of 6936 km s^{-1} giving total velocity width of $\sim$260 km s^{-1}.

Moment maps were generated including only points above 3σ and only

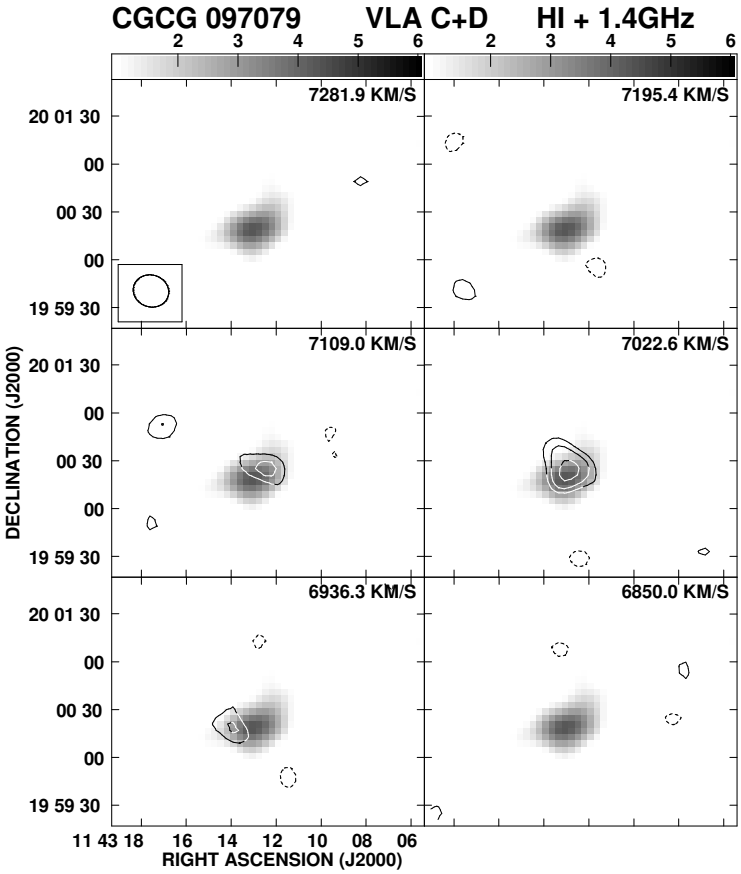

Figure 6.9: CGCG 097079: The HI channel maps in contours has been superimposed on the gray scale single channel continuum image obtained from the same data with a resolution of $\sim$21″. The contour levels are 0.3 × (-4, -2.82, 2.820, 4, 5.65 ...) mJy/beam.

three channels with a clear detection were combined. A superposition of the the HI total-intensity contours on the DSS blue-band image show the south-eastern peak of HI emission to be coincident with the bright starforming region believed to be formed due to the ram pressure compression of the ISM. Most of the HI emission is on the north-western side of this peak, along a similar PA as that of the radio-continuum tail. A superposition of the contours of HI emission on a VLA B-array radio continuum image made

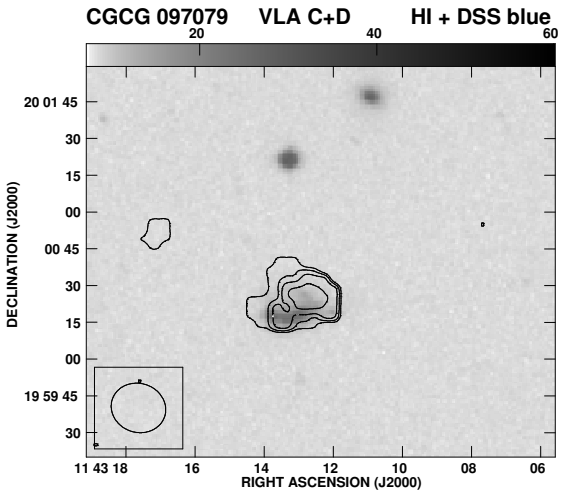

Figure 6.10: CGCG 097079: Total intensity HI contour map with a resolution of $\sim 21''$ has been superimposed on the DSS blue-band image. The contour levels are $2.358 \times 10^2 0$ cm^{-2} or 1.89 M$\odot$ pc^{-2} in steps of multiples of $\sqrt{2}$.

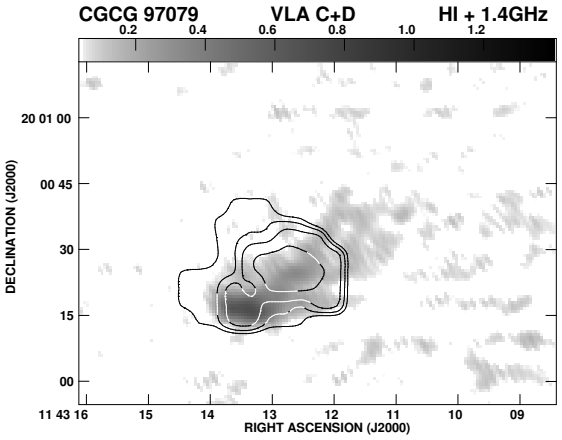

Figure 6.11: CGCG 097079: Same HI map on the 1.4GHz radio continuum image made with a resolution of $\sim 4''$. The contour levels are $2.358 \times 10^2 0$ cm^{-2} or 1.89 M$\odot$ pc^{-2} in steps of multiples of $\sqrt{2}$.

from archival data with an angular resolution of $\sim 4''$ (Fig. 6.11) as well as comparison with the continuum image of Gavazzi et al. (1995) shows that

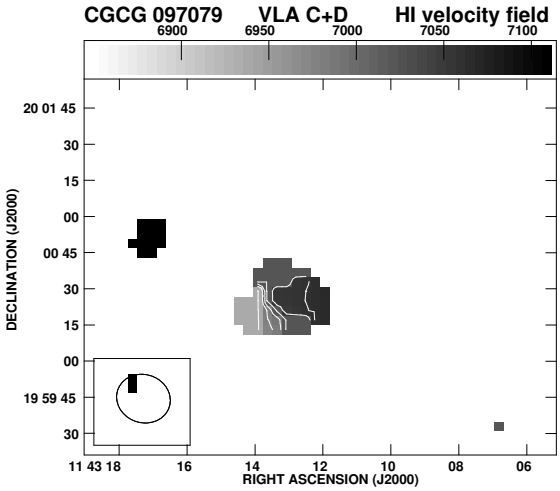

Figure 6.12: CGCG 097079: The intensity weighted HI velocity field and the line width image made from the same image cube with a spatial and spectral resolution of $\sim$21$''$ and 86 km s^{-1} respectively. The contours are 6940, 6980, 7000, 7020, 7040 and 7060 km s^{-1} from east to west

the radio continuum emission extends well beyond the HI emission. There is a hint of sharper cut off of the HI contours on the western side which is again somewhat opposite to the arc of star formation, similar to the case of the face on galaxy CGCG 097073.

To examine the velocity field with higher spectral resolution we have reduced the VLA D-array data which has a spectral resolution of 22 km s^{-1}. The channel maps of the image cube with the contours of HI emission superposed on a single channel radio continuum image made from the same data using a line free channel is shown in Fig. 6.13 . Significant HI emission above a 3σ limit has been detected in nine channels with velocities ranging from 6923 to 7117 km s^{-1} giving a total width of $\sim$173 km s^{-1}. Because of the relatively poorer spatial resolution of $\sim$45 arcsec the moment 0 image shows only a blob of emission with no evidence of any diffuse extended emission which may not have been seen in the higher-resolution image. Hence the

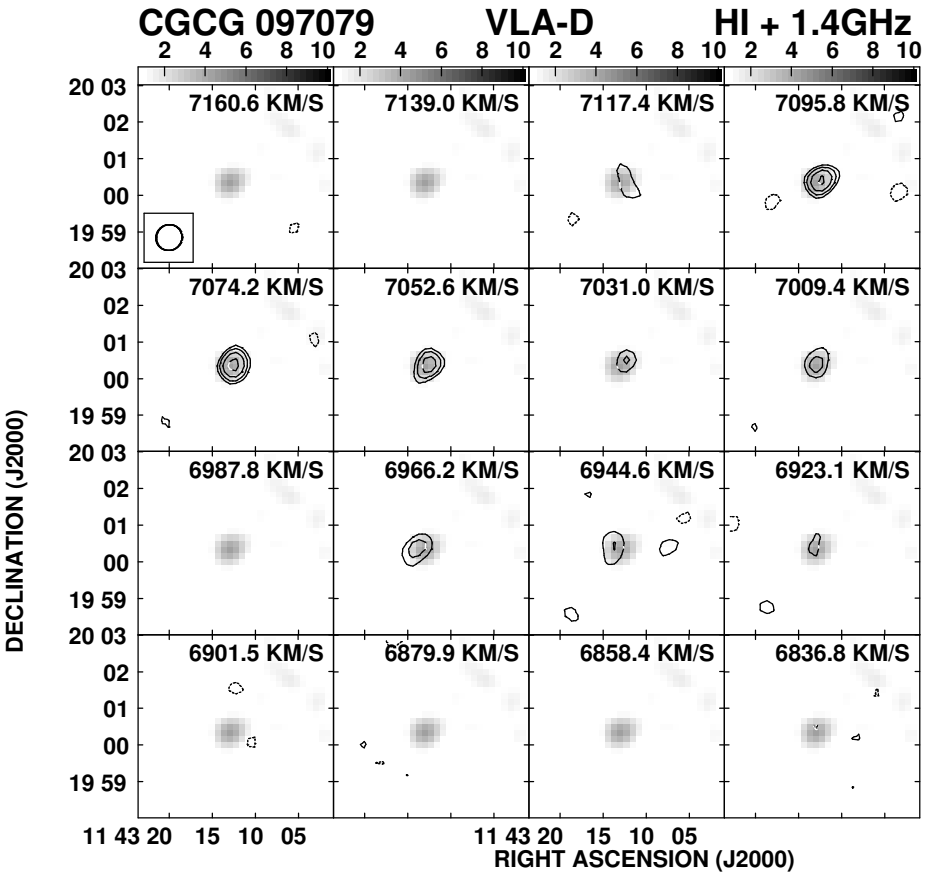

Figure 6.13: CGCG 097079: The HI channel maps in contours has been superimposed on the gray scale single channel continuum image obtained from the same data with a spatial and spectral resolution of $\sim$42″ and $\sim$22 km s^{-1} respectively. The contour levels are 0.33 × (-4, -2.82, 2.820, 4, 5.65 ...) mJy/beam.

moment maps are not presented here. However, to investigate the velocity field we have fitted a single Gaussian to HI emission in every channel whose position is marked with a + sign in Fig. 6.14. In this Figure the total intensity HI emission contours are superposed on an optical image of the galaxy with the size of the + sign signifying the error in the fit. The velocity

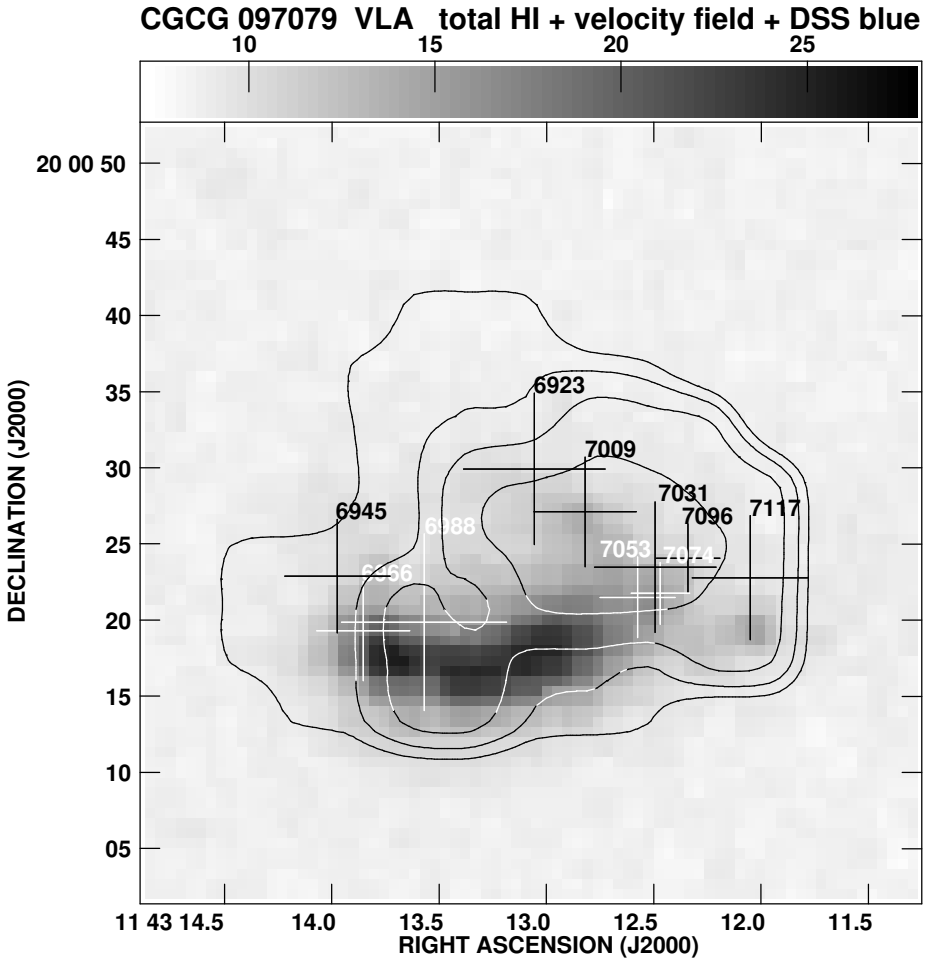

Figure 6.14: CGCG 097079: The higher spatial resolution total intensity HI contour of Fig. 6.10 has been superimposed on the DSS blue band image in gray scale. The '+' in the image marks the position of peak of the Gaussian fit to the higher spectral resolution single channel HI emission (Fig. 6.13). The size of the '+' gives the uncertainty in defining the peak. The corresponding heliocentric velocity of the higher spectral resolution channel emission has been marked clos to the '+' mark. The contour levels are 2.358×10^{20} cm^{-2} or 1.89 M$_\odot$ pc^{-2} in steps of multiples of $\sqrt{2}$. The diagonal velocity gradient and both the peaks of the HI emissions are clearly visible.

corresponding to each + sign is indicated in the Figure. The velocity of the extended emission on the north-western side has a velocity gradient which decreases from ∼7120 km s^{-1} on its south-western side to ∼6920 km s^{-1} on the north-eastern side, with the central velocity being close to the systemic velocity of the galaxy of ∼7000 km s^{-1}. The velocity of the HI gas close to the arc of star formation decreases from ∼7050 km s^{-1} on the western side to ∼6950 km s^{-1} on the eastern side. This shows that the gas in the disk as well as the more extended extra-planar HI gas which has been affected by ram pressure due to the ICM have similar kinematic properties with a same sense of rotation. It is worth noting that Hota, Saikia & Irwin (2006; Chapter 4) have found similar properties of the HI gas in the edge-on Virgo cluster galaxy NGC4438, where the elongated extra-planar gas has a similar sense of rotation as the HI gas in the disk of the galaxy.

(c) CGCG 097087

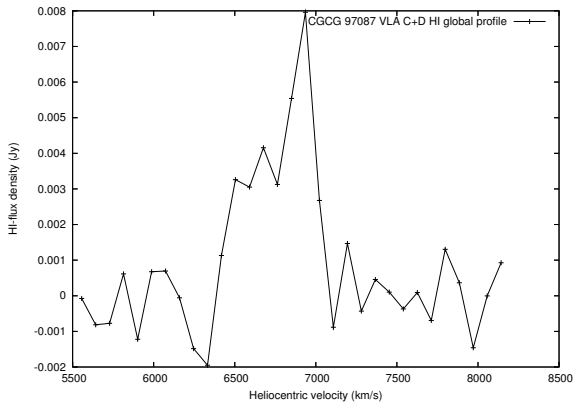

Figure 6.15: CGCG 097087: HI-global profile of the galaxy observed with a spatial and spectral resolution of ∼21″ and 86 km s^{-1} respectively.

In Fig. 6.15 we present the global HI profile of CGCG 097087 (UGC06697) taken from the image cube which has a spatial and spectral resolution of ∼21″

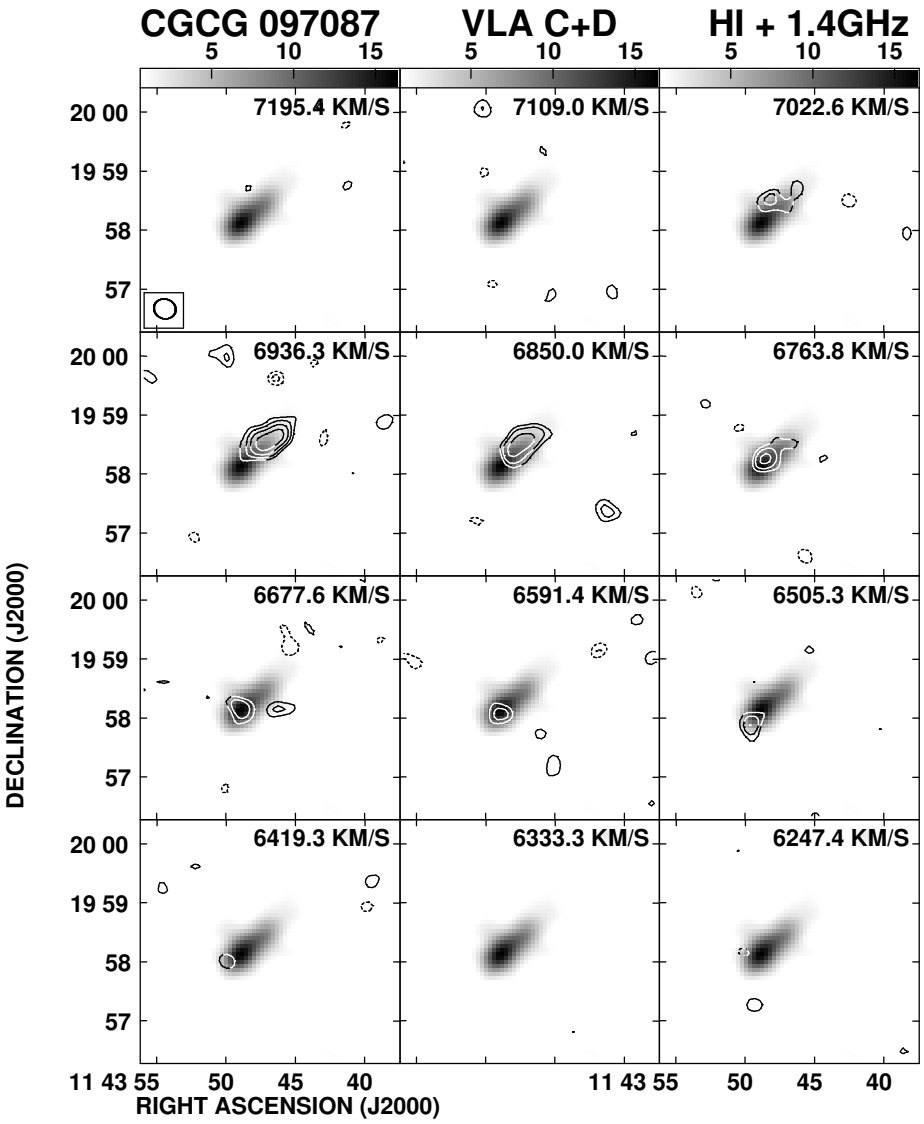

Figure 6.16: CGCG 097087: The HI channel maps in contours has been superimposed on the gray scale single channel continuum image obtained from the same data with a resolution of $\sim$21″. The contour levels are 0.3 $\times$ (-4, -2.82, 2.820, 4, 5.65 ...) mJy/beam.

and 86 km s^{-1} respectively. The profile has a wide velocity width of $\sim$600 km s^{-1} ranging from $\sim$6435 to 7030 km s^{-1}, and is very much asymmetric

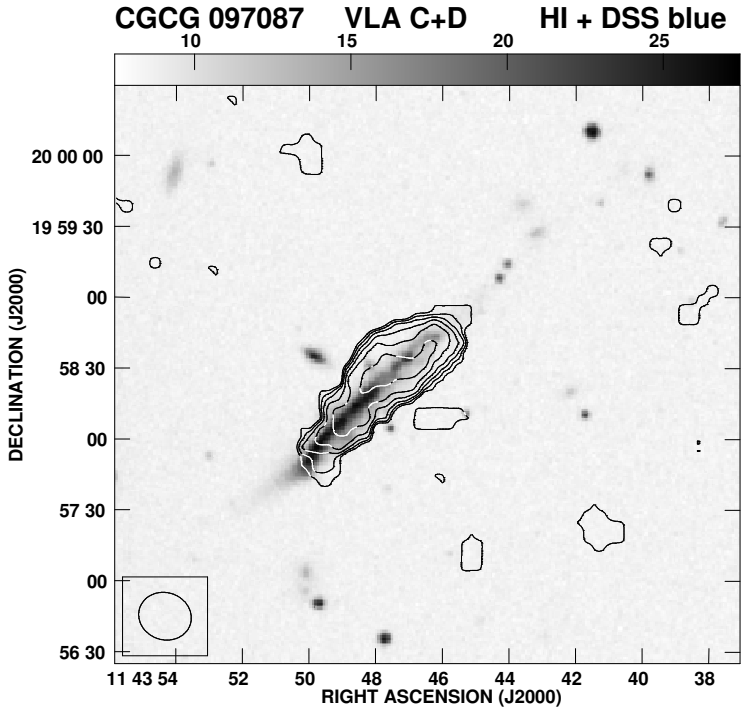

Figure 6.17: CGCG 097087: Total intensity HI contour map with a resolution of $\sim 21''$ has been superimposed on the DSS blue-band image. The contour levels are $2.358 \times 10^2 0$ cm^{-2} or 1.89 M$\odot$ pc^{-2} in steps of multiples of $\sqrt{2}$.

with respect to the systemic velocity of 6725 km s^{-1}. There is more gas on the red-shifted side of the systemic velocity, the mass being $\sim 2.9 \times 10^9 M_\odot$ compared with $\sim 1.7 \times 10^9$ M$_\odot$ on the blue-shifted side. The spectrum is consistent with that obtained with the Arecibo telescope by Gavazzi (1989). The channel maps of HI emission in contours superposed on a single-channel radio-continuum image in gray scale from a line free channel with the same resolution is presented in Fig. 6.16 . The HI emission at higher velocities are seen towards the north-west while those with lower velocities are towards the south-east. DG91 reported detection in three velocity channels, namely at 6506, 6850 and 6936 km s^{-1}. Our recent re-analysis of the data shows

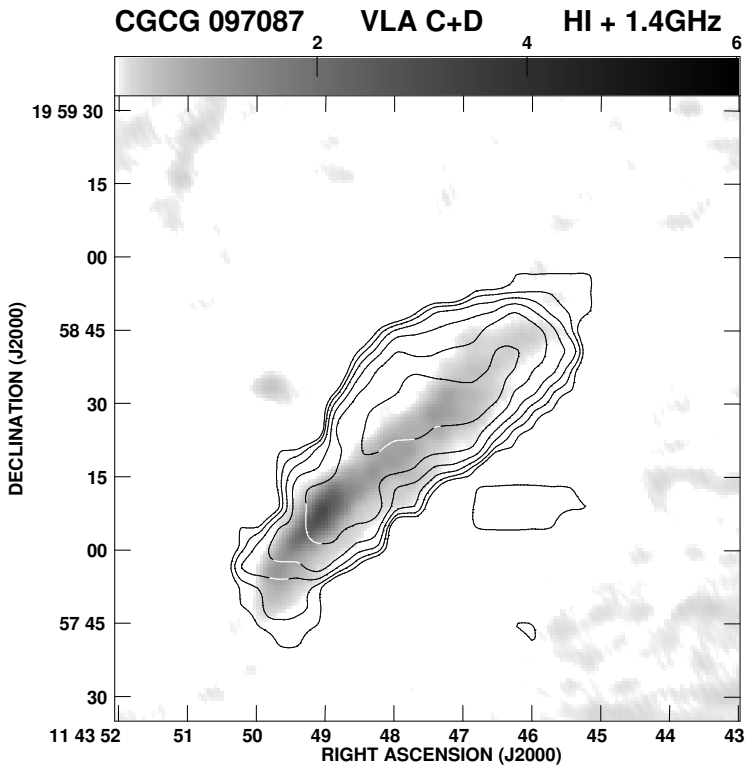

Figure 6.18: CGCG 097087: The same total intensity HI contours have been superimposed on the 1.4GHz radio continuum image made with a higher resolution of $\sim 4''$. The contour levels are $2.358 \times 10^2 0$ cm^{-2} or 1.89 M$\odot$ pc^{-2} in steps of multiples of $\sqrt{2}$.

emission in 8 channels at $\geq 3\sigma$ level over a velocity range of $\sim$6420 km s^{-1} to 7020 km s^{-1} spanning a range of $\sim$600 km s^{-1}.

We have generated the moment maps with a cut off at 3σ and shown the moment 0 image with the total-intensity HI emission contours superposed on the DSS blue-band optical image in Fig. 6.17 The total HI mass in the region of the bright optical disk of the galaxy is $\sim 1.4 \times 10^9$ M$_\odot$ compared with $\sim 3.2 \times 10^9$ M$_\odot$ for the blob of HI emission towards the north-west. The moment 0 image is shown superposed on the VLA B-array continuum image with an

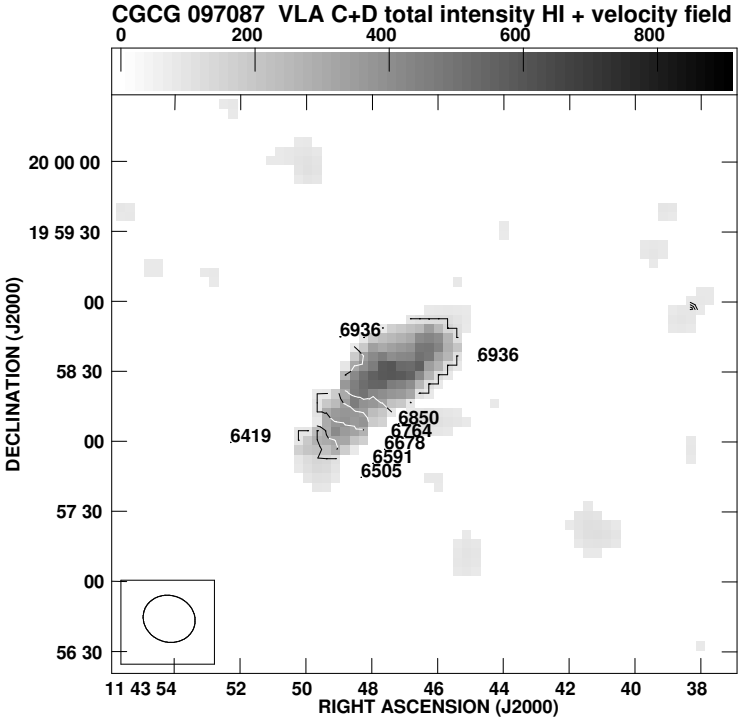

Figure 6.19: CGCG 097087: The intensity weighted HI velocity field have been superimposed on the gray scale image of the total intensity HI. The numbers close to the iso-velocity contours give the heliocentric velocity at intervals of the channel width of $\sim$86 km s^{-1}.

angular resolution of $\sim 4''$ made from archival VLA data. The tail of radio continuum and HI emission are oriented along very similar PAs and appear to be of similar extents in this Figure. However, lower resolution images of the tail by Gavazzi & Jaffe (1987) show that the tail of radio continuum emission extends to $\sim 3'$(75 kpc), much larger than the extent of HI emission which extend only up to 25kpc from the center of the galaxy (defined by the peak of the high resolution radio continuum observation).

The moment 1 map with the iso-velocity contours superposed on the HI total-intensity contours is shown in Fig. 6.19. The HI emission coincident

with the high-brightness optical disk shows evidence of solid body rotation, while the north-western region has a similar velocity of ∼6940 km s^{-1}.

6.5 Discussion and concluding remarks

HI observations of all the three galaxies CGCG 97073, 97079 and 97087 (UGC6697) in the cluster Abell 1367 which have been presented here show the detailed distribution of the gas. Earlier HI observations of these galaxies with the VLA C- and D-arrays reported by Dickey & Gavazzi (1991) showed the location of a few regions of HI emission in different velocity channels. Our analysis of their data as well as more recent VLA D-array data with higher spectral resolution have revealed further details of distribution and kinematics of the HI gas. In all the three galaxies the mass of HI gas is ∼20-30% larger on the down-stream side of the galaxies, showing that the distribution of the HI gas is affected by the ram pressure of the ICM consistent with earlier suggestions (e.g DG91).

The directions of the tails of non-thermal radio continuum as well as Hα emission suggest that CGCG 97073 is moving towards the south while CGCG 97079 is moving towards the south-east. In CGCG 97073 the HI gas appears to have a sharper gradient of the contours on the down-stream side roughly opposite to the arc of starformation region which is possibly caused by compression of gas due to the ram pressure of the ICM. There is a suggestion of a similar effect on the western side of CGCG 97079. The sharper gradient in the HI contours may be caused by the accumulation of gas in the down-stream side due to the effects of ram pressure. The total extent of the HI gas is ∼8 kpc, 8 kpc and 37 kpc for CGCG 97073, 97079 and 97087 respectively, which is much smaller than the corresponding tails

of non-thermal emission which extend for 75, 60 and 75 kpc respectively in the low-resolution images (Gavazzi & Jaffe 1987). The Hα tails also extend for distances of 50, 75 and 55 kpc respectively which are also much larger than the regions of HI emission.

Results of three-dimensional numerical simulations of a spiral galaxy moving through a hot intracluster medium with its disk inclined at different angles to the direction of motion can produce a wide range of observed structurs (e.g. Quilis, Moore & Bower 2000; Roediger & Brüggen et al. 2006 and references therein). A comparison of the distribution and kinematics of the HI gas in CGCG 97079 with the results of these simulations shows that the gas in the disk of the galaxy is pushed backwards by the ram pressure of the ICM. The gas exhibits systematic rotation about the systemic velocity and is possibly still bound to the parent galaxy.

The direction of the radio tail in CGCG 97087 (UGC6697) also suggests that this edge-on galaxy is moving towards the south-east. The HI observations show that while the gas associated with the higher brightness region of the optical galaxy exhibits solid-body rotation, most of the HI gas is pushed towards the north-west and has an almost constant velocity of $\sim$6940 km s^{-1}.

6.6 References

Abadi M.G., Moore B., Bower R.G., 1999, MNRAS, 308, 947

Bekki K., Couch W.J., 2003, ApJ, 596, 13L

Boselli A., Gavazzi G., Combes F., Lequeux J., Casoli F., 1994, A&A, 285, 69

Bosma A., Casini C., Heidmann J., van der Hulst J.M., van Woerden H.,

1980, A&A, 89, 345

Cortese L., Gavazzi G., Boselli A., Iglesias-Paramo J., Carrasco L., 2004, A&A, 425, 429

Cortese L., Gavazzi G., Boselli A., Franzetti P., Kennicutt R.C., O'Neil K., Sakai S.,2006, astro-ph/0603826

Dickey J.M., Gavazzi G., 1991, ApJ, 373, 347

dressler A., 1980, ApJ, 236, 351

Gavazzi, G., 1978, A&A, 69, 355

Gavazzi G., 1989, ApJ, 346, 59

Gavazzi G., Jaffe W., 1987, A&A, 186, 1L

Gavazzi G., Tarenghi M., Jaffe W., Boksenberg A., Butcher H., 1984, A&A, 137, 235

Gavazzi G., Contursi A., Carrasco L., Boselli A., Kennicutt R., Scodeggio M., Jaffe W., 1995, A&A,304, 325

Gavazzi G., Marcelin M., Boselli A., Amram P., Vlchez J.M., Iglesias-Paramo J., Tarenghi M., 2001a, A&A, 377, 745

Gavazzi G., Boselli A., Mayer L., Iglesias-Paramo J., Vlchez J.M.,Carrasco L., 2001b, ApJ, 563, 23L

Gunn J.E., Gott J.R. III J., 1972, ApJ, 176, 1

Hota A., Saikia D.J., Irwin J.A., 2006, MNRAS (in preparation; Chapter 4)

Kantharia N.G., Ananthakrishnan S., Nityananda R., Hota A., 2005, A&A, 435, 483 (Chapter 5)

Katz N., White S.D.M., 1993, ApJ, 412, 455

Quilis V., Moore B., Bower R., 2000, Sci, 288, 1617

Roediger E., Brüggen M., 2006, MNRAS, 369, 567

Schulz S., Struck C.,2001, MNRAS, 328, 185

Sun M., Vikhlinin A, 2005, ApJ, 621, 718

Vollmer B., Cayatte V., Balkowski C., Duschl W.J., 2001, ApJ, 561, 708

West M.J., Villumsen J.V., Dekel A., 1991, ApJ, 369, 287

CHAPTER 7

Conclusions and future work

7.1 Concluding remarks

This thesis presents an observational study of a few nearby galaxies which are good candidates for studying different processes such as superwinds in starburst galaxies, nuclear outflows in active galaxies and ram pressure stripping and tidal interactions in clusters or groups of galaxies, which could lead to gas-loss or displacement of gas from the disk of the host galaxy. Using radio continuum and HI observations with the GMRT and the VLA we have found morphological and kinematic evidences of these processes affecting the gas in galaxies. We identify features like tails of radio continuum and HI emission, compressed total-intensity HI contours, asymmetric HI−emission global profile, blue-shifted HI−absorption lines, trailing velocity field of the extra-planar emissions as signatures of such processes. Identification of these features and studies of these processes in larger samples covering a large redshift range would help understand global gas loss processes and implications on galaxy evolution. The results on different galaxies discusses in this thesis are presented below.

- In NGC1482 we have imaged the central starforming region with the VLA and found that it lies at the base of the Hα and X-ray outflow

bi-cone and presumably driving the superwind outflow. From the low-frequency, radio-continuum luminosity we have estimated the energy supply from the supernovae to drive the outflow to be $\sim 10^{57}$ ergs. However, an estimate of the total energy in all the different components of the outflow is required before determining whether the energy in the supernovae is adequate to drive the superwind. In our HI observation with the GMRT we found two blobs of HI−emission with masses $\sim 10^8$ $M_\odot$ on opposite sides of the central starforming region orthogonal to the outflow axis with a central gap in the emission map. Apart from these rotating HI blobs we have detected multi-component HI−absorption against the central region. Although the peak absorption lies near the optical systemic velocity of the galaxy and shows sign of gas rotation the absorption profile is asymmetric towards the blue-shifted side; it has an HI−absorption component having maximum blue-shift of 160 km s^{-1} while a feature on the red-shifted side has a maximum red-shift of 90 km s^{-1} relative to the optical systemic velocity. These observations suggest that HI clouds are possibly driven outwards by the superwind outflow, clearing off gas from the central region of this S0 galaxy.

- NGC6764 is a composite galaxy which has an AGN and exhibits evidence of starburst activity. We have imaged the bi-polar radio-bubbles oriented roughly along the minor-axis of the galaxy. The radio bubbles are dominated by synchrotron plasma and have a north-south asymmetry in brightness and extent. The bubbles exhibit a lateral asymmetry in its spectral index distribution. We found that features in the radio bubbles seem to correlate with Hα filaments extending out from the nuclear region. The velocity gradient of the Hα emission from

this region suggests a possible minor-axis outflow. We have imaged the nuclear region with high resolution which shows the radio nucleus, extended emission which could form the base of the bubbles and a possible jet-like structure towards the south-west. The HI observations show a higher concentration of HI on both ends of the stellar bar with a central depletion which could be due to ionisation or phase transition to molecular gas. We have detected an HI−absorption line against the central continuum source with peak absorption near the systemic velocity. There is a weak HI−absorption component blue-shifted by 120 km s^{-1} with respect to the systemic velocity. A CO line ratio map, a plume of CO emission and a component of CO-line emission blue-shifted by 110 km s^{-1}, similar to that of HI absorption component, all suggest that the atomic and molecular gas are being kinematically affected. All these features suggest that the AGN-driven radio bubble outflow, and superwind from the young starburst in this composite galaxy have been driving the ISM outwards in the vicinity of the central region of this galaxy.

- In NGC4438 we have unambiguously identified the nucleus of the galaxy. The nucleus has an inverted radio spectrum confirming it to be an AGN. A mini double-lobed structure with lobes asymmetric in size, brightness and distance from the nucleus is seen. Both these lobes have associated Hα and soft X-ray emission in the shape of a shell. This asymmetry could possibly be due to the asymmetric distribution of the ISM primarily due to ram pressure of the ICM. At lower resolution we have detected the western diffuse emission at 617 MHz with the GMRT. This western diffuse emission co-spatial with most of the stripped ISM

components have a flatter spectrum at higher frequencies suggesting possibilities of contributions from both thermal and non-thermal components. In our HI observations we have detected HI from the disk of the galaxy, which was not detected earlier, in addition to extra-planar HI gas which is displaced from the disk. The iso-velocity contours appear to diverge at the interface between the disk and the extra-planar gas, while at larger distances they appear to curve inwards. These are similar to those seen in the Virgo cluster galaxy NGC4522 which is undergoing ram pressure stripping. We have discovered a 50 kpc long faint tail of HI having a mass of 140 million solar mass to the north-west of the NGC4438−NGC4435 system. This HI−tail partially coincides with an extremely faint ($\mu_v > 28$) stellar tail, which has been seen in deep optical imaging of intra-cluster light. Such tails have not been predicted by the simulations of interaction between NGC4435 and NGC4438. Hence it seems to be a remnant of some past event involving stellar and gas loss processes in the evolution of this system. At a similar velocity to that of the tail we also have imaged the dwarf irregular galaxy IC3355 which lies close to the tail and seems to comprise of two velocity systems at optical wavelengths.

- In our observations of the group of galaxies Ho 124 with the GMRT we have found that the tidal radio continuum bridge has a very steep (-1.8) spectral index possibly due to the aging of the plasma in it. NGC2814 has a radio continuum tail pointing in a different direction from the radio-bridge. Our HI observations showed a large one-sided HI loop to the north of the edge-on galaxy NGC 2820, trailing the galactic rotation. There is no radio continuum Hα and X-ray counterpart to this

giant HI loop. On the side opposite to the loop the total intensity HI contours are seen compressed. Similarly, in the galaxy NGC2814 HI and radio continuum contours again look compressed on the side opposite to the radio continuum tail. We have estimated that the superwind cannot create such a large one−sided HI loop but ram pressure of the group medium with the assistance from tidal interaction is the most plausible explanation. In the same group, NGC2805 shows accumulation of HI on the down-stream side opposite to the side showing a starformtion arc. The HI loop, compressed HI and radio continuum contours, radio continuum tails and the starformation arc strongly support a paradigm in which evolution of the Ho 124 group is governed by both tidal forces due to the interaction and ram pressure due to motion of the member galaxies in the IGrM.

- To further study the effects of ram pressure stripping, we imaged the cluster A1367 in HI where three of its galaxies have the longest, multi-phase, ram pressure stripped tails. In all the three galaxies HI gas seems to accumulate on the down-stream side, with the HI gas being opposite to the side exhibiting arcs of starformation in two of the galaxies. The HI contours on the down-stream side are do not resemble the radio continuum or Hα tails which extend for distances of 50−75 kpc. The HI gas appears bound to the galaxy showing 20-30% higher concentration on the down-stream side as expected in hydrodynamic simulations of ram pressure stripping.

In this study we have found a number of interesting results on a few nearby galaxies where different gas-loss processes have modified the morphology and kinematics of the ISM and/or the stellar distribution of the

respective parent galaxies. We have found evidence of blue-shifted HI absorption lines driven outwards by the starburst-driven superwinds and/or AGN-driven nuclear outflows. The synchrotron plasma outflowing from an AGN in a composite galaxy has been suggested to be interacting with the superwind which also drives other components of the ISM outwards. In groups or clusters of galaxies we have discovered an HI loop, HI tails, regions of compressed HI, trailing velocity fields, slow-rotating extra-planar gas, displaced ISM and asymmetries in various radio continuum or HI features as evidences of ram pressure stripping mechanism affecting the member galaxies. The results obtained from this study illustrate the manifestations of gas loss processes in galaxies existing in different environments, and should provide valuable insights for future investigations with larger statistical samples towards a more complete understanding of gas loss processes in galaxies and their implications on galaxy evolution.

7.2 Future work

In the case of starburst-driven superwinds, the contributions of thermal and non-thermal radio-continuum emitting plasma to the outflowing gas is not well known. Although diffuse halos of radio continuum emission are known, the fraction of energy carried by the relativistic particles in the superwind outflow is not well determined. Deep, high-resolution, low-frequency observations may reveal the relativistic gas entrained in the superwind outflow. Similarly contributions from molecular gas, dust and neutral gas are poorly known. Recent high-sensitivity and high-resolution observations have revealed molecular outflows in a few galaxies such as M82, NGC253, NGC2146

and NGC6764. Detecting the superwind entrained HI either in emission or absorption from a well-defined sample of starburst-driven superwinds would help not only estimate the contribution of neutral gas to the outflow but also can constrain models on efficiency of the supernovae energy driving the outflow. A multiwavelength study of a well-defined sample of ULIRGs with known outflows should provide important inputs towards understanding these aspects. At radio wavelenghts observations with the GMRT with its unique configuration of antennas would provide information over a range of angular scales from one observing run.

Amongst nearby galaxies with an AGN, such as the Seyferts, issues such as the driving force or the energy imparted to the ISM are still not well understood, although the jets could be as energetic as the superwind. Some of these systems which exhibit both AGN and starburst phenomena will serve as good cases to understand the interplay between these two forms of activity. As in the case of NGC3079, observations with the GMRT at longer wavelengths with a range of resolutions are expected to reveal new aspects of these galaxies. In the case of Seyferts with bright radio jets, HI studies have stressed largely on probing the neutral gas in the nuclear regions. Future HI observations could help probe jet-ISM interaction as well and help us understand the physics of these interactions.

Ram pressure stripping has been invoked to understand the properties of the gaseous components of cluster galaxies for long, but the fate of the gas stripped from galaxies is not very clear. Recently 50 to 100 kpc long tails of HI, Hα, X-ray and radio continuum emission have been discovered. Since only a few such long-tailed objects are known, the evolution of the gas in the tails are poorly constrained. The stripped cooler gas may condense to form stars or they may get vaporised coming in contact with the hot ICM. For the

long tails seen in X-ray emission magneto-hydrodynamic simulations have suggested the presence of relatively strong magnetic fields for the stability of such long, soft X-ray emitting tails. This would also increase the probability of detecting these tails at low radio frequencies due to synchrotron ageing of the radiating particles. In NGC4388 and NGC4438 the long HI tails are very close to the optically faint stellar tails, but the possible correlations need further investigation. The velocity fields of the stripped HI tails are also unclear; they would provide important inputs towards understanding possible turbulence in the tails. Since very few such tails are known, it would be interesting and important to detect such long tails in HI as well as in low-frequency radio continuum emission using both the GMRT and the VLA.